Advanced Materials Research Laboratory

Department of Mechanical & Aerospace Engineering

University of Strathclyde

The Influence of Microstructural Condition and Applied Load on the Tribological Response of Ferrous Alloys in Sliding

Ronnie George Woodward

A thesis submitted in fulfilment of the requirements
for the degree of Doctor of Philosophy

September 2022

Abstract

The wear of ferrous alloys is an important context in mechanical engineering. There are moving parts in nearly every mechanical system, and this therefore means that components must experience contact. This contact is inevitably accompanied by wear, and manifests through the loss of material and changes in geometry. Engineers seek to understand the way in which materials wear to extend component lifespans, reduce maintenance frequency, and improve user safety.

The wear of materials is dependent on many factors, and is not an innate property such as strength. A particular alloy can exhibit acceptable wear resistance in one context and unfavourable resistance in another. Volume losses are instead dependent on the material properties, testing variables, and environmental conditions, which together make up the tribosystem. Only through investigation of the complete tribosystem can general wear predictions and characterisations be made.

This thesis seeks to improve the state-of-the-art of ferrous tribology, with an aim of investigating the potential for life extension of mechanical components, and to push the current mechanistic understanding of how ferrous alloys wear.

The tribological response of various ferrous alloys has been investigated herein through pin-on-disc sliding wear tests under various conditions. A number of materials are examined, ranging from cast iron to alloy steels to stainless steels. Four novel experimental chapters investigate different sets of variables, their subsequent effect on the tribosystem, and present the results, discussions, and key conclusions of the thesis. Apart from the wide variety of materials tested, other variables investigated include the applied load, microstructural condition, and immersion media.

The first experimental chapter compares the sliding wear resistance of seven alloys under the same load in the dry regime. The resultant volume losses highlight the significance of beneficial oxidative wear in such scenarios, where the alloys steel and cast iron outperformed the stainless steels due to the formation of protective oxide shields.

The second experimental chapter centres on tribocorrosion, featuring the sliding wear of grey cast iron, AISI 4330 alloy steel, and 15-5PH stainless steel under three

applied loads in the dry regime and while submerged in NaCl solution. It was found that in the dry regime, the alloy steel outperformed the stainless steel for all three loads due to the ease of protective oxide formation, whereas this ranking was inverted in the NaCl regime.

The third experimental chapter focusses on the microstructural evolution and sliding wear response of grey cast iron when subjected to spheroidising annealing heat treatments. At 6kg applied load, a non-linear transition occurred for the ten-day and fifteen-day samples, causing a significant increase in volume losses. This was attributed to the destruction of the cast iron surface integrity, causing significant deformation and resulting in severe wear.

The fourth experimental chapter examines grey cast iron in the quenched and tempered condition. The harder samples tempered at 400°C experienced higher volume losses than those tempered at 500°C due to experiencing brittle fracture, whereas the softer samples tempered at 500°C were able to slightly deform and therefore avoid these brittle tendencies.

The key findings of this thesis elucidate the macro and micro damage mechanisms of (primarily) ferrous alloys in sliding applications. The conclusions drawn are therefore practical, and of value in the engineering industry where refinement and optimisation are always sought.

Dedication

This thesis is dedicated to all British engineers, scientists, researchers, and scholars, particularly – but not limited to – those of the pre-industrial age up until the end of the second industrial revolution. These include the great minds of Hooke, Newton, Watt, Kelvin, Maxwell, and others who advanced our understanding of the world.

A key standout among such individuals is the late John Anderson (1726 – 1796), posthumous founder of Anderson's College, which eventually became the University of Strathclyde. Anderson, in addition to being a renowned natural philosopher of the time, was unique among his peers for his personal views – he believed that the working classes, of both genders, should receive an education. The author is proud to have attended the institution founded through his bequest.

Acknowledgements

Declaration of Authenticity and Author's Rights

This thesis is the result of the author's original research. It has been composed by the author and has not been previously submitted for examination which has led to the award of a degree.

The copyright of this thesis belongs to the author under the terms of the United Kingdom Copyright Acts as qualified by the University of Strathclyde Regulation 3.50. Due acknowledgement must always be made of the use of any material contained in, or derived from, this thesis.

Signed:

Date: 08/10/2022

Structure of the Thesis

This thesis is divided into eight chapters. The first three chapters serve as introductory, background, and methods chapters. The next four chapters are experimental in nature, and contain the key findings and discussion of the thesis. The final chapter concludes the thesis with summarising remarks and recommended future work. A list of each chapter follows:

1. Introduction to Metallic Sliding Wear
2. Review of Select Tribological Literature
3. Materials & Methods
4. Comparative Tribological Assessment of Various Engineering Alloys
5. The Influence of Load on Dry and Tribocorrosive Sliding of AISI 4330 and 15-5PH against Cast Iron
6. The Influence of Cementite Spheroidizing Duration on the Microstructure and Sliding Wear Response of Grey Cast Iron against AISI 4330
7. The Influence of Tempering and Annealing on the Microstructure and Sliding Wear Response of G350 Grey Cast Iron
8. Conclusions and Recommendations

Throughout the present study, the novel experimentally-obtained results are compared and contrasted with technical literature, such as journal articles, textbooks, and online material specification sheets. As each chapter is discrete and capable of being read individually, without the context of the surrounding chapters, they each contain their own review of selected literature. Thus, the general review of literature in Chapter 2 does not contain references specific to any chapter, but instead covers literature and information relevant for all chapters and materials in general. Each chapter therefore has its own bibliography containing the references cited in that chapter for the reader's benefit. A more detailed description of each chapter follows:

Chapter 1 introduces the reader to tribology, sliding wear, metallic materials, and other considerations of the thesis.

Chapter 2 reviews the key foundational literature associated with the thesis.

Chapter 3 discusses the materials examined in the present study and the methodology used to achieve this.

Chapter 4 contains a preliminary material selection and testing study, where seven materials are tribologically evaluated in dry sliding wear.

Chapter 5 examines three materials selected from the previous chapter in dry and saltwater sliding.

Chapter 6 examines two of the aforementioned materials in dry sliding wear after varying the material microstructures through various degrees of spheroidising heat treatment.

Chapter 7 examines one of the aforementioned materials in dry sliding wear after varying the material microstructure through various degrees of quench and temper heat treatment.

Chapter 8 concludes the thesis by providing summarising remarks, key conclusions, and recommendations for future work following on from the present study.

Research Output

Parts of this thesis have been published in journal articles, presented at conferences/symposia, and won awards throughout the PhD, as listed below:

Journal Articles

- Ronnie G. Woodward, Athanasios Toumpis, Alexander Galloway, Fiona Sillars, Tiziana Marrocco, Maider Olasolo & Andrew Wallace (2021) *The Influence of Load on Dry and Tribocorrosive Sliding of AISI 4330 and 15-5PH against Cast Iron*, Tribology Transactions
  Based on Chapter 5

- Ronnie G. Woodward, Athanasios Toumpis, Alexander Galloway (2021) *The Influence of Cementite Spheroidizing Duration on the Microstructure and Sliding Wear Response of Grey Cast Iron against AISI 4330*, Wear
  Based on Chapter 6

- Ronnie G. Woodward, Athanasios Toumpis, Alexander Galloway (2022) *The Influence of Tempering and Annealing on the Microstructure and Sliding Wear Response of G350 Grey Cast Iron*, Wear
  Based on Chapter 7

Technical Report

- Ronnie G. Woodward, MacTaggart, Scott & Co Ltd, Oil and Gas Innovation Centre (2019) *Selection and Testing of New Materials for Quiet Radial Piston Pumps*
  Based on Chapter 4

Conferences

- Ronnie G. Woodward, Athanasios Toumpis, Alexander Galloway (2019) *Sliding Wear Assessment of Various Alloys for Pumping Applications: A Comparative Study*, Doctoral Researchers Group, Strathclyde Doctoral

School, 1st Doctoral School Multidisciplinary Symposium, Glasgow, UK

Based on Chapter 4

- Ronnie G. Woodward, Athanasios Toumpis, Alexander Galloway (2019) *Sliding Wear Assessment of Various Alloys for Pumping Applications: A Comparative Study*, Society of Tribologists and Lubrication Engineers, Tribology Frontiers Conference, Chicago, IL, USA

  Based on Chapter 4

- Ronnie G. Woodward, Athanasios Toumpis, Alexander Galloway, Tiziana Marrocco (2020) *Sliding Wear of Steels Against Cast Irons*, 48th Scottish Microscopy Society Virtual Symposium, Scotland, UK

  Based on Chapter 5

Awards

- Winner – Images of Research, University of Strathclyde, Glasgow, UK (2019)
- Runner-up – JEOL SEMple Microscopy Competition, Scotland, UK (2020)

Preface

The projects presented herein are the output of three years' work from August 2018 – October 2021 (with another year to write up while working in industry ~ August 2022) spent by the author undertaking the PhD as part of the Advanced Materials Research Laboratory in the Department of Mechanical and Aerospace Engineering at the University of Strathclyde. The author also attended Strathclyde as an undergraduate student, studying MEng aero-mechanical engineering from 2013 – 2018. Numerous world events occurred in the four years since the inception of the PhD, most notably the rise and spread of COVID-19 throughout the developed world. The subsequent government reaction, including lockdown restrictions, the closure of schools and universities, and travel restrictions, significantly affected this thesis.

Sliding wear is a ubiquitous context in human society, particular since the industrial revolution, and it therefore warrants academic and industrial study. The conclusions drawn from this thesis are of a practical nature and serve to improve the state of the art of ferrous tribology in engineering applications, such as those found in mechanical machinery and components such as brake discs. In particular, the findings regarding the damage mechanisms of grey cast iron are valuable in terms of heat treatment selection and desired microstructural condition for a variety of applications. On the other hand, certain findings and conclusions drawn are fine in scale such as those regarding the resultant atomic crystallographic arrangement of tempered cast iron, and have consequences of greater concern to an industrial metallurgist.

It is the hope of the author that this thesis (and associated publications) aid current and future tribologists in their quest to push the boundaries of mechanical engineering.

Table of Contents

Chapter 1.

Introduction to Metallic Sliding Wear

1.1.   Tribology and Wear

The wear of solids is an innate consequence of their physical interaction with the world. Skin, components, parts, tools, and surfaces inevitably come into contact with one another during their life, the consequence of which in most cases is material loss. In most industrial contexts, it is desirable to minimise this wear to extend component lifespans [1.1]. Gloves are worn, components are lubricated, and working surfaces are altered geometrically, chemically, and microstructurally, to reduce the loss of material. In science and engineering, the reduction of material loss, and resultant extension of component lifespans, is critical to ensure the safe operation of machinery and to improve economic efficiency. This loss of material through mechanical action is termed wear, the study of which is called tribology (Greek – tribos – to rub) [1.2].

A common form of industrial wear is sliding, where two surfaces are in contact during respective movement (Figure 1.1). Sliding wear is seen in numerous instances, from arthritic joints in the human body [1.3] to disc brakes in automobiles [1.4], and has been the subject of intense study since the early 20th century. In particular, engineers were initially interested in the nature of contact mechanics between deformable surfaces [1.5], the relationship between mechanical properties and wear resistance, and the mechanistic action of material removal through sliding wear. Other forms of wear also exist, such as from particle impact [1.6], abrasive action [1.7], and fretting [1.8], and fall under the umbrella of tribology.

Unlike mechanical properties such as strength, hardness, and ductility (in equilibrium conditions), the sliding wear response of a particular material is a product of the entire tribosystem, and not simply an intrinsic material property [1.9]. Material specification sheets do not display a wear resistance value for a particular metal, instead they may only give a general indication for a certain process envelope of specific conditions, such as grey cast iron for use as disc brake rotors [1.10]. This is because the wear response is dependent not just on material properties, but also on external factors such as load, speed, component geometry, temperature, humidity, surface finish, and others [1.9]. A material which might be optimally wear resistant in one instance may be entirely unsuitable in another, due to a change in such variables. The entire system must therefore be carefully considered when selecting materials for tribological purposes.
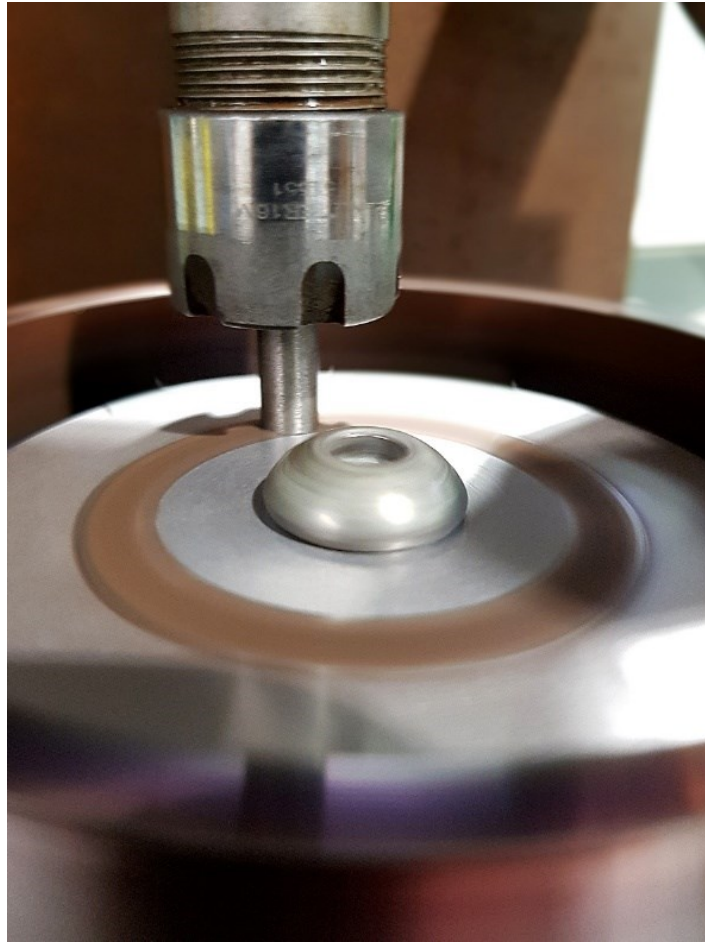
Figure 1.1 - Sliding wear test in progress.

Tribology encompasses a wide range of fields, from palaeontology to biomedical science to entomology [1.11], [1.12]. In these fields, the exact tribological subject matter varies significantly – palaeontological tribology focusses on discerning the typical diets and chewing habits of dinosaurs [1.11]. Entomological tribology, on the other hand, can deal with the frictional behaviour and wear of the skeletal thoracic hinge peg used by click beetles to propel themselves into the air [1.12]. In mechanical engineering, the subject matter is typically machinery contexts, involving components and parts in contact. The physical surfaces studied are therefore engineering materials – polymers, composites, ceramics, or metals. Of these, the most studied and well-established material family in tribological research is the metals group [1.13], due to their widespread use in mechanical engineering.

1.2.   Metallic Materials in Nanoscale Contact

Metallic surfaces are often treated to a designated level of roughness/smoothness [1.14] through machining, polishing, lapping, or grinding. These techniques aim to achieve an even surface, free from local protrusions and warped curvatures [1.15] by progressively removing material in smaller and smaller stages until the acceptable finish and roughness are achieved. In metallography, samples are often ground and polished to achieve a mirror finish, and strain-free surface. Despite this level of polish, all surfaces are rough at the nanoscale and exhibit peaks and valleys and local areas of protrusions, termed asperities [1.16]. These asperities rise upward away from the bulk of the metal and are the first point of contact between two surfaces. When such bodies gently meet, the true area of contact is significantly smaller than the whole surface of the sample due to only the tallest asperities touching [1.17]. Under increased applied load, or if any relative movement arises between the surfaces, then these asperities may deform and fracture, exposing the next highest range of asperities and increasing the true area of contact. In theoretically perfect sliding under theoretically perfect conditions, consideration is given to individual asperity contact and deformation, with the resultant forces and wear behaviour calculated [1.18].

As metals exhibit intermediate properties of ductility and brittleness, multiple modes of damage often occur on metallic components [1.19]. Many damage mechanisms can also occur in both a brittle and ductile fashion [1.20]. The evaluation of wear is therefore multifaceted, and requires investigation and evaluation using multiple techniques to develop a mechanistic understanding. A distinction can first be made between damage that removes material, versus damage that simply deforms material. This is usually determined by the exact damage mechanism occurring [1.21], but can also be a factor of the material structure. For example, grey cast irons often experience material removal due to spallation of the metallic matrix above a graphite flake cavity [1.22]. Other alloys with more homogeneous microstructures, such as steels, do not have these weak areas and so have greater fracture toughness values than grey cast irons [1.23]. Despite this, all metallic materials do experience material removal at asperity junctions, and this material removal mechanism can operate through the plastic shearing of multiple layers, with an additional fracture behind these layers from which they detach from (Figure 1.2) [1.21]. In cases where one of the contact faces is ductile enough to deform, instead of fracturing like in the previous example, a

rounding of the asperity tips occurs as material is displaced downward longitudinally and widened laterally [1.24].
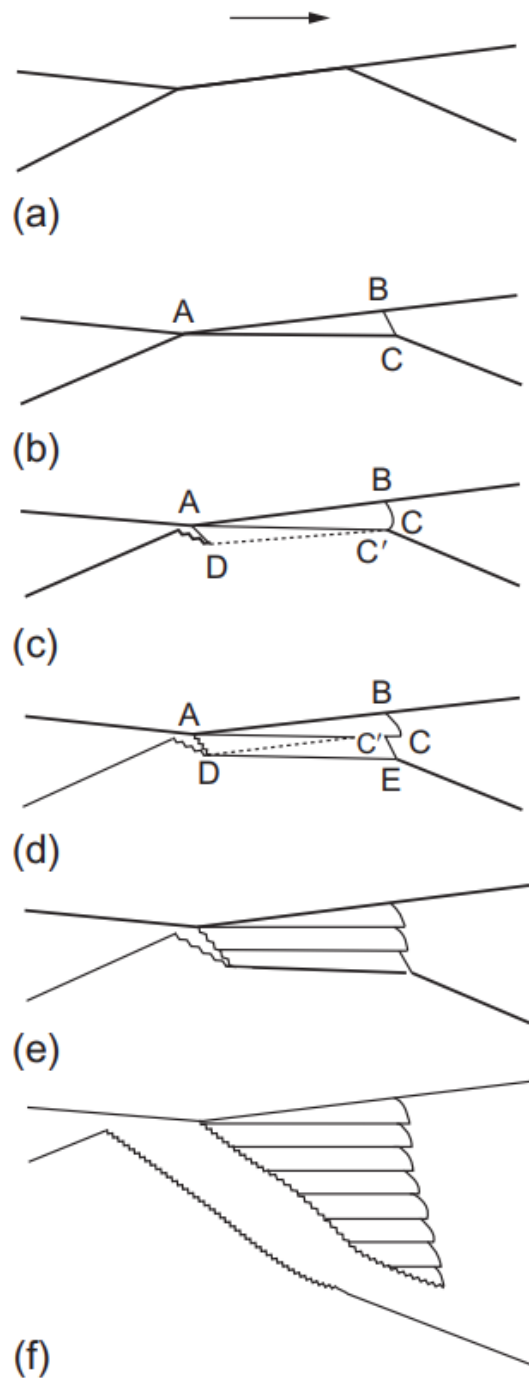
Figure 1.2 - Schematic of asperity fracture: (a) Asperities from two bodies in contact, (b) Plastic deformation of shear layer on bottom body, (c) Shear crack initiates while another layer is plastically deformed, (d) Continuation of shear crack at the root while further layers are plastically deformed, (e) Plastically deformed zone begins to detach from bottom body along shear crack, (f) Complete particle detachment. Adapted from [1.25].

The mechanisms of how asperities deform and fracture is critically important for understanding how materials wear at the nanoscale, however, in practice, and indeed throughout this thesis, the materials in question (see Chapter 3) are prepared and used in a relatively rough condition, with most only being ground to the micro level. In this instance, consideration of individual asperities, and their contact mechanics, is redundant due to the large areas of contact and macroscale damage occurring. A more pertinent discussion is therefore how metals deform at the micro and macroscale during sliding.

1.3. Macro and Micro Damage Mechanisms of Metallic Materials

A solid body sliding over a counter body results in wear. The type and severity of wear is determined by a number of factors including materials, geometry, sliding conditions, and environment [1.9]. Assuming that such variables are held constant, the wear response is then governed by the sample materials. Metallic materials wear differently from ceramics [1.26], which in turn wear differently from polymer composite materials [1.27]. Metallic tribology, therefore, requires a broad knowledge of damage mechanisms to assess if the wear is significant. Investigation of this wear is important because not all damage is significant enough to affect industrial components. Moreover, wear in some infrequent circumstances can be seen as beneficial. For example, when machinery is first used, such as a new engine, a "running-in" period may arise where several hours of use are required to produce enough wear to initiate the steady state operation [1.28]. Despite tribologists' best efforts, wear can usually only be minimised rather than completely inhibited. Analysing and evaluating the wear is therefore necessary to ensure that only the minimum damage is occurring, rather than an unusual highly damaging mode of wear that requires intervention.

The typical damage mechanisms in metallic sliding contexts are scuffing, scoring, ploughing (Figure 1.3), smearing, and spallation, and are thoroughly discussed by Hutchings and Shipway [1.19]. Scuffing is simply a roughening of the surface, featuring texture changes from the unworn material, but without significant changes in geometry. Scoring marks are small troughs cut into the material from a harder area on the counter body. Ploughing is an extension of this, where long furrows follow the

direction of sliding continuously. Smearing features in plastically deforming materials, where local lateral displacement of material overlaps other areas of the surface, often resulting in delamination or spallation. Spallation can be seen in many instances, and is where a chunk of material detaches from the surface. This is both an end result of other damage mechanisms, or as a mechanism in itself, such as with the previously discussed cast irons. In certain conditions, polishing of the worn surfaces is also possible where smoothening occurs without significant damage [1.29] (this is the opposite of scuffing).
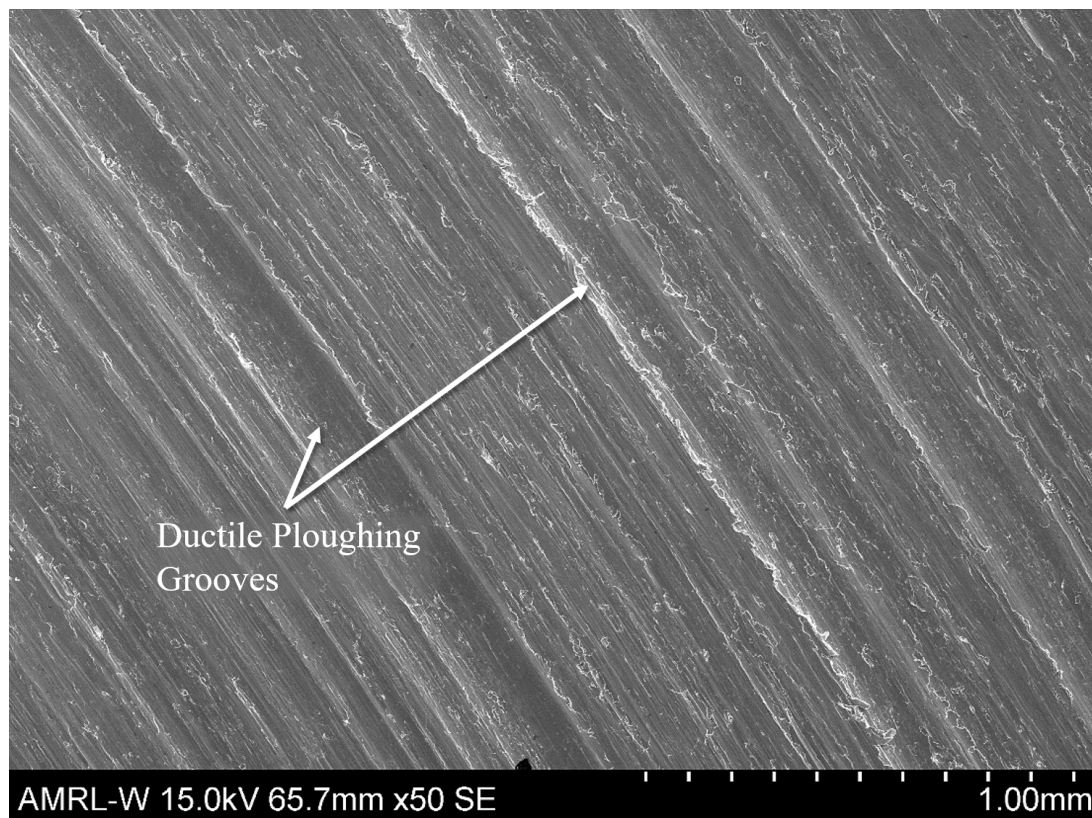
Figure 1.3 - Ductile ploughing (plastic flow) on a bronze sample.

A distinction is made in tribological literature between brittle versus ductile tendencies, and is often attributed as a key factor in whether a material is wearing rapidly or slowly [1.30]. Depending on the sliding context, either mode can be beneficial. A scuffed surface is more likely to occur on a hard, brittle material (see Chapter 4), where minor plastic deformation is resisted. Ploughing, on the other hand, is more often seen in ductile contexts, especially versus a harder counter body, where the material has been deformed easily and ploughed through. However, ploughing can also occur in a brittle fashion, where the trough features a multifaceted fracture surface

and exposed grains (Figure 1.4) [1.20]. The higher volume loss of brittle ploughing is because creation of the trough is actively removing material, whereas in the ductile fashion, material may primarily be displaced instead of removed. Spallation is primarily a brittle mode, as it involves fracture and crack propagation adjacent to the removed chip [1.31]. In unfavourable material pairings, such as when a much harder material (such as martensitic steel) is in contact with a much softer material (such as FCC bronze), the softer material will wear significantly and display high volume losses accompanied by continuous ploughing a ductile fashion (see Chapter 4). For this reason, such material combinations are avoided in industrial applications and instead substituted with more suitable alloys. On the other hand, when two materials of significant hardness are in contact, scuffing is likely to occur. Following this, if the tribological conditions are unfavourable, brittle fracture is likely to occur, resulting in high volume losses and wear rates.
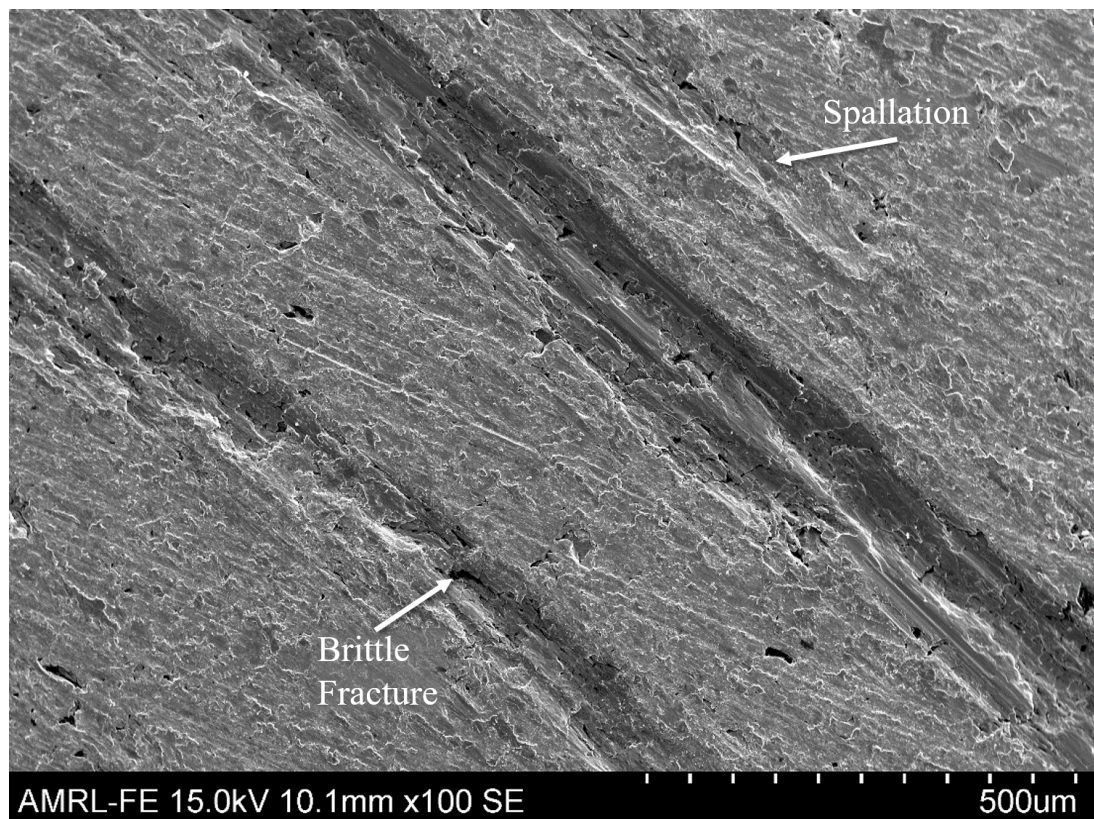
Figure 1.4 - Brittle damage on a cast iron sample.

1.4.   Passivity of Metallic Materials

The passivity of an alloy is a significant factor in predicting its wear behaviour [1.32]. Passivity and is governed primarily by the chemical composition of the material. All elements have an electrochemical reactivity that dictate whether such elements tend to form compounds to increase thermodynamic stability [1.33]. Metallic materials feature a range of electrochemical reactivities. Gold is similar to the noble gasses in that it is unreactive in most circumstances. This chemical stability is the reason gold has been found in its metallic form for thousands of years prior to industrialisation [1.33]. Iron, on the other hand, is unstable in atmospheric conditions and has a tendency to exist as a compound with other elements. Unlike gold, iron is only found in ores such as magnetite (Fe_3O_4), hematite (Fe_2O_3), and Wüstite (FeO), and must be extracted from these ores using chemical reduction and heat. The electrochemical reactivity of iron is responsible for the tendency of iron alloys to rust, in an attempt to revert back to more stable forms such as these.

Because of this electrochemical potential, iron has a negative Gibbs free energy, and is more stable in compounds than in its metallic form. The surfaces of ferrous materials, therefore, have a thin iron oxide layer, where the outermost layer has reacted with atmospheric oxygen to form a passive film [1.34]. The growth-rate of this passive film, as well as its thickness, density, toughness, and adherence to the metallic substrate can vary, depending on the exact chemical composition of the alloy. For alloy steels and cast irons, which are relatively reactive in comparison to more passive alloys, the iron oxide outer layer has a tendency to grow quickly (i.e. these alloys corrode easily). For industrial applications, such oxidation is insignificant due to only the outer nanometres oxidising, which can actually have a protective effect. Once the outermost layer of atoms oxidises, it can often shield the rest of the metal from corroding further, acting as layer of paint. Conversely, the opposite is also true in many circumstances, due to the structure of iron oxides. When active ferrous alloys corrode, such as cast irons or alloy steels, the passive iron oxide film is flaky and easily detaches from the metallic substrate. This spallation of iron oxide exposes fresh metallic atoms underneath to the atmosphere, which can then oxidise further. In unfavourable corrosive conditions, or in high temperature environments, this mechanism of oxidation – spallation – oxidation can eat its way through the metal, compromising the component, and may cause failure.

A number of factors govern whether a passive film will adhere to a metallic surface, such as the continuity of the layer, density of the layer, and the Pilling-Bedworth ratio (the ratio of the specific volume of the oxide to the specific volume of the metal [1.35]). In corrosive and tribocorrosive contexts, the most desirable is the one that provides the greatest protection to the alloy underneath. Stainless steel and aluminium both show highly passive films on their external surfaces which prevent them from corrosion [1.36]. For stainless steel, these beneficial properties come from their alloying content, which often have a minimum of 11 wt% chromium. This significant chromium content results in the formation of a chromium oxide layer on the surface, instead of iron oxide as with active alloys. This chromia film is beneficial to the alloy as it is highly adherent, and more thermodynamically stable, and therefore, prevents further corrosion into the bulk structure [1.37].

In the sliding context, passive films and oxidational properties are a large influence on the wear behaviour of metallic materials. This is because the first contact of sliding samples is between their respective films instead of metal-to-metal contact as previously assumed [1.38]. The stimulation of, destruction of, or re-growth of said layer can be influential in whether two materials experience high or low wear rates and thus volume losses. For ferrous alloys such as cast irons and alloy steels, the discussion of a new wear mechanism is therefore necessary to accurately conduct tribological characterisation.

1.5.   Oxidative Wear

When two materials meet in sliding, energy is inputted to the contact area. This energy is dissipated through various ways [1.38], such as material removal. However, energy is also outputted thermally in the form of heat build-up. Temperature rises have long been associated with sliding wear [1.39], and primarily take two forms: the general temperature increase of the sample, and flash temperature rises between the contact faces [1.40]. Flash temperatures refer to the instantaneous increases over a small time window often in the realm of hundreds of degrees Celsius [1.41]. Both of these thermal outputs influence the tribological behaviour of the alloys through various ways, the most pertinent of which is their effect on passive film growth.

Temperature is a key influence on the growth rate of passive films [1.42], and the thermal output from sliding wear results in a competitive action between removal and

re-growth. At the initiation of sliding, the counter body removes a section depth of the passive layer. At this stage, the thermal output is low, so for fast sliding speeds, a further section of the oxide film is removed with each cycle. However, as sliding continues, the bulk temperature and the instantaneous flash temperatures grow, which accelerate the re-growth rate of the oxide [1.43]. Should this rate exceed the period of the sliding contact, then with each cycle, the thickness of the oxide increases. The increased depth of oxide coverage then reduces the thermal output from sliding, which reduces the growth rate of the layer until an equilibrium is reached between material removal and re-growth rate. In tribological contexts, this competitive action is called oxidation – scrape – re-oxidation [1.44]. The relationship between material removal and oxide regrowth rate is influenced by material chemistry, sliding speed, and applied load. Assuming constant sliding conditions, three general regimes can be discerned: alloys with regrowth rates slower than material removed through sliding, those with equal regrowth rates, and those with regrowth rates that exceed the rate of material removal.

In many sliding conditions, active alloys such as cast irons and alloy steels fall into the latter two categories, where their oxide layer is allowed to build up faster than it wears. This results in a phenomenon called oxidative wear (Figure 1.5) [1.45], and is a highly beneficial wear regime in terms of component longevity. This is because the oxide is not necessarily removed from the tribosystem with each wear cycle, as assumed previously, but instead is often worn, sheared, ground, and spread on the surface of the samples without complete destruction [1.46]. This changes its morphology from a weak, porous, flaky film into a smooth, adhering, lubricating glaze layer. The glaze layer has many positive effects, most notably shielding the underlying substrate from material removal and thermal softening [1.47]. It also has the benefit of reducing frictional force between the two bodies, and can form a mixed glaze layer with graphite when sliding with cast irons is involved [1.48]. Stainless steels, for all of their corrosion resistant properties, perform poorly in sliding in comparison to cast irons and alloy steels because of their poor balance between material removal and chromia regrowth rates [1.9]. This is attributed to the slower initial parabolic growth rates of chromium oxide for stainless steels than iron oxide for cast irons and alloy steels [1.9]. With each wear cycle, the chromia film is unable to regrow to the required

thickness and therefore metallic matrix wear also occurs, resulting in high volume losses.
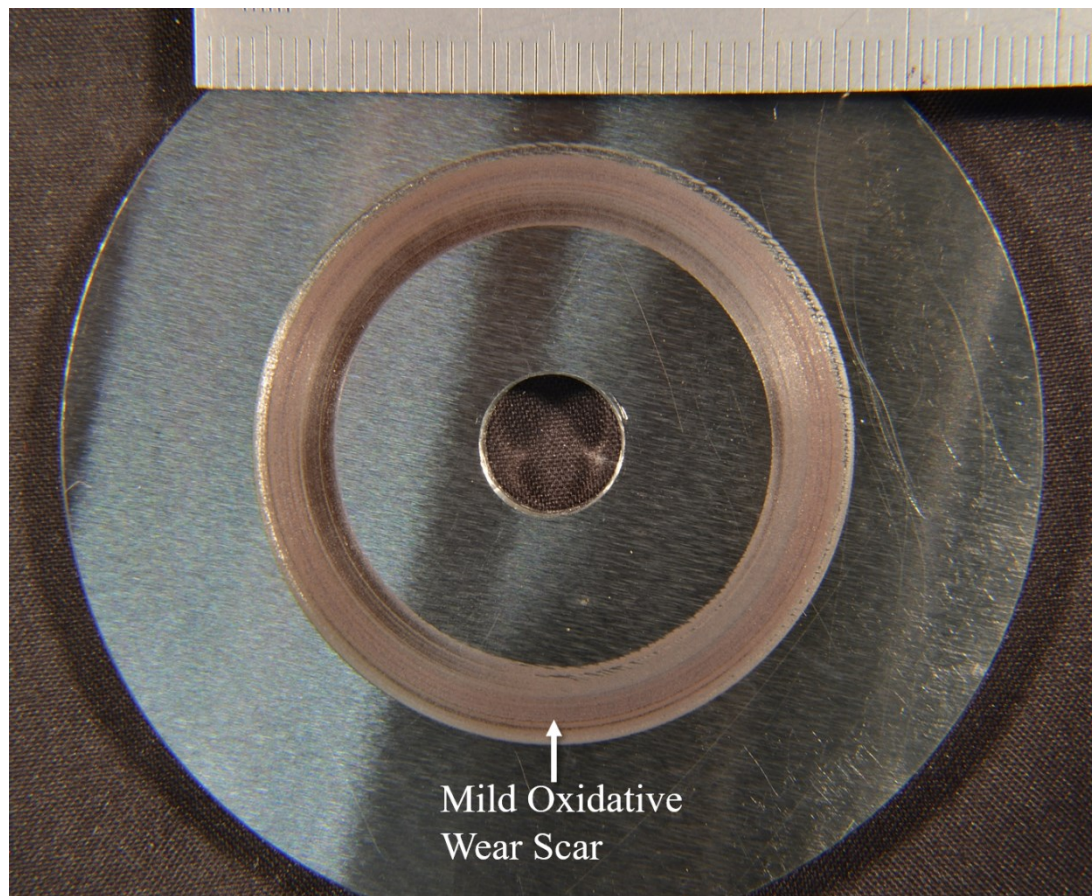
Figure 1.5 - Mild oxidative wear on an alloy steel.

This wear of the underlying metal is detrimental to the geometry of the sample and also to the counter body, as sliding wear against the metallic matrix results in harsher wear mechanisms and rougher surfaces. To simplify and rank types of wear such as oxidative and matrix wear, a categorisation of the two general types is often utilised [1.49]. Tribological literature often categorises wear into a binary choice of mild or severe [1.50]. This allows general conclusions to be drawn based on the volume loss and visual appearance of the scar. Mild wear results in heavily oxidised wear scars and low volume losses, with oxidative wear being the primary damage mechanism occurring [1.51]. Mild wear is easily discerned by visual inspection of the resultant worn surfaces through the dark red/brown discolouration from oxidation. In these instances, little damage to the metallic matrix has occurred as speed/load were not sufficient to break through the oxidative glaze layer and run-in to the bulk substrate.

Severe wear is the opposite of this, where mechanical damage has occurred to the metallic matrix, and results in high volume losses. These can easily be discerned by their bright, reflective appearance due to the multifaceted metallic matrix (Figure 1.6).
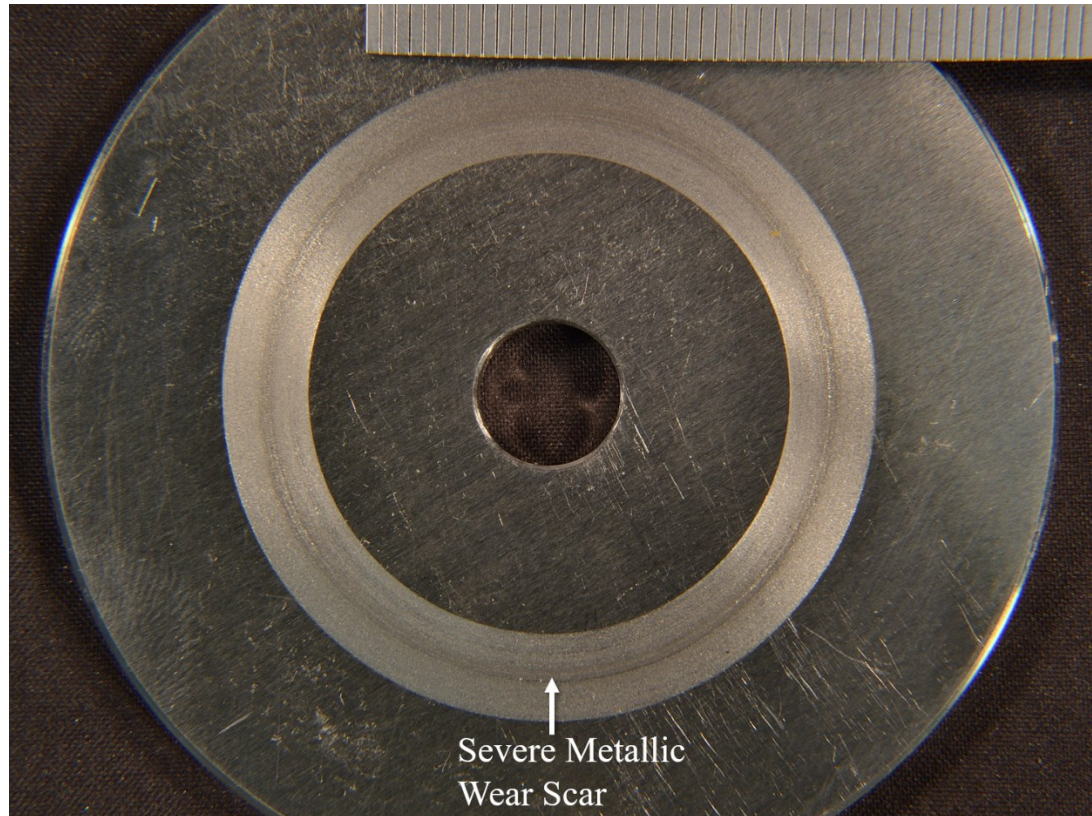
Figure 1.6 - Severe metallic wear on a stainless steel.

Transitions between wear regimes are often seen in tribological studies, and involve a significant change in wear volume losses, either from mild wear to severe wear, or vice versa [1.51]. There are two types of transitions: those that occur during sliding, without changing input variables, and those that describe the relationship between volume loss and a changing input variable, such as speed or load [1.28]. Transitions of the first type are transient in nature and can occur after some time has lapsed. They are usually thermal related, in that once sufficient heat has built up, the mechanism of wear changes in some way to produce more or less wear. For example, if a particular alloy is susceptible to thermal softening, then it may take some time for the frictional heat to increase to a suitable temperature where the material is soft enough to plastically deform instead of fracturing in a brittle manner, resulting in less wear [1.28]. The second type of transition is usually seen plotted on results graphs against

an input variable, and shows a large increase/decrease (often in the realm of 10x to 100x) in volume loss [1.22]. These are instances of non-linear behaviour of the tribosystem where the changing variable reaches a critical value that significantly changes the wear rate. For example, the dominant wear mechanism may be oxidative wear up until a certain load where the protective oxidative layer is destroyed and the mode changes to severe wear.

1.6.   Sliding Wear Configurations

Numerous types of sliding wear exist in mechanical systems. The motion and geometry of a brake pad against a brake disc is different to that of a piston inside a cylinder. The micro-movement/vibrational oscillation (fretting) of bolted parts in contact is different again. All such damaging contexts, despite being classified as types of sliding wear, require distinct experimental methods of study to accurately simulate and quantify the resultant damage.

- Unidirectional sliding wear is the term given to the relative motion observed in disc brakes and rotary piston pumps between pads and tyre flats. This type of sliding involves constant movement in a single direction, i.e. circular. Often, the wear experienced by one contact face is continuous, as it tracks the elliptical path, while the counter body sees cyclic wear as a portion of the contact path experiences contact once per rotation. In flat unidirectional sliding wear, debris can often become entrapped inside the wear scar, and contribute to abrasive action, producing more severe conditions [1.19].

- Reciprocal sliding wear is best described by the engine piston/cylinder contact regime. Here, the contact faces feature relative movement in two directions, and therefore feature changing speeds and accelerations as the cycles ramp up and ramp down. In examination of the worn faces, directionality is less pronounced, due to experiencing two opposite directions. In reciprocating sliding wear, particle entrapment is observed less frequently, due to the change of direction at the end of each cycle resulting in the debris being displaced towards the ends of the scar and out of the tribosystem.

- Fretting is a specific example of sliding wear (usually reciprocal) over small distances. This occurs when surfaces that are designed to be in stationary contact, such as bolted plates, instead exhibit small relative vibrations/oscillations [1.19]. Wear can then occur at these junctions and result in component failure due to it amplifying corrosion or reducing fatigue lifespan. Fretting wear occurs over very small distances and can therefore go undetected in mechanical systems. The order of distance is usually in the realm of microns but can even occur over nanometres.

Sliding wear can be simulated and studied in the laboratory setting through various apparatus. These apparatus, or test rigs, are sometimes entitled *tribometers* in tribology literature. A wide variety of test rigs exist, which often correspond to the desired type of sliding wear to be simulated. By approximating the conditions seen during the industrial context, tribologists can produce more representative data that may be applicable to extending the component lifespan.

The most common type of sliding wear test rig is the pin-on-disc configuration (Figure 1.7(a)). This features a flat-ended, stationary pin worn against a concentric rotating disc, and is the best example of unidirectional sliding wear. These test rigs are commonplace in tribology laboratories due to their ease of construction. A related testing configuration is the reciprocal pin-on-plate geometry (Figure 1.7(c)), which also features a pin in contact with a flat body, but this flat bodied plate is in reciprocating motion, instead of rotational. This testing configuration is more suitable for studying the wear of piston cylinders in normal use, and in high frequency use can simulate fretting conditions.

Other types of sliding wear test rigs also exist, such as block-on-ring (Figure 1.7(b)), twin disc (Figure 1.7(d)), and ring-on-ring (Figure 1.7(e)).

In this thesis, the type of sliding discussed and studied is unidirectional sliding wear, tested using the pin-on-disc configuration.
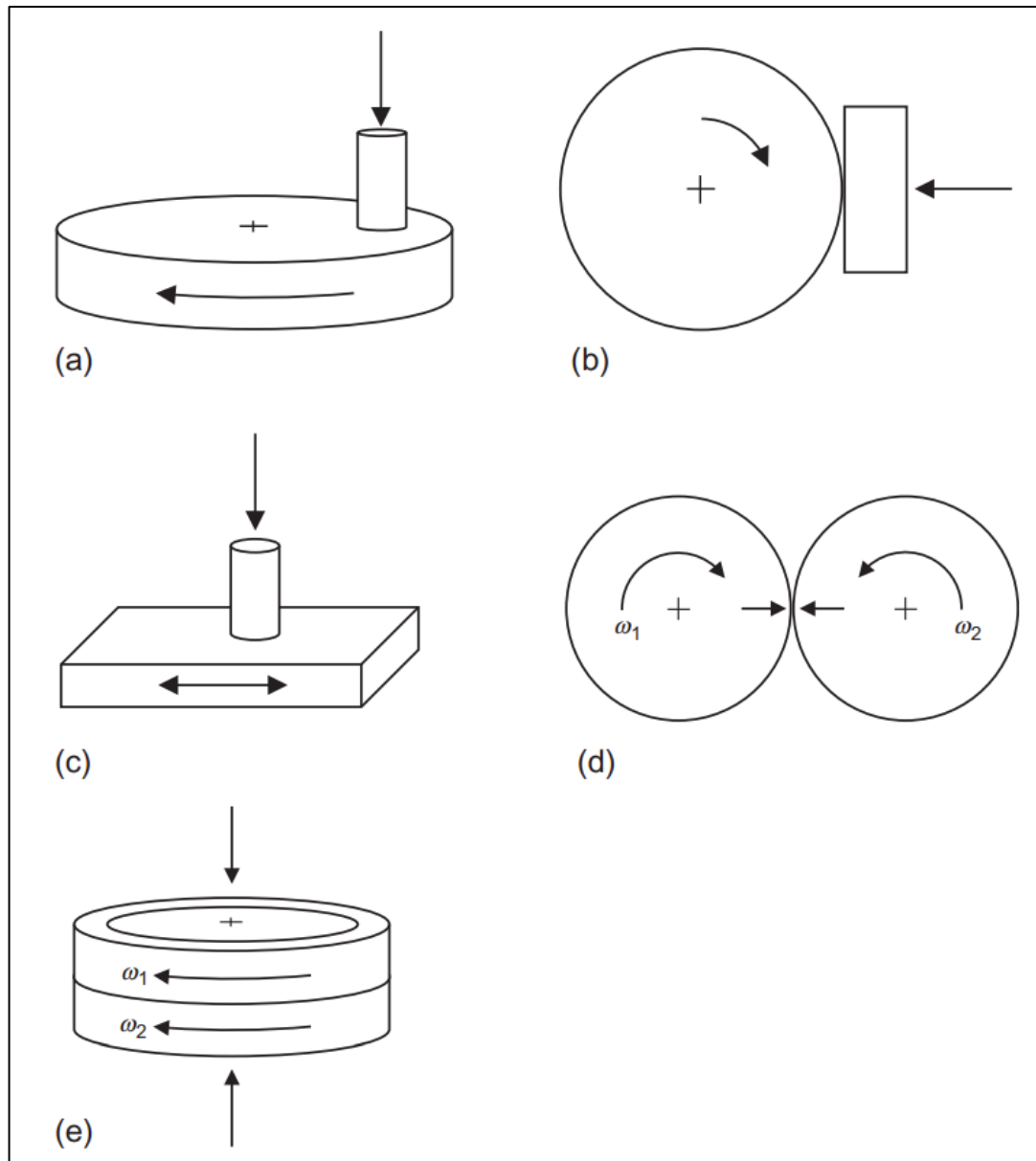
Figure 1.7 - Sliding wear test configurations. (a) pin-on-disc (b) block-on-ring (c) pin-on-reciprocating plate (d) twin disc (e) ring-on-ring [1.19].

1.7.   Motivation, Aims, and Scope of the Thesis

Tribologists study material wear to estimate and improve the lifespans of mechanical components. In many mechanical engineering contexts, the lifespan of a component or tool is determined by volume losses [1.1], and if these can be mitigated or reduced, then life extension can provide financial and environmental advantages. Iron is the base metal for thousands of engineering alloys due to its abundance, affordability, and mechanical properties. Components made of ferrous alloys are therefore the subject

of intense study in all engineering fields, including tribology. For example, a key area of study involving ferrous tribology is in the automotive engineering industry, where tribologists seek to improve the lifespan of various components, such as disc brakes [1.4], [1.52], [1.53], piston cylinders [1.46], [1.54], [1.55], and valve seats [1.56]–[1.58]. Disc brakes have been rigorously studied for many decades due to their ubiquitous safety-critical presence and their purpose as a near-consumable component. The tribocorrosive wear of piston cylinders was historically a significant problem, due to sulphur contaminants in fuel resulting in synergistic action between the reciprocal motion causing mechanical wear, and chemical attack from sulphuric acid. Valve seats frequently experience wear in the form of impact and fretting (see Section 1.6), and have frequently been studied to minimise these effects and improve fuel injection efficiency, and thus engine performance.

This thesis forms part of an effort to improve mechanical systems, and seeks to push the state-of-the-art of (primarily) ferrous alloys in unidirectional sliding. To this end, the thesis presents four novel experimental chapters, which focus on specific tribological contexts, including dry sliding wear in hydraulic pumping applications, tribocorrosive sliding wear in saltwater conditions, and automotive cast iron sliding in various microstructural conditions achieved through different heat treatments. The overarching aim of the thesis is to investigate the potential for life extension of mechanical components, and to improve the current mechanistic understanding of how ferrous alloys wear.

A list of objectives follows:

- To identify and select (primarily ferrous) engineering alloys to study.
- To quantify and characterise the wear occurring for the selected engineering alloys when subjected to sliding wear in different conditions.
- To analyse the sliding wear results and provide industrial context with scientific relevance, using accompanying experimental methods.
- To provide results that serve to improve the performance of mechanical components in industrial machinery.

To push the state-of-the-art of ferrous tribology, experimental testing and characterisation is utilised. The central experimental method used is pin-on-disc testing; a reliable tribology technique that can generate sliding wear data in most

laboratory settings (see Chapter 3). Numerous alloys in various conditions are tested in this pin-on-disc configuration to generate sliding wear data. This data mostly consists of volume losses which are then analysed and associated with the material and test conditions. The primary pin-on-disc testing is accompanied by numerous other characterisation and analysis methods, such as optical and scanning electron microscopy, x-ray diffraction, stylus profilometry, and energy dispersion spectroscopy, to provide context, and allow for deeper delving into the meaning and significance of the results.

The four experimental chapters of the thesis are presented separately, and each follow a slightly different focus and tribology sub-field. Within each chapter, an introduction section first covers the context and introduces the reader to any background topics regarding the problem statement. This allows for specificity and distinction between each chapter. Next, experimental methods unique to that chapter are introduced, along with which materials (and in what conditions) are being studied. The experimental results are then presented along with scientific discussion about their relevance and significance, before concluding with the key points. The thesis concludes with a general conclusions chapter that covers some common findings shared between the four chapters and also raises further avenues of study.

A wide variety of alloys are examined in this thesis, ranging from pearlitic cast irons and martensitic alloy steels to precipitation hardened stainless steels and leaded bronze. Apart from the chosen materials examined, the principal input variable modified between sliding wear tests is the applied load, to simulate three degrees of contact pressure between the sliding samples (full details of the experimental methodology are given in Chapter 3). The wide scope of the thesis allows for a variety of findings to be presented which are applicable in several engineering contexts.

The novelty of the thesis is derived from the specific contexts studied within each experimental chapter. Chapter 4 discusses seven materials, in 11 combinations which have not been paired before. In addition to this providing unique sliding wear data for future material selection purposes, the chapter also shows examples of pairings not typically seen in industry, such as martensitic steels worn against a leaded-tin bronze, for scientific novelty. Chapter 5 revolves around the novel environmental sliding conditions for the three studied materials, simulating environments observed in marine

applications such as seawater pumps. In this environment, little to no research has been conducted for the chosen materials individually, and certainly not in pairings. The novelty of Chapters 6 and 7 arises from the incremental heat treatments applied within. Chapter 6 is the first-of-a-kind study involving the cementite-spheroidising heat treatment of grey cast iron, of which there has not been any other studies, to the author's knowledge. Such treatments may be applied in instances where ease of machining, or a particular degree of ductility is required. The chapter then goes a step further to be the first study to characterise the damage mechanisms occurring for each degree of heat treatment against low alloy steel, and categorises the wear for each applied load. Chapter 7 features a novel study into four degrees of quench and temper heat treatments for grey cast iron and is unique in its presentation of qualitative data such as damage mechanisms and subsurface deformation. These novel aspects of the thesis therefore push the bounds of industrial tribology, and make contributions to established scientific literature. This is also evidenced through the publication of three of the four experimental chapters as journal articles.

The overall hypothesis of the thesis, generally, is two-fold:

- That volume losses from wear will generally increase with applied load.
- That volume losses will generally decrease with increasing surface hardness of the materials.

These hypotheses are derived from the established tribological wisdom in early wear literature (see Chapter 2) but are not concrete in conviction. For example, the presence of non-linear wear phenomena (see Section 2.3) may result in a sudden change in the resultant wear.

To understand where each chapter resides within the tribological state-of-the-art, a brief history of sliding wear technical literature must first be covered, including major publications and theories from the early 20th century. This is covered in Chapter 2. Further reviews of relevant literature including more recent developments with advanced technology are found within the introduction to each chapter, citing articles and passages particularly pertinent to that chapter.

References

[1.1] C. Lipson, "Introduction," in *Handbook of Mechanical Wear*, 1st ed., C. Lipson

and L. V. Colwell, Eds. Ann Arbor: The University of Michigan Press, 1961, p. 1.

[1.2] OED Online, "tribology, n," *Oxford University Press*, 1966. [1.Online]. Available: https://www.oed.com/view/Entry/205734. [1.Accessed: 05-Oct-2021].

[1.3] P. Podsiadlo, M. Kuster, and G. W. Stachowiak, "Numerical analysis of wear particles from non-arthritic and osteoarthritic human knee joints," *Wear*, vol. 210, no. 1–2, pp. 318–325, 1997.

[1.4] P. J. Blau, J. J. Truhan, and E. A. Kenik, "Effects of the exposure to corrosive salts on the frictional behavior of gray cast iron and a titanium-based metal matrix composite," *Tribol. Int.*, vol. 40, no. 9, pp. 1335–1343, 2007.

[1.5] E. Holm, R. Holm, and E. I. Shobert, "Theory of hardness and measurements applicable to contact problems," *J. Appl. Phys.*, vol. 20, no. 4, pp. 319–327, 1949.

[1.6] J. G. A. Bitter, "A Study of Erosion Phenomena Part I," *Wear*, vol. 6, pp. 5–21, 1963.

[1.7] O. A. Zambrano, Y. Aguilar, J. Valdés, S. A. Rodríguez, and J. J. Coronado, "Effect of normal load on abrasive wear resistance and wear micromechanisms in FeMnAlC alloy and other austenitic steels," *Wear*, vol. 348–349, pp. 61–68, 2016.

[1.8] S. Mischler, "Triboelectrochemical techniques and interpretation methods in tribocorrosion: A comparative evaluation," *Tribol. Int.*, vol. 41, no. 7, pp. 573–583, 2008.

[1.9] G. Rasool and M. M. Stack, "Mapping the role of Cr content in dry sliding of steels: Comparison between maps for material and counterface," *Tribol. Int.*, vol. 80, pp. 49–57, 2014.

[1.10] W. D. Cram, "Load-Stress Factors," in *Handbook of Mechanical Wear*, 1st ed., C. Lipson and L. V. Colwell, Eds. Ann Arbor: University of Michigan Press, 1961, p. 65.

[1.11] G. M. Erickson *et al.*, "Complex dental structure and wear biomechanics in

hadrosaurid dinosaurs," *Science (80-.).*, vol. 338, no. 6103, pp. 98–101, 2012.

[1.12] O. Bolmin, L. Wei, A. M. Hazel, A. C. Dunn, A. Wissa, and M. Alleyne, "Latching of the click beetle (Coleoptera: Elateridae) thoracic hinge enabled by the morphology and mechanics of conformal structures," *J. Exp. Biol.*, vol. 222, no. 12, 2019.

[1.13] P. J. Blau, "Fifty years of research on the wear of metals," *Tribol. Int.*, vol. 30, no. 5, pp. 321–331, 1997.

[1.14] ASM International, "Machining of Cast Irons," in *Volume 16: Machnining Processes*, pp. 648–666.

[1.15] G. Dieter, "Machining of Metals," in *Mechanical Metallurgy*, 3rd ed., D. Bacon, Ed. London: McGraw-Hill Book Company, 1988, p. 679.

[1.16] I. Hutchings and P. Shipway, *Surface topography and surfaces in contact*, 2nd ed. Elsevier Ltd., 2017.

[1.17] J. F. Archard, "Contact and rubbing of flat surfaces," *J. Appl. Phys.*, vol. 24, no. 8, pp. 981–988, 1953.

[1.18] I. Hutchings and P. Shipway, "Simple Theory of Sliding Wear: The Archard Wear Equation," in *Tribology: Friction and Wear of Engineering Materials*, 2nd ed., Oxford: Butterworth - Heinemann, 2017, p. 116.

[1.19] I. Hutchings and P. Shipway, "Sliding Wear," in *Tribology: Friction and Wear of Engineering Materials*, 2nd ed., Butterworth - Heinemann, 2017, p. 293.

[1.20] R. G. Woodward, A. Galloway, and A. Toumpis, "The Influence of Tempering and Annealing on the Microstructure and Sliding Wear Response of G350 Grey Cast Iron," *Wear*, vol. 496–497, no. 204283, 2022.

[1.21] I. Hutchings and P. Shipway, "Plasticity-dominated wear," in *Tribology*, 2nd ed., Elsevier Ltd., 2017, pp. 122–125.

[1.22] R. G. Woodward, A. Toumpis, and A. Galloway, "The influence of cementite spheroidizing duration on the microstructure and sliding wear response of grey cast iron against AISI 4330," *Wear*, vol. 488–489, p. 204155, 2022.

[1.23] J. A. P.-S. Elorz, D. F. Gonzalez, and L. F. Verdeja, "Properties of Grey Cast

Irons," in *Physical Metallurgy of Cast Irons*, 1st ed., Springer, 2018, p. 69.

[1.24] B. Bhushan, "Contact Between Solid Surfaces," in *Introduction to Tribology*, 2nd ed., Columbus: John Wiley & Sons, Ltd., 2013, p. 91.

[1.25] T. Kayaba and K. Kato, *Wear of Materials*. ASME, 1979.

[1.26] I. Hutchings and P. Shipway, "Sliding Wear of Ceramics," in *Tribology: Friction and Wear of Engineering Materials*, 2nd ed., Butterworth - Heinemann, 2017, p. 145.

[1.27] I. Hutchings and P. Shipway, "Sliding Wear of Polymers," in *Tribology: Friction and Wear of Engineering Materials*, 2nd ed., Butterworth - Heinemann, 2017, p. 151.

[1.28] P. J. Blau, "How common is the steady-state? The implications of wear transitions for materials selection and design," *Wear*, vol. 332–333, pp. 1120–1128, 2015.

[1.29] R. G. Woodward *et al.*, "The Influence of Load on Dry and Tribocorrosive Sliding of AISI 4330 and 15-5PH against Cast Iron," *Tribol. Trans.*, vol. 0, no. 0, pp. 1–16, 2021.

[1.30] E. Rodriguez, M. A. González, H. R. Monjardín, O. Jimenez, M. Flores, and J. Ibarra, "Heat treated twin wire arc spray AISI 420 coatings under dry and wet abrasive wear," *Met. Mater. Int.*, vol. 23, no. 6, pp. 1121–1132, 2017.

[1.31] N. P. Suh, "The delamination theory of wear," *Wear*, vol. 25, no. 1, pp. 111–124, 1973.

[1.32] D. Landolt and S. Mischler, "Introduction," in *Tribocorrosion of Passive Metals and Coatings*, Lausanne: Woodhead Publishing, 2011, p. 18.

[1.33] W. D. Callister and D. G. Rethwisch, "Electrochemical Considerations," in *Materials Science and Engineering: An Introduction*, 8th ed., John Wiley & Sons, Ltd., 2010, p. 681.

[1.34] S. Virtanen, "Passivity of Metals and Alloys," in *Tribocorrosion of Passive Metals and Coatings*, 1st ed., D. Landolt and S. Mischler, Eds. Woodhead Publishing, 2011, p. 12.

[1.35] C. Xu and W. Gao, "Pilling-bedworth ratio for oxidation of alloys," *Mater. Res. Innov.*, vol. 3, no. 4, pp. 231–235, 2000.

[1.36] W. D. Callister and D. G. Rethwisch, "Ferrous Alloys," in *Materials Science and Engineering: An Introduction A*, 8th ed., John Wiley & Sons, Ltd., 2010, p. 397.

[1.37] S. Virtanen, "Nature of Passive Films in Relation to Protection," in *Tribocorrosion of Passive Metals and Coatings*, D. Landolt and S. Mischler, Eds. Woodhead Publishing, 2011, p. 18.

[1.38] K. Kato, "Wear modes at asperity contacts in tribochemical wear," in *Tribocorrosion of Passive Metals and Coatings*, 2011, p. 79.

[1.39] J. F. Archard, "The temperature of rubbing surfaces," *Wear*, vol. 2, no. 6, pp. 438–455, 1959.

[1.40] T. F. J. Quinn, "The effect of 'hot-spot' temperatures on the unlubricated wear of steel," *ASLE Trans.*, vol. 10, no. 2, pp. 158–168, 1967.

[1.41] T. F. J. Quinn, "Role of oxidation in the mild wear of steel," *Br. J. Appl. Phys.*, vol. 13, no. 1, pp. 33–37, 1962.

[1.42] F. H. Stott, "High-temperature sliding wear of metals," *Tribol. Int.*, vol. 35, no. 8, pp. 489–495, 2002.

[1.43] T. F. J. Quinn, J. L. Sullivan, and D. M. Rowson, "Origins and development ambient temperatures," *Wear*, vol. 94, pp. 175–191, 1984.

[1.44] I. Hutchings and P. Shipway, "Oxidative Wear," in *Tribology: Friction and Wear of Engineering Materials*, 2nd ed., Butterworth - Heinemann, 2017, p. 127.

[1.45] F. H. Stott and G. C. Wood, "The influence of oxides on the friction and wear of alloys," *Tribol. Int.*, vol. 11, no. 4, pp. 211–218, 1978.

[1.46] A. G. Macdonald and F. H. Stott, "The influence of load and surface treatment on the corrosive wear of cast iron in oil-sulphuric acid environments," *J. Mater. Sci.*, vol. 23, no. 2, pp. 629–636, 1988.

[1.47] F. H. Stott, "The role of oxidation in the wear of alloys," *Tribol. Int.*, vol. 31,

no. 1–3, pp. 61–71, 1998.

[1.48] J. L. Sullivan, T. F. J. Quinn, and D. M. Rowson, "Developments in the oxidational theory of mild wear," *Tribol. Int.*, vol. 13, no. 4, pp. 153–158, 1980.

[1.49] J. F. Archard and W. Hirst, "The wear of metals under unlubricated conditions," *Proc. R. Soc. Lond. A.*, vol. 236, 1956.

[1.50] T. F. J. Quinn, "Review of oxidational wear. Part I: The origins of oxidational wear," *Tribol. Int.*, vol. 16, no. 5, pp. 257–271, 1983.

[1.51] S. C. Lim, M. F. Ashby, and J. H. Brunton, "Wear-rate transitions and their relationship to wear mechanisms," *Acta Metall.*, vol. 35, no. 6, pp. 1343–1348, 1987.

[1.52] M. W. Shin, K. H. Cho, S. J. Kim, and H. Jang, "Friction instability induced by corrosion of gray iron brake discs," *Tribol. Lett.*, vol. 37, no. 2, pp. 149–157, 2010.

[1.53] C. W. Park, M. W. Shin, and H. Jang, "Friction-induced stick-slip intensified by corrosion of gray iron brake disc," *Wear*, vol. 309, no. 1–2, pp. 89–95, 2014.

[1.54] R. Ghasemi and L. Elmquist, "The relationship between flake graphite orientation, smearing effect, and closing tendency under abrasive wear conditions," *Wear*, vol. 317, no. 1–2, pp. 153–162, 2014.

[1.55] R. S. Montgomery, "Run-in and glaze formation on gray cast iron surfaces," *Wear*, vol. 14, no. 2, pp. 99–105, 1969.

[1.56] D. H. E. Persson, S. Jacobson, and S. Hogmark, "Effect of temperature on friction and galling of laser processed Norem 02 and Stellite 21," *Wear*, vol. 255, no. 1–6, pp. 498–503, 2003.

[1.57] A. Renz, B. Prakash, J. Hardell, and O. Lehmann, "High-temperature sliding wear behaviour of Stellite®12 and Tribaloy®T400," *Wear*, vol. 402–403, no. February, pp. 148–159, 2018.

[1.58] S. C. Tung, K. Brogan, and Y. Wang, "Tribological evaluation of oil pump relief valve coatings compatible with an aluminum oil pump body," *Wear*, vol. 250–251, no. 1–12, pp. 690–705, 2001.

Chapter 2.

Review of Select Tribological Literature

2.1.   Historical Overview

Knowledge of friction and wear has existed for thousands of years, with many comprehensive examples given by Dowson [2.1]. An overview of tribological history is covered by Ciulli [2.2], citing many examples listed by Dowson [2.1], such as the use of frictional heat between wooden sticks to create fire. Other examples from millennia past include the use of vegetable oil and animal fat to lubricate the shafts and sockets at the fulcrum sockets of large doors. The Romans made use of bearings at least 2000 years ago, with this technology found on the sunken ship in Lake Nemi, Italy. Cuilli [2.2] discusses tribology and lubrication through the various epochs up to present day, focussing centrally on fluid technology and friction reduction. However, the article does not specifically cover important literature related to material removal through sliding, nor does it cover other historical sliding literature from the early 20th century (see Section 2.2.) that became the foundation of modern tribology research. Examination of such work (see Section 2.2.) is important because (despite simplifying the mechanisms seen in reality) they lay the foundation for many modern hypotheses (see Chapters 4 – 7).

An overview of 20th century tribological research was conducted by Blau [2.3] who covered publications on the wear of metals from the 1940s to the 1990s. In addition to this historical recount, Blau [2.3] also comments on the share of different tribological fields, and notes that sliding is the most investigated area of tribology from the 1970s to the 1990s at the bi-annual Wear of Materials conferences. It was also noted that, from 1977 to 1995, the percentage of wear conference papers involving metallic materials peaked in 1985 at approximately 70% and then declined to approximately 40%, showing that metallic conference papers still possessed a plurality of publications (Figure 2.1) [2.3]. All materials examined in the herein are metallic alloys (almost all ferrous) and it is therefore pertinent to focus on publications in the same sub-field of tribology.
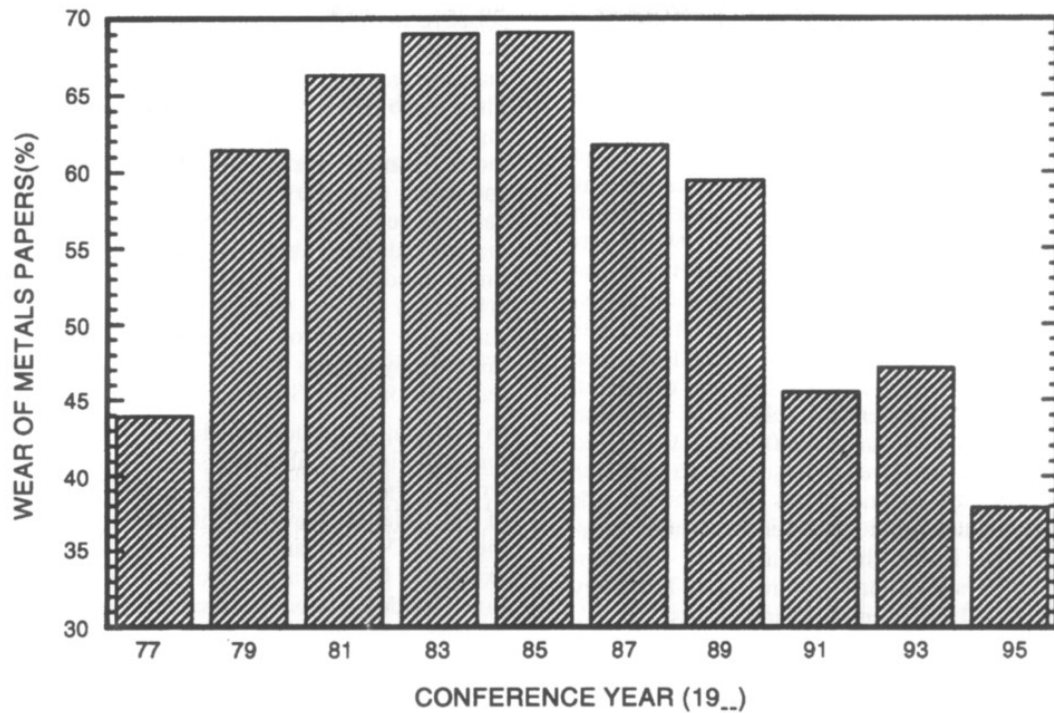
Figure 2.1 - Percentage share of conference papers focussing on metals [2.3].

2.2.   Early Wear Investigations

Some of the first significant tribology publications focussed primarily on the nature of hardness and wear, and on the nanoscale contact between two surfaces, making use of asperity theory to model how damage occurs. Hardness is an important property in tribology, as it often a reasonable indicator of wear resistance [2.4]. All four experimental chapters (Chapters 4 – 7) in this thesis use hardness as a metric for predicting wear performance.

An early investigation by Bishop et al. [2.5] studied the indentation and stress distribution of solid materials using a conical indenter and found that, the resultant stress could be approximated by assuming a spherical indenter, and that the contact pressure could be related to the yield strength of the material. Holm et al. [2.6] studied the nature of indentation hardness using a spherical ball, involving one hard material indenting a softer material and modelling the resultant deformation. The nature of hardness and its relationship to the yield strength of a material was discussed, and concluded that one can be substituted for the other depending on the application. These simplifications allowed other authors such as Hirst [2.7] and Archard [2.4], [2.8] to elaborate on wear mechanisms and contact mechanics going forward.

In 1952, Burwell and Strang [2.9] investigated the relationship between wear rate and load, and found that the wear rate varies transiently based on the ratio of applied load to the sample hardness. It was found that at very low contact pressures, a hydrodynamic pressure separates the sample faces, producing low wear rates. At higher pressures, below one third of the sample hardness, the wear rate was linearly related to the distance of travel and load, and is independent of the apparent area of contact. At loads higher than one third of the sample hardness, the same relations apply, however, a sensitivity to further increases in load arises. The authors [2.9] also noted the fundamental mechanisms of wear damage, including adhesion/galling, corrosion, the presence of loose abrasive material, ploughing, and other erosive damage. These mechanisms would be developed further and refined in subsequent literature, as well as further subdivided into other mechanisms for detailed analysis (see Sections 2.3. – 2.5.).

Archard [2.4] was among the first to derive a model for material removal by relating the material hardness, applied load, and distance travelled. The model states that the volume of material removed is proportional to the frictional work input to the contact face, and became known as Archard's Wear Equation. Archard's wear equation [2.4] is significant in tribological studies as it relates several key parameters and allows for an approximation of material removed during sliding. It has been accepted in the tribology community as a basic relationship which under ideal conditions is a good model for sliding. The model relies on asperity contact theory, and omits consideration of key variables such as sliding speed, temperature output, hardness of the counter body, passive films, microstructure, subsurface microstructural evolution, and mechanisms such as micro cracking and spallation. Therefore, the model is inapplicable in most sliding scenarios, as all such variables play a key role in most tribosystems.

Archard and Hirst [2.8] were among the first to distinguish between the two primary wear modes of mild oxidative wear and severe metallic wear (Figure 2.2). It was found that when steady state wear was achieved, the volume loss was not proportional to the apparent area of contact, but was instead proportional to load for certain ranges of values until a change to the surface morphology is reached which then causes a shift to a milder or more severe regime. Stylus profilometry was used to characterise the cross-sectional profiles of mild and severe wear scars and it was noted that the

distinction can be observed using this method. The different mechanisms were also observed, where Archard and Hirst [2.8] noted that "mild wear involves the slow removal of the tips of the higher asperities… Severe wear occurs by a mechanism on a much larger scale of size and damage appears to take place by welding and plucking of the surfaces" [2.8].
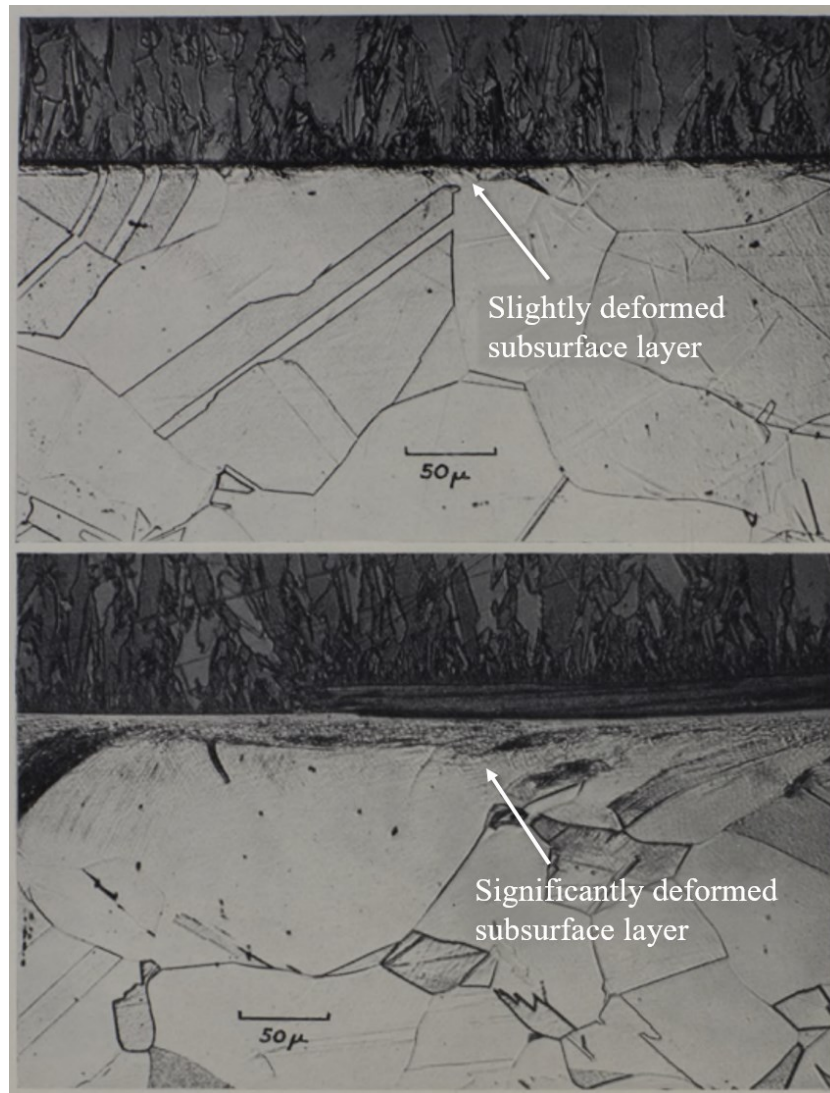
Figure 2.2 - Cross-sectional optical micrograph of two brass samples after sliding wear. (a) Slightly deformed subsurface layer from mild wear, and (b) significantly deformed subsurface layer from severe wear [2.8].

Khruschov [2.10] explored the relationship between hardness and wear resistance, and found that linear trend was often seen, with higher and lower gradients for pure metals and alloyed steels, respectively. The author [2.10] also proposed an additive rule of mixtures effect, where for heterogeneous materials, the total wear resistance can be

expressed as the sum of the volumetric wear resistances of the various constituents, as is seen for mechanical properties in composite materials.

Although not directly used in this thesis, these early publications just discussed form the basis of modern tribology research and as such are described and credited. Instead, most findings from the four experimental chapters (Chapters 4 – 7) instead stand on more recent studies specific to said chapter.

2.3.   Non-linear Wear Phenomena

Many tribology contexts involve non-linear relationships and feature large changes, commonly termed *transitions*, in volume loss values and wear rates.

These transitions can be transient in nature or can be dependent on input variables such as applied load or speed. Studies of transient wear transitions typically focus on the changing wear rates at the start of experiments (the running-in period). Hirst and Lancaster [2.7] examined natural and induced transitions in wear behaviour with changing experimental variables. The authors [2.7] verified that the volume lost from sliding was independent of the apparent area of contact but was proportional to distance travelled. It was also found that the breakdown of the outer film at the beginning of sliding, termed the running-in period, was critical in determining the transition load which resulted in a transition to severe wear. At the transition load, the authors posited that the rate of passive film growth was balanced with the material removal rate, and that the transition load can be shifted by changing one of these rates, such as the inclusion of a film-forming additive which promoted faster passive film growth. The proportionality of the wear rate was also commented on, whereby both regimes, mild and severe, experienced the same gradient of wear rate increases, just shifted according to the transition. The researchers [2.7] also noted that the development of a beneficial outer surface layer was instrumental in the running-in period for industrial machinery when first used.

Studies of externally induced transitions examine the influence of volume loss versus a typical parameter(s), such as sliding speed, load, or temperature, and plot the influence of each and their exact correspondence to the transition to a higher or lower wear regime. Lancaster [2.12] explored the nature of induced transitions for 60/40 brass sliding on hardened steel. These mechanisms of such transitions were attributed to the formation or breakdown of surface films on the sample wear surface. The author

[2.12] then investigated many transitions through the variation of several experimental parameters, such as ambient temperature and sliding speed. Wear rates were found to experience a transition from slightly increasing to significantly decreasing at approximately 300°C. Similar trends with sudden transitions were also observed for sliding speed. The influence of oxide growth rates on the wear rate was discussed, with observations on the fact that heat increases, either from frictional input or external stimuli, increases the growth rates of such films. At a critical temperature for each sliding combination, the re-growth rate of the film exceeded the removal rate, reversing the trend and transitioning to a mild wear regime. Lancaster [2.12] also found that upon spallation of the adhered oxide-hardened layer, fresh metal was exposed which may temporarily have undergone severe wear on this localised scale until oxide growth on the exposed area reached a critical rate.

Lim and Ashby [2.11] investigated wear transitions by analysing numerous wear resistance data (Figure 2.3). It was concluded that the load-dependent transition from mild to severe was a result of the breakdown of the protective oxide layer (see Section 2.5), which exposed the underlying metal to damage, creating high volume losses. The authors [2.11] also found that the velocity-dependent transition, from severe to mild wear, was a result of a transformation to martensite caused by sliding.
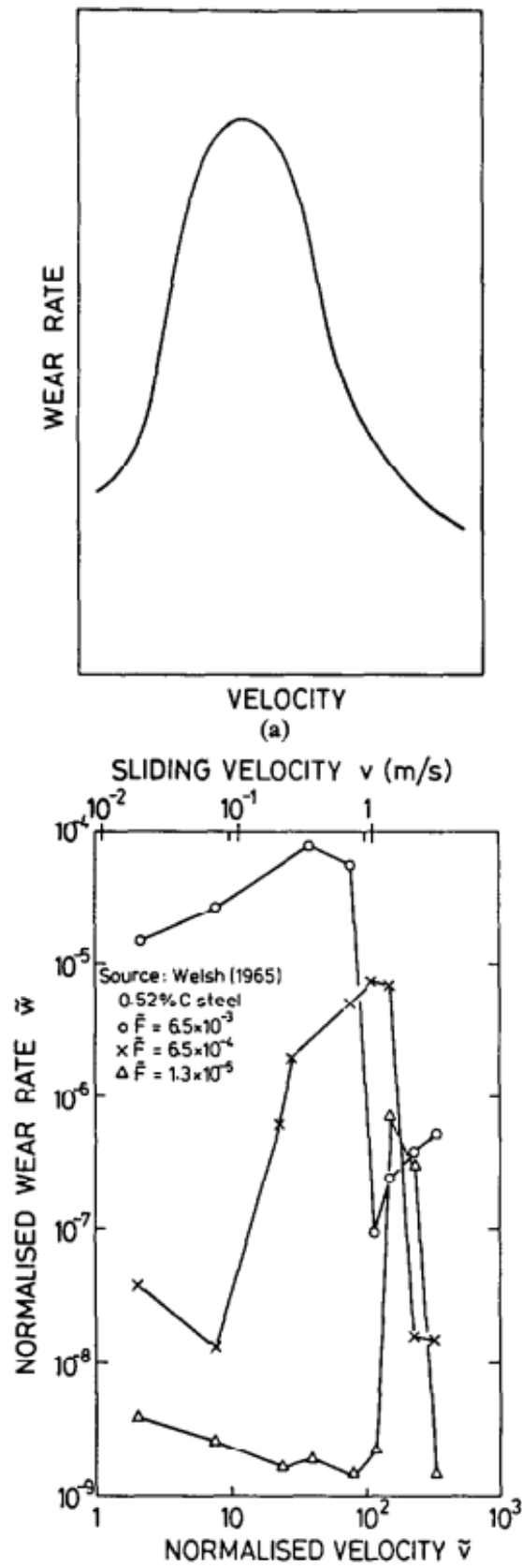
Figure 2.3 - Typical wear rate transitions from changing applied load in schematic form (top) and experimental data (bottom) [2.11].

Two publications by Blau [2.13], [2.14] discussed the fundamental mechanisms of wear, such as the nature of transient wear behaviour, the onset of transitions, and the mechanistic action of material removal. In terms of transient wear behaviour, the running-in period was discussed [2.13], where the transition from initial running-in wear at the commencement of sliding creates a variable wear rate that reduces with time, to the linear steady state region where volume loss becomes proportional to sliding distance. Blau [2.13] noted that the majority of sliding wear research focusses on the steady-state phase of wear, and tends to ignore the initial running-in period. The importance of the initial running-in period is also commented on, whereby the phenomenon allows for components to properly fit together evenly. The dangers of ill-fitting components can create contact pressures significantly higher than desired, and therefore create higher wear rates and temperature rises following on [2.13].

Blau also defined [2.14] the two types of transitions as induced and natural, whereby the former was brought about by a change in variables such as load, speed, or contact conditions, and the latter was initiated by changes during the wear regime such as running-in phenomenon, breakdown of a passive film, or thermal softening [2.14], causing the instantaneous wear response to change. Mechanistically, natural transitions can arise due to several reasons, such as the proposed quad-cyclic surface transitions involving surface deformation and spallation. In this model (Figure 2.4) [2.14], the surface (Stage 1) is plastically deformed, asperities smoothed out, and the near subsurface is strain hardened into a "highly deformed layer" (HDL) (Stage 2). The next stage involves thickening of the HDL and crack initiation as strain hardening increases to a maximum that can be sustained by the material (Stage 3). The final stage involves crack propagation and chip spallation after maximum strain hardening has occurred, generating debris/wear particles. The strongest plateaus (macro asperities) remain, supporting a progressively increased load as other areas spall and detach (Stage 4). These plateaus eventually fracture and spall as they are eventually sheared off to expose fresh smoother material underneath to begin the cycle again (Stage 1) [2.14].

Further discussion on induced wear transitions takes place in Chapter 6, where increasing load causes volume losses to increase non-linearly.
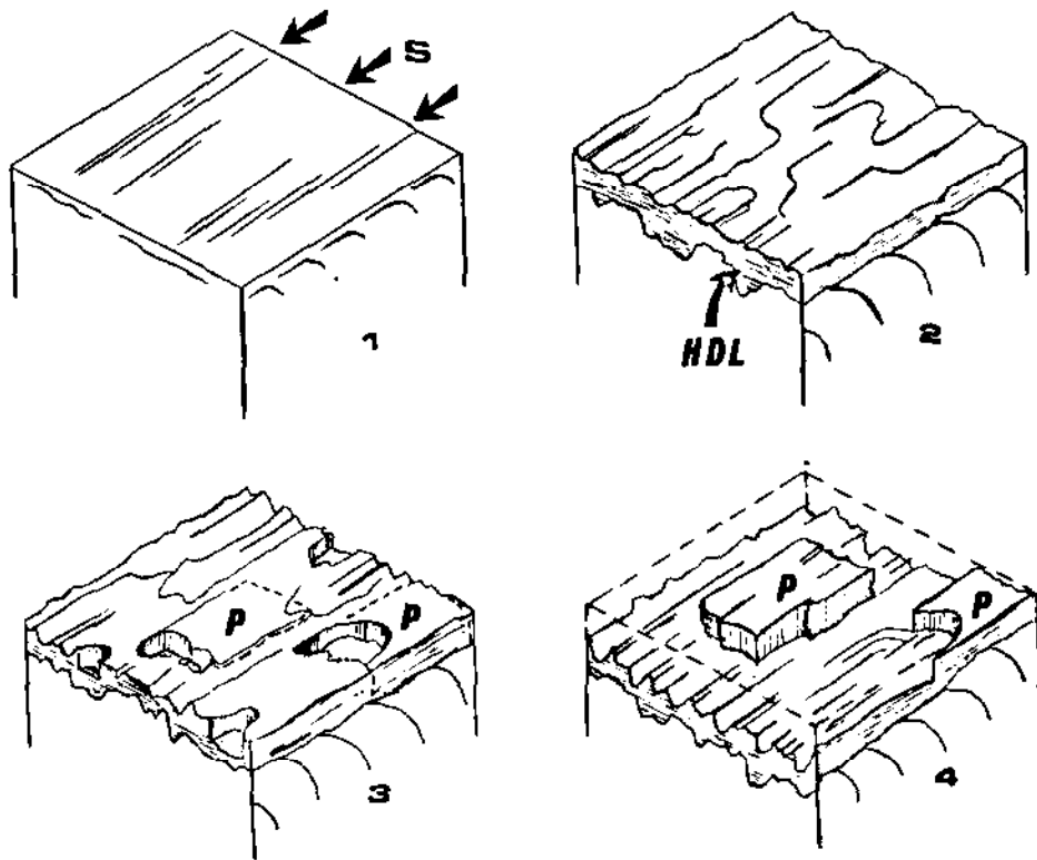
Figure 2.4 - The four proposed stages of material removal from severe wear. (1) Flattened and polished surface with strain hardening. (2) Thickening of the surface layer and crack initiation at maximum strain hardening. (3) Crack propagation and spallation of chips, leaving only the strongest plateaux to support the load. (4) Fracture and removal of the highest plateaux, leaving only the polished surface to begin the cycle again [2.14]. S – Sliding direction, HDL – highly deformed layer, P – plateau.

2.4.   Microstructural Effects of Wear

While hardness was historically used to predict wear resistance and the performance of metals in sliding, it became clear that microstructural morphology also influenced the wear response, and that hardness could not be solely relied on for wear predictions. Such developments stimulated further research on the influence of microstructure on wear and vice-versa.

Nakajima and Mizutani [2.15] investigated the subsurface deformation of three carbon steels after sliding at various speeds. It was found that sliding wear increased the

frequency of dislocations, which piled up around cementite plates. It was also noted that the resultant wear was dependant on the nature of the subsurface deformation due to strain hardening and dislocation pile up, because this then influenced the mechanisms of wear occurring. The fracture properties of the BCC crystal structure were also commented on, as this can change depending on many variables such as sliding speed or temperature. As sliding speed increased, or as temperature decreased, the mode of fracture changed from ductile to brittle, resulting in higher volume losses. However, it was also noted [2.15] that temperature increased with sliding speed which may counteract the change to brittle fracture modes.

Moore [2.16] investigated the influence of microstructural constituents on the wear resistance of multiple steels in various conditions using abrasive sliding tests. It was noted that wear resistance increased with the volume fraction of pearlite. Moore [2.16] also noted that the pearlitic areas were particularly wear resistant, but were also effective at reinforcing surrounding ferrite grains from deforming significantly. For martensitic steels, it was found [2.16] that the wear resistance and hardness were linearly related to the square root of the carbon wt%, which was thought to be due to increases in carbon content raising the flow stress of the material.

Mutton and Watson [2.17] studied the wear of two steels and several pure metals in sliding/abrasion tests. The two tested steels were used in various microstructural conditions, including spheroidite, pearlite, and tempered martensite (Figure 2.5).
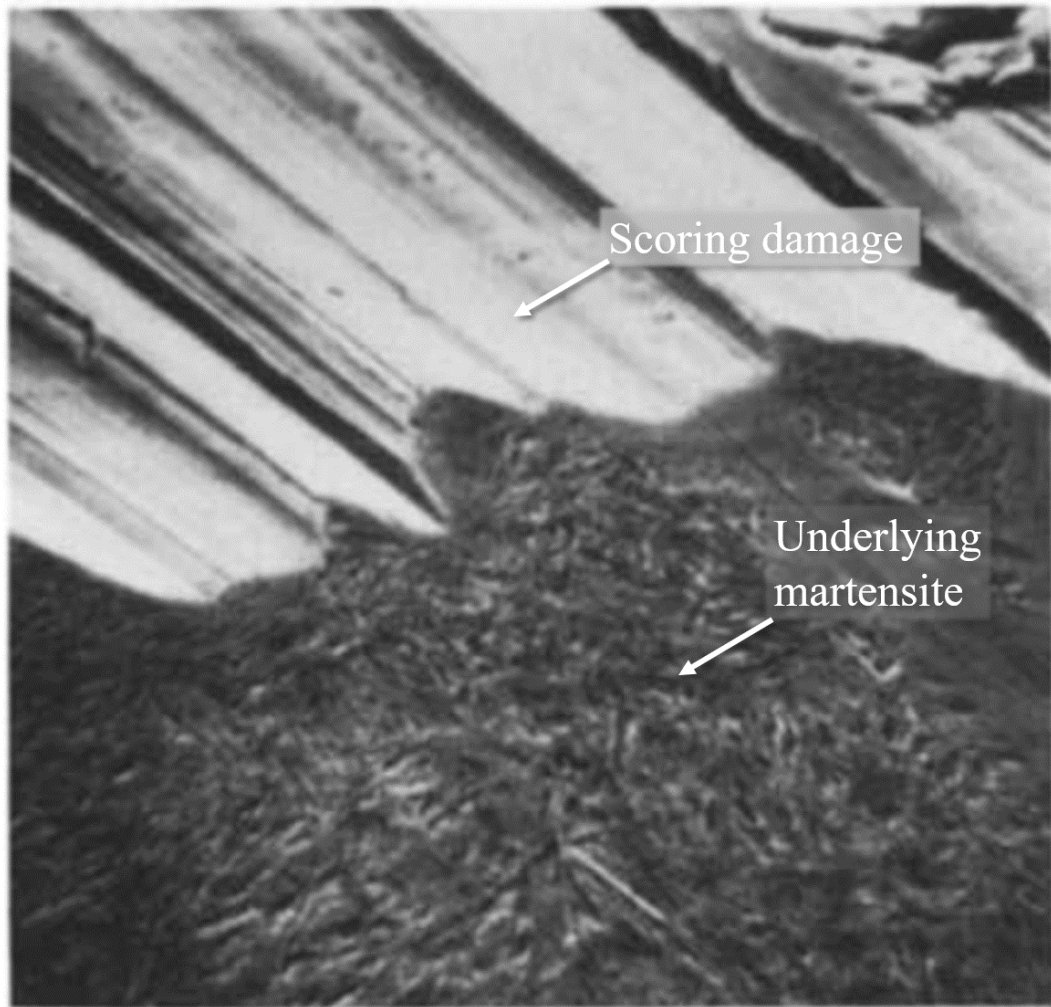
Figure 2.5 - Tilted view of sliding/abrasive wear scar showing martensitic microstructure on the cross-section [2.15].

Additional commercially pure metals, such as aluminium, copper, nickel, iron, and molybdenum, were also tested [2.17]. The results showed that the pure metal hardness was linearly related to wear resistance, whereas the steels showed non-linear relations between their hardness and wear resistance (Figure 2.6). The authors [2.17] concluded that this non-linear relationship between hardness and wear was due to the tendency for plastic flow to occur when a harder area wears a softer one. As plasticity is determined by microstructural morphology (i.e. cementite lamellae versus spheroidal form), the level of plastic flow varies between the conditions and can thus produce different wear rates [2.17].
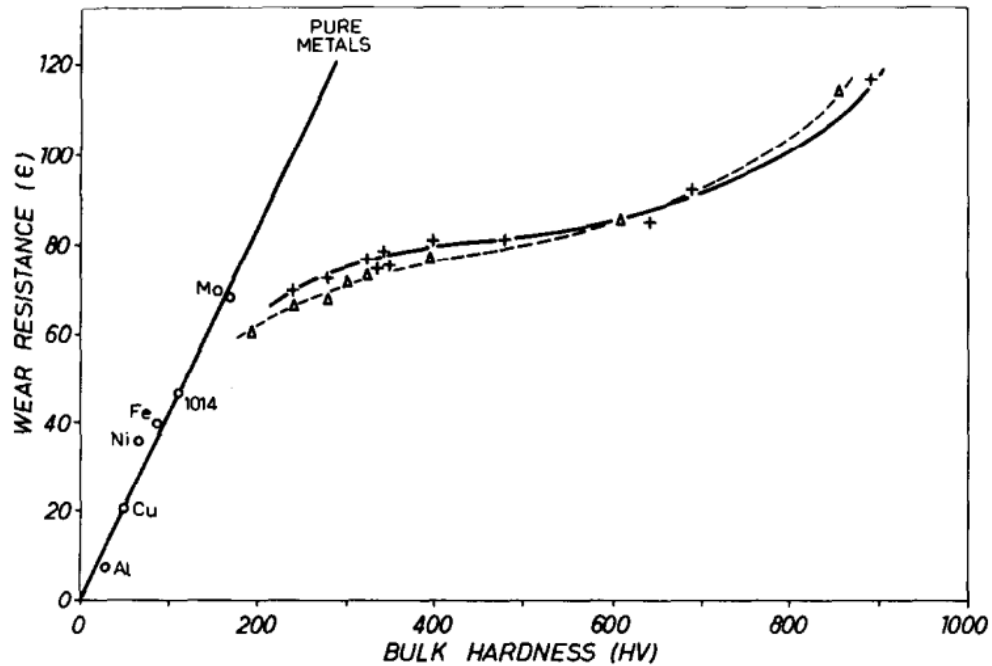
Figure 2.6 - Wear resistance curves highlighting the linear relationship between hardness and wear resistance for pure metals (straight line) and the non-linear relationships for steels (curved lines) [2.17].

Xu and Kennon [2.18] investigated the nature of hardness, microstructure, and wear resistance by testing numerous steels in various conditions. It was noted that the wear resistance measurements progressed linearly with increasing hardness, for materials with similar microstructures, and the value of hardness was therefore used to estimate the wear volume losses. However, the authors [2.18] noted the morphology of cementite (whether it be cementite within pearlite or pro-eutectoid carbide networks) gives different wear responses and therefore creates non-linear wear behaviour with respect to hardness. Increased toughness was also commented on as a positively correlated property with wear resistance, as this reduces the tendency of subsurface cracks to propagate into the material and cause chip spallation [2.18].

Suh [2.19] discussed the nature of material removal during sliding wear, and attributed the majority of it to the delamination of chips due to dislocation pile-up near the surface (Figure 2.7). The author [2.19] raised several issues with the earlier theories of wear using only contact mechanics, and in particular criticised the Archard wear equation [2.8] due to it ignoring the physical metallurgy of the material, making unreasonable assumptions, and not accounting for different sliding conditions. Suh

[2.19] instead proposed that material removal predictions should take the microstructure of the material into account, namely, through dislocations creating voids that eventually fracture and delaminate chips from the matrix. It was also noted that these dislocations tended to pile up around hard particles within the metallic matrix, causing the particle to eventually either collapse or delaminate from the matrix, initiating the crack which leads to chip spallation [2.19].
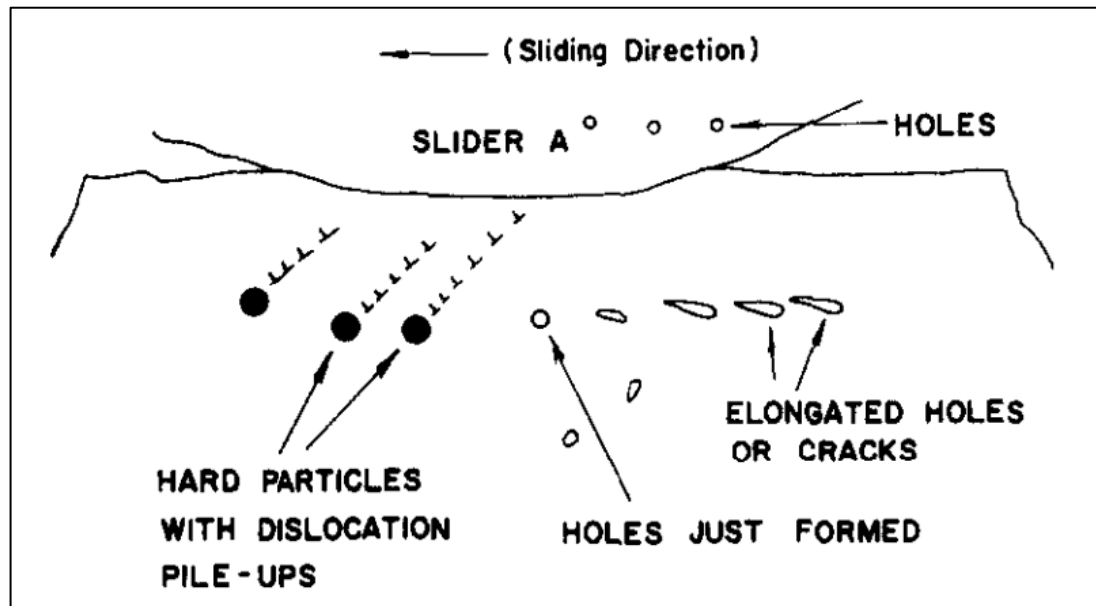
Figure 2.7 - Proposed mechanism of chip removal featuring dislocation pile ups near the surface eventually forming holes which coalesce into cracks before spallation/delamination [2.19].

Garbar and Skorinin [2.20] studied the subsurface deformation of low alloy steel after sliding in a reciprocating friction rig in the self-mated configuration. The authors [2.20] primarily examined dislocation density and distribution, and found that this increased significantly near the worn surface, in comparison to the base metal. Metallic grains at the surface were elongated and deformed in the direction of sliding and the regions between these deformed grains and the undisturbed grains was found to be a weak area where crack propagation occurred. Grain orientation and positioning were also discussed, and it was found that grain boundaries normal to the sliding direction hindered dislocation movement, and that frictional damage initiated along such boundaries [2.20].

The effects of sliding on subsurface ferrous microstructure were studied by Wang [2.21], who conducted wear experiments with two ferrous alloys, 52100 and 1080

steel, in various microstructural conditions. It was concluded that such wear produced laminated structures of different regional sections, such as a white etching layer on the surface, followed by a strain hardened zone with distortion in the direction of sliding. Evidence of this strain hardening was seen when plotting micro indentation hardness versus depth beneath the surface, and was measured to increase significantly just under the surface, at a factor of approximately three. It was also concluded that the wear responses of different alloys is dependent on the energy expenditure associated with such deformation and/or transformation [2.21].

Hutchings and Shipway [2.22] reported that the depth of subsurface deformation can vary depending on the material and sliding conditions, and that there is often competitive action between strain hardening and incidental stress relief annealing caused by the high temperatures associated with sliding. The authors [2.22] also address the nature of surface layers produced by sliding, and state that these can be categorised in two ways. The first is the previously mentioned oxide glaze layer, and the second is a layer of heavily refined metallic grains mixed with oxides, resulting from being heavily distorted and strained by the sliding process (Figure 2.8) [2.22].

Further discussion on the microstructural effects of wear (and the tribological influence of microstructure) are discussed in Chapters 6 and 7, where heat treatments are utilised to alter the microstructure of the studied materials (Chapter 3).
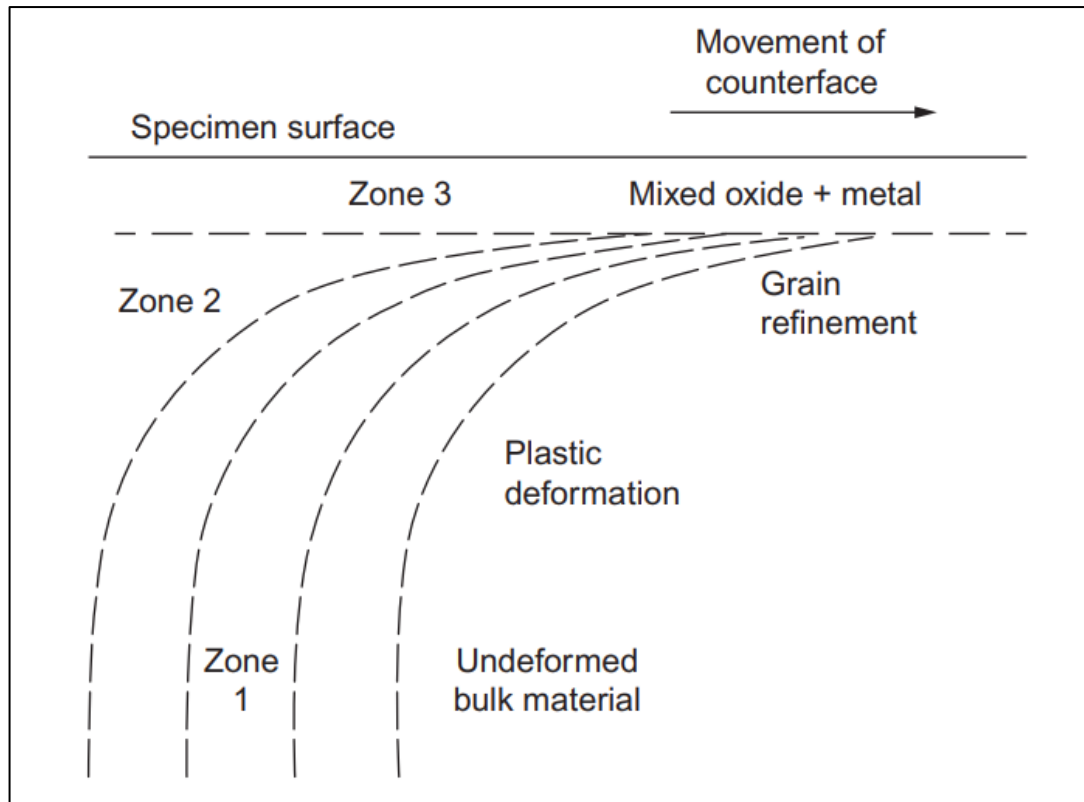
Figure 2.8 - Schematic of subsurface deformation featuring three latitudes. Zone (1) un-deformed base material. Zone (2) plastic deformation and grain refinement. Zone (3) mixed metallic/oxide layer [2.22].

2.5.   Oxidative Wear Research

As previously discussed, one of the primary damage modes of ferrous alloys in sliding is oxidative wear. This involves one or both of the sliding surfaces forming a thick layer of oxide that shields the underlying metallic substrate from damage [2.23].

The significance of oxidative wear has been known for some time, with one of the first publications on the subject by Fink [2.24] in 1930. The author [2.24] recognised that oxygen in the surrounding atmosphere was essential to produce mild wear on railway steel, after experiments in both inert gas and normal atmosphere produced varying results. The first analysis of wear debris was conducted by Rosenberg and Jordan [2.25], who found that the wear rate in air was 50 times less than that same experiment in hydrogen. X-ray diffractometry (XRD) analysis of the particles from the hydrogen tests showed only iron, however the particles from the air tests were Fe_2O_3 and Fe_3O_4. Similar analysis of debris generated from small amplitude

vibrational sliding was carried out by Thum and Wunderlich [2.26], who also detected Fe_2O_3 from x-ray diffractometry. Mailander and Dies [2.27] examined soft iron against chromium steel in unidirectional sliding for various applied loads and speeds, from 30N to 600N, and from 1m/s to 3m/s. The researchers [2.27] found that wear rate increased linearly with load and speed, but experienced a maximum at 150N and 1m/s, and then decreased to the levels of the previous load values. The wear debris at this most severe condition had the largest proportion of metallic material and FeO, and the minimum value of Fe_2O_3 [2.27].

Stott and Wood [2.28] investigated the atmospheric effects on oxidative wear and found that through varying the partial pressure of oxygen during the test, oxide growth is affected. The authors [2.28] noted that as oxygen partial pressure increased, the presence of oxide islands on the wear surface increased. As the oxygen partial pressure was then decreased again, these oxide islands persisted and remained in place even when oxygen was reduced to a level below that at which the islands could initially form. It was concluded that such protective oxide glazy layers result from the scale already present on pre-oxidised samples, or generated purely from the oxides produced during sliding. Glaze layers purportedly consist of "fine, crystalline oxide particles, typically 10 to 50 nm in diameter, which are compacted onto a substrate of alloy, oxide layer, or compressed coarse wear debris" (Figure 2.9) [2.28].

Stott [2.29] also produced a comprehensive overview of beneficial oxidative wear in sliding. The author discussed the high temperature required for forming an oxide layer, and how it can be supplied either through the instantaneous flash temperatures, or supplied externally from ambient sources. The theory of critical thickness of oxide flakes [2.29] is discussed, where once this critical value is reached, spallation of the oxide occurs, resulting in wear. Melting of the oxide glaze layer is also discussed, whereby a combination of high speed and load supply enough input energy for molten oxide to exist between the contact faces, which is less effective at reducing wear than the dry glaze layer [2.29].
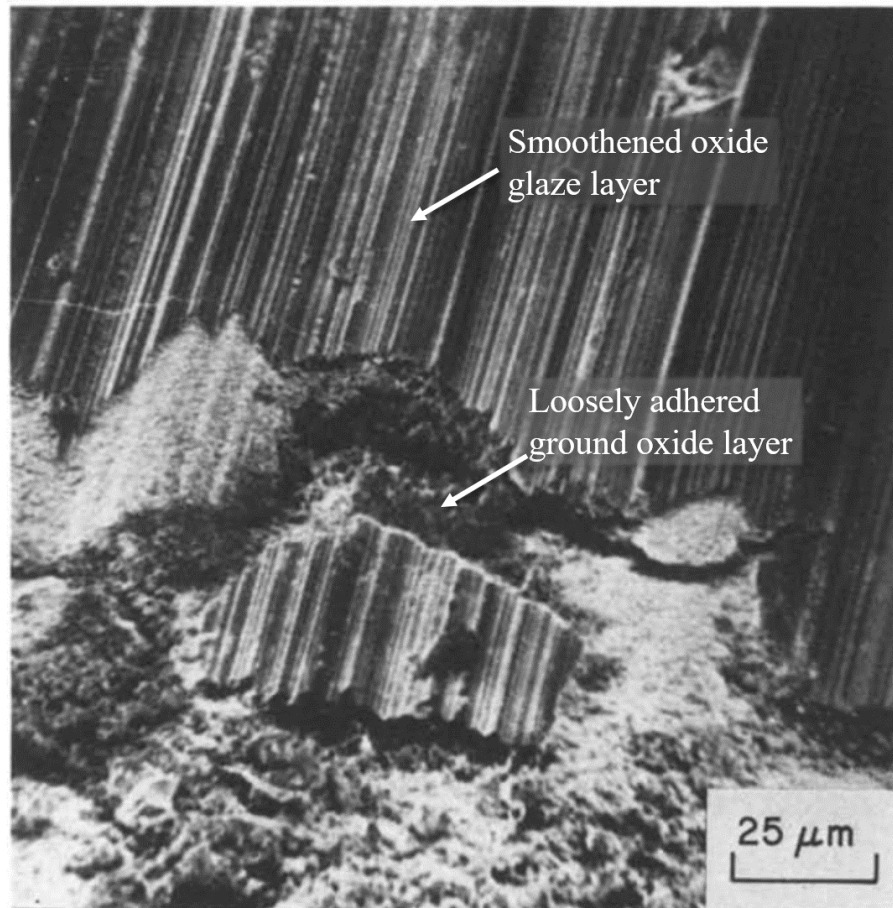
Figure 2.9 - Smooth polished area of oxide glaze layer (top) and fractured, damaged area (bottom)
[2.28].

Stott and Jordan [2.30] examined the effect of elevated temperatures on the oxidative wear of high-speed steel and high chrome steel. It was found that the wear rate was highly correlated to the ambient temperature and applied load. At 550°C and 600°C, protective oxidative glaze layers were established which shielded the samples from metallic contact. The layers subsequently broke down at higher loads, resulting in severe wear. However, at 500°C, severe abrasive wear took place for the high speed steel combinations due to the wearing of hard oxide particles. The researchers [2.30] found that smaller sliding grooves on the wear scar did allow for loose oxide powder penetration into the contact area to facilitate mild oxidative wear. In contrast, the softer high chrome steel had larger sliding grooves and thus managed to retain debris in the wear scar to promote mild wear.

Quinn [2.31] presented the hypothesis that the mild oxidative wear of steels involved newly exposed fresh metal oxidising upon contact during the flash temperature hot spots between asperities. The author [2.31] noted that two mechanisms of oxide wear particle generation exist:

(1) The oxide layer can instantaneously grow on exposed metallic asperities at a rate much faster than the time of contact, which then exists but is relatively unaffected until shear removal after several contact cycles, or that:

(2) The oxide layer instead grows consistently over the course of several contact cycles continuously until being shear removed.

After evaluating the validity of each proposed mechanism, the conclusion drawn [2.31] was that the second has a higher likelihood to be seen in most instances, due to the dependency of oxide growth on contact time, and thus sliding speed which had previously been observed by Archard [2.32]. Quinn [2.31] also commented on the likelihood of oxidation to occur during or after contact had occurred, and stated that the rate of quenching of the wear scar after contact made it unlikely for oxidation to occur after this, meaning most oxidation occurs during contact [2.31].

Quinn [2.33] related the oxidational wear rate to the asperity contact radius. It was concluded that the wear rate was proportional to the applied load if the resultant oxide compound does not change (such as from Fe_2O_3 to Fe_3O_4). This was deduced from the plots of wear rate versus load which experienced two transitions at 12N and 32N where the wear rate decreased and increased respectively. After investigation of the resultant oxide products it was found that these wear rate shifts corresponded to changes in the type of oxide, from Fe_3O_4 at 12N to FeO at 32N (Figure 2.10). The authors also noted that the wear rate surface and temperature of the worn surfaces are related because shifts in wear rate correspond to shifts in temperature.

Quinn [2.34] managed to qualitatively observe the hot spots generated from sliding contact by using a transparent sapphire disc as the counter body. Using photography and videography, the hot spots could be observed by photographing the sliding process from underneath to see the lower end of the pin (Figure 2.11). The author posited that the luminescent hot spots were in actual fact the real area of contact between the contact faces, with the number of instantaneous hot spots indicating that the real rea of contact was 1000x less than the apparent area of contact. Colour temperature

measuring estimated the hot spots to be in the region of 1100°C – 1200°C, with a hot spot of this colour appearing in almost every photograph.
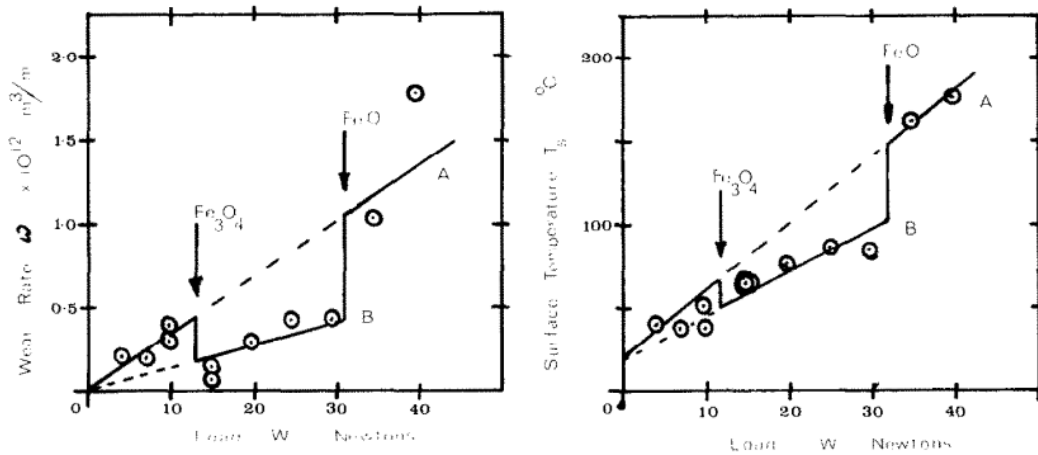
Figure 2.10 - Graphs plotting wear rate against load (left), and surface temperature against load (right) showing that changes in wear rate approximately correspond to changes in temperature, and thus compound of oxide formed [2.33].

Oxidative wear research is referenced throughout the thesis, in all experimental chapters, as it was a frequently observed phenomena in all experimental chapters (by virtue of the studied materials (Chapter 3)).
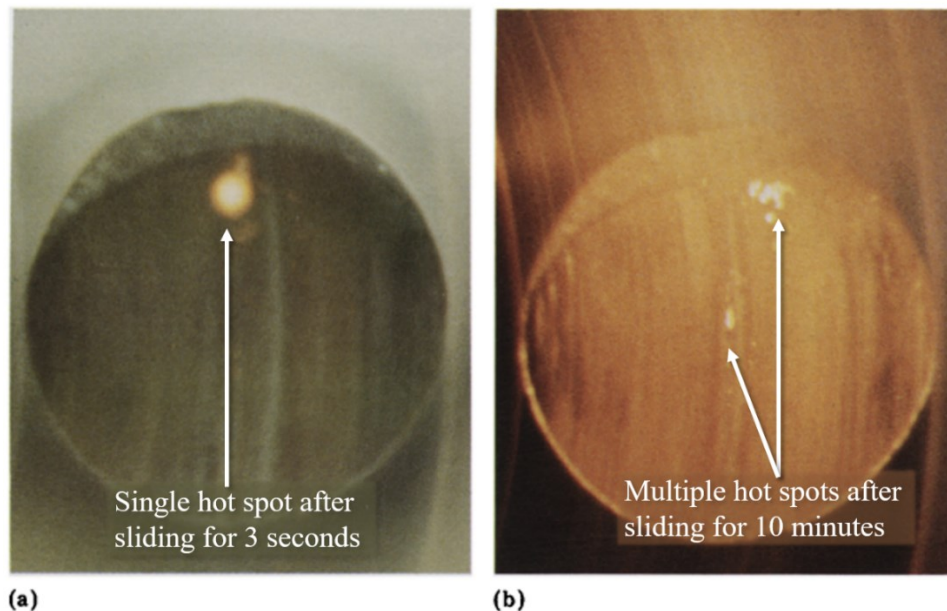
Figure 2.11 - Photographs of hot spots generated on a hardened tool steel pin during sliding against a sapphire disc, (a) after 3 seconds, and (b) after 10 minutes [2.31].

2.6.   Concluding Remarks

This literature review has discussed general references common to all experimental chapters (Chapters 4 – 7) throughout the thesis. Such studies form the foundation of modern wear research, and are still frequently cited and referred to in most wear publications.

- Oxidative wear is present and discussed in all experimental chapters, as the active alloys discussed in each chapter have a tendency to oxidise in air. Sliding wear amplifies this tendency.
- Microstructure is also thoroughly discussed in most chapters (especially Chapters 4, 6, and 7) where the subsurface deformation produced by sliding damage is related to the bulk microstructural constituents.
- Non-linear wear phenomena are most-discussed in Chapter 6 where changing the applied load causes a disproportionate increase in volume losses.

The experimental chapters (Chapters 4 – 7) also feature small literature reviews, which mostly cover research and materials specific to that chapter.

References

[2.1] D. Dowson, *History of Tribology*, 2nd ed. London, New York: Wiley, 1998.

[2.2] E. Ciulli, "Tribology and Industry: From the Origins to 4.0," *Front. Mech. Eng.*, vol. 5, no. September, pp. 1–12, 2019.

[2.3] P. J. Blau, "Fifty years of research on the wear of metals," *Tribol. Int.*, vol. 30, no. 5, pp. 321–331, 1997.

[2.4] J. F. Archard, "Contact and rubbing of flat surfaces," *J. Appl. Phys.*, vol. 24, no. 8, pp. 981–988, 1953.

[2.5] R. F. Bishop, R. Hill, and N. F. Mott, "The theory of indentation and hardness tests," *Proc. Phys. Soc.*, vol. 57, no. 3, pp. 147–159, 1945.

[2.6] E. Holm, R. Holm, and E. I. Shobert, "Theory of hardness and measurements applicable to contact problems," *J. Appl. Phys.*, vol. 20, no. 4, pp. 319–327, 1949.

[2.7] W. Hirst and J. K. Lancaster, "Surface film formation and metallic wear," *J.*

Appl. Phys., vol. 27, no. 9, pp. 1057–1065, 1956.

[2.8] J. F. Archard and W. Hirst, "The wear of metals under unlubricated conditions," *Proc. R. Soc. Lond. A.*, vol. 236, 1956.

[2.9] J. T. Burwell and C. D. Strang, "On the empirical law of adhesive wear," *J. Appl. Phys.*, vol. 23, no. 1, pp. 18–28, 1952.

[2.10] M. M. Khruschov, "Principles of abrasive wear," *Wear*, vol. 28, no. 1, pp. 69–88, 1974.

[2.11] S. C. Lim, M. F. Ashby, and J. H. Brunton, "Wear-rate transitions and their relationship to wear mechanisms," *Acta Metall.*, vol. 35, no. 6, pp. 1343–1348, 1987.

[2.12] J. K. Lancaster, "The formation of surface films at the transition between mild and severe metallic wear," *Proc. R. Soc. London. Ser. A. Math. Phys. Sci.*, vol. 273, no. 1355, pp. 466–483, 1963.

[2.13] P. J. Blau, "On the nature of running-in," *Tribol. Int.*, vol. 38, no. 11-12 SPEC. ISS., pp. 1007–1012, 2005.

[2.14] P. J. Blau, "How common is the steady-state? The implications of wear transitions for materials selection and design," *Wear*, vol. 332–333, pp. 1120–1128, 2015.

[2.15] K. Nakajima and Y. Mizutani, "Structural change of the surface layer of low carbon steels due to abrading," *Wear*, vol. 13, pp. 283–292, 1969.

[2.16] M. A. Moore, "The relationship between the abrasive wear resistance, hardness and microstructure of ferritic materials," *Wear*, vol. 28, no. 1, pp. 59–68, 1974.

[2.17] P. J. Mutton and J. D. Watson, "Some effects of microstructure on the abrasion resistance of metals," *Wear*, vol. 48, no. 2, pp. 385–398, 1978.

[2.18] L. Xu and N. F. Kennon, "A study of the abrasive wear of carbon steels," *Wear*, vol. 148, no. 1, pp. 101–112, 1991.

[2.19] N. P. Suh, "The delamination theory of wear," *Wear*, vol. 25, no. 1, pp. 111–124, 1973.

[2.20] I. I. Garbar and J. V. Skorinin, "Metal surface layer structure formation under

sliding friction," *Wear*, vol. 51, no. 2, pp. 327–336, 1978.

[2.21] Y. Wang, T. Lei, and J. Liu, "Tribo-metallographic behavior of high carbon steels in dry sliding III. Dynamic microstructural changes and wear," *Wear*, vol. 231, no. 1, pp. 20–37, 1999.

[2.22] I. Hutchings and P. Shipway, "Microstructural changes below the wearing surface," in *Tribology: Friction and Wear of Engineering Materials*, 2nd ed., Oxford, Cambridge: Butterworth - Heinemann, 2017, pp. 119–120.

[2.23] I. Hutchings and P. Shipway, "Oxidative Wear," in *Tribology: Friction and Wear of Engineering Materials*, 2nd ed., Butterworth - Heinemann, 2017, p. 127.

[2.24] M. Fink, "Wear Oxidation - A new Component of Wear," *Trans. Am. Soc. Steel Treat.*, vol. 18, p. 1026, 1930.

[2.25] S. J. Rosenberg and L. Jordan, "Influence of oxide films on the wear of steels," *J. Res. Natl. Bur. Stand. (1934).*, vol. 13, no. 2, p. 267, 1934.

[2.26] A. Thum and W. Z. Wunderlich, "No Title," *Metallkunde*, vol. 27, p. 277, 1935.

[2.27] R. Mailander and K. Dies, "Beitrag zur Erforschung der Vorgange beim VerschleiB," *Arch. fur das Eisenhuttenwes.*, no. 10, 1943.

[2.28] F. H. Stott and G. C. Wood, "The influence of oxides on the friction and wear of alloys," *Tribol. Int.*, vol. 11, no. 4, pp. 211–218, 1978.

[2.29] F. H. Stott, "The role of oxidation in the wear of alloys," *Tribol. Int.*, vol. 31, no. 1–3, pp. 61–71, 1998.

[2.30] F. H. Stott and M. P. Jordan, "The effects of load and substrate hardness on the development and maintenance of wear-protective layers during sliding at elevated temperatures," *Wear*, vol. 250–251, no. PART 1, pp. 391–400, 2001.

[2.31] T. F. J. Quinn, "Role of oxidation in the mild wear of steel," *Br. J. Appl. Phys.*, vol. 13, no. 1, pp. 33–37, 1962.

[2.32] J. F. Archard, "The temperature of rubbing surfaces," *Wear*, vol. 2, no. 6, pp. 438–455, 1959.

[2.33] T. F. J. Quinn, D. M. Rowson, and J. L. Sullivan, "Application of the

oxidational theory of mild wear to the sliding wear of low alloy steel," *Wear*, vol. 65, no. 1, pp. 1–20, 1980.

[2.34] T. F. J. Quinn and W. O. Winer, "The thermal aspects of oxidational wear," *Wear*, vol. 102, no. 1–2, pp. 67–80, 1985.

Chapter 3.

Materials & Methods

3.1.   Materials

Seven alloys are examined in the present study; these are G350 grey cast iron, AISI 4330 low alloy steel, 15-5PH precipitation hardened stainless steel, Nitronic 60 austenitic stainless steel, AISI 420 martensitic stainless steel, 905M39 nitriding steel, and CuSn7Zn4Pb7 bronze. Although seven alloys are examined in total, the various heat treatments employed throughout the study result in 17 conditions tested. The alloys are herein listed in order of most-frequently to most-rarely employed in this thesis.

This selection of materials was derived from the academic-industrial project (see Chapter 4) at the beginning of the PhD, which included a material selection and testing study for pumping applications. However, the materials discussed herein have numerous other industrial uses, and are not limited to employment in one single field.

3.1.1.   *EN-GJL-350 (G350) – Grey Cast Iron*

EN-GJL-350 is a grey cast iron employed in numerous engineering applications, such as disc brakes and slipper pads [3.1], which require good wear resistance. The alloy was employed in all experimental chapters and was used in many conditions. The name G350 refers to its tensile strength in the as-cast condition, namely a minimum of 350MPa [3.2]. Throughout this thesis, G350 is simply referred to as cast iron. As a result of its chemical composition (carbon and silicon) (Table 3.1), the alloy possesses graphite flakes interspersed throughout the matrix. The graphite flakes are slightly variable in size, shape, and distribution, but are typically I-A/C-5 in accordance with ISO 945-1 [3.3], depending on location within the sample. The matrix of G350 in the as-cast form is fully coarse pearlite (Figure 3.1), but is readily heat treatable and can be both hardened and softened easily.

G350 grey cast iron is subjected to various heat treatments throughout the present study. In Chapters 4 and 5, the alloy is hardened through oil quench and tempering. This involved raising the temperature of the samples to 900°C before quenching in oil, and tempering at 400°C for 90 minutes. This resulted in a change from coarse pearlite to a fully martensitic matrix. In Chapter 6, the alloy is softened through subcritical spheroidizing annealing heat treatments. This involved soaking the samples for extended periods at a high temperature below the eutectoid temperature. Samples were held at 700°C for various durations, ranging from five to 15 days. This resulted in a

change from coarse pearlite to various degrees of spheroidized carbides in a ferritic matrix. In Chapter 7, the alloy is subjected to two heat treatments, where the samples used as discs were quenched and tempered to various degrees while the samples used as pins were furnace-cool annealed. The disc heat treatments involved raising the temperature of the samples to 900°C before quenching in oil, and tempering at various temperatures from 400°C to 700°C for 24 hours. This resulted in various degrees of tempered martensite, featuring both acicular lath microstructure and spheroidized carbides in a ferritic matrix. The annealing process involved raising the temperature of the samples to 900°C before setting the furnace to room temperature and cooling over a 12 hour period, producing a mixture of coarse pearlite and ferrite.

Figure 3.1 - Microstructure of G350 grey cast iron [x500 – etched].

Table 3.1 - Chemical composition of G350 cast iron, obtained from supplier certificate.

Material	C	Cr	Cu	Mn	Mo	P	S	Si	Fe
G350	3.35	0.25	0.65	0.7	0.25	0.15	0.055	2.75	Bal.

3.1.2.   *AISI 4330 – Low Alloy Steel*

AISI 4330 is a low alloy steel frequently used in oil, gas, and aerospace industries for high strength applications [3.4]. In the oil and gas industry, AISI 4330 is often used as drilling jars due to its ability to withstand shock loading and high stress concentrations [3.5]. In the aerospace industry, the alloy sees employment as forgings in aircraft landing gears [3.6]–[3.8].

This alloy was studied in Chapters 4, 5, and 6, and was employed in the normalised, quenched, and tempered condition. The designation AISI 4330 refers to its chemical composition (Table 3.2), with the 43 referring to nickel-chromium-molybdenum and the 30 referring to 0.3 wt% carbon content. The microstructure of AISI 4330 was tempered martensite, with fine spheroidised carbides interspersed throughout a ferritic matrix. These features are hypothesised to produce good tribological performance in thanks to the relatively high resultant hardness.

Table 3.2 - Chemical composition of AISI 4330, obtained from supplier certificates.

Material	C	Cr	Ni	Cu	Mn	Mo	P	S	Si	Al	V	Co	Nb	Fe
AISI 4330	0.33	1.4	3.2	0.18	0.26	0.58	0.005	0.001	0.07	0.01	0.121	0.012	0.002	Bal.

3.1.3.   *15-5PH – Precipitation Hardened Stainless Steel*

The stainless steel, 15-5PH, is used primarily in the aerospace industry for high strength and toughness applications [3.9] where particular tailoring of properties is required. Common uses of the alloy include valve parts, shafts, gears, and chemical processing equipment [3.10]. Other applications include certain nuclear power plant components and missile systems [3.11].

The grade refers to the chemical composition (Table 3.3) of the alloy, with 15 wt% chromium and 5 wt% nickel. This alloy is precipitation hardened, meaning that it is heat treated in a particular method, similar to a quench and temper treatment, to achieve the desirable properties. Precipitation hardened materials are subjected to heat treatments, which begin with soaking at an elevated temperature to allow for the complete dissolution of all alloying elements within the metallic matrix. The sample

is then quenched which "locks" the alloying elements in solution at room temperature. The sample is then subjected to ageing heat treatments, which involve reheating for a length of time at temperature, allowing for the partial precipitation of micro constituents out of the matrix. However, instead of softening the alloy, as tempering does for conventional heat treatments, the ageing process strengthens and hardens the alloy. The precipitates strengthen the metallic matrix by serving a reinforcement role, and by preventing dislocation movement, and therefore plastic deformation, from occurring. The difference here lies in the size of the micro constituents; for precipitation hardened alloys, the micro constituents are minute (nanoscale) and require a transmission electron microscope to resolve. For tempering of normal alloys, large carbide globules precipitate, which do not serve to hinder dislocation movement and therefore soften the alloy.

15-5PH was used in Chapters 4 and 5 in the present study in the H1075 condition, meaning that the ageing treatment was performed at 1075°F, resulting in a tempered martensitic microstructure. This is expected to produce favourable wear performance.

Table 3.3 - Chemical composition of 15-5PH, obtained from supplier certificates.

Material	C	Cr	Ni	Cu	Mn	Mo	P	S	Si	Al	V	Co	Nb	Fe
15-5PH	0.03	14.36	5.24	3.16	0.59	0.34	0.02	0.001	0.35	0.012	0.075	0.085	0.204	Bal.

3.1.4.   *Nitronic 60 – Austenitic Stainless Steel*

Nitronic 60 is a stainless steel (Table 3.4), bespoke designed for wear resistance and high temperature applications [3.12]. It is reported to have favourable wear resistance for a corrosion-resistant alloy, as well as having good galling resistance [3.13]. This galling resistance has led to the alloy also being used as fasteners, due to more repeated uses before failure [3.14].

The crystallographic arrangement of Nitronic 60 at room temperature is face-centred cubic (FCC), meaning that the alloy is softer and more ductile than ferritic and martensitic alloys. Due to this crystallographic arrangement, it is expected to

experience more strain hardening from sliding wear damage than the martensitic alloys. Nitronic 60 was studied in Chapter 4.

Table 3.4 - Chemical composition of Nitronic 60, obtained from supplier certificates.

Material	C	Cr	Ni	Mn	P	S	Si	N	Fe
Nitronic 60	0.07	16.4	8.3	8.2	0.04	0.002	3.82	0.17	Bal.

3.1.5.   *AISI 420 – Martensitic Stainless Steel*

AISI 420 is a high strength and high hardness stainless steel used in blades, cutlery, and surgical equipment [3.15]. Its high hardness allows it to be used in bladed applications such as knives and scissors [3.16], while its corrosion resistance sees it used in alkali chemical processing applications [3.17].

AISI 420 has a relatively high carbon content (Table 3.5) for a stainless steel, and is thus readily heat treatable to achieve high hardness and strength, resulting from its martensitic microstructure. Its high hardness is expected to produce favourable sliding wear performance. AISI 420 was employed in Chapter 4.

Table 3.5 - Chemical composition of AISI 420, obtained from supplier certificates.

Material	C	Cr	Ni	Mn	P	Mn	S	Si	Fe
AISI 420	0.22	13.29	0.18	0.34	0.018	0.34	0.001	0.46	Bal.

3.1.6.   *905M39 – Nitriding Steel*

Grade 905M39 (Table 3.6), is a medium carbon, chromium aluminium molybdenum alloy steel with good wear resistance and ease of nitriding [3.18]. Nitriding is a surface modification technique used to harden the outer surface layer of the material by forcibly diffusing nitrogen into the outermost surface resulting in a supersaturated solution and nitrogen precipitation (see Chapter 4). The alloy is frequently employed in the automotive and textile industry as connecting rods and clutch plates [3.19]. In

more wear-intensive applications, it is used as gears, pinons, and cams, often in the nitrided condition [3.20].

Nitriding steel was used in rolled condition, with alternating lighter bands of ferrite/pearlite and darker bands thought to be bainite or fine pearlite. The samples were nitrided and this could be seen through a darkening of the bainitic bands, and the precipitation of nitride compound networks near the surface (see Section 4.3.1). Such microstructural features are hypothesised to produce low resultant volume losses. Nitriding steel was studied in Chapter 4.

Table 3.6 - Chemical composition of the nitriding steel, obtained from supplier certificates (prior to nitriding).

Material	C	Cr	Mn	Mo	P	S	Si	Al	Fe
Nitriding Steel	0.39	1.6	0.5	0.2	0.025	0.025	0.25	1.1	Bal.

3.1.7.   CuSn7Zn4Pb7 – Bronze

CuSn7Zn4Pb7 bronze is a copper-based alloy with tin and lead (Table 3.7) used in bearing applications [3.21]. The alloy is a standard lead-tin bronze and is an affordable multi-use material for bearings. It sees common use in slide bearings, and bearing bushings in rotating machinery [3.22].

Due to its copper base, the alloy possesses an FCC crystallographic structure, resulting in a soft and malleable alloy. Like Nitronic 60, this expected to result in surface strain hardening from sliding wear. This material was pre-selected by the industrial collaborator as part of Chapter 4.

Table 3.7 - Chemical composition of the bronze alloy, obtained from supplier certificates.

Material	Sn	Pb	Zn	Fe	Ni	Sb	P	Cu
Bronze	6.4	6.07	3.58	0.18	0.54	0.1	0.04	Bal.

3.2.   Methods

Numerous metallurgical techniques were used to quantify wear loss and characterise wear behaviour. Pin-on-disc sliding wear testing, optical microscopy, scanning electron microscopy (SEM), energy dispersion spectroscopy (EDS), stylus profilometry, and hardness measurements were discussed in all experimental chapters (Chapters 4 – 7). X-ray diffractometry (XRD) was used in Chapters 6 and 7.

3.2.1.   *Pin-on-disc Sliding Wear Testing*

Sliding wear testing was conducted using a custom built pin-on-disc tribometer (Figure 3.2). The tribometer rig consisted of a vertically suspended three-phase motor (pointing up), with the disc sample holder mounted on the motor shaft which was allowed to rotate using a controller. The surrounding support structure of the rig continued vertically above this, and featured an arm shaft offset above the disc sample holder. The arm was mounted onto the arm shaft, and held the collet which would in turn hold the stationary pin sample. The rotation of the arm shaft allowed for precise control over the pin displacement, and the collet mounted in the arm allowed for the contact faces of the pin and disc to be perfectly aligned. Various masses were applied to the top of the collet which result in various contact pressures between the pin and disc.

The pin-on-disc configuration was selected to generate sliding wear test data to allow for the closest approximation to the contact conditions seen in the pump studied during the academic-industrial project (Chapter 4). As the pump was a rotary-piston type and experienced unidirectional sliding wear between the contact faces of the internal tyre and slipper pads, the pin-on-disc configuration was a better configuration than other types of test rig (see Section 1.6).
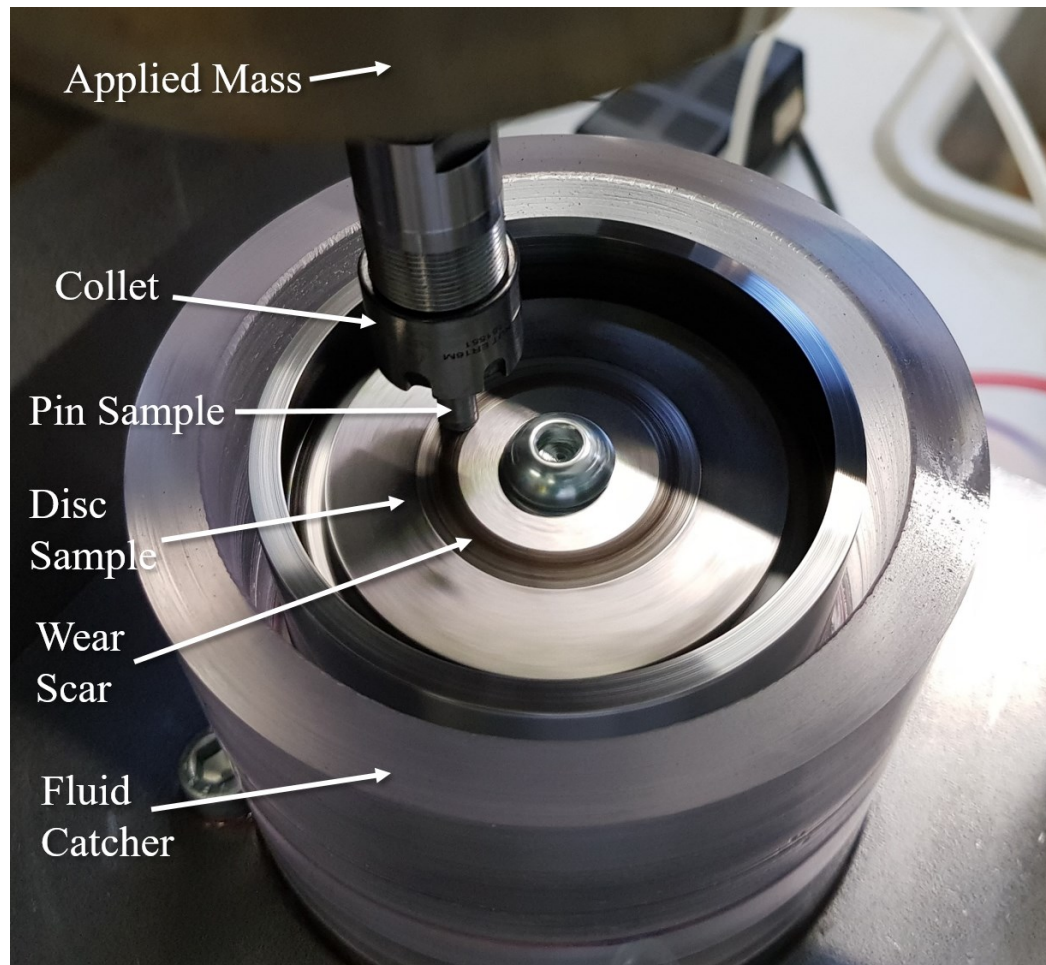
Figure 3.2 - Pin-on-disc testing rig.

Testing followed the procedure of ASTM G99-17: *Standard Test Method for Wear Testing with a Pin-on-disc Apparatus* [3.23]. ASTM G99-17 describes two methods of carrying out pin-on-disc tests. Both follow the same procedure, but the first uses testing parameters such as loads, speeds, and materials as described in the standard (Table 3.8), while the second only follows the procedure but uses different test parameters.

Table 3.8 - ASTM G99-17 [3.23] pin-on-disc testing parameters (not employed in this thesis).

Load (N)	Speed (m/s)	Distance (m)	Pin dia (mm)	Atmos	Temperature (°C)	Humidity (%)	Track dia (mm)
10.0	0.1	1000.0	10.0	Air	23.0	12 - 78	12 - 78

In this thesis, pin-on-disc tests followed only the procedure of G99-17, meaning that different testing parameters to those described in the standard were employed. This was to allow for accurate simulation of the conditions seen in the pump manufactured by the industrial collaborator.

The standard describes how to conduct pin-on-disc testing as follows:

- Immediately before testing, clean the pin and disc samples using solvents to remove adhered grease and other contaminants. Use non-film-forming solvents to accomplish this.
- Weigh the samples to the nearest 0.0001g.
- Insert the pin and disc samples securely in the testing rig and ensure contact faces are perpendicular (± 1°).
- Add the chosen masses to the top of the pin. Hold the pin out of contact with the test and start the motor and select the appropriate sliding speed, then stop the motor.
- Set the timer or revolution counter to the desired limit and begin the test. Tests should not be interrupted or restarted.
- Remove the samples from the test rig and repeat the cleaning steps involving non-film-forming solvents to clean the contact faces.
- Re-weigh the samples to the nearest 0.0001g.
- Repeat the test with additional samples to obtain sufficient data for statistically significant results.

Applied masses of 2kg, 4kg, and 6kg were used in Chapters 5, 6, and 7, and an applied mass of 6kg was used in Chapter 4. To allow for continuity between chapters, the same sliding speed and distance were used for all tests. Input variables include the applied load (Chapters 5, 6, and 7), materials (Chapters 4, 5, and 6), microstructural condition (Chapters 6 and 7), and environment (Chapter 5).

To ensure accurate measurements, the rig was calibrated prior to each testing regime. This was achieved by ensuring the motor was mounted at a 90 degree angle to ensure concentric motion. The concentricity of the disc holder rotational movement was measured while in motion, using a dial test indicator (DTI). The mounting of the motor was then adjusted to minimise any disturbances.

To ensure accurate mass loss measurement, the analytical mass balance, accurate to 0.0001g, was calibrated before each test.

All tests were conducted three times to generate representative data.

3.2.2.   Optical Microscopy

Optical microscopy was used to inspect and characterise material microstructures. This was achieved using a metallographic inverted microscope (Figure 3.3) (Olympus GX-51) at various magnifications. Samples were prepared for this by sectioning, hot mounting in Bakelite, grinding, and polishing. This resulted in a smooth, strain-free surface which was representative of the material microstructure and suitable for optical microscopy.

In most cases, the samples were inspected in the etched condition, which consisted of preferentially corroding certain areas of the sample to highlight microstructural features. For G350 cast iron, AISI 4330, and the nitriding steel, Nital (3% nitric acid / 97% ethanol) was used as the etchant. Kallings reagent was used as the etchant for 15-5PH and AISI 420. Nitronic 60 was electrolytically etched. Ferric chloride was used to etch the bronze.

The Nital etching process can be summarised as follows:

- Etching should be conducted over a short window of time.
- If necessary, produce Nital solution by mixing nitric acid and ethanol in a 3% / 97% ratio.
- Soak a ball of cotton wool in the Nital solution.
- Gently rub the soaked cotton wool over the specimen in a circular motion, covering all areas. Ensure adequate lighting allows for a detailed inspection of the sample surface.
- Once the sample surface turns a light-brown colour (5 – 30 seconds), stop rubbing and rinse the specimen in hot water.
- Blow dry the sample as fast as possible.

Etching processes for the other alloys are described in detail in the ASM handbook [3.24].

Figure 3.3 - GX-51 inverted optical microscope [3.25].

3.2.3.   *Scanning Electron Microscopy (SEM)*

Scanning electron microscopy (SEM) is a method of visualisation using high energy electrons. SEM imaging involve firing a high energy beam of electrons into the sample. This then excites the atoms in the sample, causing them to emit their own electrons. The intensity of the received electrons depends primarily on the sample surface topography, allowing for an image to be produced based on the received electrons [3.26]. In back scatter mode, electrons from the incident beam are reflected (back scattered) towards the gun. As heavier elements with larger nuclei are more likely to reflect electrons, they appear brighter, whereas lighter elements with smaller nuclei appear darker due to less backscatter. SEM inspections were used frequently to analyse wear scars produced from sliding wear tests. Backscatter mode was used to highlight the presence of oxides on the wear scar surface. SEM was conducted using a Hitachi SU-6600 microscope (Figure 3.4).
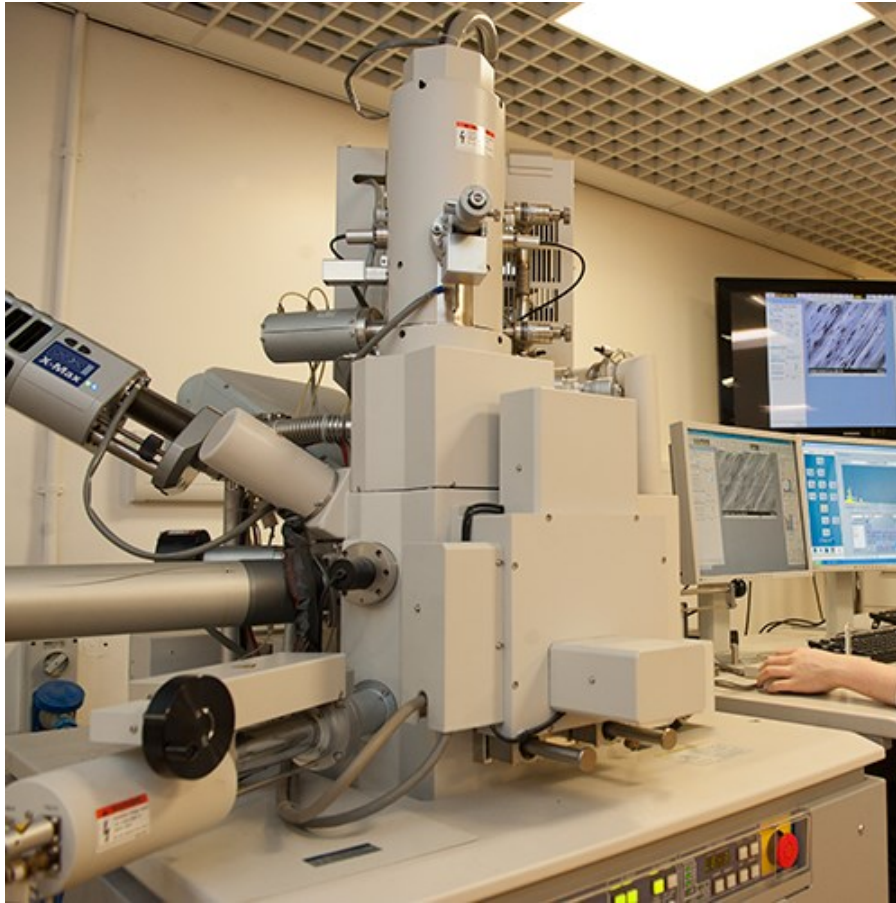
Figure 3.4 - Hitachi SU-6600 scanning electron microscope [3.27].

3.2.4.   Energy Dispersion Spectroscopy (EDS)

Energy dispersion spectroscopy (EDS) is a method through which the sample surface is bombarded with electrons at sites of interest to determine elemental composition. As the area is impacted by the electrons, complex electron interactions cause the atoms to emit their x-rays, the frequency of which is detected and used to determine the elements present. As each element has a unique atomic electron arrangement, the characteristics of the emitted x-rays can be used to determine the elemental source, and is thus useful when characterising the microstructures of metals. EDS is particularly useful for identifying areas of interest in highly alloyed materials where multiple types of intermetallics or non-metallic inclusions are present. Herein, the most common use of EDS is for evaluating the coverage of oxides on the wear scar surface to determine whether mild or severe wear has taken place.

3.2.5.   Hardness Measurement

Hardness is the ability of a material to resistant indentation, and is a key mechanical property in tribological studies. Higher hardness correlates positively with wear resistance in most contexts (see Chapter 2), and is a good indicator for how a material will wear. To measure hardness, micro and macro indentation tests are used in a Vickers hardness measurer (Figure 3.5) (Mitutoyu MVK-G1).

Figure 3.5 - Mitutoyu micro-indentation hardness measurer [3.28].

Hardness measurement involves indenting the surface of the sample with a diamond pyramid of known dimensions and measuring the resultant indent. The dimensions of the indent are used by the Vickers measurement machine to calculate the hardness value of the sample. Two methods, micro indentation and macro indentation, were used in the present study – referring to the relative size of the indent on the sample. For materials with a heterogeneous microstructure, such as cast iron or bronze, using macro indentation hardness is a better indicator of bulk hardness, due to local disparities caused by varying microstructures.

All micro indentation hardness values were averaged from 10 measurements, and all macro indentation hardness measurements were averaged from five measurements.

3.2.6.   *Stylus Cross-sectional Profilometry*

Cross-sectional profilometry was used to measure the resultant wear scar cross-section after sliding wear tests using a Mitutoyu Surftest SV2000. This involved dragging a fine contact stylus across the wear scar (Figure 3.6) to map the horizontal and vertical components of the surface. X and Y coordinates were then outputted which allowed for plotting of the cross-section to inspect the width, depth, and areas of interest. Profilometry is particularly useful for comparing the depth of scars on different samples, as well as highlighting large peaks and troughs caused by ploughing action.

Figure 3.6 - Stylus profilometry of a disc wear scar.

3.2.7.   X-ray Diffractometry (XRD)

X-ray diffractometry (XRD) is a method of phase identification and internal stress measurement. Atomic structures and crystallographic arrangements can be identified using XRD by firing a beam of x-rays into a sample. The crystalline structure of the sample then diffracts the x-rays into many different directions specific to the sample material. By measuring the resultant angles and intensities of the diffracted x-rays, many material parameters such as electron cloud density, mean atomic positioning, chemical bonding, and crystallographic disorder can be determined [3.29]. In materials engineering contexts, XRD is primarily used for identifying metallic phases and quantifying residual stresses remaining in the material after deformation. A Bruker D8 Advance was used for XRD (Figure 3.7) in Chapters 6 and 7.
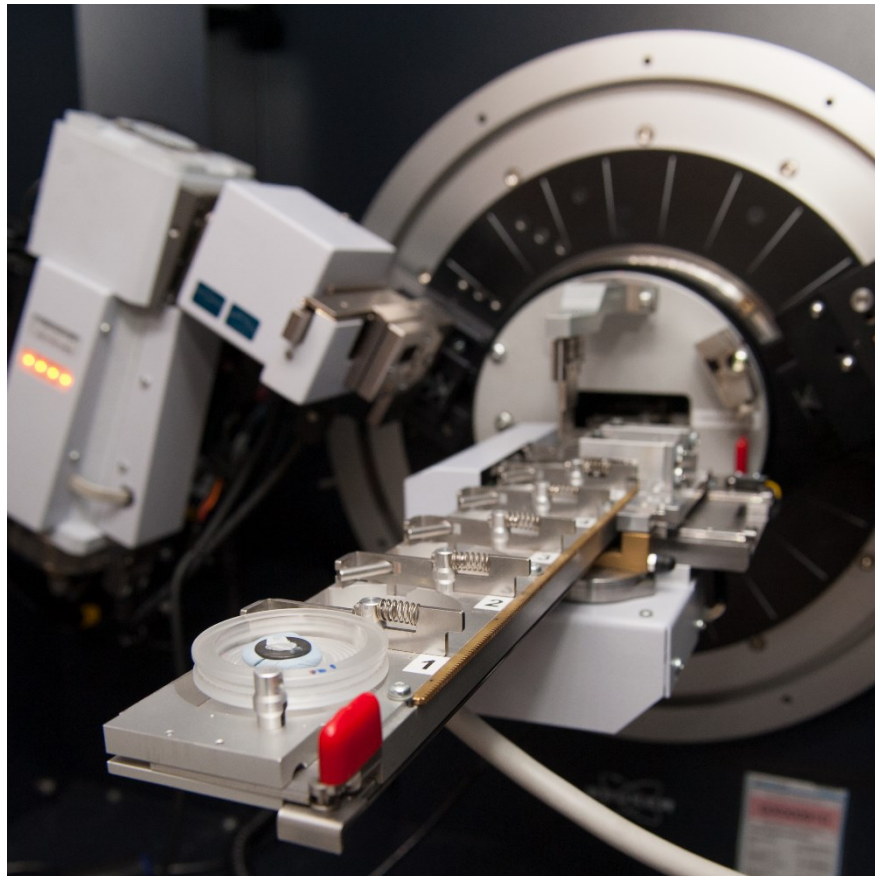
Figure 3.7 - Bruker D8 Advance x-ray diffractometer [3.30].

3.2.8.   Heat Treatments

All experimental chapters feature heat treatments (Figure 3.8) of the tested materials. In tribological contexts, the thermal history of the alloy is important to consider

because this determines the condition of the microstructure, thus its mechanical properties such as strength, toughness, hardness, etc.

G350 grey cast iron is used in various conditions throughout the thesis. These conditions were achieved through three types of heat treatment: quenching and tempering, subcritical annealing, and furnace cool annealing. Quenching and tempering involves raising the temperature of the sample to a high temperature (approximately 900°C), which is above the eutectoid temperature, and quenching into oil to rapidly cool the sample. This quench results in a transformation to martensite, a hard crystallographic phase. To recover some toughness and ductility, the samples are then tempered by reheating to an intermediate temperature (approximately 400°C) for approximately 1 – 2 hours. In Chapter 4, pearlitic cast iron is heat treated through quenching and tempering by an external heat treatment engineering company to achieve a martensitic matrix. In Chapter 5, a similar quenching and tempering heat treatment is conducted by the author to achieve a microstructure similar to that seen in the previous chapter.

Figure 3.8 - Heat treatment of the discs used in Chapter 7.

Chapter 6 features subcritical annealing, whereby the pearlitic cast iron samples are heated to an elevated temperature of 700°C, which is below the eutectoid temperature, and left to soak for a significant length of time. This provides the thermal energy to allow for cementite lamellae to rearrange into a spheroidal morphology in a drive to reduce surface area, resulting in a softer, more ductile microstructure. As the subcritical annealing temperature is below the eutectoid temperature, no crystallographic phase change takes place.

Chapter 7 features two series of heat treatments of cast iron (i.e. one for the pin and one for the disc). The discs are subjected to quenching and tempering heat treatments with varying temperatures of tempering to produce a variety of tempered martensitic matrices. The pins are slow furnace cool annealed from their prior martensitic matrix to a mix of pearlite and ferrite. Furnace cool annealing involves raising the temperature of the samples to a high temperature above the eutectoid temperature, before then programming the furnace to 10°C and leaving the samples to cool at the natural rate of the furnace.

References

[3.1] L. Wei, Z. Zhang, S. Nie, and W. Xiangyang, "Direct and indirect corrosion wear erformance of AISI 630 steel for the slipper/swashplate pair in a water hydraulic pump," *Proc. Inst. Mech. Eng. Part J J. Eng. Tribol.*, vol. 233, no. 10, pp. 1605–1615, 2019.

[3.2] British Standards Online, "Founding - Grey cast irons," in *BS EN ISO 1561*, 1997, p. 38.

[3.3] BSI Standards Online, "BS EN ISO 945-1:2019 BSI Standards Publication: Microstructure of cast irons," 2019.

[3.4] All Metals & Forge Group, "AISI / Alloy Steel 4330," *Alloy Steel*. [3.Online]. Available: https://steelforge.com/alloy-steel-4330/. [3.Accessed: 07-Aug-2022].

[3.5] "AISI 4330, 4330V, 4145, 4150 - ALLOY STEEL," *Virgamet*. [3.Online]. Available: https://virgamet.com/aisi-4330v-4145-4150-alloy-steel. [3.Accessed: 17-Sep-2022].

[3.6] "AISI 4330 Alloy Steel (UNS J24045)," *AZO Materials*. [3.Online]. Available: https://www.azom.com/article.aspx?ArticleID=6670. [3.Accessed: 17-Sep-2022].

[3.7] "AISI 4330 / 4330V STEEL," *Waldun Steel*. [3.Online]. Available: https://waldunsteel.com/products/aisi-4330-4330v-steel/. [3.Accessed: 17-Sep-2022].

[3.8] "4330 ALLOY STEEL," *Rickard Metals*. [3.Online]. Available: https://rickardmetals.com/products/alloy-steel/4330-alloy-steel/. [3.Accessed: 17-Sep-2022].

[3.9] Aircraft Materials, "15-5PH Stainless Steel (AMS 5659 / AMS 5862)." [3.Online]. Available: https://www.aircraftmaterials.com/data/alstst/ams5659.html. [3.Accessed: 07-Aug-2022].

[3.10] "15-5PH Stainless Steel," *CIVMATS*. [3.Online]. Available: https://www.civmats.com/grades/GRADES-15-5PH.HTML. [3.Accessed: 17-Sep-2022].

[3.11] "15 5PH (AMS 5659, UNS S15500)15 5PH (AMS 5659, UNS S15500)," *Smith Metal*. [3.Online]. Available: https://www.smithmetal.com/15-5ph.htm. [3.Accessed: 17-Sep-2022].

[3.12] Electralloy, "Nitronic 60," pp. 1–28, 2013.

[3.13] "Nitronic 60," *Langley Alloys*. [3.Online]. Available: https://www.langleyalloys.com/2022/09/05/nitronic-60/. [3.Accessed: 17-Sep-2022].

[3.14] "NITRONIC 60 (Alloy 218) (UNS S21800)," *HPA Alloys*. [3.Online]. Available: https://www.hpalloy.com/Alloys/descriptions/NITRONIC60.aspx. [3.Accessed: 17-Sep-2022].

[3.15] Chisen Forged Product, "AISI 420 Stainless Steel (SS420, UNS S42000)." [3.Online]. Available: https://www.forgedproduct.com/forging-materials/ss420-astm-aisi-420-stainless-steel.html. [3.Accessed: 07-Aug-2022].

[3.16] "SS420 Grade AISI 420 Stainless Steel Properties, Heat Treatment, Hardness, Magnetic," *World Material*. [3.Online]. Available: https://www.theworldmaterial.com/ss420-astm-aisi-420-stainless-steel-grade/. [3.Accessed: 17-Sep-2022].

[3.17] "Stainless Steel - Grade 420 (UNS S42000)," *AZO Materials*. [3.Online]. Available: https://www.azom.com/article.aspx?ArticleID=972. [3.Accessed: 17-Sep-2022].

[3.18] Smiths Metal, "EN41 Steel (905M39)." [3.Online]. Available: https://www.smithmetal.com/en41.htm. [3.Accessed: 07-Aug-2022].

[3.19] "905M39 Nitriding Steel," *West Yorkshire Steel*. [3.Online]. Available: https://www.westyorkssteel.com/steel-specifications/bs-steel/bs970/905m39/. [3.Accessed: 17-Sep-2022].

[3.20] "EN41 (905M39)," *Thames Stockholders*. [3.Online]. Available: https://www.thamesstock.com/assets/pdf/steels/en41-905m39-datasheet.pdf. [3.Accessed: 17-Sep-2022].

[3.21] Bronze Lube, "CuSn7Zn4Pb7 Cast Bronze Bearing." [3.Online]. Available: https://www.bronzelube.com/portfolio_skills/cusn7zn4pb7-cast-bronze-bearing/. [3.Accessed: 07-Aug-2022].

[3.22] "CuSn7Zn4Pb7," *iz-metal*. [3.Online]. Available: https://www.iz-metal.com/datasheet/CuSn7Zn4Pb7.pdf. [3.Accessed: 17-Sep-2022].

[3.23] ASTM Standards, "ASTM G99 - 17: Standard Test Method for Wear Testing with a Pin-on-Disk Apparatus."

[3.24] G. Petzow, *Metallographic Etching*. ASM International, 1999.

[3.25] Purdue University, "Olympus GX-51," *Optical Microscopy*. [3.Online]. Available: https://engineering.purdue.edu/MSE/research/facilities/CharacterizationFacilities/OpticalMicroscopy/OlympusGX51. [3.Accessed: 07-Aug-2022].

[3.26] T. F. J. Quinn, "Scanning Electron Microscopy (SEM) and surface topographical analysis," in *Physical Analysis for Tribology*, Cambridge: Cambridge University Press, 1991, pp. 61–64.

[3.27] U. of Strathclyde, "Scanning Electron Microscopes," *Range of Analyses*. [3.Online]. Available: https://www.strath.ac.uk/research/advancedmaterialsresearchlaboratory/rangeo fanalyses/compositionalanalysis/scanningelectronmicroscopes/. [3.Accessed: 07-Aug-2022].

[3.28] M. & M. de L. D'occasion, "MITUTOYO MVK G1." [3.Online]. Available: http://qomino.com/c/dim/portfolio/mitutoyo-mvk-g1/. [3.Accessed: 07-Aug-2022].

[3.29] T. F. J. Quinn, "X-ray Diffraction techniques," in *Physical Analysis for Tribology*, Cambridge: Cambridge University Press, 1991, pp. 98–123.

[3.30] U. of Strathclyde, "X-ray Diffractometry," *Range of Analyses*. [3.Online]. Available: https://www.strath.ac.uk/research/advancedmaterialsresearchlaboratory/rangeo fanalyses/compositionalanalysis/x-raydiffractometerxrd/. [3.Accessed: 07-Aug-2022].

Chapter 4.

Preliminary Material Selection: Comparative Tribological Testing of Engineering Alloys

Abstract

This chapter is expanded from a technical report produced for a hydraulic pump manufacturer in central Scotland. It investigates the wear performance of heat-treated and nitrided components, and compares them to the performance of untreated, commercially available alloys of the same type. The project originated as a collaborative feasibility study to determine if highly processed, heat treated, nitrided materials could be substituted out for more commercially available, untreated alloys. The dry sliding wear properties of Nitronic 60, AISI 420, 15-5PH, AISI 4330, G350 grey cast iron, nitrided medium-carbon steel, and leaded bronze were investigated using pin-on-disc sliding wear tests.

Materials were tested in combinations using a pin sample and a disc sample. Benchmark materials, employing the currently used, highly processed, pumping materials were first tested to provide a reference for which to compare the performance of a variety of different materials to ascertain if a suitable combination could be used for economic purposes. An initial choice of materials was first presented by the author to the pump manufacturer, while the final choice of materials and combinations to test were decided collaboratively. The pin-on-disc results broadly divide the material testing combinations into three groups from best to worst: combinations with cast iron pins, with Nitronic 60 pins, and self-mated/bronze combinations. This is attributed to the high matrix hardness from the heat-treatment and favourable oxide/graphite lubrication properties inherent to cast irons.

4.1.   Introduction

Engineering alloys can feature a wide range of wear resistances, depending on the specific base material, microstructural condition and surface treatment. Comparative studies are therefore valuable to allow for direct comparisons and to highlight contrasts in wear responses. In this chapter, the sliding wear testing of numerous engineering alloys under identical conditions is reported on for material selection purposes, and to allow for three shortlisted alloys to be discussed further in the next chapter (Chapter 5). Seven engineering alloys, ranging from alloy steel, to bronze, to stainless steel are examined, the results of which are compared and contrasted with a specialist nitrided steel used in hydraulic pumping components. Nitriding is a surface modification technique for alloys that require extreme wear resistance [4.1]. This is accomplished by diffusing nitrogen into the outer surface layers of a component to increase the indentation hardness and wear resistance [4.2]. By comparing the nitrided steel to several untreated alloys, the tribological benefit is contextualised and quantified. The six other engineering alloys tested in this chapter are: G350 grey cast iron, AISI 4330 alloy steel, 15-5PH precipitation hardened stainless steel, AISI 420 martensitic stainless steel, Nitronic 60 austenitic stainless steel, and a leaded-tin bronze . A general overview of these alloys is given in Chapter 3.

Extensive discussions on the physical and mechanical properties of cast irons were given by Angus [4.3], who described the alloy family in great detail. In regards to dry sliding wear, Angus [4.3] noted that the qualities required include: "Good thermal conductivity… Ability to resist galling… Good frictional properties… Reasonable strength… Freedom from surface volume changes caused by phase transformation… Low elastic modulus to accommodate thermal stress" [4.3]. Cast iron optimally fulfils these criteria in combination and is therefore justified as a suitable sliding material. Angus [4.3] also discussed the effective thermal properties of grey cast irons, the importance of which were stressed in disc and drum brake design for automobiles [4.3]. In addition to their usage as low strength components with complex geometries, grey cast irons see frequent usage in sliding wear and damping applications. This is due to the unique presence of graphite flakes throughout the matrix of grey cast irons.

An overview of grey cast iron in sliding was produced by LaBelle [4.4], who commented on graphite flake morphology and its relationship to wear resistance. The

author [4.4] noted that the graphite in cast irons can shear out along the wear surfaces and prevent metal to metal contact, acting as a dry lubricant and prohibiting the localised welding of asperities. Experiments involving engine cylinders showed that increases in graphite flake size and frequency improved scuffing (see Chapter 1 (surface texture roughening)) resistance [4.4].

The frequent industrial usage of cast iron has also stimulated scientific research. Montgomery [4.5] investigated the running-in of grey cast iron in engine piston cylinders, and noted that this transient process improved component conformity and reduced dimensional irregularities. The author also displayed images of the graphite lubrication layer and showed that this was a product of wear, and was not present on unworn surfaces. In samples showing the graphite layer, the surface of the layer was smoother than that of the underlying bulk metal surface, indicating that the smoothening of the worn surfaces may have been due to the graphite layer coverage of local peaks and troughs, rather than the polishing of the metallic surface [4.5].

Eyre et al. [4.6] compared the wear of flake graphite grey cast iron with nodular graphite grey cast iron in pin on disc sliding wear tests. The researchers [4.6] found that nodular iron experienced lower wear rates than the flake graphite cast iron due to the lower fracture toughness associated with the flake tip morphology, resulting in more material removal than with the nodular graphite cavities which do not show such high stress concentrators. The presence of adhered black oxide products on the wear surface was also discussed, which was observed to rest on top of a hardened surface layer, the composition of which was unclear. The nature of transitions to severe wear was also discussed, and it was noted that the outputted temperature from sliding under increased loads and at high speeds may have caused thermal softening of the sample surface, lowering the indentation hardness and disrupting the oxide layer due to increased plastic deformation.

Kawamoto et al. [4.7] studied cast iron in sliding under a vacuum and compared it to sliding in ambient atmospheric conditions, and focussed on the "frictional hardened layer", the term used to describe the tribologically transformed zone. The authors [4.7] noted that non-linear behaviour was seen for the sliding in air tests, where increasing sliding speed caused a local maximum at 1.5m/s that then decreased at greater speeds. This was attributed to the influence of the generation and breakdown of the passive

oxide film, because no maximum was seen for the tests conducted under vacuum. Instead, only a decrease in wear with increasing speed was observed, however, this began at a higher wear rate because only mechanical wear took place in the absence of oxidation. The formation of the tribologically transformed zone was also found to be independent of oxidational properties because it was present in both of the tests conducted under vacuum and in those conducted in air, and was thus a product of only thermal and deformation factors rather than oxidational.

Graphite can also be beneficial in the nodular (spheroidal) form, or in the "worm" form where the flakes appear shortened and rounded (compacted graphite cast iron). Slatter et al. [4.8] studied the impact wear resistance of compact cast iron for automotive applications. After being induction heated and quenched, for automotive applications, the authors [4.8] found that coarse martensite had formed in the surface zone of the alloy, and that in some instances, this led to brittle fracture during impact wear testing. In other cases, the heat treatment caused a transformation to fine martensite which was more uniform throughout the matrix and did not cause such adverse reactions. In terms of wear resistance, the samples heat treated to a depth of 2mm outperformed those heat treated to a depth of 3mm. The authors attribute this to the finer-grained martensite produced by the 2mm heat treatment.

Three stainless steels (Nitronic 60, 15-5PH, and AISI 420) are examined in this chapter. Stainless steels are often suboptimal material choices for many sliding wear applications due to their poor wear resistance in comparison to cast irons and alloys steels [4.9], [4.10]. This is primarily due to two reasons: (1) their poor resistance to galling and seizure (which are forms of severe adhesive wear), and (2) their elemental composition, namely their high chromium content and resultant passivity, which prohibit them from beneficially forming iron oxides so easily as other ferrous materials [4.11]. Ironically, it is these properties, which bestow stainless steels their excellent corrosion resistance, that are partly responsible for their poor wear performance.

Bhusan [4.12] reported that stainless steels in the self-mated configuration experienced twice as poor galling resistance than all other steels, with the exception of the Nitronic series of alloys. While discussing the benefits of strain hardening during sliding, Hutchings and Shipway [4.13] noted that "austenitic stainless steels,

for example, are notoriously susceptible to galling yet work-harden rapidly" [4.13], evidencing the reputation for poor wear and galling resistance for certain stainless steels. Nevertheless, in contexts which require a combination of sliding and corrosion, such as with seawater machinery or bearings in corrosive environments, and where cost precludes the more exotic alloys such as stellite, stainless steels do see tribological action [4.9].

Both martensitic stainless steels discussed in this chapter (15-5PH and AISI 420) have received little attention from researchers in their unmodified state, with most publications examining these alloys after some surface modification, such as nitriding or hard face depositing, with the aim of improving their wear resistance. Dumas et al. [4.14] investigated the surface integrity and subsurface deformation of 15-5PH from machining. Wear and machining overlap in certain aspects; the key difference is that material removal is deliberate in machining, rather than incidental in tribology. The authors [4.14] found that the machining process produced a 2μm deep tribologically transformed zone beneath the surface, which was 25% harder than the surrounding material. This increase was attributed to the Hall-Petch effect, as the tribologically transformed zone featured highly refined grains in comparison to the bulk material.

Bain et al. [4.15] studied AISI 420 in dry sliding wear after annealing and tempering heat treatments. The alloy was heat treated in various ways, using three tempering processes and three annealing processes, before being subjected to pin-on-disc testing. The volume loss results on the tempered samples showed a positive correlation between tempering temperature and wear, whereas the annealed samples showed a negative correlation, suggesting that two different wear regimes were arising at a transition point in hardness. However, the absolute magnitude of the tempered sample volume losses were lower than that of the annealed ones.

The austenitic stainless steel, Nitronic 60, is a commercial alloy manufactured to be simultaneously resistant to corrosion and galling [4.16]. The manufacturer (Electralloy) advertises that during button on block galling resistance tests, Nitronic 60 outperforms numerous other stainless steels, including the harder martensitic alloys [4.17]. Such beneficial properties are attributed to the chemical composition of the alloy, as Nitronic 60 has high silicon and nitrogen concentrations. Such additions were reported by Korshunov [4.18] to increase wear resistance and strength, respectively.

The manufacturer [4.17] refers to the high galling resistance of Nitronic 60, however, it is critical to note that galling resistance does not always directly correlate proportionally with wear resistance.

Hsu et al. [4.19] compared three austenitic stainless steels (type 304, 316, and Nitronic 60), and found that Nitronic 60 experienced the highest volume losses at the highest load. The authors [4.19] also noted that this high wear rate did not appear to affect the 440C counter face, and that the worn Nitronic 60 face remained "relatively smooth". The likelihood of surface hardening was also discussed, which was primarily attributed to the stress-induced phase transformation to martensite. These hardened regions were observed in microstructural cross-sectional characterisations as grey regions, where type 304 and Nitronic 60 displayed greater increases in surface hardness in comparison to type 316. Finally, the authors [4.19] concluded by explaining that overly hardened surface layers may also be unfavourable, because "(a) the surface material will be more subject to fracture; (b) the hard surface material will damage the opposing surface; (c) continued plastic deformation will be forced into the interior, leading to increased galling tendencies"[4.19].

The final examined alloy is CuSn7Zn4Pb7, hereinafter referred to as bronze. Bronze sees industrial usage in less severe wear applications such as bearings and bushes [4.20]. The bronze discussed in this chapter is alloyed with lead, which is known to be useful in sliding applications and machining due to it precipitating out of solution as relatively large spherical globules which can act as a solid lubricant in a similar manner to graphite in cast irons. Bowden and Tabor [4.21] investigated the role of metallic thin surface films and their reduction of friction and wear. The authors [4.21] found "some signs of smearing of extruded lead" on the sample worn surfaces. Such copper-lead alloys have historically featured in thin-wall crankshaft bearings in internal combustion engines. Further examples are discussed by Hutchings and Shipway [4.9], who noted the distinction between copper-based and aluminium-based bearings, with the higher fatigue strength of copper alloys leading to their greater usage in crankpin (big-end) bearings that experience high loads.

Several publications by Prasad [4.22], [4.23] have studied the sliding wear behaviour of bronze alloys. Prasad et al. [4.22] tested a leaded tin bronze at multiple sliding speeds. The authors [4.22] found that at the lowest sliding speed of 0.42m/s,

microcracking was the dominant wear mechanism and propagated along the lead –
matrix interface, causing large volume losses and preventing lead from being smeared
onto the surface in a beneficial manner. In contrast, at higher sliding speeds of 2.68m/s
and 4.60m/s, this effect was diminished by thermal softening caused by higher
frictional input, allowing the lead to form a beneficial low friction film which reduced
direct metal contact.

A large-scale study was conducted by Prasad [4.23] of three leaded tin bronzes and an
aluminium bronze in dry sliding wear tests, with an aim of investigating the links
between alloying content, microstructural features, and wear response. The researcher
[4.23] found that the volume losses of the leaded tin bronzes decreased with increasing
sliding speed, while the opposite was observed for the aluminium bronze. This
difference was attributed to the suppression of micro-cracking and the promotion of
effective lead smearing. It was also concluded that the "mere presence of a lubricating
phase does not mean improved sliding wear behaviour" [4.23], where favourable
behaviour was more a product of the sliding parameters rather than the microstructural
condition and morphology. At a sliding speed of 0.42m/s, micro cracking and
spallation were the common wear mechanisms, but at a speed of 4.60m/s, the wear
mechanisms changed to plastic deformation and the formation of a heavily deformed
transfer layer [4.23].

The numerous tribology studies of the materials discussed in this chapter indicate that
they are credible potential choices for use in most sliding applications, and can
certainly be compared to a nitrided steel. However, the specificity of the materials and
the particular testing parameters of this chapter preclude the existence of relatable
studies to discuss, and therefore novel experimental data is generated from which
conclusions can be drawn.

4.2.   Materials and Methods

4.2.1.   Materials

Seven materials, as described in Chapter 3, were examined for this chapter. Cast iron was received from the industrial collaborator in the heat treated condition.

4.2.2.   Experimental Methodology

Wear behaviour was examined using dry pin-on-disc sliding wear tests as described in Section 3.2.1. and followed the procedure of ASTM G99 [4.24]. A single applied load of 6kg was used for all tests.

Pin-on-disc material testing combinations are displayed in Table 4.1.

Accompanying methods used to analyse the results are described in Chapter 3.

Table 4.1 - Pin-on-disc material testing combinations.

Pin Material	Disc Material				
	15-5PH	AISI 420	AISI 4330	Bronze	Nitrided Steel
Grey Cast Iron	3	3	3	3	3
Nitronic 60	3	3	3	3	-
15-5PH	3	-	-	-	-
AISI 420	-	3	-	-	-
AISI 4330	-	-	3	-	-

4.3.   Results

Pin-on-disc material combinations are hereafter referred to in the format: *disc vs pin.*

4.3.1.   Microstructural Characterisation

AISI 4330, 15-5PH, and AISI 420 exhibited tempered martensitic microstructures (Figure 4.1) due to their chemical composition and thermal history. Their microstructures appear similar, apart from slight differences in coarseness, with the 15-5PH being more distinct and less tempered than AISI 4330 and AISI 420.
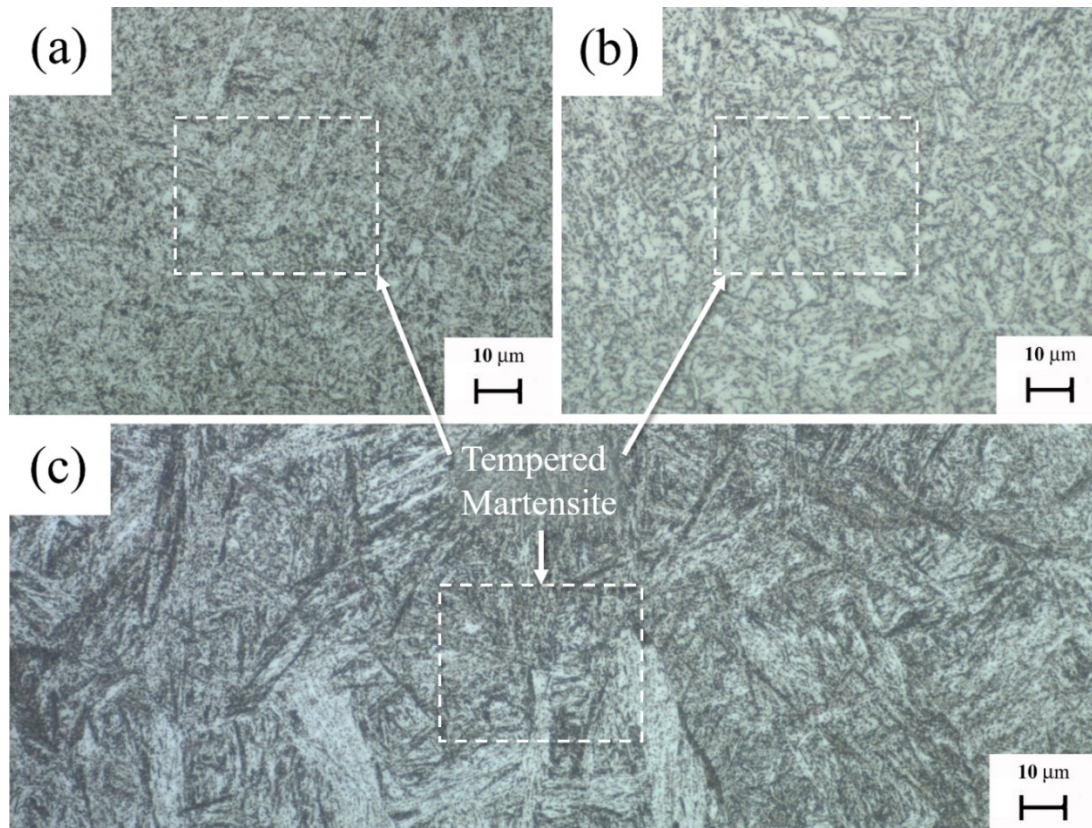
Figure 4.1 - Microstructure of (a) AISI 4330 (b) AISI 420 (c) 15-5PH, showing tempered martensite [x500- etched].

Nitronic 60 exhibited a coarse FCC austenitic microstructure (Figure 4.2) with annealing twins and segregated inclusions showing directionality from rolling. Occasional slip lines showing localised deformation in certain grains can also be observed.
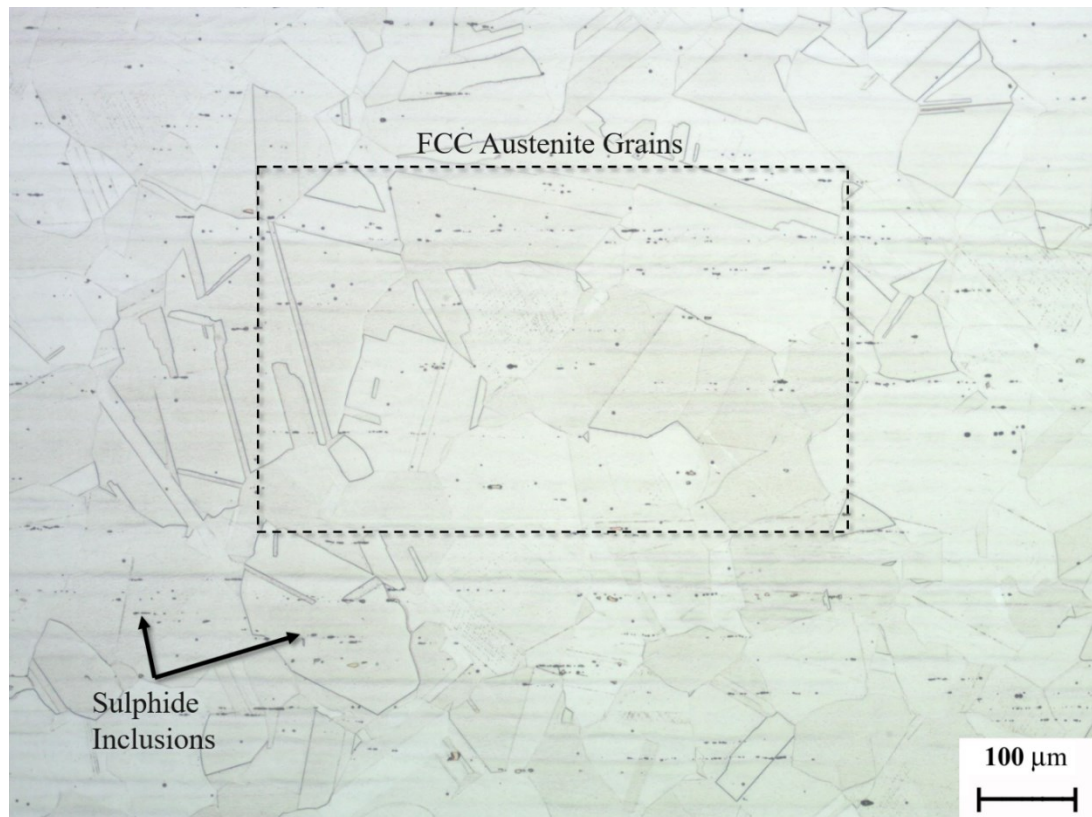
Figure 4.2 - Microstructure of Nitronic 60, showing coarse austenite grains [x100 - etched].

The bronze contained lead globules and intermetallic compounds (most likely lead-tin) dispersed throughout its coarse FCC matrix (Figure 4.3). This alloy displayed the largest grains of all materials discussed in the thesis. Certain grains, depending on their orientation, also showed frequent slip lines, most likely from the processing underwent during manufacturing.
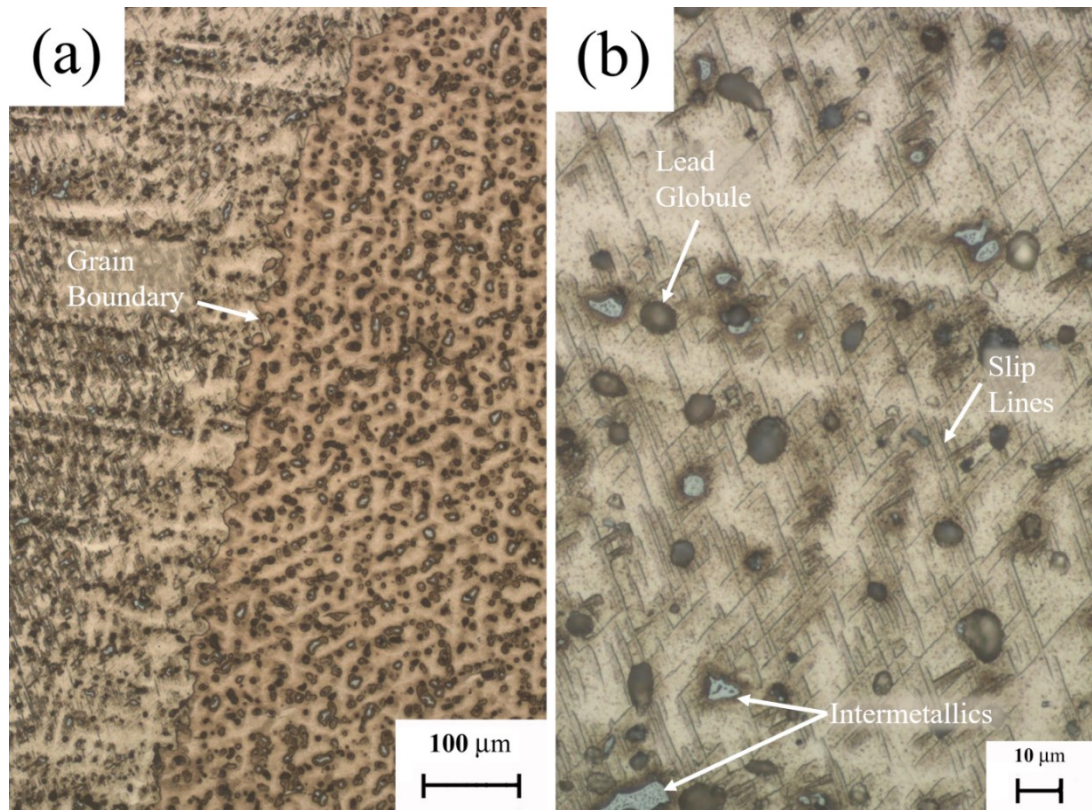
Figure 4.3 - Microstructure of bronze at (a) x100 (b) x500 magnification, showing very coarse FCC grains, intermetallic compounds, and lead globules [etched].

EDS showed that the globules dispersed throughout the bronze were indeed lead rich, and that the intermetallics were compounds of tin (Figure 4.4, Table 4.2).
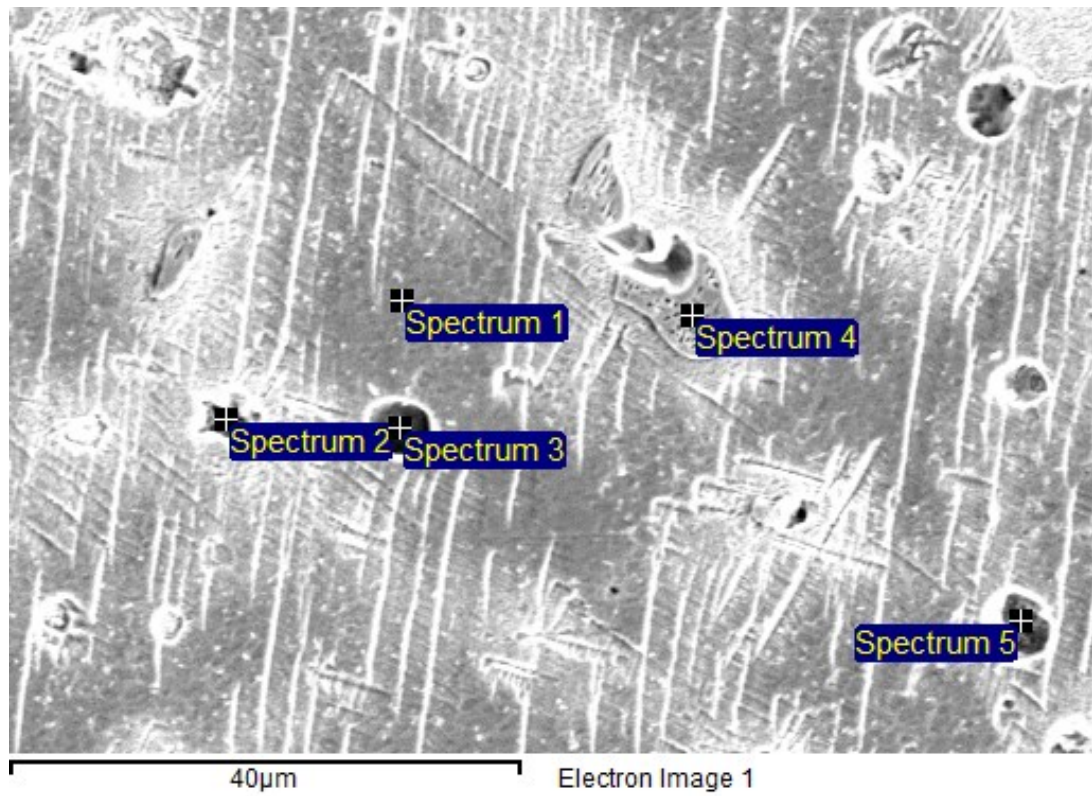
Figure 4.4 - EDS spectra locations on bronze.

Table 4.2 - EDS results associated with Figure 4.4.

Spectrum	C	O	Si	P	Fe	Ni	Cu	Zn	Sn	Pb
1	4.47	-	-	-	0.33	0.51	87.03	5.39	2.28	-
2	2.53	1.09	-	-	-	-	18.47	4.37	3.1	70.44
3	6.94	16.82	13.55	-	-	-	48.02	-	4.47	10.2
4	4.75	1.74	-	0.39	-	0.97	60.54	-	31.62	-
5	12.15	6.22	1.6	-	-	-	64.8	-	7.46	7.77

Grey cast iron displayed coarse graphite flakes of type I-A/C-5 in accordance with ISO 945. These were surrounded by a tempered martensitic matrix, with infrequent inclusions and micro constituents such as titanium carbo-nitrides and sulphides (Figure 4.5, 4.6).
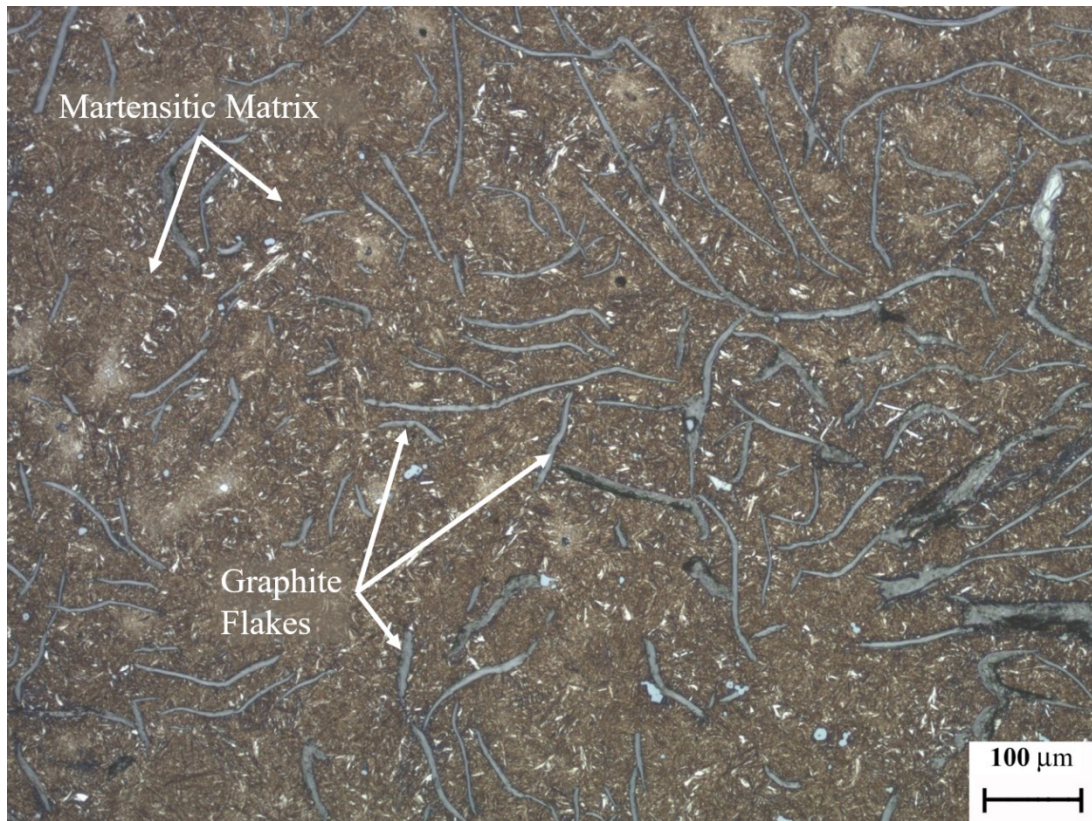
Figure 4.5 - Microstructure of grey cast iron, showing graphite flakes and martensitic matrix [x100 - etched].
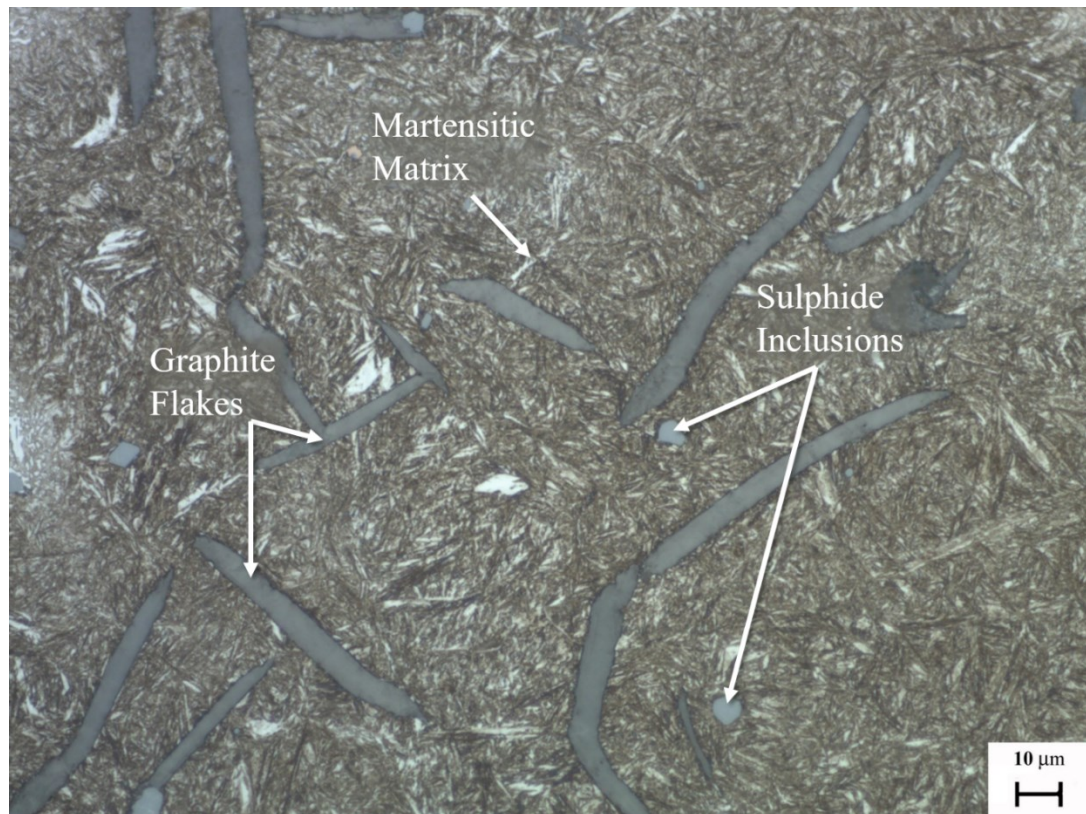
Figure 4.6 - Microstructure of grey cast iron, showing graphite flakes, martensitic matrix, and sulphide inclusions [x500 - etched].

The nitrided 905 M39T displayed a banded ferritic/bainitic microstructure (Figure 4.7). Networks of nitride compounds exist at the surface, from the super saturation of nitrogen causing these compounds to precipitate out of solution.
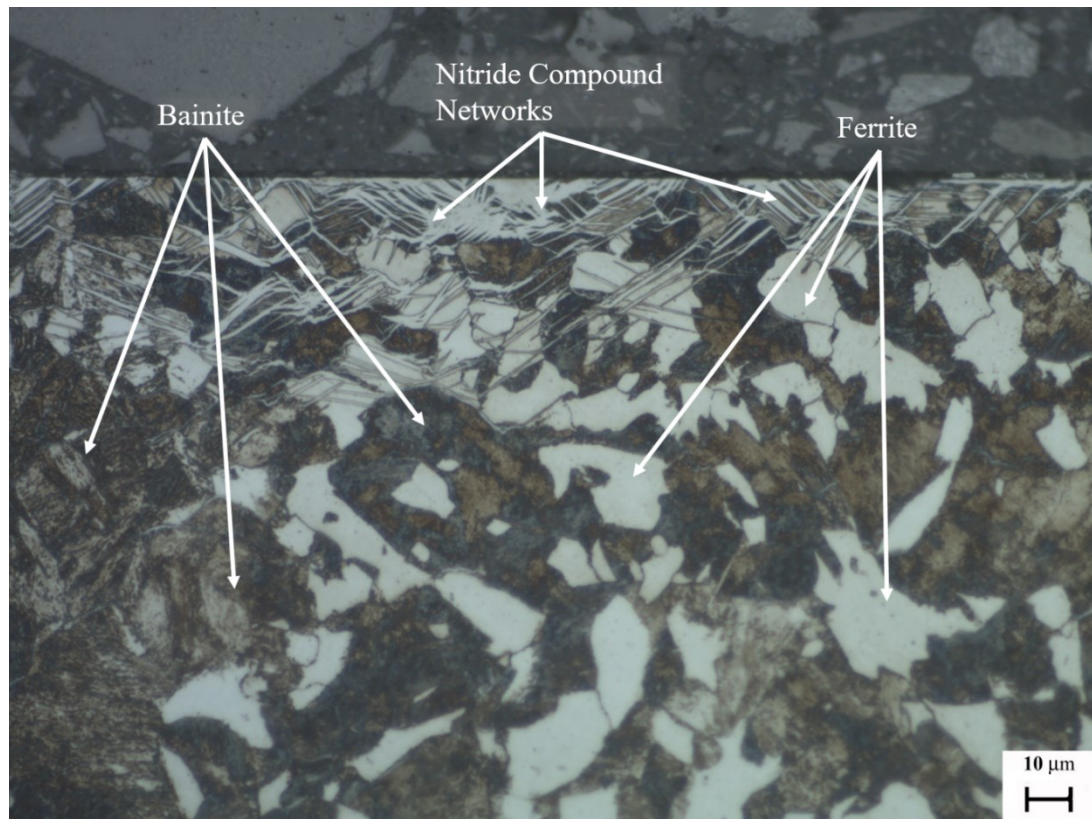
Figure 4.7 - Microstructure of nitrided M39T, showing nitride compounds at the surface [x500 - etched].

EDS showed that the white networks were indeed nitrogen rich, and that the concentration of nitrogen decreased moving into the bulk material (Figures 4.8, 4.9, Tables 4.3, 4.4), indicating that the nitriding achieved its primary purpose of being a case hardening surface treatment.
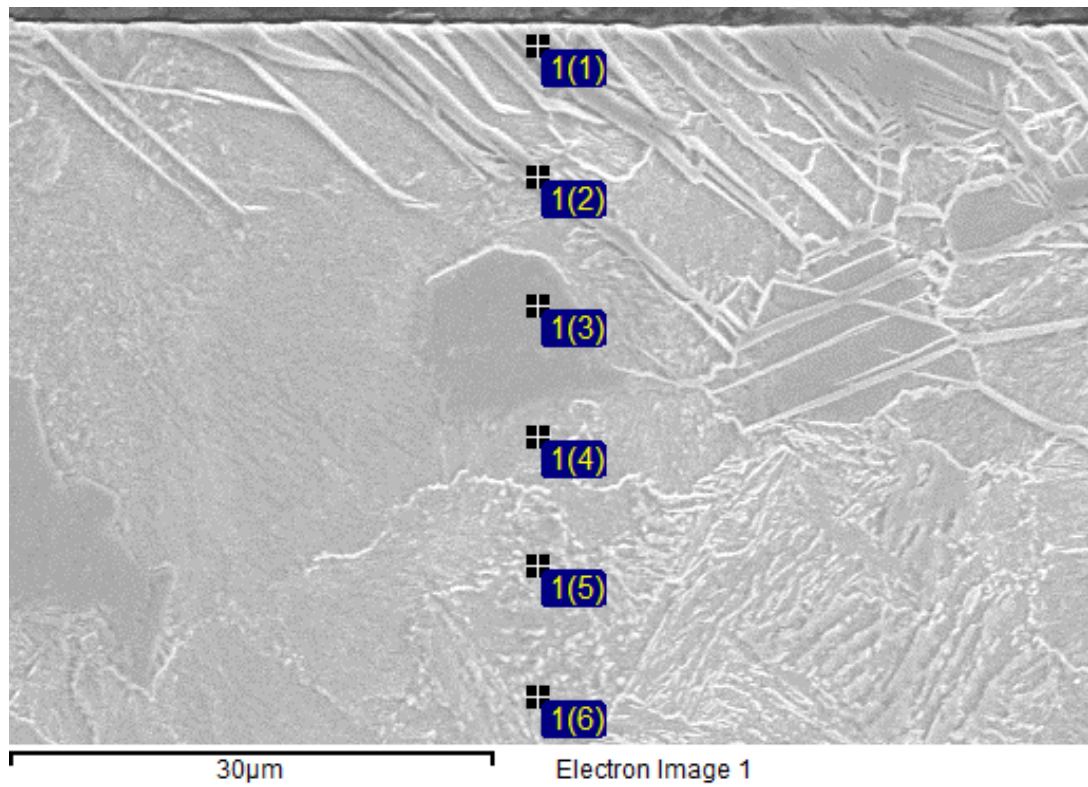
Figure 4.8 - EDS spectra locations on nitrided M39T.

Table 4.3 - EDS results associated with Figure 4.8.

Spectrum	C	N	Al	Si	Cr	Mn	Fe	Cu
1	3.53	9.87	0.92	0.35	1.39	0.65	83.3	-
2	3.51	9.58	0.86	0.39	1.41	0.55	83.71	-
3	3.77	3.49	1.01	0.39	1.67	0.57	89.1	-
4	5.37	4.42	1.24	0.55	1.82	0.72	85.88	-
5	5.13	3.82	1.24	0.45	2.02	0.66	85.99	0.69
6	6.17	4.13	1.28	0.47	1.68	0.58	84.68	1.01
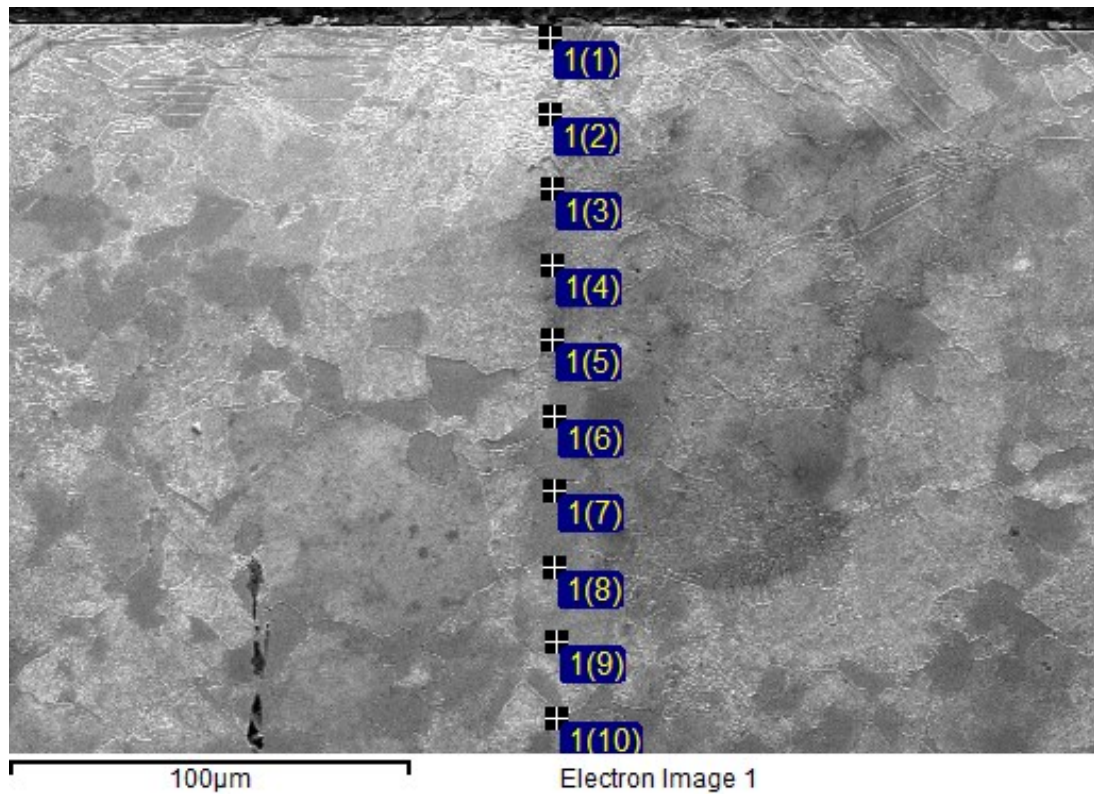
Figure 4.9 - EDS spectra locations on nitrided M39T.

Table 4.4 - EDS results associated with Figure 4.9.

Spectrum	C	N	Al	Si	Cr	Mn	Fe	Cu
1	8.29	8.6	1.57	0.59	1.69	0.41	78.33	-
2	6.01	4.73	1.35	0.49	1.56	0.56	85.31	-
3	6.52	4.68	1.29	0.51	1.57	0.6	83.46	1.04
4	6.37	4.11	1.18	0.4	1.61	0.67	85.4	-
5	9.91	4.77	1.4	0.36	2	0.79	79.31	1.13
6	9.6	4.08	1.28	0.4	1.87	0.66	80.94	1.15
7	7.54	2.83	1.04	0.32	1.4	0.47	86.41	-
8	8.4	3.52	1.24	0.4	1.91	0.68	83.09	0.76
9	7.79	2.52	1.06	0.4	1.42	0.54	86.26	-
10	9.67	4	1.37	0.38	2.01	0.67	80.93	0.96

Vickers macro and micro indentation hardness measurements (Figure 4.10) showed that the hardest materials were the nitrided steel and cast iron, followed by the martensitic alloys, then the FCC alloys, i.e. Nitronic 60 and bronze.
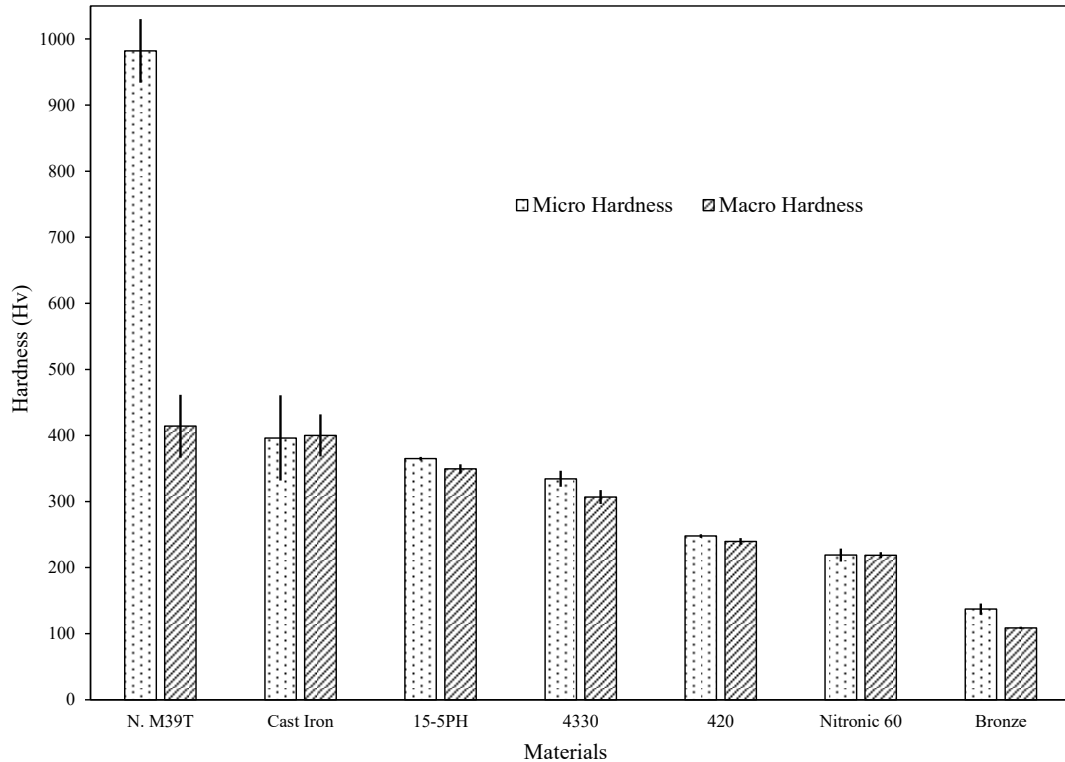
Figure 4.10 - Vickers macro and micro indentation hardness of the tested materials. N = 5 for macro indentation hardness values and N = 10 for micro indentation hardness values.

4.3.2.   Volume Losses

The disc volume loss values (Figure 4.11) fall into groups according to the corresponding pin. The self-mated discs and bronze discs experienced the greatest volume losses; followed by the discs worn against Nitronic 60 pins; followed by the discs worn against cast iron pins. The nitrided M39T disc exhibited the lowest volume losses. The self-mated AISI 4330 combination exhibited the greatest volume loss but also had a large standard deviation, indicating variation in results.
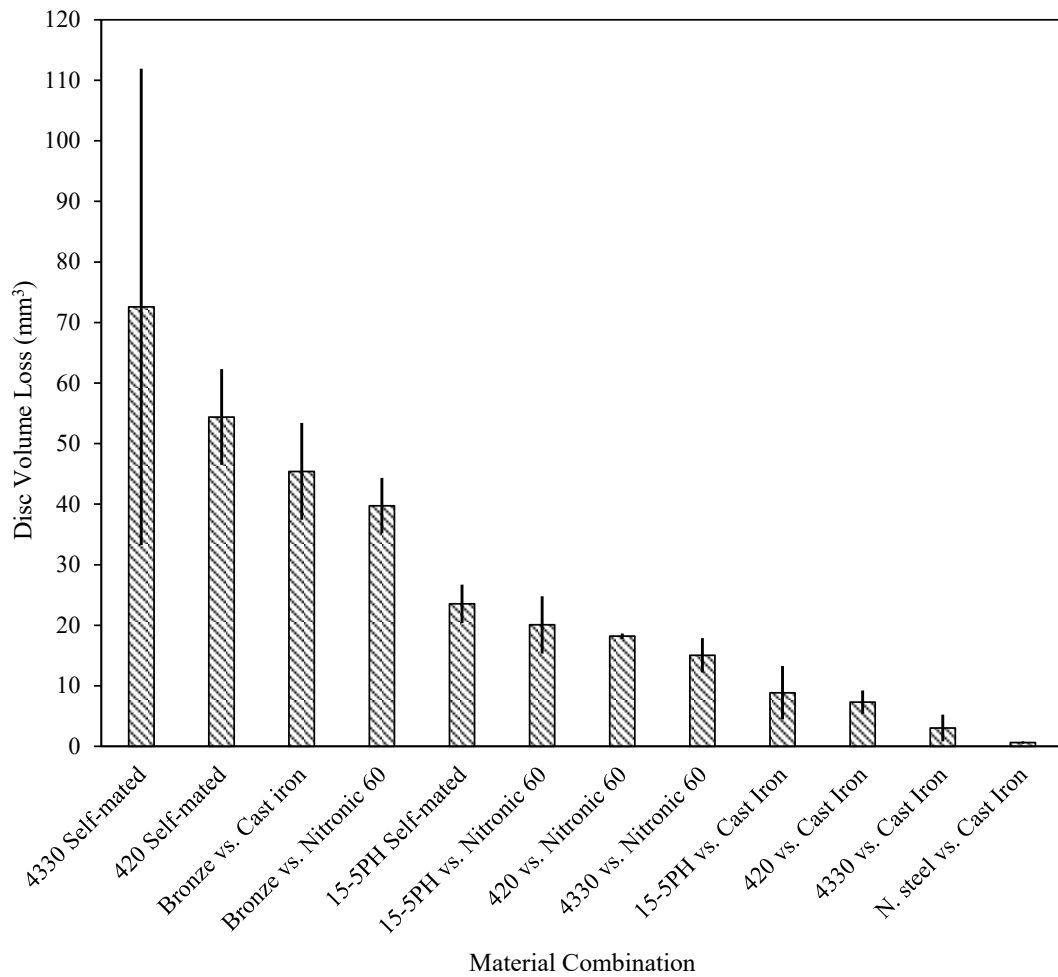
Figure 4.11 - Disc volume loss values, showing the poor performance of the self-mated materials. N = 3 for all tests.

The pin volume loss results (Figure 4.12) follow approximately the same trends as the discs, but with the bronze position inverted (i.e. their corresponding pins exhibited low losses).
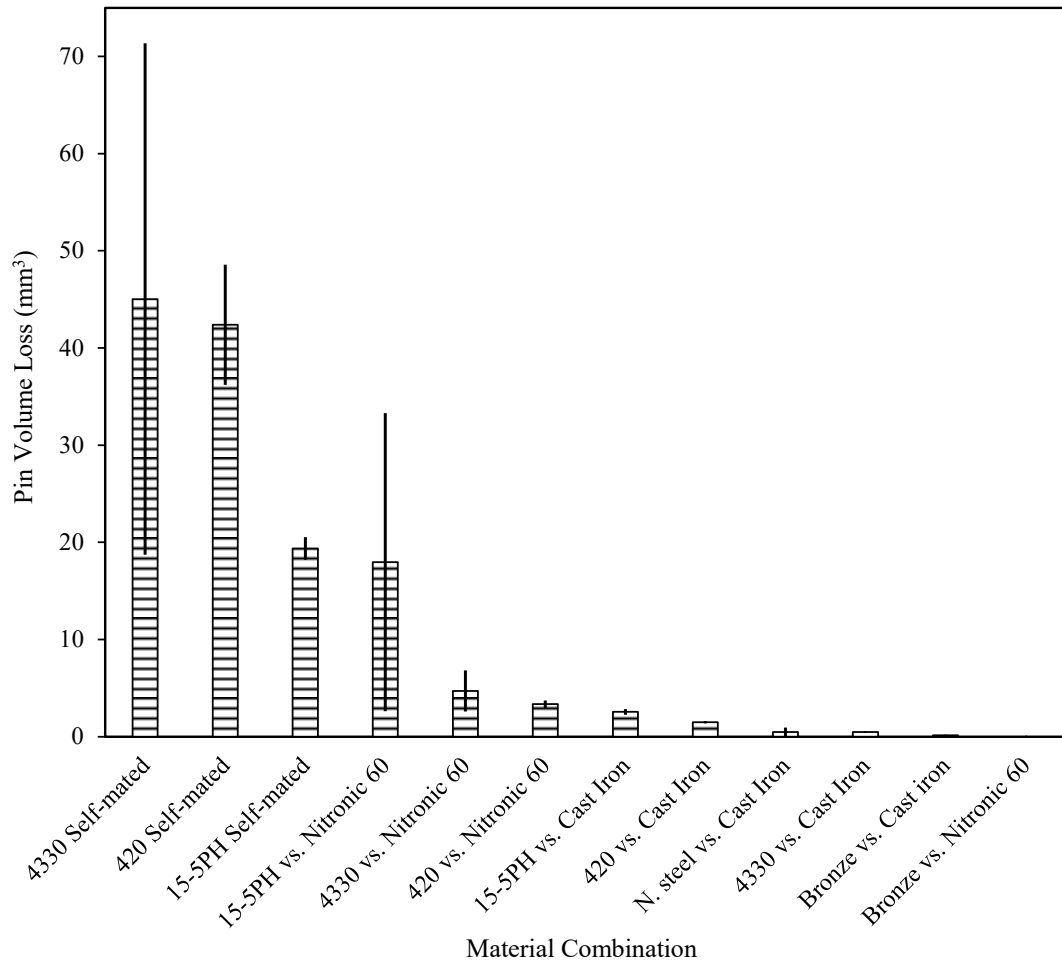
Figure 4.12 - Pin volume loss values, showing that the pins worn against bronze experienced almost no wear. N = 3 for all tests.

The combined pin and disc volume loss values (Figure 4.13) show that the results correlate to each other in most cases (apart from the bronze combinations), with high disc wear corresponding to high pin wear.
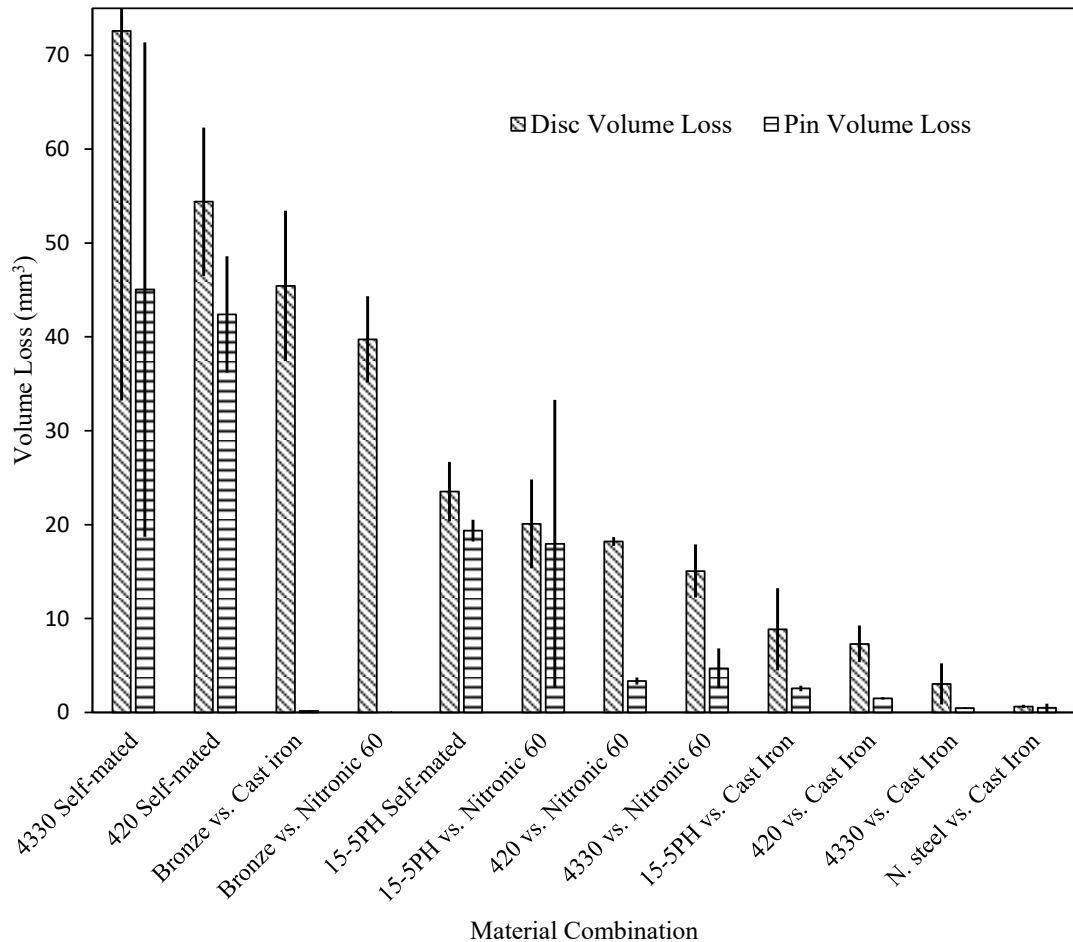
Figure 4.13 - Pin and disc volume loss values, showing good agreement. N = 3 for all tests.

4.3.3.   *Wear Scar Topography*

Examination of disc wear scars (Figures 4.14 – 4.17) revealed the dominant mechanisms of deformation, such as brittle fracture, plastic flow, and/or oxidative wear. The nitrided steel vs. cast iron combination (Figure 4.14) produced a shallow and narrow scar. Due to the hardness of the nitrided steel disc, the cast iron pin was unable to produce a scar comparable to the other combinations. Instead, the surface of the disc displays only mild scuffing. At higher magnifications, the scar resembles those seen on the nitrided AISI 420 samples by Li et al. [4.25].
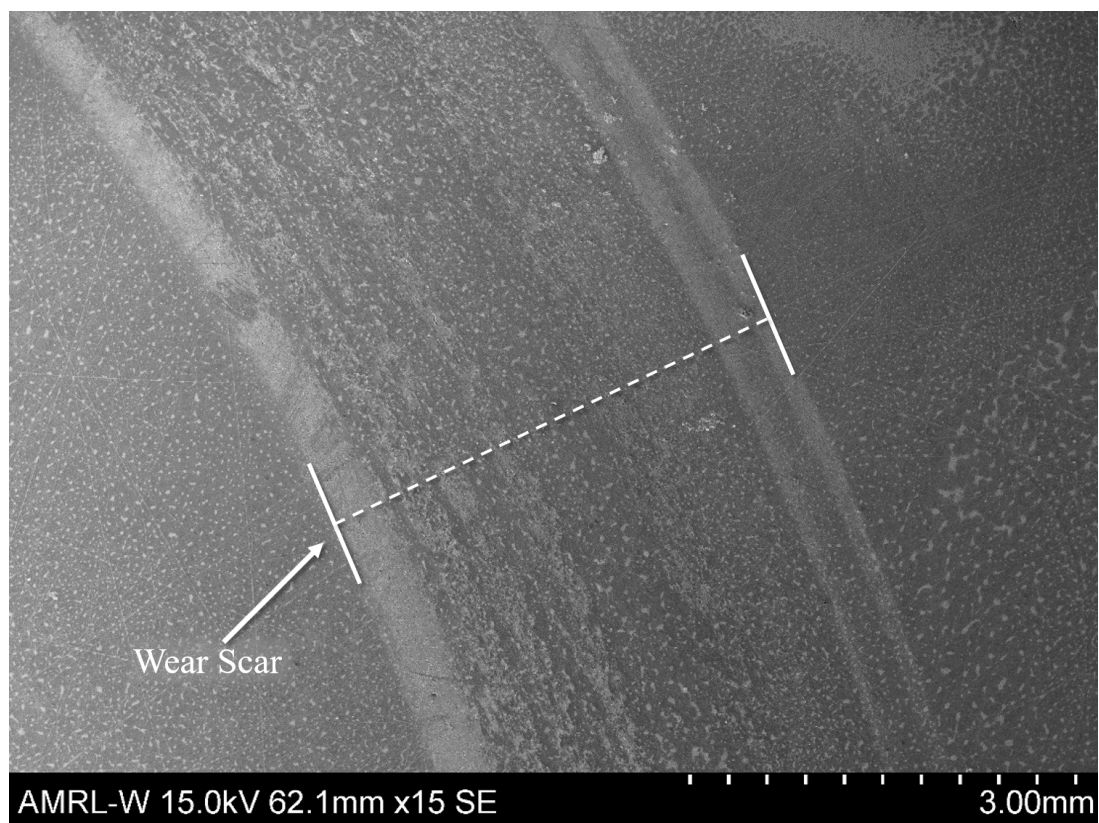
Figure 4.14 - Disc wear scar produced on a nitrided M39T from a cast iron pin.
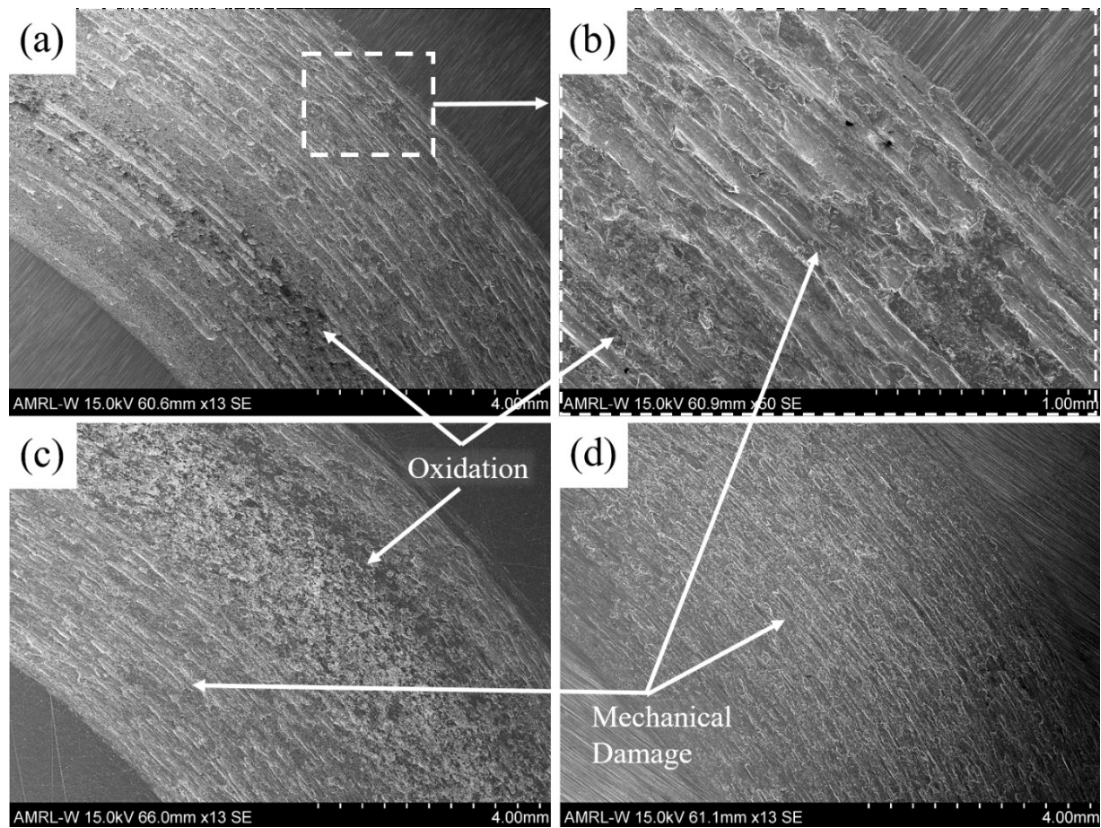
Figure 4.15 - Disc wear scars from (a) self-mated AISI 4330 (b) self-mated AISI 4330 (c) self-mated AISI 420 (d) self-mated 15-5PH.

The self-mated disc wear scars displayed a variety of damage mechanisms, often with different mechanisms occurring on the same scar. The self-mated AISI 4330 (Figure 4.15(a),(b)) and AISI 420 (Figure 4.15(c)) wear scars both displayed areas of oxidative wear and areas of mechanical ductile damage such as scoring and smearing. The self-mated 15-5PH (Figure 4.15(d)) scar only displayed mechanical damage in a more brittle fashion.
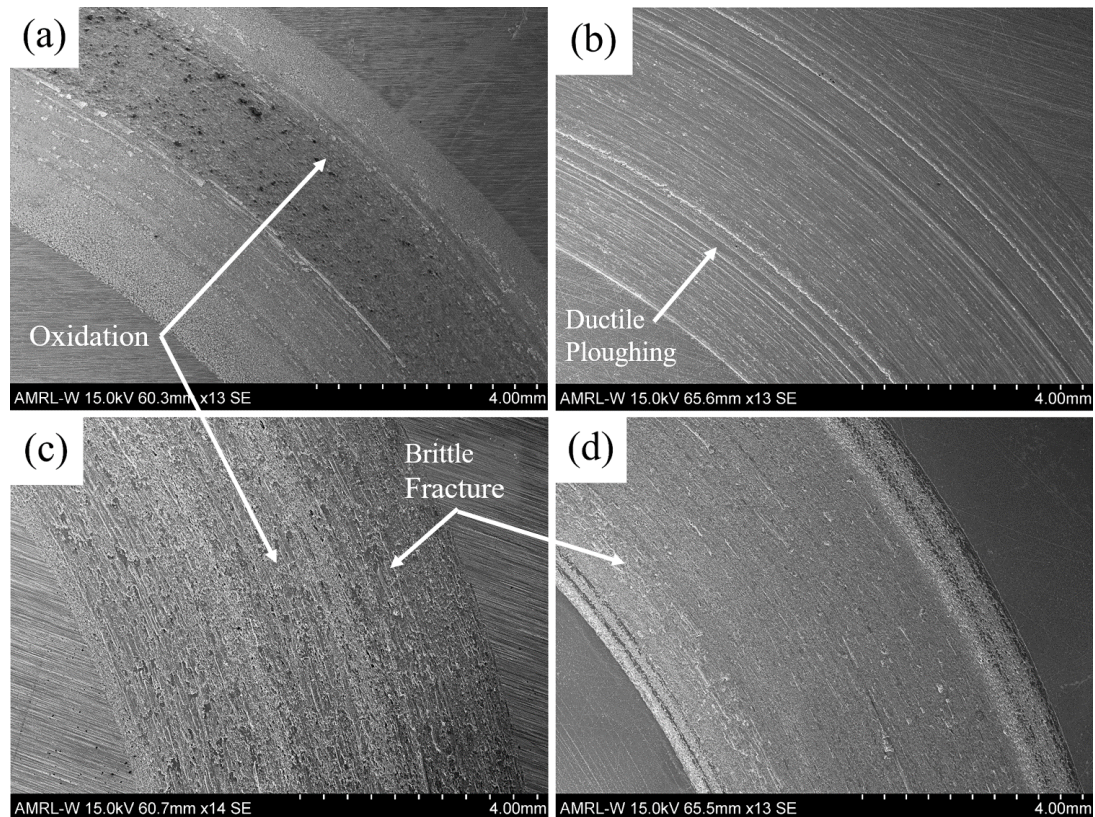
Figure 4.16 – Disc wear scars produced from (a) AISI 4330 vs. cast iron (b) bronze vs. cast iron (c) 15-5PH vs. cast iron (d) AISI 420 vs. cast iron.

Material combinations with low hardness, such as the bronze or AISI 420 discs, formed wear scars through plastic flow (Figures 4.16(b), 4.17(b, d)), while others such as 15-5PH and AISI 4330 were dominated by brittle fracture (Figure 4.16(c), 4.17(c)) or oxidative wear (Figures 4.16(a)). The discs which scarred through brittle fracture also displayed the typical sub-mechanisms such as scuffing, scoring, and smearing, whereas the plastically-deforming bronze displayed unbroken ploughing.
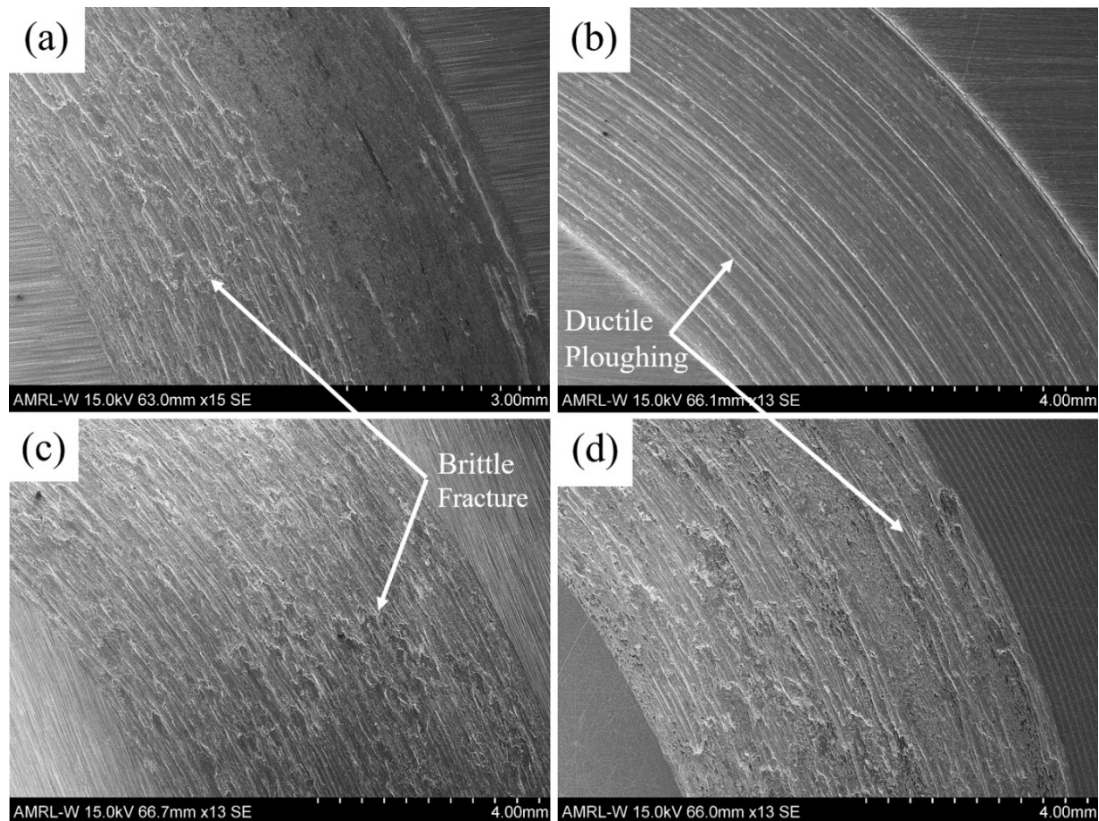
Figure 4.17 - Disc wear scars produced from (a) AISI 4330 vs. Nitronic 60 (b) bronze vs. Nitronic 60 (c) 15-5PH vs. Nitronic 60 (d) AISI 420 vs. Nitronic 60.

The profilometry measurements (Figures 4.18, 4.19) revealed varying wear scar cross-sections. Some discs, such as the bronze, exhibited a distinct U-shape with an upward-pointing lip at either side. Other scar cross-sections were more angular in their appearance, with areas of varying depth, such as with AISI 4330. The average maximum scar depth (Figure 4.20) showed good agreement with the disc volume loss values.
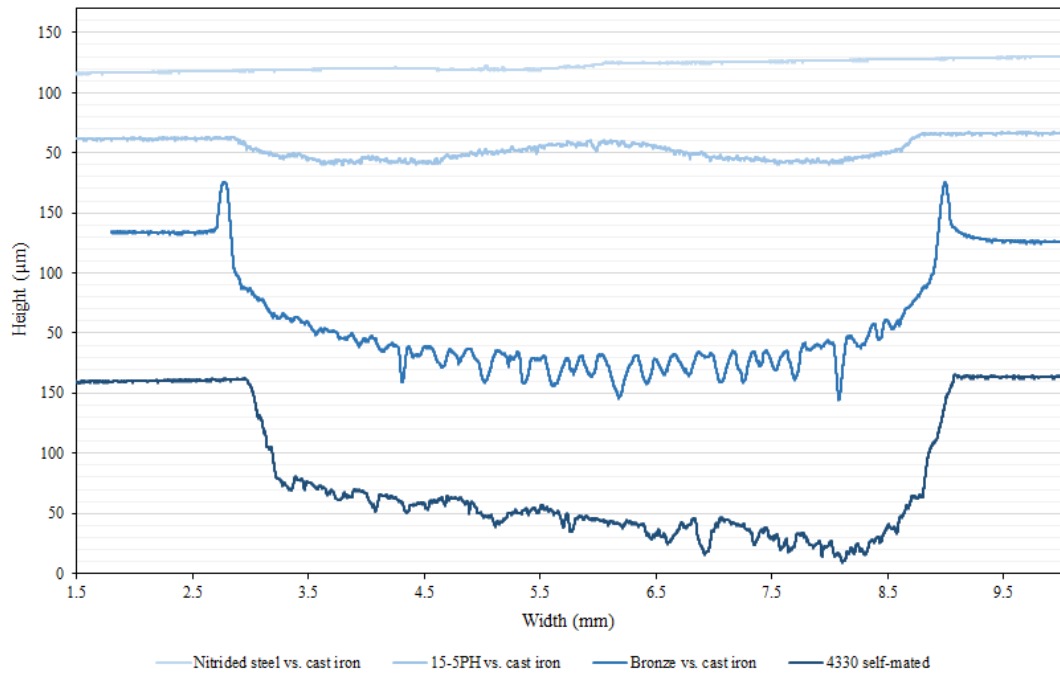
Figure 4.18 - Selection of scar cross-sectional profiles.
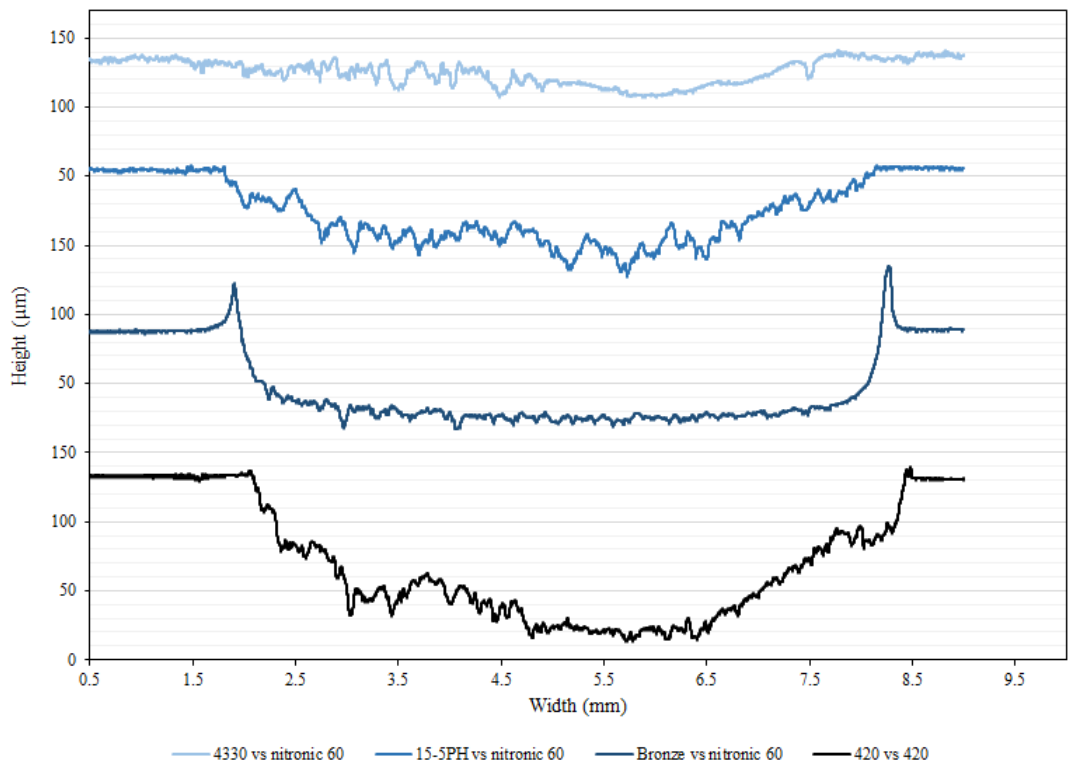
Figure 4.19 - Selection of scar cross-sectional profiles.
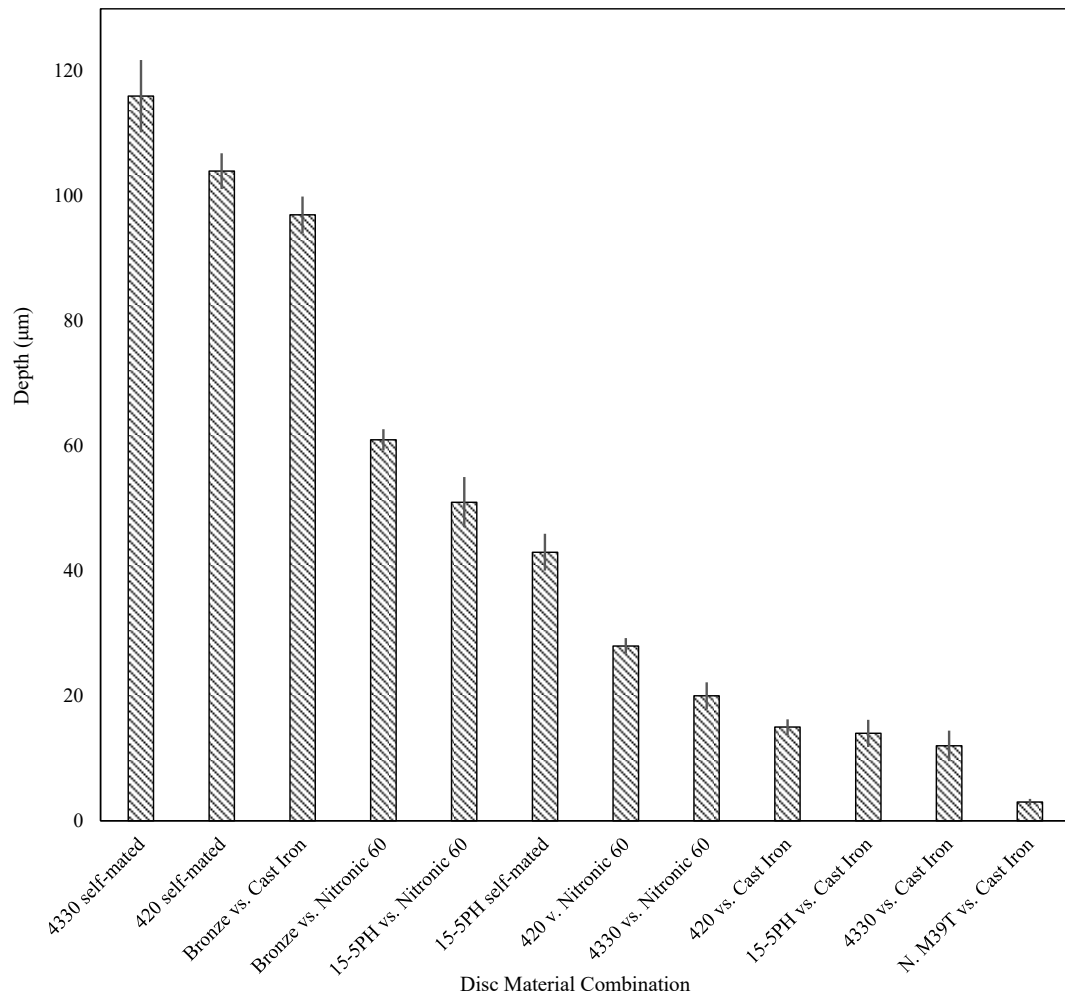
Figure 4.20 - Comparison of disc wear scar depth, showing good agreement with the prior volume loss values. N = 3 for all measurements.

4.3.4.   Subsurface Deformation

The cross-section of the bronze disc (vs. Nitronic 60 pin) wear scar (Figure 4.21) showed an increased frequency of slip lines, elongation and directionality of the dispersed lead particles and intermetallics, and strain hardening near the surface (Figure 4.21(b)). Micro-hardness measurements showed an increase from 123 HV in the bulk material, to 216 HV at a distance of 30μm from the surface.
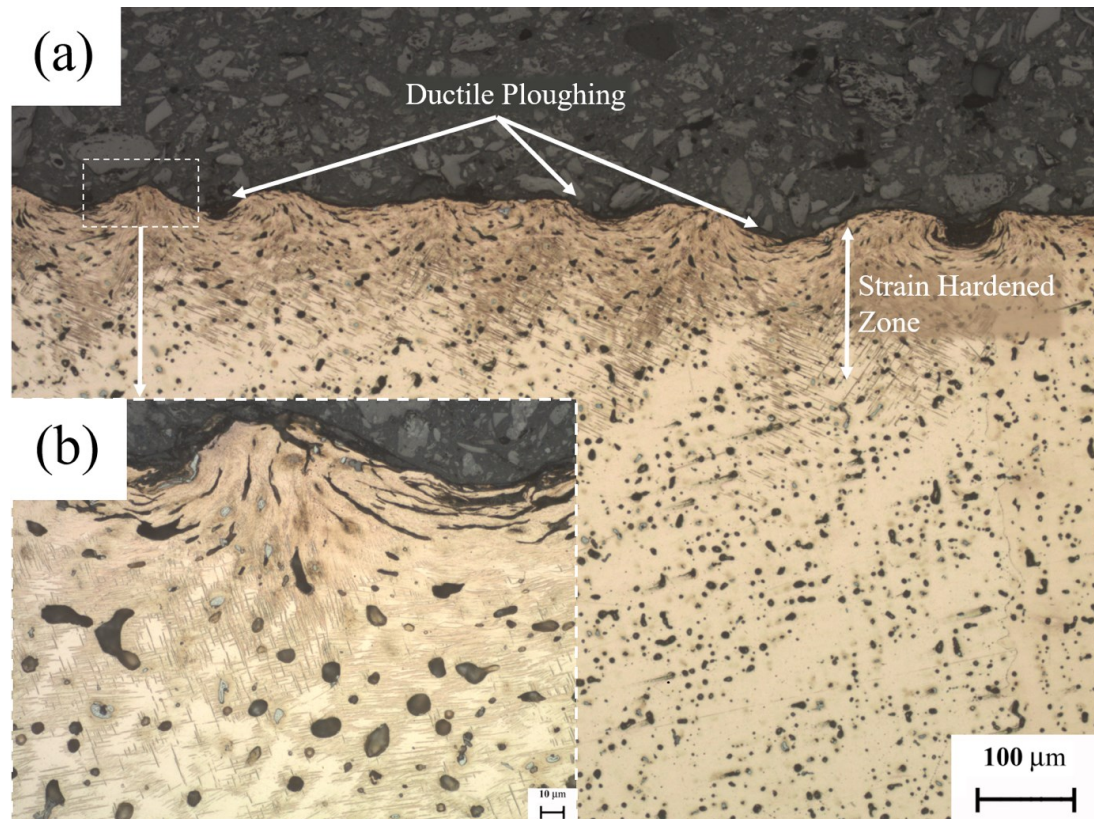
Figure 4.21 - Subsurface deformation on a bronze disc at (a) x100 (b) x500 magnification [etched].

The cross-sections of the cast iron pin (Figure 4.22) showed that the metal matrix above graphite flakes spalled off as debris, and that the remaining graphite can be sheared out of place along the surface of the metal. The spallation of graphite flake cavities a dominant damage mechanism of grey cast irons (see Chapters 6 and 7). In opposition to the subsurface inspection of the bronze and Nitronic 60 samples, the cast iron pins do not exhibit any plastic deformation. This is due to the stiffness of the martensitic matrix of the heat treated pins.
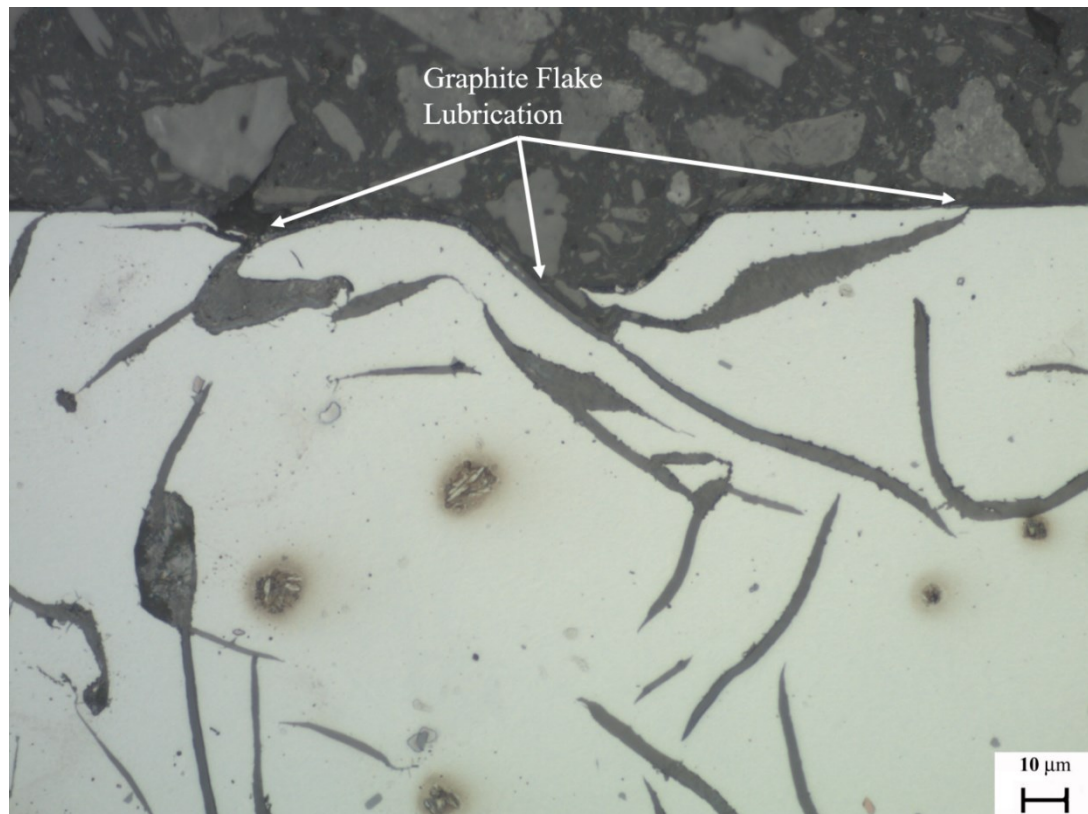
Figure 4.22 - Subsurface deformation on a cast iron pin [x500 - as-polished].

Nitronic 60 (Figure 4.23) demonstrated extreme plastic deformation with grain distortion and an increased frequency of slip lines near the surface (Figure 4.23(b)).
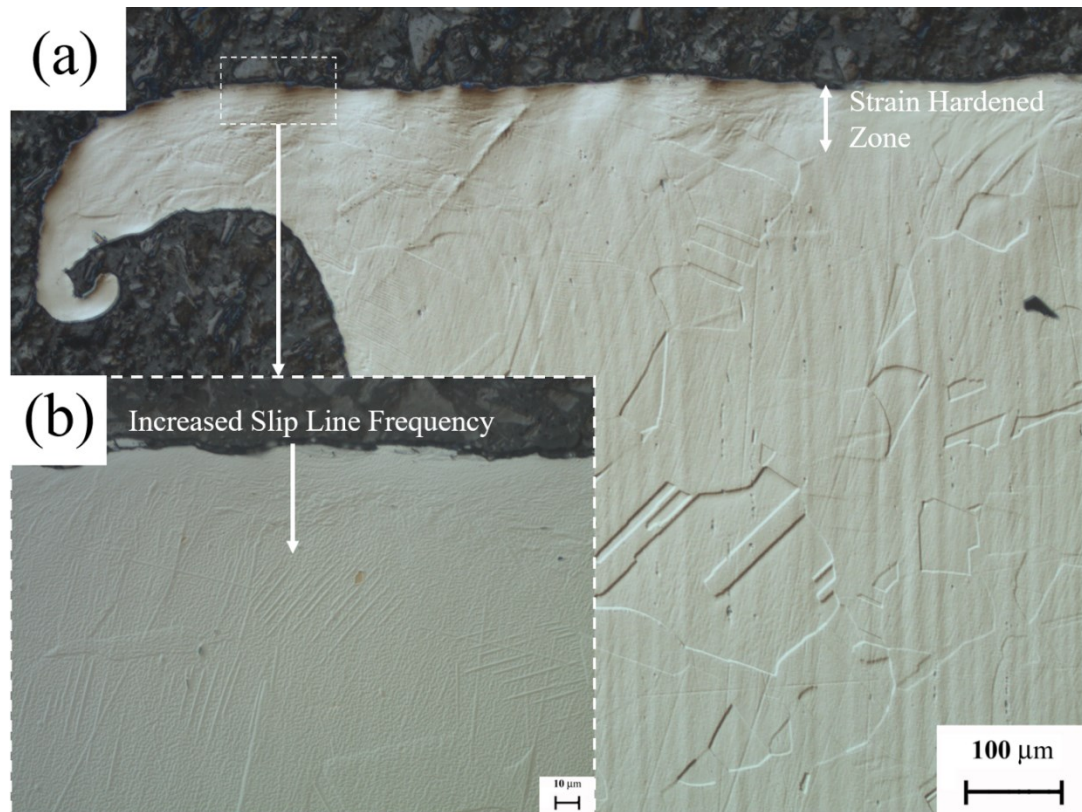
Figure 4.23 - Subsurface deformation on a Nitronic 60 pin at (a) x100 (b) x500 magnification [4.DIC/polarised light].

4.4.   Discussion

4.4.1.   Microstructure & Hardness

The hardness of the alloys (Figure 4.10) follows a logical order in accordance with their microstructure. The FCC alloys, bronze and Nitronic 60, are the softest and most ductile of the examined materials due to their FCC crystallographic arrangement, which exhibits more slip planes and therefore more plasticity. The bronze is softer than Nitronic 60 (partly) due to it displaying larger grains (and therefore less grain boundary obstructions to dislocation glide), and its frequent lead globules (which are particularly soft). Next in order of increasing hardness are the martensitic steels; AISI 420, AISI 4330, and 15-5PH (Figure 4.1). The variation of these alloys is thought to be primarily governed by the degree of tempering, but is also influenced by chemical composition and residual stresses, among other factors. Grey cast iron follows with an unexpectedly (despite the presence of soft graphite) hard microstructure due to its martensitic crystallographic arrangement (Figures 4.5, 4.6). The micro indentation

119

hardness values of this alloy display a higher standard deviation than the other alloys due to indentations occasionally being placed on large graphite flakes which introduces scatter. The hardest allow tested is the nitrided M39T (Figure 4.7), with an average bulk hardness of approximately 425 HV and a near-surface hardness of almost 1000 HV due to the case hardening introduced from the nitriding process. The large difference in values between the macro indentation and micro indentation hardness of the nitrided steel are due to the location of the indentations; the macro indentations were within the bulk material, while the micro indentations were placed close to the surface and therefore fall within the nitrided band.

The nitriding treatment applied to M39T resulted in a case hardening effect, with the outer skin of the material exhibiting high concentrations of Nitrogen (Figure 4.8, Table 4.3), boosting its hardness to almost 1000HV. The EDS results indicate this concentration decreases with depth into the material; at a depth of approximately 250μm, the concentration of Nitrogen was as approximately 2.5% (a significant value in terms of alloying content) (Figure 4.9, Table 4.4). When cross-referencing this depth to the wear scar depth produced from sliding against heat treated cast iron (Figure 4.20), it is clear that the scar depth of ~5μm was still well within the nitrided layer.

Microstructural morphology is significant in governing the wear performance of a particular material combination, even without consideration of its counter-part. The volume loss results (Figures 4.11 – 4.13) show that cast iron performs optimally for a number of different discs. This is attributed primarily to its chemical composition (Table 3.1) allowing for oxidation but is also partially due to its microstructural morphology being optimal for wear applications. Firstly, its hard martensitic matrix (Figure 4.6) resists deformation, allowing for the pin to maintain structural integrity against moderately hard materials such as the martensitic steels. The matrix is also punctuated with numerous coarse flakes, allowing for beneficial graphite lubrication. LaBelle [4.4] even noted that the cavities of such graphite flakes can be beneficial to sliding under lubricated conditions, as they act as reservoirs to hold the lubricant and ensure adequate coverage.

4.4.2. *Wear Performance Ranking*

The disc volume loss results (Figure 4.11) can be broadly divided into three groups according to their corresponding pins. In order of increasing volume losses, the combinations broadly fall into the cast iron pin group, the Nitronic 60 pin group, and the self-mated group. This ranking is disrupted slightly by the bronze discs, which are considered special cases due to their soft FCC structure (the only discs of this nature) (Figures 4.2, 4.3). The order of cast iron pin, Nitronic 60 pin, self-mated pin is derived from microstructural features. The martensitic matrix of cast iron (Figures 4.6, 4.10) resists plastic deformation from ploughing. It also readily oxidises, due to its chemical composition (Table 3.1), and forms beneficial oxide layers during sliding wear which can protect the underlying material. The self-mated combinations exhibit the greatest volume losses due to matching hardness values, which therefore cause self-damage (the exact mechanism of this is not well understood, but is known to be avoided in industrial applications). The Nitronic 60 combinations do not have the benefits of cast iron nor the drawbacks of being self-mated (but do exhibit surface strain hardening (Figure 4.23) and therefore lie in the intermediate volume loss range.

The nitrided steel disc vs. cast iron displays the lowest volume loss (Figure 4.11), which is ascribed to the significant surface hardness (Figure 4.10) produced by the nitriding treatment. This disc hardness in conjunction with the hard martensitic matrix of the cast iron pin resulted in minimal wear for both samples. The beneficial oxidational and lubrication properties of graphite are also postulated to contribute to the low volume losses, secondarily, discussed further in Section 4.3.

The three martensitic steels are next in order of increasing disc volume loss (Figure 4.11), and fall in the same order for both the cast iron pin and the Nitronic 60 pin groups: AISI 4330, AISI 420, and 15-5PH. These alloys display a repeated pattern: AISI 4330 experienced the lowest volume losses while 15-5PH wore the most. This is postulated to be due to a number of competing factors. AISI 4330 is thought to exhibit the lowest volume losses since it is a low alloy steel which oxidises during dry sliding wear, as seen on every disc wear scar (Figures 4.15(a) – 4.17(a)). As discussed in Section 1.5 this oxidation can confer favourable sliding wear performance due to it providing dry lubrication and shielding the underlying metallic substrate from further damage.

The two other martensitic alloys are stainless steels which do not readily oxidise to form iron oxides on their surfaces, but instead form the slower-growing chromium oxide. These chromium-based compounds have a lower parabolic growth rate than iron oxides [4.11], and therefore cannot provide the same level of protection as the iron oxides that chemically active alloys such as cast iron and AISI 4330 form. The stainless steels, therefore, experience higher volume losses due to their matrices being exposed.

AISI 420 exhibits lower volume losses than 15-5PH for both cast iron pins and Nitronic 60 pins. This is attributed to the more tempered microstructure of AISI 420 (Figure 4.1) allowing it to deform slightly instead of experiencing brittle fracture behaviour like the less-tempered 15-5PH. This slightly higher ductility allows for material to be ploughed and displaced instead of simply removed (Figure 4.17(d)), so is beneficial in terms of pure volume loss value comparisons. This is in contrast to the results obtained by Bain [4.15], who established that volume loss increased with tempering temperature. This suggests that a trade-off exists whereby a certain level of ductility is favourable, but excessive plasticity leads to more wear as ploughing begins to occur. Despite the brittle fracture displayed by 15-5PH, the subsurface deformation discussed by Dumas [4.14] was also exhibited, and is discussed in Chapter 5.

The combinations using Nitronic 60 pins represent an intermediate grouping, lying between the favourable results of the cast iron pin group and negative results of the self-mated group. In comparison to the combinations with cast irons pins, the wear scars produced from these tests have fewer areas of oxidative wear and, macroscopically, have larger areas of damage (larger areas of scoring, smearing and ploughing (Figure 4.17)). As Nitronic 60 is a stainless steel, it does not possess the aforementioned favourable oxidative wear performance that cast iron does, but does experience surface strain hardening (Figure 4.23) as described by Hutchings [4.13].

Self-mated combinations, and combinations using bronze discs were the worst performing group, with deep scars (Figures 4.15, 4.20) and large volume losses (Figures 4.11 – 4.13). It is postulated that the applied load of 6kg produced a stress too great for the bronze material. As noted by Baker [4.26], bronzes in sliding are particularly sensitive to the contact pressure. The damage observed in the self-

mated/bronze group is a result of metal-to-metal contact and therefore the category of "severe" wear is applied in accordance with the relevant literature [4.27].

4.4.3.   Damage Mechanisms

The largest distinction in damage mechanisms observed herein, is the difference between brittle fracture damage versus plastic flow damage. There is a complex relationship between ductility and volume loss, whereby the volume lost to wear cannot be easily predicted by the hardness/ductility of one of the samples. Instead, both must be taken into account and even then, in certain circumstances one mechanism is more favourable than the other [4.13].

The bronze discs produced poor wear results (Figure 4.11) because of the low hardness of the coarse FCC structure (Figure 4.3) [4.28] and the presence of lead globules throughout the matrix (Figure 4.4, Table 4.2). In this case, it is thought that the lead particles, instead of acting as solid lubricants [4.23], [4.29]–[4.31], merely softened the alloy as described by Buchanan et al. [4.31]. The beneficial effects of lead solid lubrication, described by Prasad [4.23], were not observed in the current testing regime, with the lack thereof attributed to the experimental conditions. The applied load of 6kg is thought to be too great of a force to allow for it, instead the globules are either instantly flattened and smeared out to the point of uselessness, or are, more likely, to instead experience pull-out and exit the tribosystem.

A key distinction in the differing wear performance of the cast iron and Nitronic 60 pins lies in the effectiveness of graphite/oxide solid lubrication demonstrated by the former compared to the strain hardening exhibited in the latter. The volume losses were generally lower for the cast iron pins than for the Nitronic 60 pins (Figure 4.12). This indicates that the solid lubrication of graphite combined with a hard matrix is more effective than a soft matrix which strain hardens following deformation. Oxide products and graphite in cast iron form a protective film over the pin surface, effectively protecting the underlying metal from wear [4.32]. This oxide/graphite film eventually wears down, allowing for the matrix to be worn until fresh graphite is exposed/oxidation occurs which can again form a protective film. This periodic cycle of graphite/oxide lubrication followed by matrix wear is repeated continually.

A similar periodic wear regime occurs for the Nitronic 60 pins, but with strain hardening instead of oxidation/graphite exposure. Initial contact with the disc surface

will deform the pin end-face into ploughed grooves (Figure 4.23). This strain hardens the surface, increasing the wear resistance gradually until the material becomes too brittle to deform. Brittle fracture then occurs, exposing the underlying fresh material to the same sequence which repeats continually, in a manner described by Blau [4.33] (see Chapter 2).

The superior performance of the cast iron pins lies in the timing of these periodic wear cycles. Both the lower wear stage (i.e. the graphite lubrication stage or the strain hardened stage) is longer for the cast iron than for Nitronic 60. The graphite/oxide is able to act as a barrier for a longer duration than the strain hardened zone lasts for Nitronic 60, resulting in a longer time between matrix wear for the cast iron, and therefore lower volume losses. Outside of these temporal effects, it is doubtful that the strain hardened Nitronic 60 zone reaches the same hardness value of the cast iron martensitic matrix. The Nitronic 60 at its maximum wear resistant period is therefore still likely to experience higher volume losses than the cast iron pin, when sliding against the same disc material. This attribution is in line with the conclusions drawn by Hsu et al. [4.19] who also commented that the strain hardening effects of austenitic steels in sliding may become unfavourable if the surface material becomes more likely to fracture.

The favourable behaviour of cast iron is primarily due to its ease of surface oxidation, arising from is chemical composition and microstructure (low Chromium content; localised galvanic cells forming between graphite flakes and matrix). However, as this study only uses one set of experimental variables, the optimum performance of cast iron may be the result of a local minima occurring in the non-linear relationships displayed with changing load or speed, as noted by Kawamoto [4.7] when sliding in ambient conditions. Kawamoto [4.7] noted that a local maximum in volume loss occurred at a sliding speed of 1.5m/s but decreased at greater speeds. Applied to the work reported herein, cast iron may be optimally responding to the present set of experimental variables but could perform poorly at lighter and heavier loads, or slower and faster sliding speeds.

The relatively thick graphite lubrication layer on the surface of cast iron components observed by Montgomery [4.5] was not replicated in this chapter. Although the geometry of the graphite flake cavities was observed to allow for this smearing, no

surface layer was seen, indicating that either (a) the type of graphite flake lubrication did not occur, (b) the particular cross-sections of the particular examined cast iron pins did not display this type of graphite flake lubrication, or (c) the sample post-test treatment of washing in acetone and methanol removed it. It is theorised that the most likely option is the former, as other researchers [4.34]–[4.36] have found that graphite flake lubrication is less likely to occur with harder and stiffer matrices like the martensite of the cast iron.

The low wear rate of the cast iron is firstly due to its oxidative wear properties, and secondly due to its hard matrix resisting wear. If both of these mechanisms are the first to act then little opportunity for graphite lubrication wear exists (i.e. if the matrix does not wear down then no graphite flakes become exposed or extruded). If such adverse conditions existed herein, it is postulated that the cast iron would behave poorly, as the martensitic matrix is stiff and does not deform plastically. Behaviour similar to the martensitic compacted cast iron that was obtained by Slatter et al. [4.8] may arise, however, the martensite needles of the cast iron are fine-grained. As those authors [4.8] noted, the finer-grained martensite did not exhibit such catastrophic brittle fracture in the finer-grained martensite.

4.5.   Conclusions

The dry sliding wear performance of seven engineering alloys has been assessed with the aim of providing novel comparative data for future material selection and research purposes. The ranking derived from the pin-on-disc results is industrially relevant, particularly where commercially available materials (instead of specialised tribological alloys) are sought. The material wear performance established three principal groups: combinations using cast iron pins, combinations using Nitronic 60 pins, and self-mated and bronze disc combinations. The key conclusions of the investigation can be summarised as follows:

- The nitrided steel vs. cast iron combination yielded the lowest disc volume loss and one of the lowest pin volume losses. These values result from the high hardness of the nitrided disc surface (982 HV). The marginally poorer results of the AISI 4330 vs. cast iron combination bring into question the cost-effectiveness of surface engineering treatments such as nitriding.

- Material microstructures were indicative of sliding wear performance. The worst-performing discs were the lead-alloyed bronze, followed by the tempered martensitic alloys (AISI 4330, AISI 420, 15-5PH), with the best performing being the nitrided steel samples (which showed frequent networks of nitride compounds at the surface). The cast iron pins displayed a martensitic structure with homogeneously dispersed graphite flakes. These produced lower volume losses than the austenitic pins of Nitronic 60.

- The cast iron was the best performing pin due to graphite and oxide products acting as solid lubricants. The highest volume losses resulted from the self-mated and bronze disc combinations. The poor performance of these combinations was reflected in the wear scar cross-sections which showed the deepest scars in this chapter.

- For cast iron and Nitronic 60 combinations, AISI 4330 produced superior results to AISI 420 and 15-5PH. This is due to the more rapid formation and continual reformation of an oxide film on the surface of AISI 4330 because of its chemically active surface.

- The wear mechanisms were influenced by the material hardness, as seen in the corresponding scar morphology. Softer alloys such as bronze and AISI 420 exhibited scars generated through plastic flow whereas harder alloys like the 15-5PH displayed a tendency to brittle fracture. The brittle fracture combinations displayed instances of scuffing, ploughing interrupted by smearing, and oxidative wear. The plastic flow wear scars displayed unbroken ploughing and oxidative wear.

References

[4.1] D. Pye, "Why Nitride?," in *Practical Nitriding and Ferritic Nitrocarburizing*, ASM International, 2003, pp. 13–22.

[4.2] D. Pye, "How does the nitriding process work?," in *Practical Nitriding and Ferritic Nitrocarburizing*, ASM International, 2003, pp. 23–29.

[4.3] H. T. Angus, "Dry Sliding Wear," in *Cast Iron: Physical and Engineering Properties*, 2nd ed., London, Boston: Butterworths, 1976, pp. 293–298.

[4.4] J. E. Labelle, "Wear resistance of cast iron components," in *Handbook of Mechanical Wear*, C. Lipson and L. V. Colwell, Eds. Ann Arbor: University of Michigan Press, 1961, p. 378.

[4.5] R. S. Montgomery, "Run-in and glaze formation on gray cast iron surfaces," *Wear*, vol. 14, no. 2, pp. 99–105, 1969.

[4.6] T. S. Eyre, R. F. Iles, and D. W. Gasson, "Wear characteristics of flake and nodular graphite cast iron," *Wear*, vol. 13, no. 4–5, pp. 229–245, 1969.

[4.7] M. Kawamoto and K. Okabayashi, "Wear of Cast Iron in Vacuum and the Frictional Hardened Layer," *Wear*, vol. 17, pp. 123–138, 1971.

[4.8] T. Slatter, R. Lewis, and A. Jones, "The Influence of Induction Hardening on the Impact Wear Resistance of Compacted Graphite Iron (CGI)," *Wear*, vol. 270, no. 3–4, pp. 302–311, 2011.

[4.9] I. Hutchings and P. Shipway, "Applications and case studies," in *Tribology: Friction and Wear of Engineering Materials*, 2nd ed., Butterworth - Heinemann, 2017, pp. 314–318.

[4.10] B. Bhushan, "Contact Between Solid Surfaces," in *Introduction to Tribology*, 2nd ed., Columbus: John Wiley & Sons, Ltd., 2013, p. 91.

[4.11] G. Rasool and M. M. Stack, "Mapping the role of Cr content in dry sliding of steels: Comparison between maps for material and counterface," *Tribol. Int.*, vol. 80, pp. 49–57, 2014.

[4.12] B. Bhusan, "Wear of Metals and Alloys," in *Introduction to Tribology*, 2nd ed., New York: Wiley, 2013, p. 372.

[4.13] I. Hutchings and P. Shipway, "Sliding Wear," in *Tribology: Friction and Wear of Engineering Materials*, 2nd ed., Butterworth - Heinemann, 2017, p. 293.

[4.14] M. Dumas *et al.*, "Evolution of the surface integrity while turning a fillet radius in a martensitic stainless steel 15-5PH," *Procedia CIRP*, vol. 87, pp. 101–106, 2020.

[4.15] A. Bain *et al.*, "Wear and microstructure analysis on AISI420 stainless steel by annealing & tempering process under dry sliding conditions," *Adv. Mater.*

Process. Technol., vol. 00, no. 00, pp. 1–11, 2021.

[4.16] L. Duensing, "Understanding Nitronic Alloys," *Modern Metals*, no. 10, Tipton, Indiana, pp. 12–12, Nov-2016.

[4.17] Electralloy, "Nitronic 60," pp. 1–28, 2013.

[4.18] L. G. Korshunov, Y. N. Goikhenberg, and N. K. Chernenko, "Effect of alloying and heat treatment on the structure and tribological properties of nitrogen-bearing stainless austenitic steels under abrasive and adhesive wear," *Met. Sci. Heat Treat.*, vol. 49, no. 5–6, pp. 217–226, 2007.

[4.19] K. L. Hsu, T. M. Ahn, and D. A. Rigney, "Friction, wear and microstructure of unlubricated austenitic stainless steels," *Wear*, vol. 60, no. 1, pp. 13–37, 1980.

[4.20] G. C. Pratt, "Materials for Plain Bearings," vol. 18, pp. 62–88, 1973.

[4.21] F. P. Bowden and D. Tabor, "The lubrication by thin metallic films and the action of bearing metals," *J. Appl. Phys.*, vol. 14, no. 3, pp. 141–151, 1943.

[4.22] B. K. Prasad, A. K. Patwardhan, A. H. Yegneswaran, and A. K. Patwardhan, "Factors Controlling Dry Sliding Wear Behaviour of a Leaded Tin Bronze," *Mater. Sci. Technol.*, vol. 12, pp. 427–435, 1996.

[4.23] B. K. Prasad, "Sliding wear behaviour of bronzes under varying material composition, microstructure and test conditions," *Wear*, vol. 257, no. 1–2, pp. 110–123, 2004.

[4.24] ASTM Standards, "ASTM G99 - 17: Standard Test Method for Wear Testing with a Pin-on-Disk Apparatus."

[4.25] Y. Li, Y. He, J. J. Xiu, W. Wang, Y. J. Zhu, and B. Hu, "Wear and corrosion properties of AISI 420 martensitic stainless steel treated by active screen plasma nitriding," *Surf. Coatings Technol.*, vol. 329, no. August, pp. 184–192, 2017.

[4.26] H. J. Baker, "The friction and wear of hardened steel, phosphor bronze and cast iron under controlled sliding conditions," *Int. J. Mach. Tool Des. Res.*, vol. 3, no. 3, pp. 459–466, 1963.

[4.27] J. F. Archard and W. Hirst, "The wear of metals under unlubricated conditions," *Proc. R. Soc. Lond. A.*, vol. 236, 1956.

[4.28] Hall E. O., "The deformation and ageing of mild steel: III Discussion of Results," *Proc. Phys. Soc. Sect. B*, vol. 64, no. 9, pp. 742–747, 1951.

[4.29] J. P. Pathak and S. N. Tiwari, "On the mechanical and wear properties of copper-lead bearing alloys," *Wear*, vol. 155, no. 1, pp. 37–47, 1992.

[4.30] J. Gerkema, "Lead thin film lubrication," *Wear*, vol. 102, no. 3, pp. 241–252, 1985.

[4.31] V. E. Buchanan, P. A. Molian, T. S. Sundarshan, and A. Akers, "Frictional behavior of non-equilibrium Cu-Pb alloys," *Wear*, vol. 146, no. 2, pp. 241–256, 1991.

[4.32] I. Hutchings and P. Shipway, "Oxidative Wear," in *Tribology: Friction and Wear of Engineering Materials*, 2nd ed., Butterworth - Heinemann, 2017, p. 127.

[4.33] P. J. Blau, "How common is the steady-state? The implications of wear transitions for materials selection and design," *Wear*, vol. 332–333, pp. 1120–1128, 2015.

[4.34] J. Sugishita and S. Fujiyoshi, "The effect of cast iron graphites on friction and wear performance I: Graphite film formation on grey cast iron surfaces," *Wear*, vol. 66, no. 2, pp. 209–221, 1981.

[4.35] J. Sugishita and S. Fujiyoshi, "The Effect of Cast Iron Graphites on Friction and Wear Performance II: ariables influencing graphite film formation," *Wear*, vol. 68, no. 1, pp. 7–20, 1981.

[4.36] J. Sugishita and S. Fujiyoshi, "The effect of cast iron graphite on friction and wear performance III: The lubricating effect of graphite under rolling-sliding contacts," *Wear*, vol. 77, no. 2, pp. 181–193, 1982.

Chapter 5.

Saltwater Sliding Wear of AISI 4330 and 15-5PH against Cast Iron

Abstract

Environmental conditions, testing variables, and material properties significantly influence the sliding wear behaviour of all tribosystems. Such parameters affect the mechanism of wear occurring, govern how the wear scar will be categorised, and control whether wear rate transitions occur throughout the test. The present study investigated these variables using sliding wear tests of AISI 4330, 15-5PH, and heat treated cast iron in the dry and NaCl solution regime. Loads of 2kg, 4kg, and 6kg were applied to the cast iron pin in both regimes, with the volume loss results, wear scar morphology, and microstructural evolution analysed.

It was found that the AISI 4330 and 15-5PH discs produced higher volume losses in the dry regime than the NaCl regime, indicating the solution gave a beneficial effect rather than a detrimental effect versus the dry tribosystem. Beneficial oxidative wear allowed for AISI 4330 to lose less than 15-5PH in the dry regime, with their respective cast iron pins following the same result. Microstructurally, the 15-5PH wear scar cross-sections exhibited a mechanically disturbed surface layer of refined material mixed with oxides, above a layer of grains, deformed in the direction of sliding. This highlighted the significant difference between the wear of 15-5PH and AISI 4330, as the latter did not exhibit significant subsurface deformation.

5.1.   Introduction

For ferrous alloys in sliding, applied load is a critical parameter in governing the category of wear [5.1]. For the most part, this is due to load determining whether beneficial oxidative wear prevails. Most metallic materials exhibit a thin surface layer of oxides due to their negative Gibbs free energy, indicating that their oxides are more thermodynamically stable than their metallic matrices [5.2]. Such films of oxides are influenced not only by the substrate chemistry and microstructure but also by external factors. The load influences the frictional work input to the contact faces, and thus influences the kinetic energy input. This energy input to the contact faces is dissipated through different routes, such as material removal, microstructural changes, and heat [5.3]. Of these select results, the heat input has the largest influence on oxidative properties, as such temperature changes affect the parabolic growth rate of oxide layers. As load increases, frictional work also increases, resulting in greater temperature increases, and faster oxide growth. If the conditions are correct, the oxide layer grows at a faster rate than the rate of material removed through sliding. This allows the film to build up into a beneficial oxide layer which shields the underlying substrate from further damage [5.4]. This is one example of a transition from severe to mild wear. The opposite can also occur, where the material removal from sliding is more than the growth rate of the oxide layer, causing the wear regime to shift to severe metallic damage [5.5]–[5.7].

In seawater sliding contexts, such as pumps, motors, shafts, and bearings in marine environments, the occurring wear is often combined with corrosive action (referred to as tribocorrosion). In these instances, material can be removed from both sliding and corrosion synergistically, with the resultant volume loss greater than the sum of the lost material from either mechanism. Analogies can be drawn between tribocorrosion and dry oxidative sliding, however in tribocorrosive instances, the synergy established between the two mechanisms is usually detrimental instead of advantageous. This interaction results in complimentary material removal, with corrosion accelerating the wear and vice versa. Research on synergistic corrosive wear has been conducted by numerous authors [5.8]–[5.13] since the 1990s, with comprehensive reviews from Mischler [5.14], Watson [5.15], and Landolt et al. [5.16].

Additional factors in the dry and tribocorrosive sliding performance of metals are the material passivation kinetics [5.17]. Such factors control the rate at which external films grow on the material surface, which is of great significance to sliding wear and tribocorrosive resistance. For active alloys such as alloy steels and cast irons, these layers are typically fast growing, whereas for stainless steels the passive layer is slower to form [5.18]. In tribocorrosive environments, removal of the passive film on stainless steels leads to exposure of fresh metallic material underneath, which may then either repassivate or detach depending on the corrosion mechanisms occurring. Huttunen-Saarivirta et al. [5.19] compared the effectiveness of type 440B martensitic stainless steel and 304 austenitic stainless steel in NaCl solution. The authors [5.19] found that type 440B performed worse off than type 304 because of slower re-passivation, and the discontinuous nature of its passive film due to the heterogeneous microstructure consisting of ferrite, martensite, and chromium carbides [5.19]. Zhang et al. [5.20] also compared the tribocorrosive performance of martensitic stainless steel and austenitic stainless steel. The researchers [5.20] found that a cathodic shift during sliding indicated that corrosion potential increased upon damage of the passive film, and this effect increased with heavier applied loads [5.20]. López-Ortega et al. [5.21] compared the electrochemical and tribocorrosive properties of type 316 stainless steel and HSLA R4 low alloy steel. The authors [5.21] found that the stainless steel was unaffected by the potentio-dynamic polarisation tests due to its passive film, whereas the low alloy steel was significantly agitated. It was also found that only the low alloy steel showed evidence of wear-accelerated corrosion due to its reactivity, and that the rotating cell, and resultant agitation of the electrolyte, had a large impact on this synergism [5.21].

In the majority of tribocorrosion studies, samples are worn against an inert counter face such as alumina. This is to simplify electrochemical techniques by removing the galvanic effects of two metals in contact. However, rarely in industrial applications do two such dissimilar materials experience sliding contact; usually metal-to-metal contact is seen [5.22]. To compare the effectiveness of oxidative wear at different loads, under different environmental conditions, and for different compositional chemistries, this chapter discusses the dry and tribocorrosive sliding properties of cast iron pins against a low alloy steel and stainless steel discs. Such alloys see frequent usage in engineering applications, increasing the scientific relevancy of this chapter,

as there is not extensive documentation of 15-5PH or AISI 4330 in tribocorrosive literature. In addition to the combinations of materials tested in dry sliding and in NaCl sliding, the influence of load on volume loss and wear scar morphology, the sliding effectiveness of active and passive oxide layers, and the influence of microstructure in sliding wear contexts are also discussed.

5.2.   Materials & Methods

5.2.1.   Materials

Grade G350 cast iron pins, AISI 4330 low alloy steel discs, and 15-5PH precipitation hardened stainless steel discs were examined, with chemical compositions shown in Chapter 3.

To investigate the effect of a hardened matrix, the cast iron samples were heat treated after machining into pin form. This involved austenitising at 875°C, oil quenching to room temperature, and tempering at 400°C for 90 minutes, resulting in a change from the initial coarse pearlite to tempered martensite (Figure 5.1).
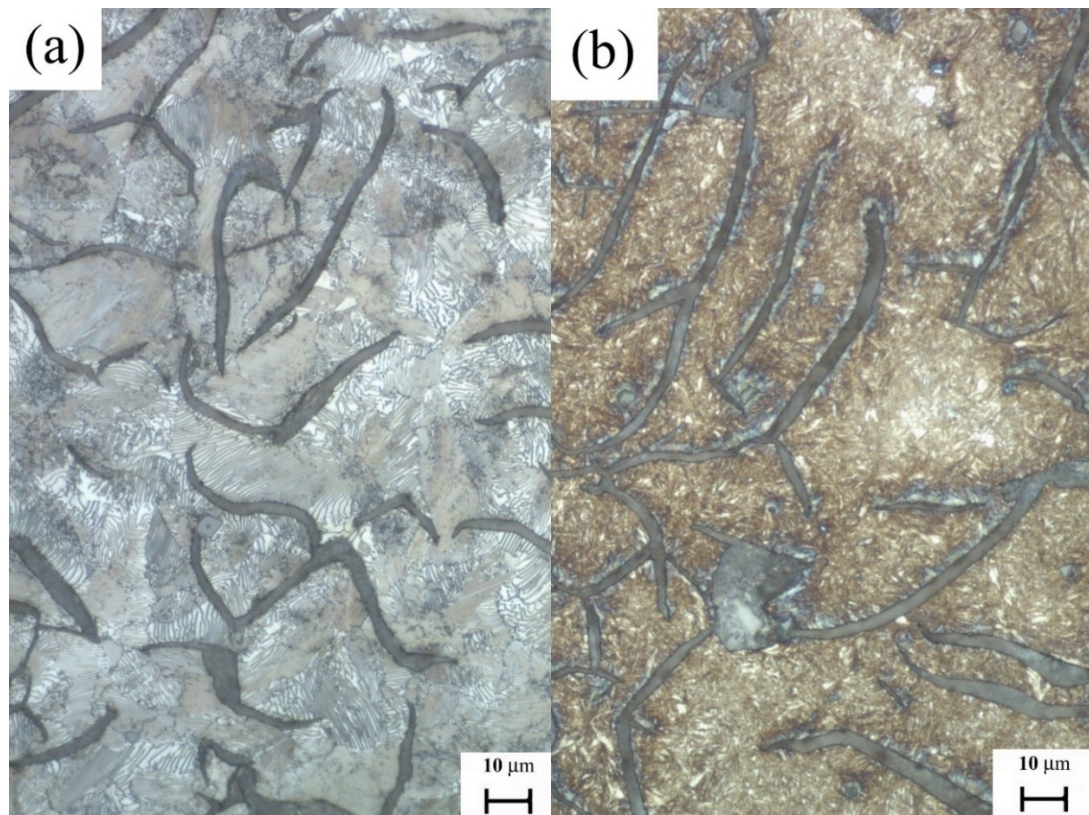

Figure 5.1 - Microstructure of (a) as-received cast iron, (b) heat treated cast iron [x500 – etched – nital].

5.2.2.   Methods

Dry and tribocorrosive wear behaviour was examined using pin-on-disc sliding wear tests and followed the procedure of ASTM G99 [5.24]. NaCl solution was used as the circulating corrosive medium for half of the pin-on-disc tests. The medium was made to approximate seawater by mixing purified water and NaCl to a 3.5wt% solution. Circulation was achieved using a micro-pump which delivered the NaCl solution from the sump to the sample holder, which then drained back into the sump. To avoid galvanic effects, samples tested in NaCl solution were shielded from the surrounding rig using rubber gaskets and grease. After each test, they were treated according to ASTM G1 [5.25], which involved pickling the samples in a solution of hydrochloric acid, hexamethylene tetramine, and water. This removed adhered grease and corrosion products (Figure 5.2), allowing for total material mass loss to be measured. To allow for fair comparisons between materials, density was used to convert mass loss values into volume loss values.
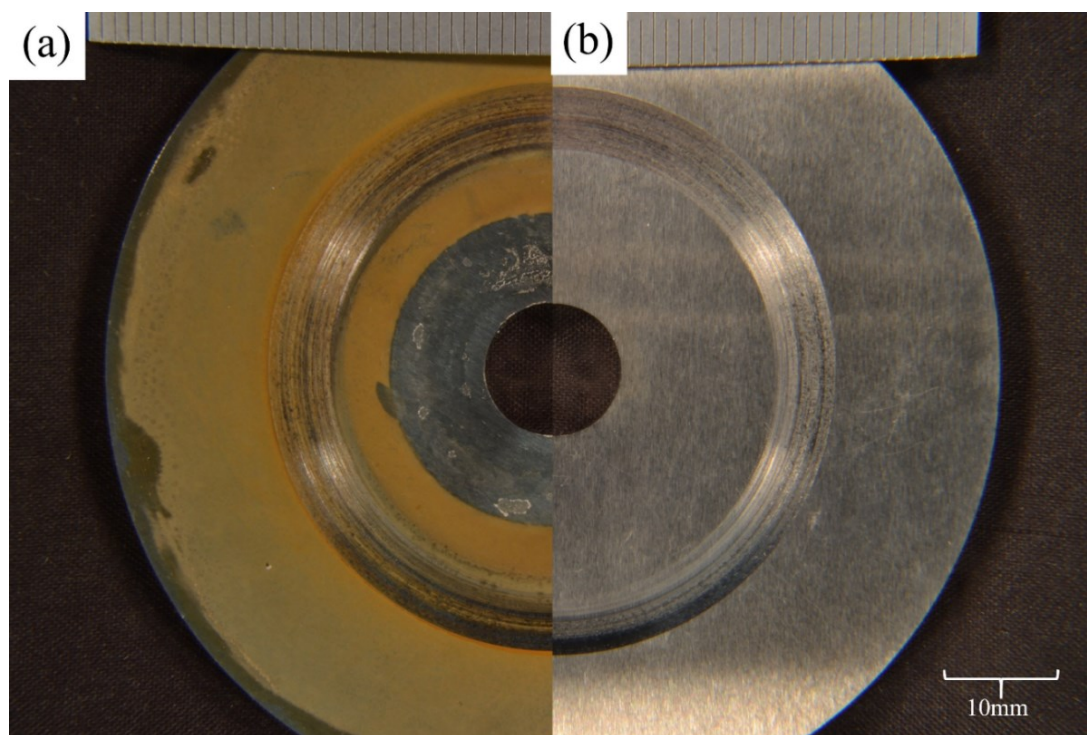
Figure 5.2 - Example of a 6kg NaCl 15-5PH disc (a) post-test, (b) following post-test treatment.

Other metallurgical techniques were utilised to further analyse the sliding wear results, as described in Chapter 3. Vickers micro-indentation hardness values are displayed in Table 5.1 (n = 10).

Table 5.1 - Micro indentation hardness of studied materials.

Material	Micro Indentation Hardness (HV$_{500gf}$)
Cast Iron	404
AISI 4330	334
15-5PH	365

Immersion corrosion tests were conducted to investigate the mass loss of the cast iron pin from immersion in the NaCl solution during the pin-on-disc tests. Such tests also served to evaluate whether the post-test pickling removed excess metallic material. Four pins were partially suspended in the circulating NaCl solution for 90 minutes (the same length of time as the pin-on-disc tests) to measure the mass change from the corrosive attack, then pickled, and measured again.

5.3.   Results

5.3.1.   *Pin-on-disc Volume Loss Values*

Disc volume losses versus applied load are shown in Figure 5.3. The highest values were observed from the dry combinations, with the NaCl combinations producing lower values and less linear changes with load.
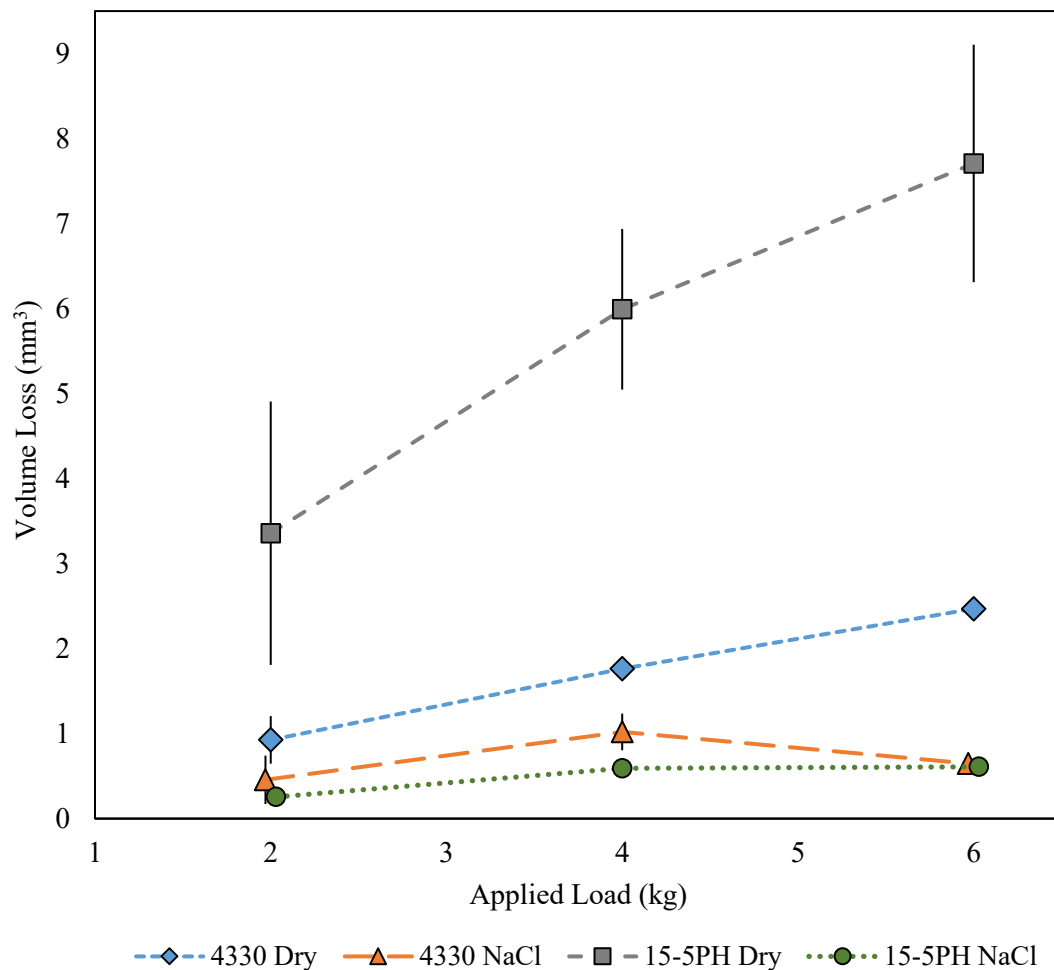
Figure 5.3 – AISI 4330 and 15-5PH disc volume loss values from wearing against cast iron the dry and NaCl regime. N = 3 for all tests.

Cast iron pin volume losses versus applied load are shown in Figure 5.4, where the opposite trend is observed. The pins tested in NaCl solution produced higher volume losses than the dry pins. The relationship between applied load and volume losses for the pins fluctuates, with increases/decreases seen as load increases for the pins tested in NaCl solution. In contrast, both dry pin plots increase linearly at different gradients.
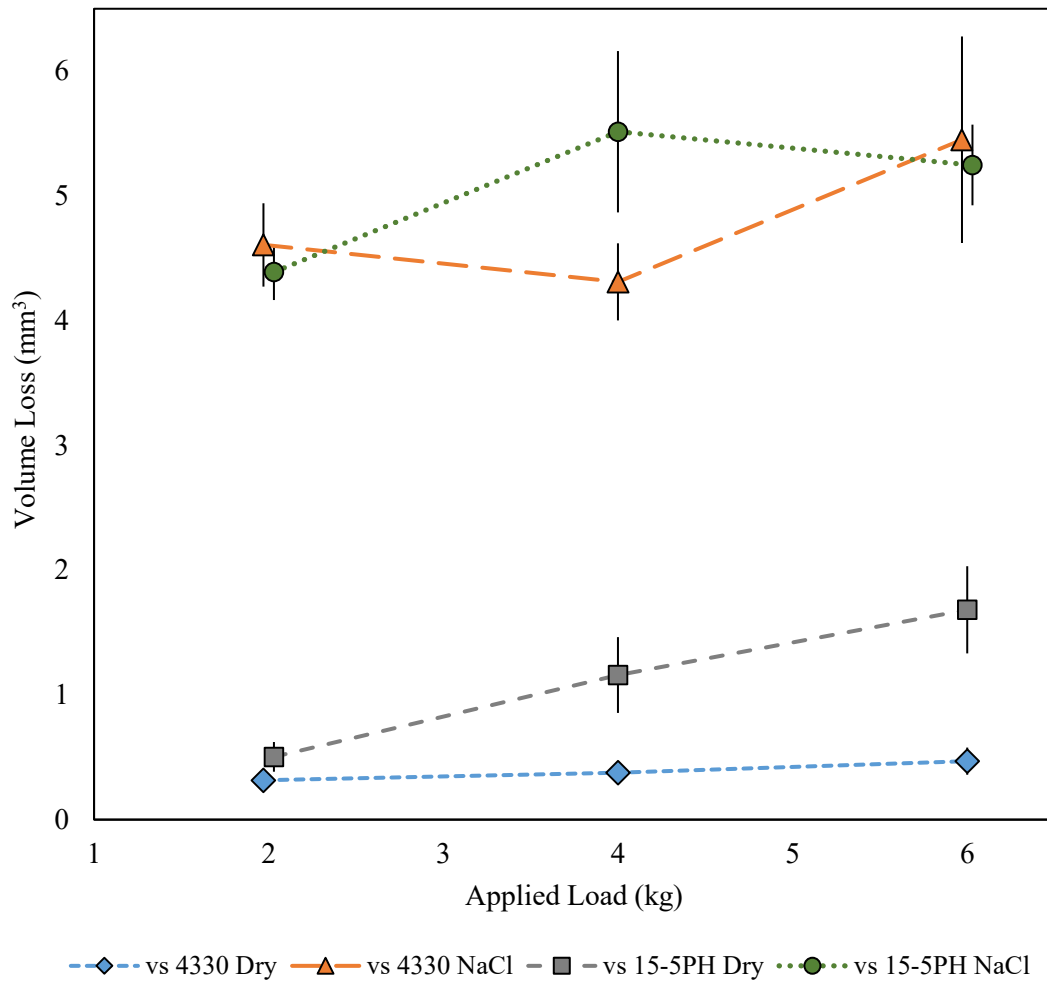
Figure 5.4 - Cast iron pin volume losses from wearing against AISI 4330 and 15-5PH in the dry and NaCl regime. N = 3 for all tests.

5.3.2.   *Worn Surface Macro Inspection*

Visual inspection of the worn surfaces indicated the mechanism and category of wear occurring just prior to the test completion. The dry discs showed a strong contrast between the materials, with the AISI 4330 discs appearing discoloured from oxidative wear (Figure 5.5(a – c)), and the 15-5PH discs appearing brighter and jagged due to mechanical damage of the matrix (Figure 5.5(d – f)). As load increases, the oxide layer thickness increases, forming a darker thick blanket coverage on the AISI 4330 scars. For the 15-5PH scars, the adhered oxide changed from a thin stripe at 2kg to a wider area at 6kg.
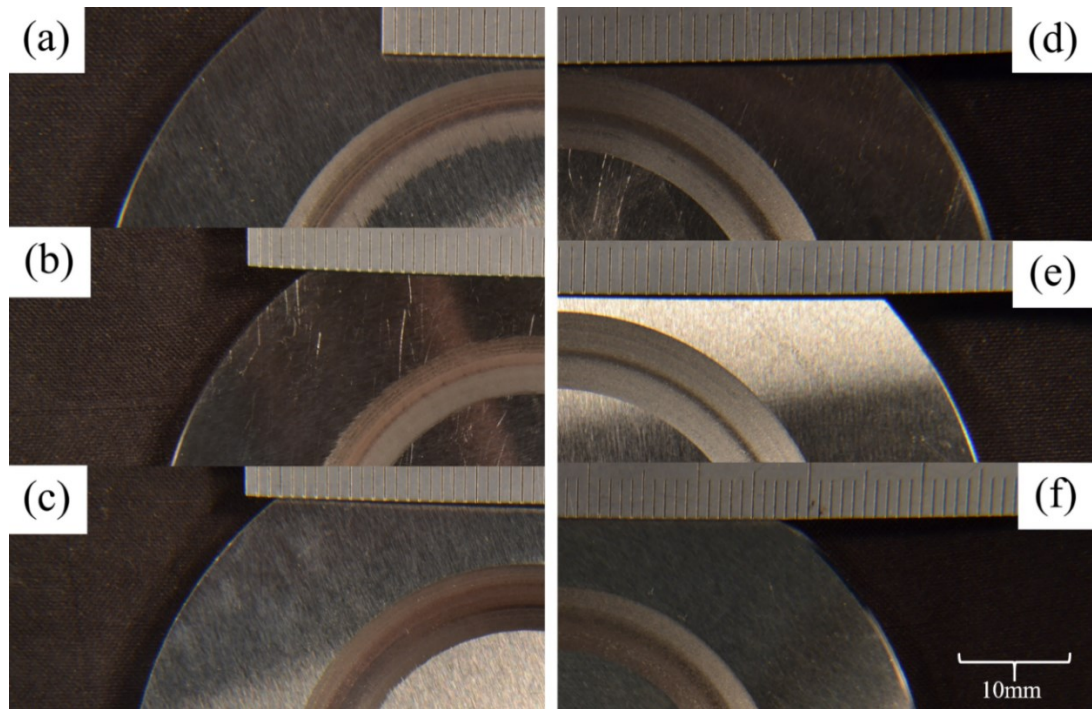
Figure 5.5 – Dry wear scars on AISI 4330 (left) and 15-5PH (right) discs from loads of (a, d) 2kg, (b, e) 4kg, (c, f) 6kg.

Similar observations were made of the dry worn pin end faces, with discoloured pin surfaces from AISI 4330 discs (Figure 5.6(a – c)) and brighter faces on the pins from 15-5PH discs (Figure 5.6(d – f)). Both sets of dry pins exhibit a dark oxide band running through the centre of the worn surface, corresponding to matching bands seen in the disc wear scars.
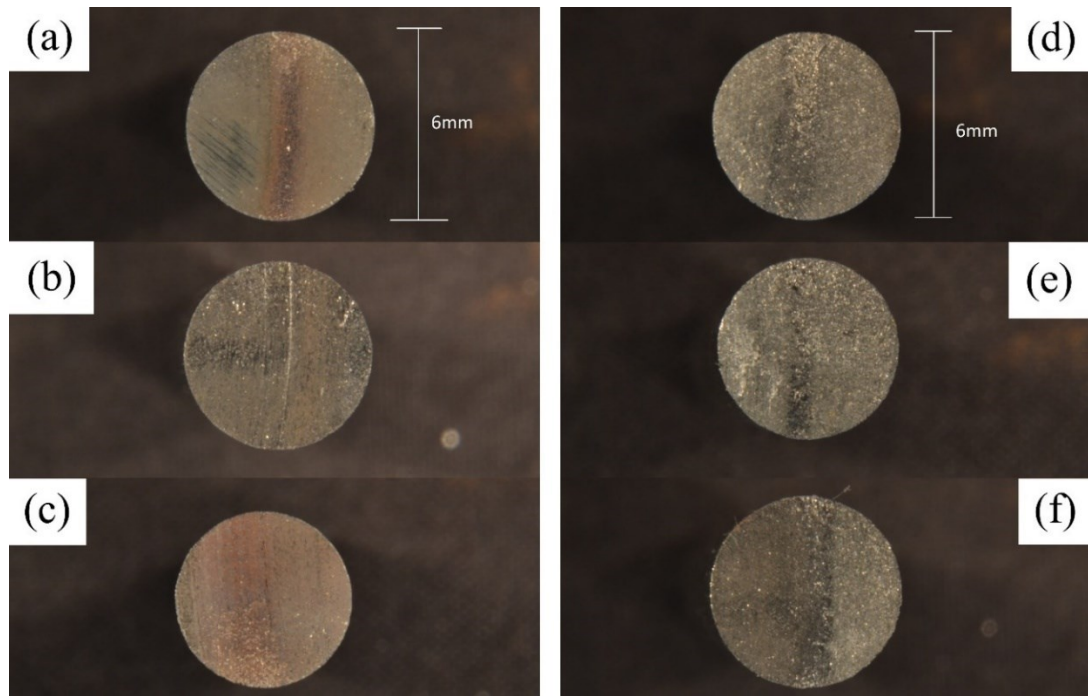
Figure 5.6 – Cast iron pin worn surfaces from dry wear against AISI 4330 (left) and 15-5PH discs (right) from loads of (a, d) 2kg, (b, e) 4kg, (c, f) 6kg.

Visual observation of the disc samples tested in NaCl solution (Figure 5.7) showed less obvious differences between the wear of 15-5PH and AISI 4330. These scars appeared as polished sections of the surface rather than structural damage, with the scar standing out among the adhered corrosion products and dissolved grease.
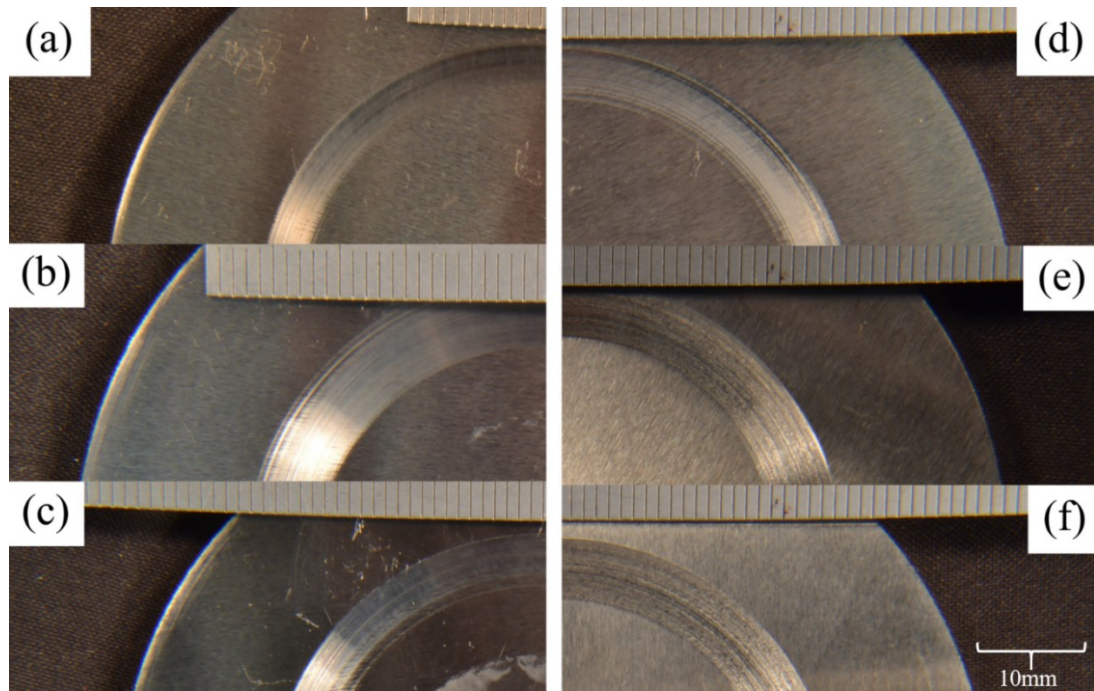
Figure 5.7 - NaCl wear scars on AISI 4330 (left) and 15-5PH (right) discs from loads of (a, d) 2kg, (b, e) 4kg, (c, f) 6kg.

The contact faces of the pins tested in NaCl solution (Figure 5.8) were likewise significantly brighter than the surrounding shaft of the pin (Figure 5.9) which showed adhered corrosion products.

Figure 5.8 - Cast iron pin worn surfaces from NaCl wear against AISI 4330 (left) and 15-5PH discs (right) from loads of (a, d) 2kg, (b, e) 4kg, (c, f) 6kg.
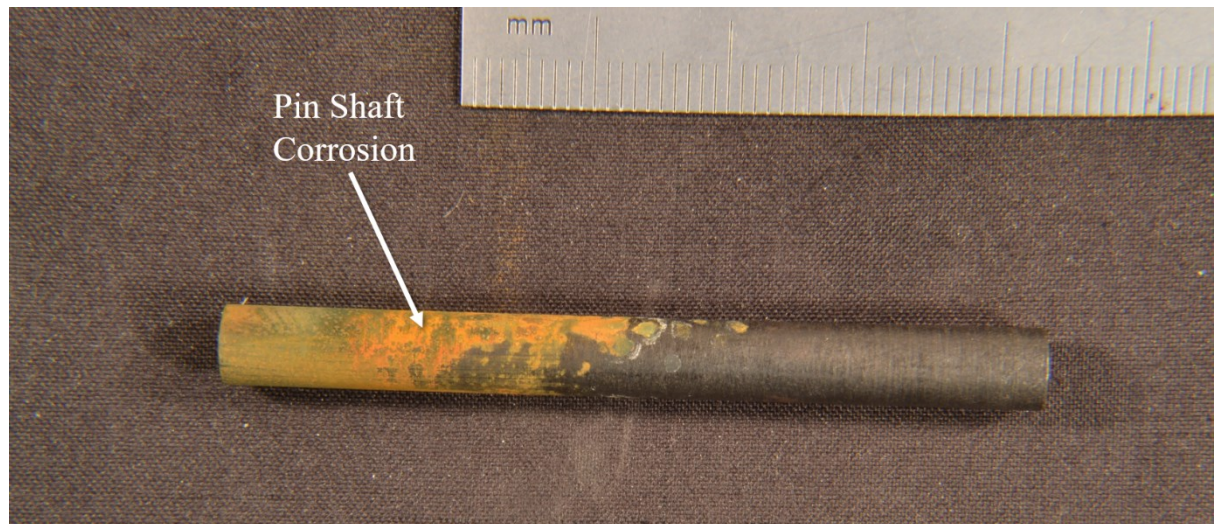
Figure 5.9 - Cast iron pin corroded shaft from tests in NaCl solution.

5.3.3.   *Disc Cross-sectional Profilometry*

The differences in wear of the dry disc materials can be observed through the wear scar cross-sectional profiles (Figure 5.10), with the 15-5PH wear scars being deeper and more jagged, whereas the AISI 4330 scars are shallower and smoother in general.
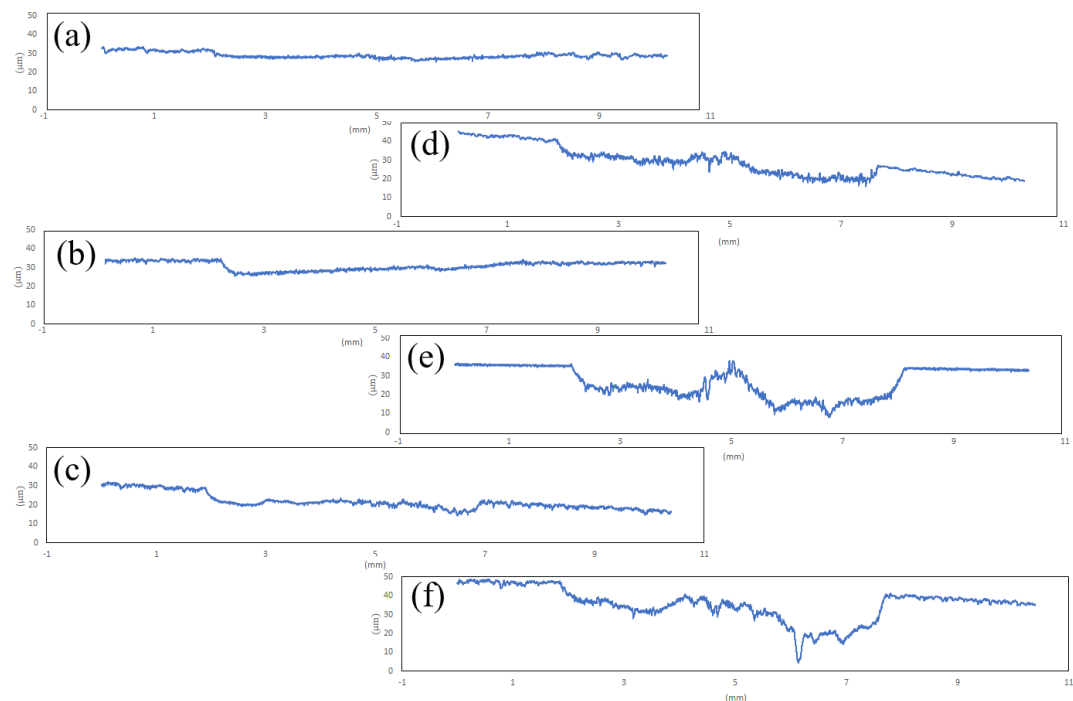
Figure 5.10 – Dry cross-sectional profiles of AISI 4330 (left) and 15-5PH (right) discs from wear of (a, d) 2kg, (b, e) 4kg, (c, f) 6kg.

For the discs tested in NaCl solution (Figure 5.11), the contrast between polishing at lighter loads and damage at higher loads can also be observed from the cross-sectional profiles, with obvious differences in surface roughness highlighting the increase from lighter to heavier loads.
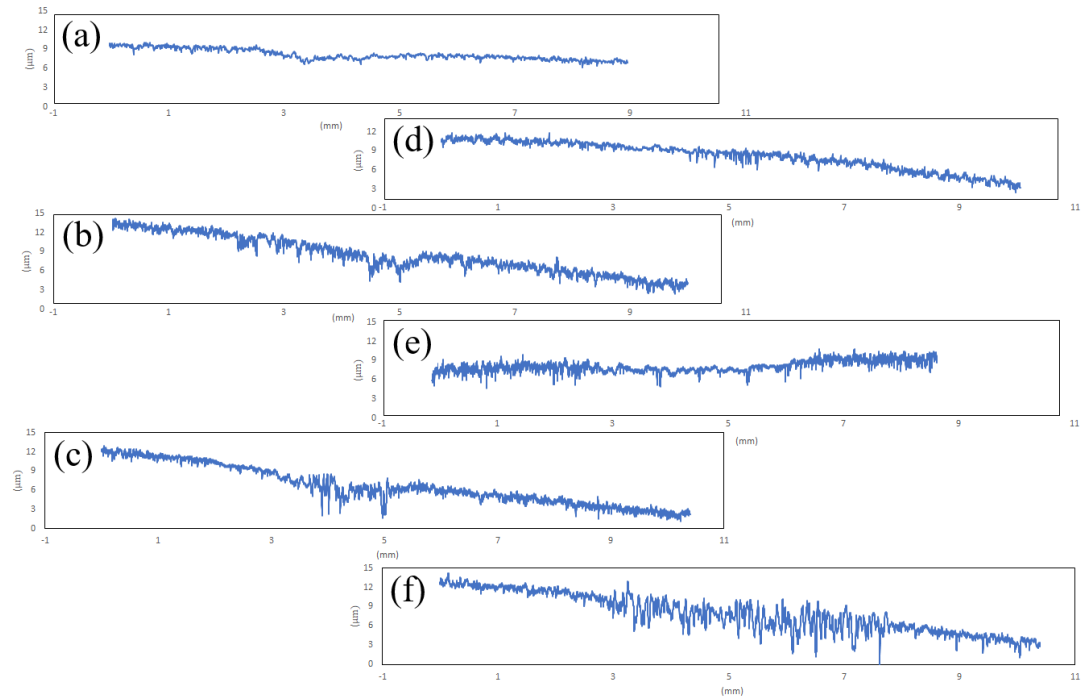
Figure 5.11 - NaCl cross-sectional profiles of AISI 4330 (left) and 15-5PH (right) discs from wear of (a, d) 2kg, (b, e) 4kg, (c, f) 6kg.

5.3.4.   Wear Scar SEM Inspection

Inspection of the wear scars through SEM also highlighted the differences between the oxidative wear of the dry AISI 4330 tests and the severe mechanical damage of the dry 15-5PH tests (Figure 5.12). A layer of oxide resides on top of the AISI 4330 wear scar, in some instances forming blanket coverage and in other instances only forming islands of oxide as with the cast pin after sliding against AISI 4330.

Figure 5.12 – Dry SEM micrographs of AISI 4330 (left) and 15-5PH (right) discs from wear of (a, d) 2kg, (b, e) 4kg, (c, f) 6kg [x100].

The 15-5PH scars show typical brittle fracture damage with instances of scuffing, scoring, and smearing. The wear scars of the accompanying cast iron pins for these combinations (Figure 5.13) show similar forms of damage, with more mechanical damage on the pins worn against 15-5PH and more oxidation products from those worn against AISI 4330 discs.
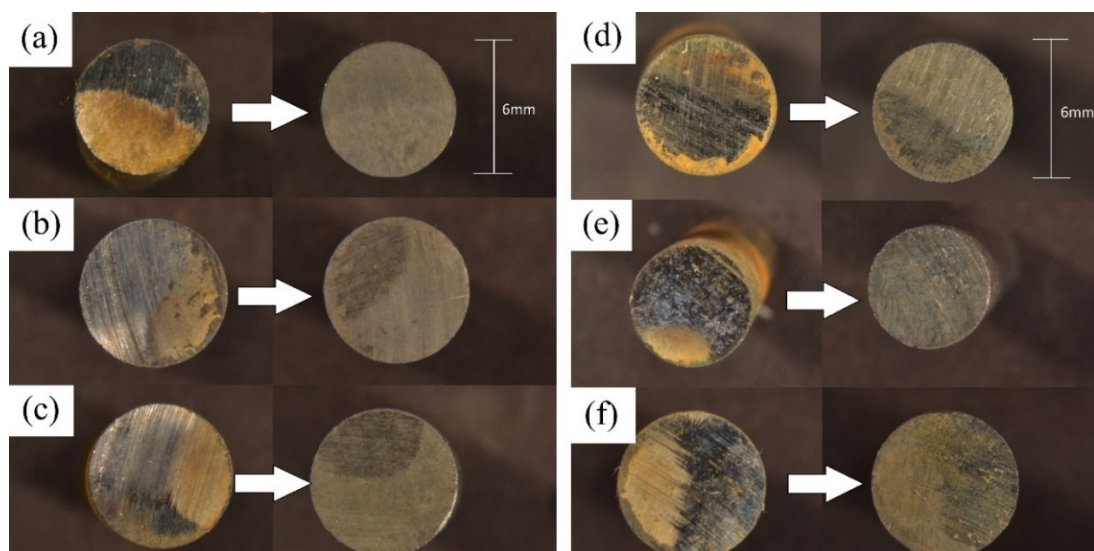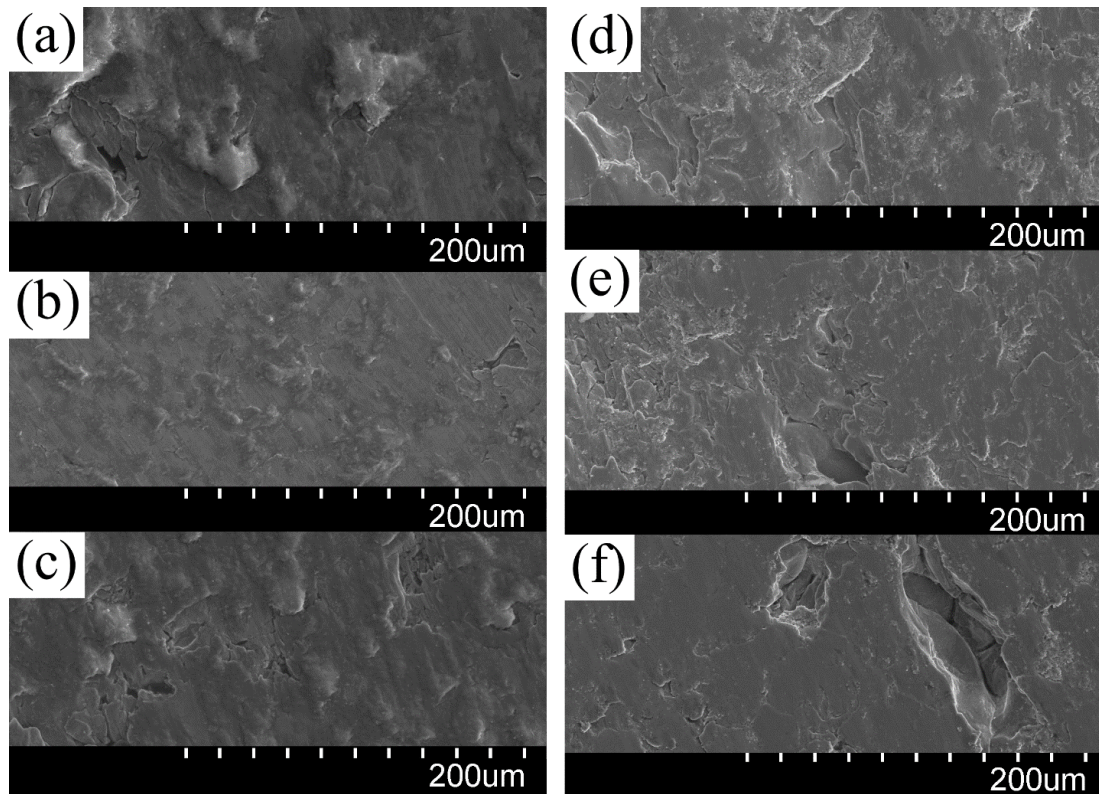
Figure 5.13 - Cast iron pin SEM micrographs from dry wear against AISI 4330 (left) and 15-5PH discs (right) from loads of (a, d) 2kg, (b, e) 4kg, (c, f) 6kg [x200].

The darkened band on the 15-5PH disc wear scar was proven to be adhered oxides using EDS (Figure 5.14, Table 5.2), showed an increase in oxygen concentration.
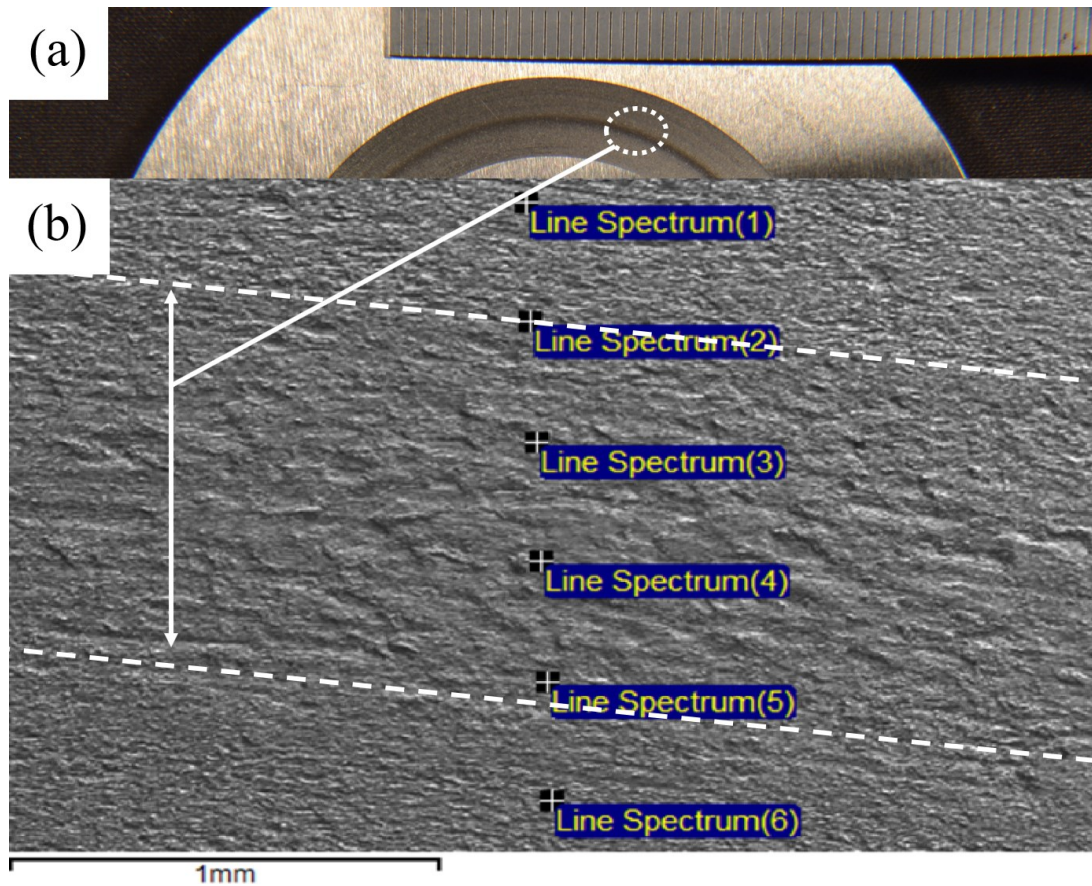
Figure 5.14 - Dry 15-5PH disc (a) macrograph (b) micrograph from a load of 2kg.

Table 5.2 – EDS spectra points from Figure 5.14.

Spectrum	C	O	Si	S	Cr	Mn	Fe	Ni	Cu
Spectrum (1)	7.00	10.43	0.41	0.00	14.13	-	69.05	4.60	4.81
Spectrum (2)	4.52	**23.57**	0.37	0.11	**10.82**	-	**54.65**	3.52	2.42
Spectrum (3)	11.93	**19.53**	1.15	0.11	**6.91**	0.56	**56.01**	2.25	1.55
Spectrum (4)	8.28	**30.14**	0.53	0.09	**9.01**	0.47	**45.66**	2.77	3.06
Spectrum (5)	4.06	7.77	0.34	0.00	13.03	0.83	66.18	4.48	3.30
Spectrum (6)	3.77	11.54	0.32	0.15	12.88	0.62	63.58	3.94	3.20

Examination of the dry pins using back-scattered electrons (BSE mode) (Figure 5.15) highlighted the different levels of oxide coverage between the pins worn against AISI 4330 and those worn against 15-5PH. Those worn against AISI 4330 show a more uniform coverage of darker areas (oxide) coverage whereas the pins worn against 15-5PH have much less, and mostly the middle oxide band previously seen in Figure 5.5.
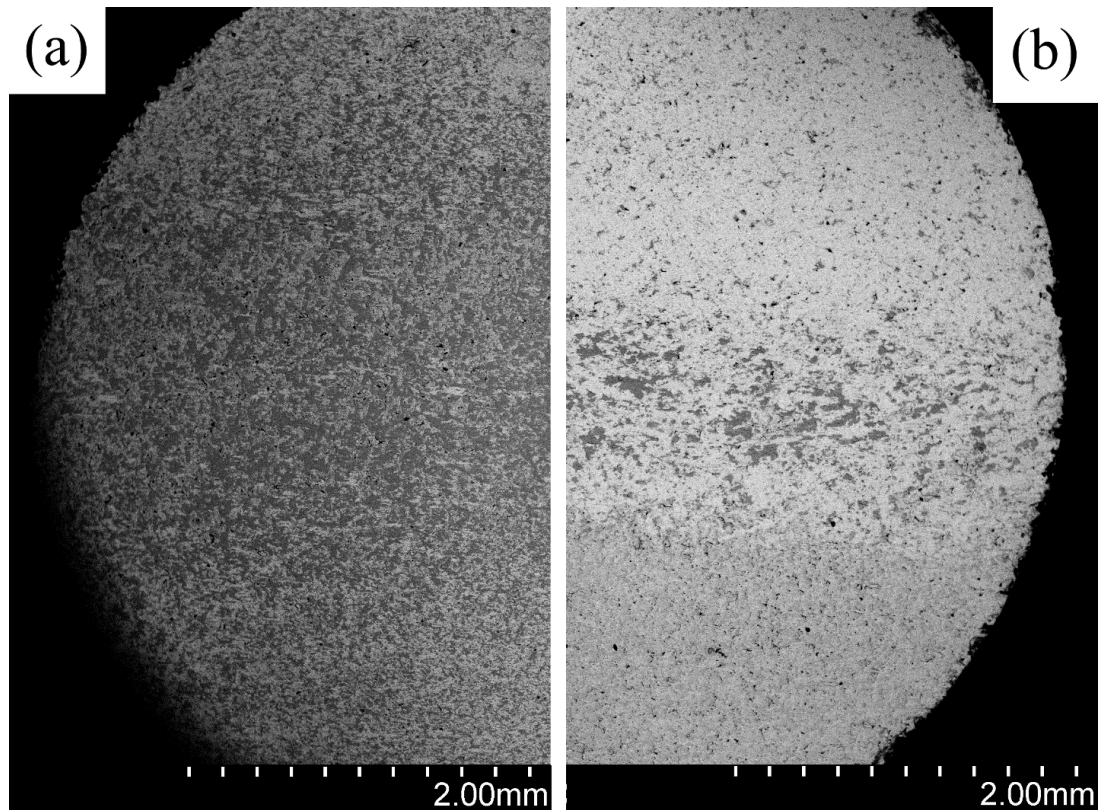
Figure 5.15 - Cast iron back-scattered SEM micrograph from dry wear against (a) AISI 4330, and (b) 15-5PH, from loads of 6kg [x20].

SEM inspection of the discs tested in NaCl (Figure 5.16) highlighted distinct differences from the dry tests. In many areas, the discs exhibit a polished scar, to a finer finish than the initial parent material finish. However, with increasing load, gross mechanical damage became more commonplace with the 15-5PH wear scars showing the brittle fracture damage seen on their dry counterparts. The AISI 4330 tests also show the polishing effect at lower loads but at the highest load exhibit damage more typical of shallow ductile ploughing, with continuous plough lines in the direction of sliding.
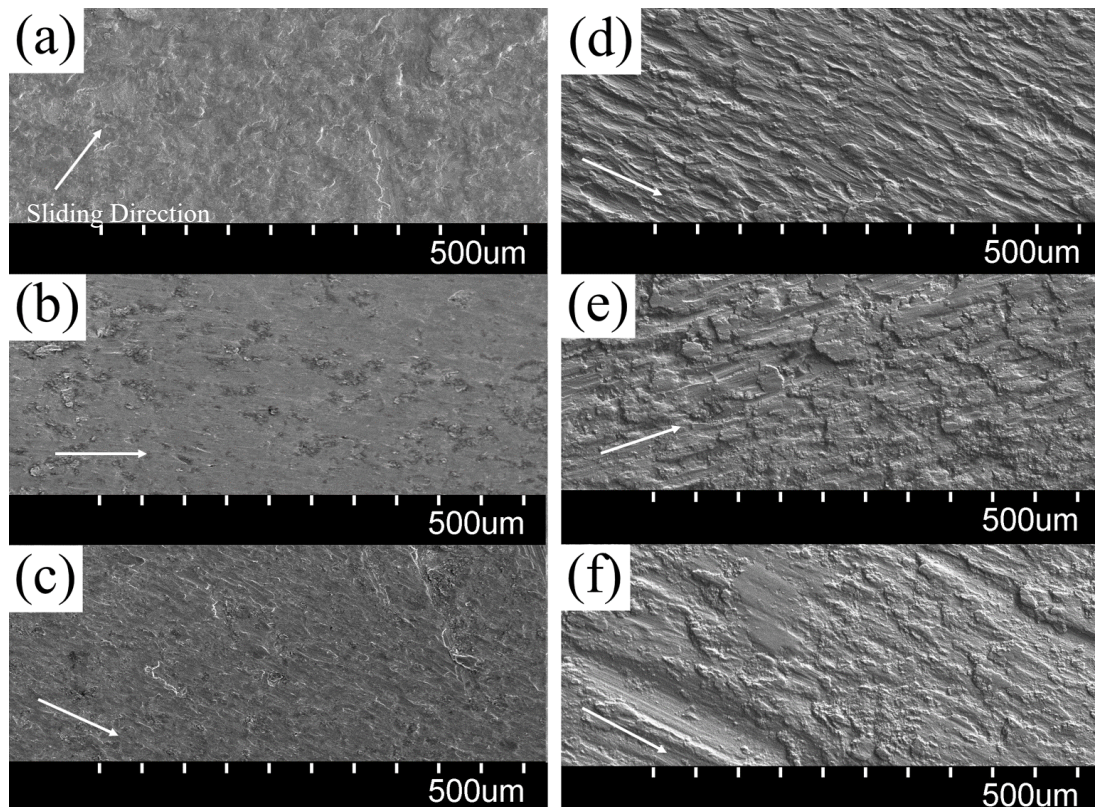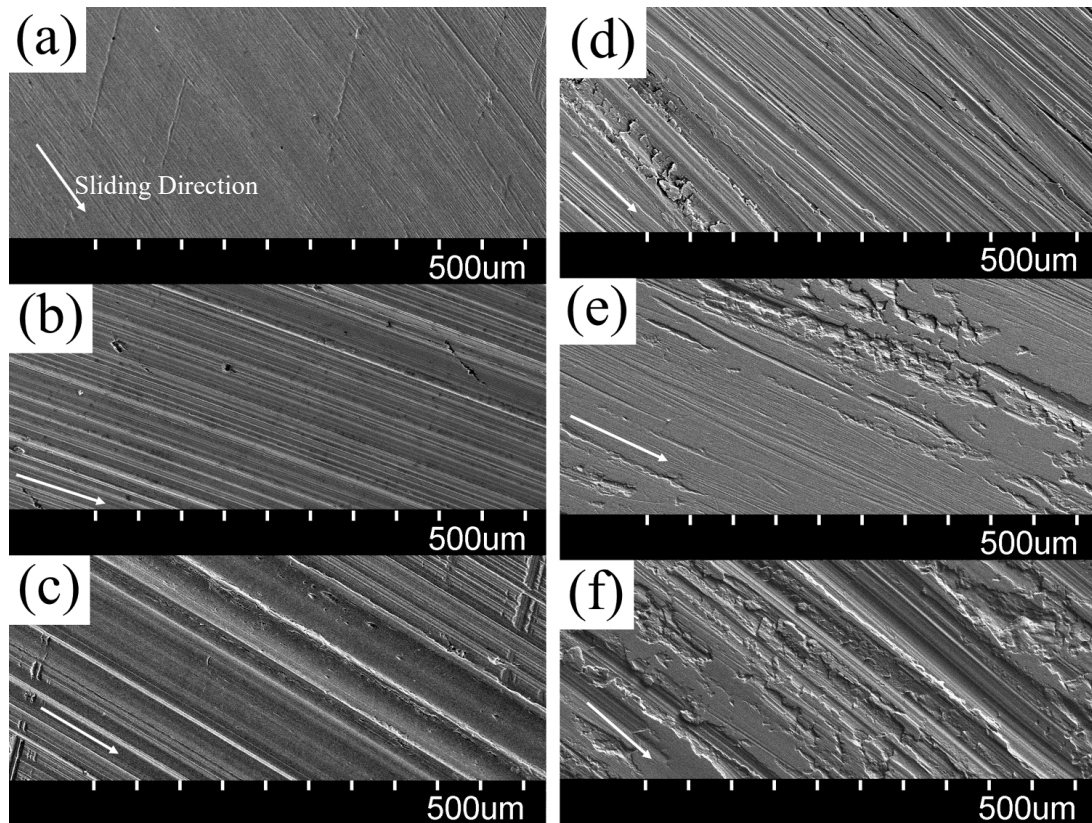
Figure 5.16 - NaCl SEM micrographs of AISI 4330 (left) and 15-5PH (right) discs from wear of (a, d) 2kg, (b, e) 4kg, (c, f) 6kg [x100].

Other distinct differences between the dry discs and NaCl discs include the remnants of grinding lines present throughout the lighter load scars of the NaCl discs (Figure 5.16(a),(c)), and the less-defined boundary of the wear scar. The grinding lines remain in cases where the surface was lightly roughened, but not to such a depth as to wear away the bottom troughs of each grinding trough. No instances of localised attack, such as pitting corrosion, were observed.

5.3.5.   *Summary of Disc Wear Scar Morphology*

Table 5.3 shows a summary of the disc wear scar morphology from all tests.

Table 5.3 – Summary of Disc Wear Scar Morphology.

Regime	Material	Load (kg)	Description	Volume Loss	Wear Mechanisms	Category
Dry	AISI 4330	2	Heavily oxidised, not fully worn-in	Low	Oxidative	Mild
		4	Heavily oxidised, not fully worn-in	Low	Oxidative	Mild
		6	Increased oxide coverage & thickness, fully worn-in	Low	Oxidative	Mild
	15-5PH	2	Matrix damage, oxide band	High	Scoring, scuffing, ploughing	Severe
		4	Matrix damage, oxide band	High	Scoring, scuffing, ploughing	Severe
		6	Matrix damage, increased oxide coverage	High	Scoring, scuffing, ploughing	Severe
NaCl	AISI 4330	2	Polished surface, not fully worn	Very Low	Polishing	Mild
		4	Polished surface, not fully worn	Very Low	Polishing	Mild
		6	Polished surface, not fully worn	Very Low	Polishing, ploughing	Mild
	15-5PH	2	Polished surface, not fully worn	Very Low	Polishing, scuffing	Mild
		4	Polished areas with matrix damage	Very Low	Polishing, scuffing, ploughing	Mild
		6	Polished areas with increased matrix damage	Very Low	Polishing, scuffing, ploughing	Mild

5.3.6.   *Microstructural Characterisation*

Microstructural investigation of the disc wear scars (Figure 5.17) highlighted the differences between the damage mechanisms of the disc alloys. In longitudinal and transverse views of the 15-5PH scars (Figure 5.17(a)), a 10µm mechanically mixed layer can be seen on the top surface of the sample. This layer stands out from the substrate due to a different sensitivity to etching and lacks the grain structure observed elsewhere. Distorted grains in the direction of sliding can be seen beneath the mechanically mixed layer, down to a depth of 27µm from the sample-Bakelite boundary. This is contrasted with the same view of the AISI 4330 wear scar which does not show such areas of interest (Figure 5.17(b)).
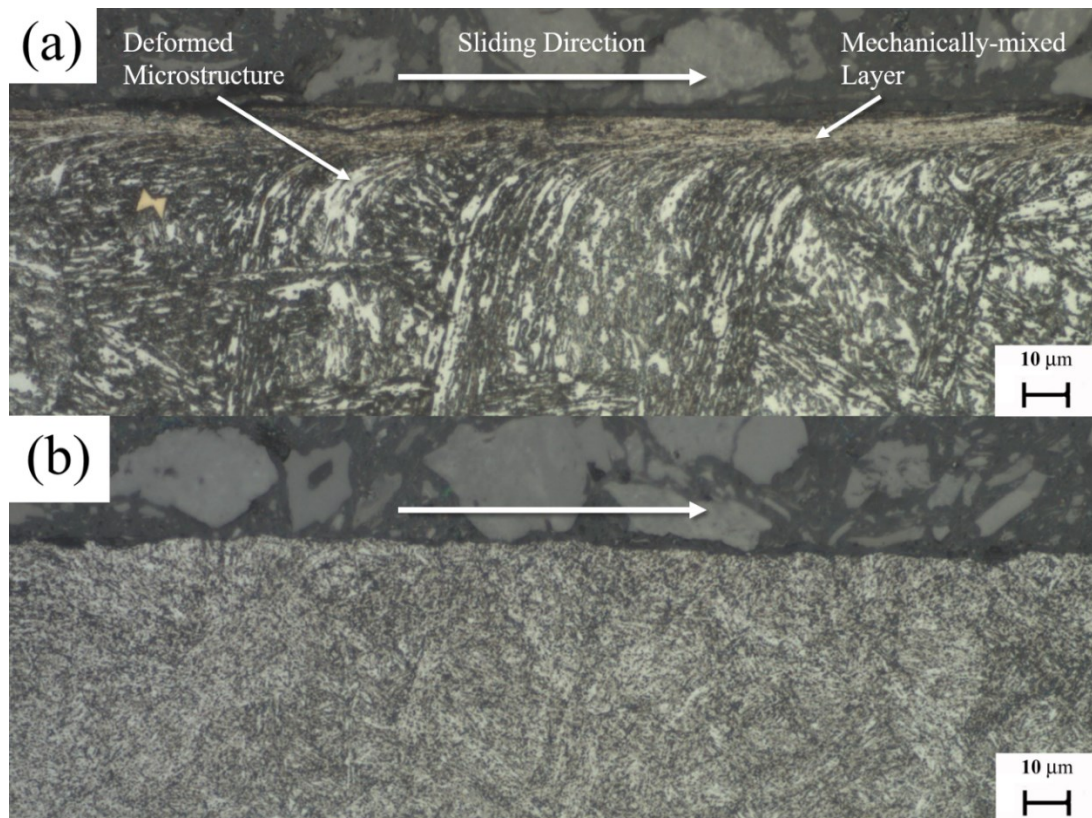
Figure 5.17 – Optical micrograph of longitudinal section of (a) AISI 4330 and (b) 15-5PH dry disc wear scars from loads 6kg [x500 – etched].

5.3.7.   Pin Immersion Corrosion Test

Mass changes from the immersion corrosion tests are shown in Table 5.4. In most cases, the samples gained mass from the adherence of corrosion products to the shaft of the pin. The overall mass change indicates the difference between the initial mass of the sample and the mass of the sample after both corrosion exposure and the post-test pickling treatment.

Table 5.4 - Mass losses from immersion corrosion tests.

Test Number	Mass Change from Corrosion (g)	Mass Change Overall (g)
1	0.0004	0.0066
2	-0.0002	0.0103
3	0.0009	0.0063
4	0.0009	0.0092
Average	0.0005	0.0081
Volume Loss (mm^3)	**-**	**0.1110**

5.4.   Discussion

5.4.1.   Categorisation of Wear Regime

The volume losses of the dry 15-5PH tests are an order of magnitude higher than the 15-5PH tests in NaCl, and more than triple the wear of the dry AISI 4330 tests (Figure 5.3). This difference is attributed to the dry 15-5PH tests being the only combination to be visually categorised as severe according to the convention established by Archard and Hirst [5.26]. Apart from the higher volume loss values and the rougher, brighter appearance of the dry 15-5PH discs (Figure 5.5), another indicator of severe wear is the increased depth of their cross-sectional profiles (Figure 5.10). As the 15-5PH discs are stainless steel, they do not possess the chemical-oxidational properties required to form uniform beneficial iron oxide layers like AISI 4330, and thus result in severe wear.

The dry 15-5PH discs do show evidence of local oxidative reactions occurring however, as they exhibit a ~1mm wide oxide band circumferentially through the scar (Figure 5.5). This oxide band is derived from the oxidational asymmetry between the 15-5PH disc and cast iron pin. As cast iron is highly reactive [5.27]–[5.29], it allows

the pin to oxidise due to the frictional heat output produced by sliding. These oxides can then be transferred to the 15-5PH disc surface. Due to only the pin readily oxidising and not the disc, the oxide band covers a small width of the disc wear scar (Figure 5.14, Table 5.2). It is postulated that the frictional work input to the contact faces is only high enough to cause oxidation at the centreline of the pin where maximum contact occurs. This is in agreement with the photographs taken by Quinn [5.30] showing the local hotspots to be near the middle of the pin.

The discs tested in NaCl solution do not subscribe to the mild/severe dichotomy due to them being submerged tests, however, volume loss values (low) and wear scar morphology (surface polishing with little matrix damage) approximate them as "mild".

5.4.2.   Influence of Dry Oxidation

AISI 4330 outperforms 15-5PH in the dry regime (Figure 5.3) due to the ease at which protective oxide layers form. Alloy steels and cast irons have a large advantage over stainless steels in this regard, due to their tendency for most of their surface oxides to be iron based. It has been previously noted [5.18], [5.31] that the passive chromium oxide layer on stainless steels grows slower than the iron oxide layers on alloy steels due to the lower parabolic growth rate of Cr_2O_3 compared to iron oxides. During the running-in period of the two combinations, both AISI 4330 and cast iron rapidly increase the growth of their oxide layers due to frictional flash temperatures and bulk temperature increases. In addition to the adhered surface oxides, any detached particles trapped in the wear scar also oxidise and mix into the surface layers. This allows the oxides to become mechanically mixed and increase in thickness, protecting them from further matrix wear. Conversely, 15-5PH differs in sliding due to the lower parabolic growth rate of chromium oxide. During the running-in period, high flash temperatures still arise but the accompanying growth acceleration is minimised due to the lower initial growth rates of Cr_2O_3. If each rotation of the disc removes a layer of particles from the contact area, then each revolution requires a new passive film to form, and if this is not faster than the time for one rotation then a protective layer is unable to build up. This mechanism of combined wear-oxidation is referred to by Hutchings and Shipway [5.32] as *oxidation – scrape – re-oxidation* [5.33].

Stainless steels form a chromium oxide (Cr_2O_3) surface film which protects the metal due to its electrochemical stability and low solubility. When this chromia film is damaged, a mixed layer of Cr_2O_3 and a spinel group oxide of iron-chromium-oxygen (chromate (III), $FeCr_2O_4$) [5.34] is formed due to local chromium depletion at the surface of the metal [5.35]. This combined Cr_2O_3 and $FeCr_2O_4$ layer is likely to be less effective than a surface layer of only iron oxides, both due to the slower growth of Cr_2O_3, and the likelihood that $FeCr_2O_4$ and Cr_2O_3 do not compact together effectively like iron oxides do. This conclusion is drawn based on observations by Guo et al. [5.36] that Cr_2O_3 is tougher and denser than iron oxides such as Fe_2O_3. In sliding contexts, the slower growth of chromium oxide layers and postulated ineffectiveness of the spinel oxides to mix effectively are jointly responsible for the inability of the 15-5PH discs to wear oxidatively. Further work should be conducted on the sliding properties of $FeCr_2O_4$.

5.4.3.   *Influence of NaCl solution*

The discs tested in NaCl solution produced lower volume loss values than the dry discs (Figure 5.3). This indicates that the NaCl solution gave a greater beneficial effect than detrimental effect versus the dry sliding tribosystem. It is suggested that the 3.5wt% NaCl solution is not corrosive enough to establish a severe tribocorrosive environment (strength and exposure time (lack of any pitting)) and instead reduces the metal-to-metal contact observed in the dry sliding regime. Water is a poor lubricant versus traditional chemicals such as grease or oil [5.37] but offers a small advantage versus the dry regime. It is also postulated that the NaCl solution mitigates detrimental effects seen in dry sliding, such as thermal softening caused by frictional input. The lack of visible corrosion attack is in agreement with Guo et al. [5.36] who noted that 15-5PH has good stress corrosion cracking resistance in NaCl solution.

Figure 5.3 shows that in the dry regime, AISI 4330 has lower volume losses than 15-5PH, but in the NaCl regime this ranking is inverted. This is attributed to a negation of high temperature dry oxidative wear and the effects of synergistic tribocorrosion on the AISI 4330 discs. Dry sliding wear produces unexpectedly high flash temperatures between the contact faces [5.30], [5.31], [5.33], [5.38]–[5.41], and this phenomenon greatly contributes towards beneficial dry oxidative wear for active alloys such as AISI 4330. In the dry regime, AISI 4330 performs more favourably than 15-5PH due to this phenomenon which is readily visible in the disc macro images

(Figure 5.5). In the NaCl regime, the circulating fluid remained consistently at room temperature and was therefore a coolant in addition to being a corrosive medium. The inhibition of flash temperatures and reduced frictional heat rises in the fluid compared to air, prevented high temperature oxidation from occurring, resulting in an increase of AISI 4330 wear relative to the 15-5PH disc. This was observed in the wear scars post-NaCl test (Figure 5.7), where the scars appeared bright and reflective as opposed to the dry tests which were covered in oxides. Moreover, AISI 4330 wore more than 15-5PH in the NaCl regime due to the increased contribution of corrosion to the tribocorrosive synergy. AISI 4330 is a low alloy steel so therefore has a higher susceptibility to the corrosive effects of the NaCl solution than 15-5PH does.

In contrast, both NaCl pin combinations have higher volume loss values than their corresponding dry combinations (Figure 5.4). This may be attributed to the volume lost from corrosion of the pin shafts. Approximately 40mm of the pin was submerged in the circulating NaCl solution causing the shaft of the pin to form the adhered layer of corrosion products (Figure 5.9). This may have increased the volume loss values of the pin, as the corrosion products were removed through the post-test pickling. The NaCl pin values are therefore comparable only to each other (because approximately the same shaft length of each pin was exposed) but not to the dry values. In future work, this should be minimised by using a sleeve to only expose the lower millimetre of the pin shaft, with care taken not to interfere with the contact face.

However, the immersion corrosion results (Table 5.4) show that the mass and volume changes from corrosion exposure, and from the post-test pickling, are insignificant in comparison to the pin sliding wear volume losses. The ratio of the mass change from corrosion to the overall mass change, also indicates that significantly more material is removed from the pickling process than is gained from the corrosion exposure, and the pickling thus removes excess metallic material in addition to the adhered corrosion products, despite the use of hexamethylene tetramine to stop metallic attack. This indicates that the higher volume losses of the pins tested in NaCl solution are due to the tribocorrosive wear occurring at the contact face. It should be noted, however, that the immersion corrosion tests were not a perfect simulation of the corrosion happening during the pin-on-disc tests. The immersion tests were missing the galvanic action between the samples, and the NaCl solution used in the immersion tests was not subject to fast rotation, which López-Ortega et al. [5.21] found was a large

contribution to corrosion. The shaft corrosion occurring during the pin-on-disc test may therefore be greater than that of the immersion corrosion tests. Due to the pickling also having the unintended side effect of attacking and etching the contact face, further inspection of the NaCl pin worn surface to investigate wear mechanisms was hindered.

5.4.4.   Influence of Load

The volume loss values of the discs tested in NaCl solution level off for the 15-5PH disc and decrease for the AISI 4330 disc between 4kg and 6kg (Figure 5.3). This change is accredited to a reduction of tribocorrosive synergism between the samples and the NaCl solution. It is well documented [5.3], [5.14]–[5.16] that wear and corrosion operate in synergy, with one mechanism influencing the other. This synergism is discussed by Kato [5.3], who notes that the input of kinetic energy increases the rate of chemical reactions on the surface of materials. Such kinetic energy inputs cause the emission of charged particles, superheated states of matter, electrostatic shocks, exposure of new fracture planes, and local flash temperature rises [5.3]. These changes are introduced from the mechanical damage caused by sliding, which then influence the rate of corrosion occurring. The corrosion then affects the aforementioned wear outputs, resulting in a synergism between the two mechanisms. In this case, it is postulated that a reduction of this synergistic effect is responsible for the change in volume loss values for the 6kg load. At this value, the increased load may prevent the NaCl solution from penetrating the contact area as effectively as at lighter loads, and thereby reduces the tribocorrosive effect of the system. This does not agree with results obtained by Zhang et al. [5.20] who found that increasing load led to more damage of the passive film and thus greater tribocorrosive potential. However, their study [5.20] used higher applied loads on average, and this effect may only be seen at loads higher than that used presently.

Another noteworthy aspect of Figure 5.4 is the differing gradients of the dry pin volume losses. Both dry pin combinations increase linearly with load, however the pin worn against AISI 4330 increases at a lesser gradient than the pin worn against 15-5PH. This is also ascribed to the formation of the oxide layer which shields the underlying matrix from severe wear. Both sets of pins exhibit signs of oxidation (Figure 5.6), however due to both AISI 4330 and its cast iron pin readily oxidising, such combinations show a much thicker and wider coverage than on the pin worn against 15-5PH. In this instance, it is suggested that the applied loads of 2kg, 4kg, and

6kg are not distinct enough to cause large differences in volume loss. The establishment and wearing of the oxide surface layer is essentially the same at each load, resulting in smaller wear increases at each load compared to 15-5PH, and thus a shallower slope. It is expected that this trend will continue with the same gradient until the oxide layer is breached, causing a transition into the severe wear regime, either through increases of load or speed. Conversely, for the dry pins worn against 15-5PH, each applied load results in a higher proportional increase in volume loss due to more mechanical damage occurring.

Both pins tested in NaCl experience similar volume loss values at 2kg and 6kg but deviate at 4kg. This deviance at 4kg load is ascribed to experimental error, as the standard deviations are larger for the NaCl pins than the dry pins. These large scatters are thought to be due to slight differences in the length of shaft exposed to the surrounding NaCl solution, which affected the height of corrosion on the shaft (Figure 5.9). If the pin happened to be placed lower in the collet, more shaft area would be exposed, causing more corrosion, and therefore a higher volume loss value.

5.4.5.   *Influence of Microstructure*

The 15-5PH discs form a mechanically mixed surface layer and display distorted grains in the direction of sliding, whereas the AISI 4330 discs do not (Figure 5.17). This contrast is attributed to different mechanical and thermal properties of the two alloys. Mechanically, the elongation value of 15-5PH is approximately 50% higher than AISI 4330 [5.42], allowing for easier grain distortion resulting in visible strain. Thermally, it is postulated that the 15-5PH softens more due to the lack of iron oxide build-up, causing a greater sensitivity to flash temperatures. In contrast, the AISI 4330 discs are somewhat insulated from thermal input by their protective oxide layer. The value of thermal conductivity for 15-5PH is less than half that of AISI 4330 [5.43], meaning any heat built up between the contact faces takes longer to dissipate into the bulk structure and thus affects the grains near the surface more. The boundary between the mechanically mixed layer and the distorted grains beneath, are known to be weak structural areas where cracks initiate before fracturing [5.44]. This also contributes to the higher dry volume loss values for the 15-5PH over AISI 4330, as the AISI 4330 discs did not experience such stress concentrations in their microstructure.

It has been noted by Wang et al. [5.39] that the hardness of martensite begins to decrease at 200°C, which is below the estimated flash temperature for dry pin-on-disc sliding in the present study. A measurement of the local hot spots through use of thermal imaging by Quinn [5.30] resulted in approximate values of 950°C for a steel pin sliding at approximately 2m/s. Wang and Zhao [5.44] also suggested that surface oxides can only provide protection to the underlying metal matrix if the metal has sufficient stiffness to support the oxide above. As the 15-5PH substrate thermally softens, it may not be rigid enough to structurally support the oxides, reducing its oxidative protection. It is then postulated that any oxides become compacted into the mechanically mixed layer instead. Huttunen-Saarivirta et al. [5.19] also noted that heterogeneous martensitic microstructures result in weaker passive films on the surface. 15-5PH features an acicular lath martensitic microstructure, whereas AISI 4330 features a more homogeneous tempered martensitic microstructure. Applying the conclusions of Huttunen-Saarivirta et al. [5.19], it can be expected that the 15-5PH passive film is more discontinuous and therefore results in more wear than AISI 4330.

Many uncertainties of the present study result from the use of cast iron as the pin material. Cast iron exhibits inherent microstructural variation through the unique presence of graphite flakes (Figure 5.1). Graphite in cast irons is variable in its morphology (size, shape, and distribution) throughout the matrix. This introduces uncertainty in the pin-on-disc tests due to graphite influencing friction and wear [5.45]–[5.49]. A study by Ghasemi and Elmquist [5.50] found that the orientation of graphite flakes throughout the matrix influenced the graphite film formation. It was noted that flakes at angles perpendicular to the sliding direction were most suited to supplying lubricative graphite to the surface. Applied to the present study, these conclusions may be relevant in producing large standard deviation values if certain pins possess unevenly distributed graphite. Indeed, microstructural characterisation of the cast iron pins showed certain regions of much finer graphite than that most commonly seen. The applied loads of the present study may also have been too great for favourable graphite film formation, as Adachi et al. [5.51] found 15N to be the optimum load.

The pin samples were heat treated to achieve a martensitic matrix (Figure 5.1(b)) but were not held at temperature for any significant length of time, so the graphite flakes remained unaffected. Any abnormal morphology of the graphite therefore remained

constant through the process. The cast iron samples were turned down from the as-cast 38mm billet to the 6mm pins used in the sliding wear tests. This was the optimum manufacturing method for reproducibility, as the graphite at the centre of the billet behaves more consistently. Little evidence of graphite solid lubrication was observed on the samples post-test, so graphite could have either been mixed in with the surface oxides, swept away by the corrosive media in the NaCl regime, or removed through post-test cleaning. The contribution of graphite to the sliding wear behaviour is therefore unknown. Sugishita and Fujiyoshi [5.52]–[5.54] noted that with increasing matrix hardness, graphite film production decreases due to an inability of the matrix to allow graphite to be sheared out in a productive manner. As the pins used in the present study were heat treated to a hardness of 400HV, the graphite flakes could have been expelled in fragments, inhibiting them from forming a protective film.

5.5.   Conclusions

The present study examined the influence of applied load on the volume loss of 15-5PH, AISI 4330, and heat treated G350 cast iron in the dry and NaCl sliding regimes. From the experimental results and corresponding analysis, the following conclusions can be drawn:

- Disc volume losses were higher in the dry regime than in the NaCl regime. This is attributed to the slight lubricative effect of the solution, as well as hard particles being removed from the system by the flowing solution.

- The inclination or disinclination of the alloys to oxidise influenced the volume losses. AISI 4330 outperformed 15-5PH in the dry regime where frictional heating and iron oxides abound but was outperformed by 15-5PH in the NaCl regime where these advantages disappear.

- In the NaCl regime, both discs experience a reduction in volume loss at 6kg applied load. This is due to the highest mass reducing the synergistic effect of corrosion to the combined tribocorrosive regime compared to the lighter loads.

- Microstructural inspection of the 15-5PH wear scar cross-sections showed a mechanically mixed layer on top of plastically distorted grains in the direction

of sliding. AISI 4330 exhibited no such microstructural alterations. The presence of these features in the 15-5PH discs is accredited to a higher elongation value and lower thermal conductivity, resulting in increased plasticity and more thermal softening.

- The shafts of the cast iron pins corroded during the NaCl tests. This therefore stopped a direct comparison between the volume loss values of the dry and NaCl values.

References

[5.1] M. Kerridge and J. K. Lancaster, "The stages in a process of severe metallic wear," *Proc. R. Soc. A Math. Phys. Eng. Sci.*, vol. 236, no. 1205, 1956.

[5.2] I. Hutchings and P. Shipway, "Fundamentals of corrosion and tribocorrosion," in *Tribology*, 2nd ed., 2017, p. 1.

[5.3] K. Kato, "Wear modes at asperity contacts in tribochemical wear," in *Tribocorrosion of Passive Metals and Coatings*, 2011, p. 79.

[5.4] W. Hirst and J. K. Lancaster, "Surface film formation and metallic wear," *J. Appl. Phys.*, vol. 27, no. 9, pp. 1057–1065, 1956.

[5.5] F. H. Stott, "The role of oxidation in the wear of alloys," *Tribol. Int.*, vol. 31, no. 1–3, pp. 61–71, 1998.

[5.6] S. C. Lim, "The relevance of wear-mechanism maps to mild-oxidational wear," *Tribol. Int.*, vol. 35, pp. 717–723, 2002.

[5.7] T. F. J. Quinn, D. M. Rowson, and J. L. Sullivan, "Application of the oxidational theory of mild wear to the sliding wear of low alloy steel," *Wear*, vol. 65, no. 1, pp. 1–20, 1980.

[5.8] T. C. Zhang, X. X. Jiang, S. Z. Li, and X. C. Lu, "A Quantative estimation of the synergy between corrosion and abrasion," *Corros. Sci.*, vol. 36, no. 12, pp. 1953–1962, 1994.

[5.9] X. X. Jiang, S. Z. Li, D. D. Tao, and J. X. Yang, "Accelerative effect of wear on corrosion of high-alloy stainless steel," *Corrosion*, vol. 49, no. 10, pp. 536–841, 1993.

[5.10] B. W. Madsen and T. A. Adler, "Passivation and repassivation kinetics of iron-aluminum alloys in 1 N H2SO4 using potential step and scratch tests," *Wear*, vol. 171, no. 1–2, pp. 215–225, 1994.

[5.11] F. H. Stott, J. E. Breakell, and R. C. Newman, "The corrosive wear of cast iron under potentiostatically-controlled conditions in sulphuric acid solutions," *Corros. Sci.*, vol. 30, no. 8–9, pp. 813–830, 1990.

[5.12] I. García, D. Drees, and J. P. Celis, "Corrosion-wear of passivating materials in sliding contacts based on a concept of active wear track area," *Wear*, vol. 249, no. 5–6, pp. 452–460, 2001.

[5.13] P. Ponthiaux, F. Wenger, D. Drees, and J. P. Celis, "Electrochemical techniques for studying tribocorrosion processes," *Wear*, vol. 256, no. 5, pp. 459–468, 2004.

[5.14] S. Mischler, "Triboelectrochemical techniques and interpretation methods in tribocorrosion: A comparative evaluation," *Tribol. Int.*, vol. 41, no. 7, pp. 573–583, 2008.

[5.15] S. W. Watson, F. J. Friedersdorf, B. W. Madsen, and S. D. Cramer, "Methods of measuring wear-corrosion synergism," *Wear*, vol. 181–183, no. PART 2, pp. 476–484, 1995.

[5.16] D. Landolt, S. Mischler, and M. Stemp, "Electrochemical methods in tribocorrosion: A critical appraisal," *Electrochim. Acta*, vol. 46, no. 24–25, pp. 3913–3929, 2001.

[5.17] S. Virtanen, "Passivity of Metals and Alloys," in *Tribocorrosion of Passive Metals and Coatings*, 1st ed., D. Landolt and S. Mischler, Eds. Woodhead Publishing, 2011, p. 12.

[5.18] G. Rasool and M. M. Stack, "Mapping the role of Cr content in dry sliding of steels: Comparison between maps for material and counterface," *Tribol. Int.*, vol. 80, pp. 49–57, 2014.

[5.19] E. Huttunen-Saarivirta, L. Kilpi, T. J. Hakala, L. Carpen, and H. Ronkainen, "Tribocorrosion study of martensitic and austenitic stainless steels in 0.01 M NaCl solution," *Tribol. Int.*, vol. 95, pp. 358–371, 2016.

[5.20] B. Zhang, J. Wang, Y. Zhang, G. Han, and F. Yan, "Comparison of tribocorrosion behavior between 304 austenitic and 410 martensitic stainless steels in artificial seawater," *RSC Adv.*, vol. 6, no. 109, pp. 107933–107941, 2016.

[5.21] A. López-Ortega, J. L. Arana, and R. Bayón, "On the comparison of the tribocorrosion behavior of passive and non-passivating materials and assessment of the influence of agitation," *Wear*, vol. 456–457, no. February, 2020.

[5.22] P. J. Blau, "An editor's perspective on the quality and content of wear research manuscripts," *Wear*, vol. 426–427, no. August 2018, pp. 1384–1390, 2019.

[5.23] BSI Standards Online, "BS EN ISO 945-1:2019 BSI Standards Publication: Microstructure of cast irons," 2019.

[5.24] ASTM Standards, "ASTM G99 - 17: Standard Test Method for Wear Testing with a Pin-on-Disk Apparatus."

[5.25] ASTM Standards, "ASTM G1 - 03: Standard Practice for Preparing, Cleaning, and Evaluating Corrosion Test Specimens."

[5.26] J. F. Archard and W. Hirst, "The wear of metals under unlubricated conditions," *Proc. R. Soc. Lond. A.*, vol. 236, 1956.

[5.27] M. W. Shin, K. H. Cho, S. J. Kim, and H. Jang, "Friction instability induced by corrosion of gray iron brake discs," *Tribol. Lett.*, vol. 37, no. 2, pp. 149–157, 2010.

[5.28] P. J. Blau, J. J. Truhan, and E. A. Kenik, "Effects of the exposure to corrosive salts on the frictional behavior of gray cast iron and a titanium-based metal matrix composite," *Tribol. Int.*, vol. 40, no. 9, pp. 1335–1343, 2007.

[5.29] A. Igual Muñoz and N. Espallargas, "Tribocorrosion mechanisms," in *Tribocorrosion of Passive Metals and Coatings*, 1st ed., D. Landolt and S. Mischler, Eds. Woodhead Publishing, 2011, pp. 121–136.

[5.30] T. F. J. Quinn and W. O. Winer, "The thermal aspects of oxidational wear," *Wear*, vol. 102, no. 1–2, pp. 67–80, 1985.

[5.31] F. H. Stott and G. C. Wood, "The influence of oxides on the friction and wear of alloys," *Tribol. Int.*, vol. 11, no. 4, pp. 211–218, 1978.

[5.32] I. Hutchings and P. Shipway, "Oxidative Wear," in *Tribology: Friction and Wear of Engineering Materials*, 2nd ed., Butterworth - Heinemann, 2017, p. 127.

[5.33] I. Hutchings and P. Shipway, "Plasticity-dominated wear," in *Tribology*, 2nd ed., Elsevier Ltd., 2017, pp. 122–125.

[5.34] C. W. Yang, J. H. Kim, R. E. Triambulo, Y. H. Kang, J. S. Lee, and J. W. Park, "The mechanical property of the oxide scale on Fe-Cr alloy steels," *J. Alloys Compd.*, vol. 549, pp. 6–10, 2013.

[5.35] R. E. Smallman and A. H. W. Ngan, "Oxidation Resistance - Alloying," in *Modern Physical Metallurgy*, 2014, p. 628.

[5.36] Q. Guo, J. Liu, M. Yu, and S. Li, "Effect of passive film on mechanical properties of martensitic stainless steel 15-5PH in a neutral NaCl solution," *Appl. Surf. Sci.*, vol. 327, pp. 313–320, 2015.

[5.37] G. W. Stachowiak and A. W. Batchelor, "Emulsions and Aqueous Lubricants," in *Engineering Tribology*, 2014, p. 67.

[5.38] S. C. Lim, M. F. Ashby, and J. H. Brunton, "Wear-rate transitions and their relationship to wear mechanisms," *Acta Metall.*, vol. 35, no. 6, pp. 1343–1348, 1987.

[5.39] Y. Wang, T. Lei, and J. Liu, "Tribo-metallographic behavior of high carbon steels in dry sliding II. Microstructure and wear," *Wear*, vol. 231, no. 1, pp. 12–19, 1999.

[5.40] Y. Wang, T. Lei, and J. Liu, "Tribo-metallographic behavior of high carbon steels in dry sliding III. Dynamic microstructural changes and wear," *Wear*, vol. 231, no. 1, pp. 20–37, 1999.

[5.41] B. K. Prasad, "Sliding wear response of a grey cast iron: Effects of some experimental parameters," *Tribol. Int.*, vol. 44, no. 5, pp. 660–667, 2011.

[5.42] Granta Design, "CES Edupack - AISI 4330." Ansys, 2019.

[5.43] Granta Design, "CES Edupack - 15-5PH H1075." Ansys, 2019.

[5.44] S. Q. Wang, M. X. Wei, and Y. T. Zhao, "Effects of the tribo-oxide and matrix on dry sliding wear characteristics and mechanisms of a cast steel," *Wear*, vol. 269, no. 5–6, pp. 424–434, 2010.

[5.45] A. Hase, "Visualization of the tribological behavior of graphite in cast iron by in situ observations of sliding interfaces," *Tribol. Int.*, vol. 138, no. March, pp. 40–46, 2019.

[5.46] R. S. Montgomery, "The mild wear mechanism of nodular iron," *Wear*, vol. 13, no. 4–5, pp. 337–343, 1969.

[5.47] G. Straffelini, C. Giuliari, M. Pellizzari, E. Veneri, and M. Bronzato, "Dry rolling-sliding wear of austempered cast iron," *Wear*, vol. 271, no. 9–10, pp. 1602–1608, 2011.

[5.48] M. Terheci, R. R. Manory, and J. H. Hensler, "The friction and wear of automotive grey cast iron under dry sliding conditions Part 1-relationships between wear loss and testing parameters," *Wear*, vol. 180, no. 1–2, pp. 73–78, 1995.

[5.49] I. Hutchings and P. Shipway, "Friction of Lamellar Solids," in *Tribology: Friction and Wear of Engineering Materials*, 2nd ed., Elsevier, 2017, pp. 63–65.

[5.50] R. Ghasemi and L. Elmquist, "The relationship between flake graphite orientation, smearing effect, and closing tendency under abrasive wear conditions," *Wear*, vol. 317, no. 1–2, pp. 153–162, 2014.

[5.51] K. Adachi, U. Cho, S. K. Sinha, and K. Kato, "Self-lubrication by formation of graphite films in the sliding of silicon nitride against cast iron," *Tribol. Trans.*, vol. 44, no. 1, pp. 41–46, 2001.

[5.52] J. Sugishita and S. Fujiyoshi, "The effect of cast iron graphites on friction and wear performance I: Graphite film formation on grey cast iron surfaces," *Wear*, vol. 66, no. 2, pp. 209–221, 1981.

[5.53] J. Sugishita and S. Fujiyoshi, "The Effect of Cast Iron Graphites on Friction and Wear Performance II: ariables influencing graphite film formation," *Wear*,

vol. 68, no. 1, pp. 7–20, 1981.

[5.54] J. Sugishita and S. Fujiyoshi, "The effect of cast iron graphite on friction and wear performance III: The lubricating effect of graphite under rolling-sliding contacts," *Wear*, vol. 77, no. 2, pp. 181–193, 1982.

Chapter 6.

Sliding Wear of Cementite-spheroidised Grey Cast Iron

Abstract

The sliding wear properties of G350 grey cast iron following various spheroidising annealing durations are discussed herein. The spheroidised samples were used as pins in sliding wear tests against AISI 4330 discs. Most testing combinations resulted in mild wear with little matrix damage to the cast iron pin or AISI 4330 disc. A transition to severe wear was observed for the highest load and longest annealing times where the overly spheroidised and ferritised cast iron matrix deformed significantly, prohibited beneficial oxidative wear from occurring, and thus damaged its disc counterpart. The depth of subsurface deformation increased with annealing time but not load. Instead, the depth peaked at 4kg applied load for each condition due to the spallation of the affected surface layer at the higher load.

6.1.   Introduction

Despite the favourable casting properties of grey cast irons [6.1], [6.2], machining is a critical manufacturing step of many components [6.3]. Numerous industrial parts are machined entirely from billets of continuously cast alloys. Others are cast into component shape and undergo machining to achieve final dimensions and produce acceptable surface finishes [6.4]. This step is necessary in the manufacture of wear components such as pump slipper pads or disc brake components that require certain roughness values. However, machining can be time consuming and expensive [6.2], especially for parts machined from solid billets.

For highly alloyed material such as tool steels [6.5], machining difficulties are alleviated through the application of subcritical annealing heat treatments [6.6], [6.7]. This subcritical soak provides the thermal energy to allow for the rearrangement of cementite lamellae into spherical carbides dispersed throughout a ferritic matrix, or to migrate towards graphite flakes in cast irons. Such rearrangements increase plasticity through an increase of dislocation travel pathways, resulting in a softer, ductile material [6.8]. This reduction in hardness allows for easier machining to take place [6.5].

The tribological effects of subcritical annealing have been examined by Bhattacharya [6.9], who found that, in mild wear regimes, the spheroidised structure showed similar wear rates to the pearlitic structures. However, in the severe wear regime, as spheroidal carbide volume increased, abrasive wear took place, indicating that the carbide globules could act as hard particles [6.9]. Wang et al. [6.10] studied the tribological properties of eutectoid steels in the pearlitic and spheroidised condition and reported that both conditions formed the same polycrystalline white surface layer during sliding. They [6.10] also noted that near the surface, in the pearlitic condition, cementite deformed towards the sliding direction and eventually fractured. However, the carbide nodules in the spheroidal condition remained structurally unaffected beneath the surface [6.10]. Fegredo et al. [6.11] examined the effects of spheroidisation on the wear rates of pearlitic railway steels. The study focussed on the average ferrite distance between the edges of carbides. The authors [6.11] noted that coarse pearlite and spheroidisation increased this length, which allowed for dislocations to move more freely, resulting in higher wear rates [6.11]. Diao et al.

[6.12] compared the wear resistance of three railway steels with different microstructures. The authors [6.12] postulated that brittle fracture results in higher mass losses in lamellar pearlitic structures than in spheroidal cementite structures, due to cracks being forced to take a, deeper route into the microstructure, perpendicular to the surface. Conversely, in spheroidal structures, cracks can travel parallel to the surface, resulting in smaller spallation. The thicker deformation layer of the spheroidised structure after sliding was also noted [6.12]. Zambrano et al. [6.13] compared the sliding properties of three steels (AISI 5160, AISI 1045 and AISI O1) with different microstructures but the same hardness value. The researchers [6.13] concluded that spheroidised cementite had higher wear losses than the pearlitic-ferritic and fully pearlitic microstructures. It was also observed that the spheroidised material had the greatest hardness increase from strain hardening, following sliding [6.13].

Few studies have investigated the influence of subcritical annealing on the microstructure of grey cast iron, and how this affects sliding wear properties at various loads. This is rectified through subjecting grey cast iron to three degrees of spheroidising heat treatments, then characterising their wear response using pin-on-disc testing with three applied loads. Additional inspection of the worn surfaces and characterisation of the microstructural changes is also included to provide an overall picture of the tribological behaviour of the alloy.

6.2.   Materials & Methods

6.2.1.   Materials

G350 cast iron pins and AISI 4330 discs were examined in the current investigation, with their nominal chemical composition shown in Chapter 3. AISI 4330 was chosen as the disc material to act as a hard ferrous alloy frequently seen in engineering applications such as gears, shafts, and axles [6.14].

Cast iron was received in the pearlitic condition with type I-A/C-5 graphite flakes in accordance with ISO 945 [6.15] as shown in Figure 6.1(a). Once machined, the pin samples were subcritically annealed at 700°C for three durations, resulting in four groups of samples with the following designations: AR (as-received), 5D (five days), 10D (ten days), and 15D (15 days). AISI 4330 was studied in the normalised,

quenched, and tempered condition (heated to 880°C; water quenched; tempered at 610°C; and air cooled), with a tempered martensitic microstructure (Figure 6.1(b)).
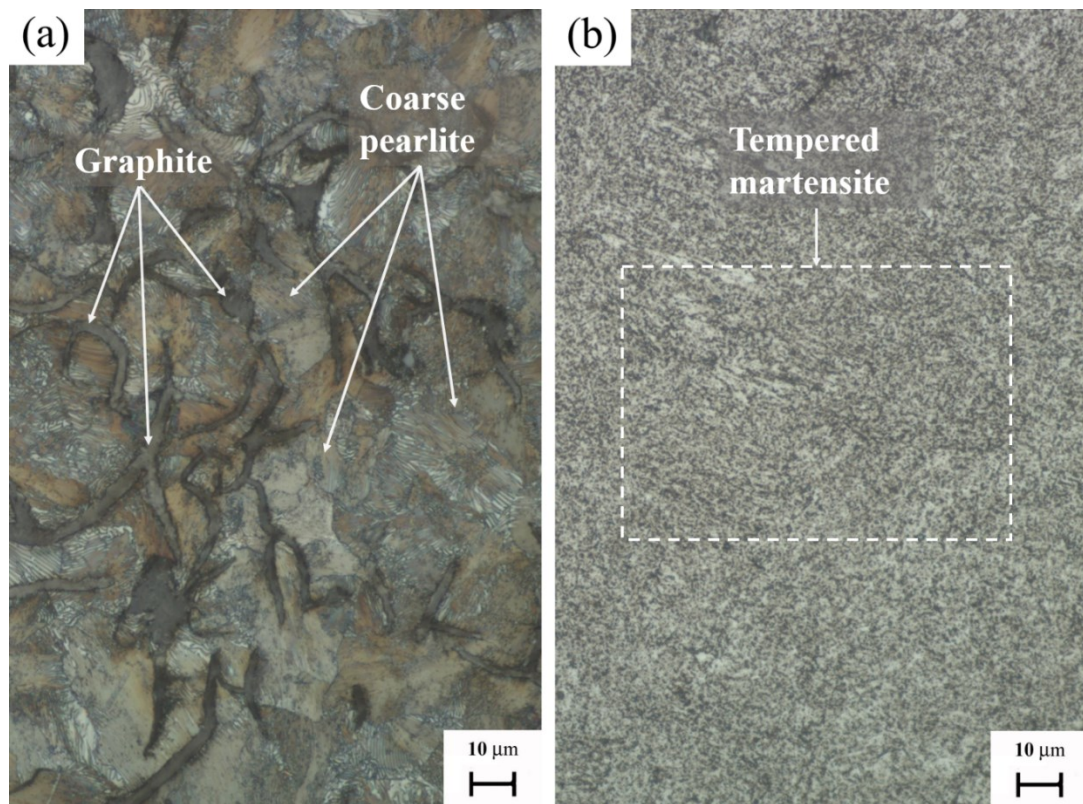

Figure 6.1 - Optical micrographs of the as-received microstructures of (a) G350 cast iron with coarse pearlitic matrix and fine graphite flakes (b) AISI 4330 low alloy steel with tempered martensitic matrix [x500 – nital].

6.2.2.   Methodology

Wear behaviour was examined using dry pin-on-disc sliding wear tests as described in Section 3.2.2, and followed the procedure of ASTM G99 [6.16]. Three loads of 2kg, 4kg, and 6kg were applied to the pin (19.62N, 39.24N, 58.83N (0.7MPa, 1.4MPa and 2.1MPa)) to explore the wear response for a range of conditions.

Other accompanying methods to further analyse the sliding wear response were utilised as described in Chapter 3.

6.3.   Results & Discussion

6.3.1.   Heat Treatment Evolution

Subcritical annealing of the cast iron resulted in coarsening, spheroidising, and ferritising of the initial pearlitic matrix (Figure 6.2). Cementite lamellae shortened and

coarsened with time into a globular spheroidised structure. Carbide aspect ratio decreased with time in a drive to reduce particle surface area.
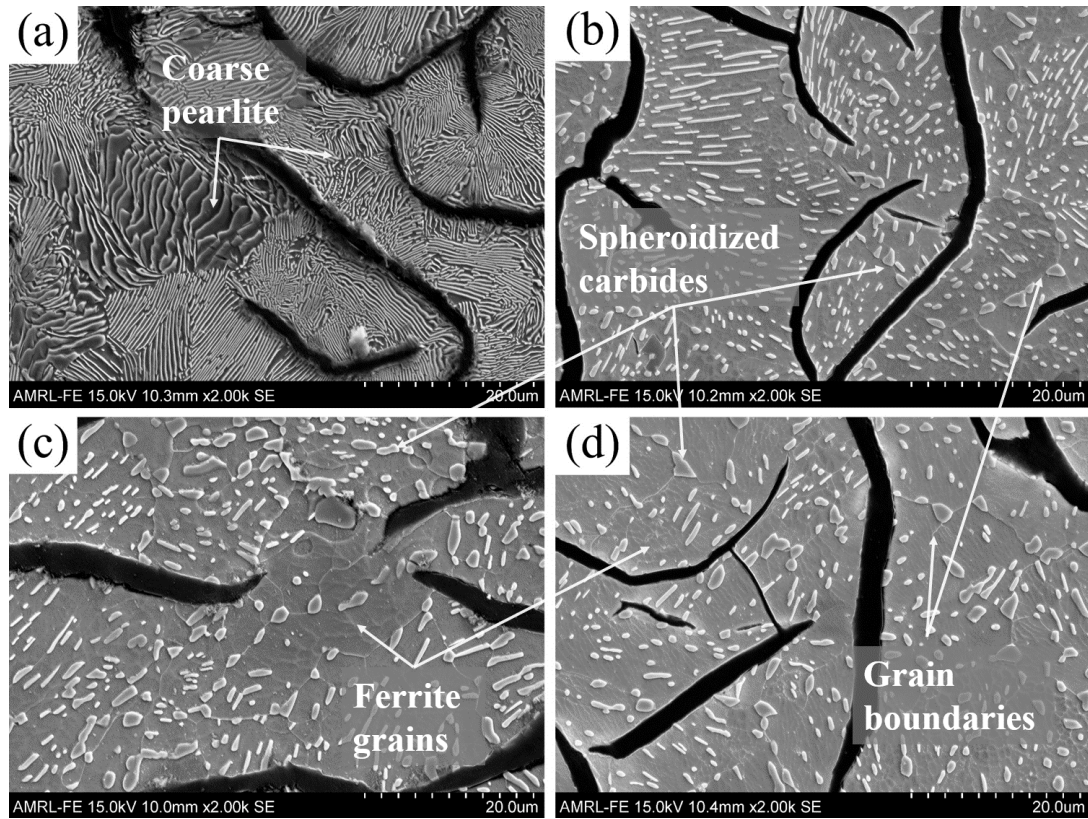

Figure 6.2 - SEM micrograph showing the cast iron pin microstructures of (a) group AR (b) group 5D (c) group 10D (d) group 15D [x2000 – nital].

Hardness measurements of the sliding wear samples (Figure 6.3) showed large differences between the AISI 4330 disc and the four G350 pin conditions. Hardness decreased with annealing time because of:

(a)   Carbide spheroidisation resulting in a greater mean free ferrite path [6.8] (Figure 6.2(b – d)).

(b)   Increased ferritisation of the matrix resulting in fewer carbide globules [6.17] (Figure 6.2(d)).

(c)   Ferrite grain growth allowing for increased dislocation slip [6.18] (Figure 6.2(c, d)).

AISI 4330 showed the highest hardness value due to its tempered martensitic matrix.
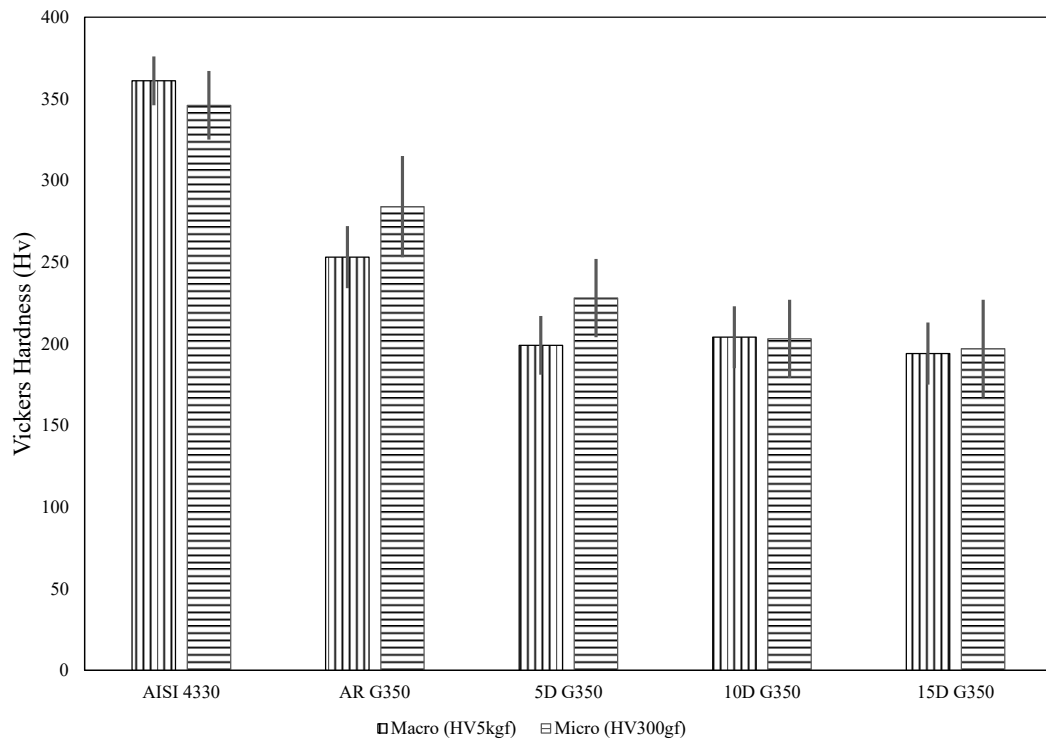

Figure 6.3 – Micro indentation and macro indentation hardness of the sliding wear materials. N = 10 for micro indentation hardness values and N = 5 for macro indentation hardness values.

6.3.2.   Sliding Wear Results

The AISI 4330 discs experienced significantly lower volume losses than the corresponding cast iron pins in most cases because of their harder martensitic matrix (Figures 6.3, 6.4, 6.5). For AR 4kg and AR 6kg, the higher disc volume losses were due to the pearlitic AR pins being harder than the three spheroidised pin conditions (Figure 6.3). Furthermore, a mismatch in volume losses appeared where the discs worn against AR pins experienced a large increase in volume loss but their corresponding AR pins did not. This discrepancy is attributed to the differing wear mechanisms of the AR pins vs. the AISI 4330 discs. In this case, the superior ductility of pearlite over martensite causes the mismatch – pearlite deforms significantly during sliding (see Section 6.3.4.) whereas martensite cannot. This resulted in higher volume loss values for the martensitic matrix as it fractured in a brittle manner and detached from the sample (see Section 6.3.3.).

Only the 5D pins produced mild wear for all loads on AISI 4330 discs (Figure 6.5). This is due to the 5D pins being softened enough not to damage the disc, while still being able to effectively oxidise at all loads. This is further discussed in Section 6.3.5.
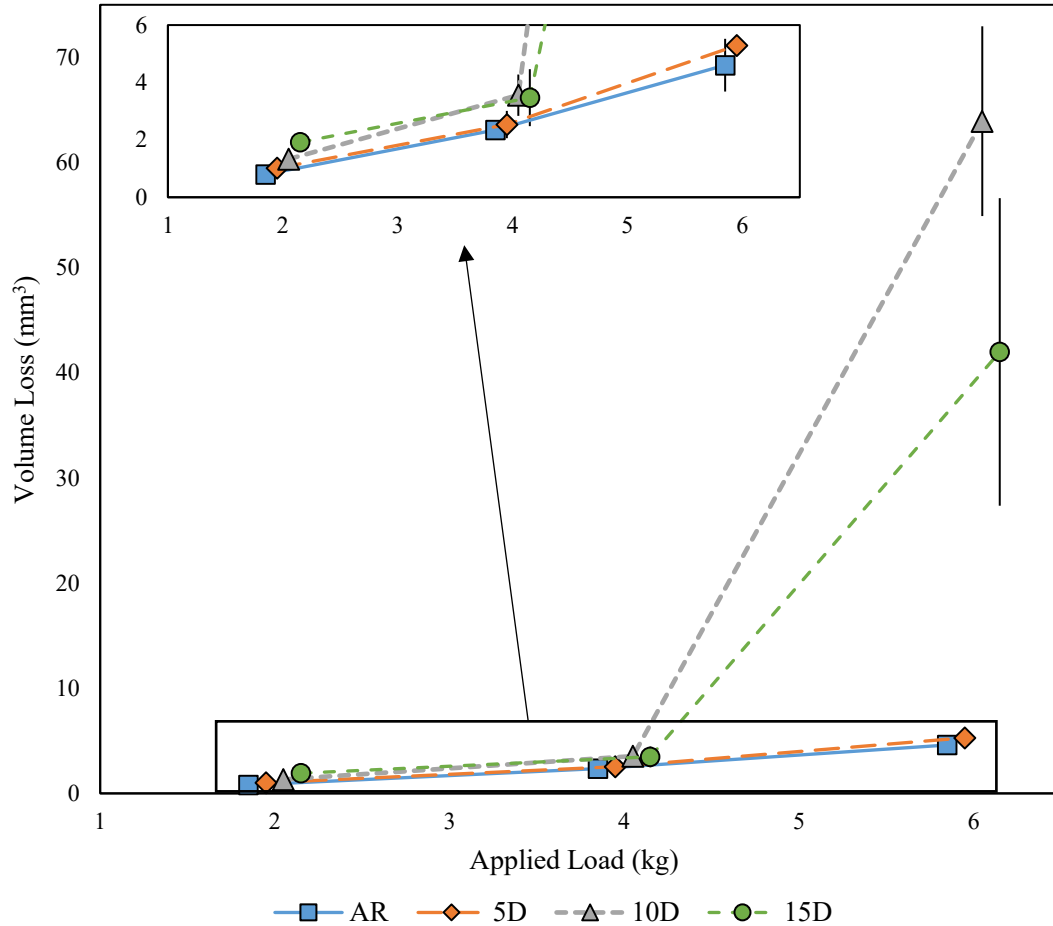

Figure 6.4 - Volume loss values of various degrees of cementite-spheroidised G350 cast iron pins from sliding against AISI 4330 discs. N = 3 for all tests.

The 10D 6kg and 15D 6kg pairs resulted in high volume losses because of the transition to severe wear for both disc and pin. In this context, severe wear arose as a result of (a) the overall pin microstructure softening through carbide spheroidisation and ferritisation, and (b) the enlargement of carbide globules which then act as abrasive particles.
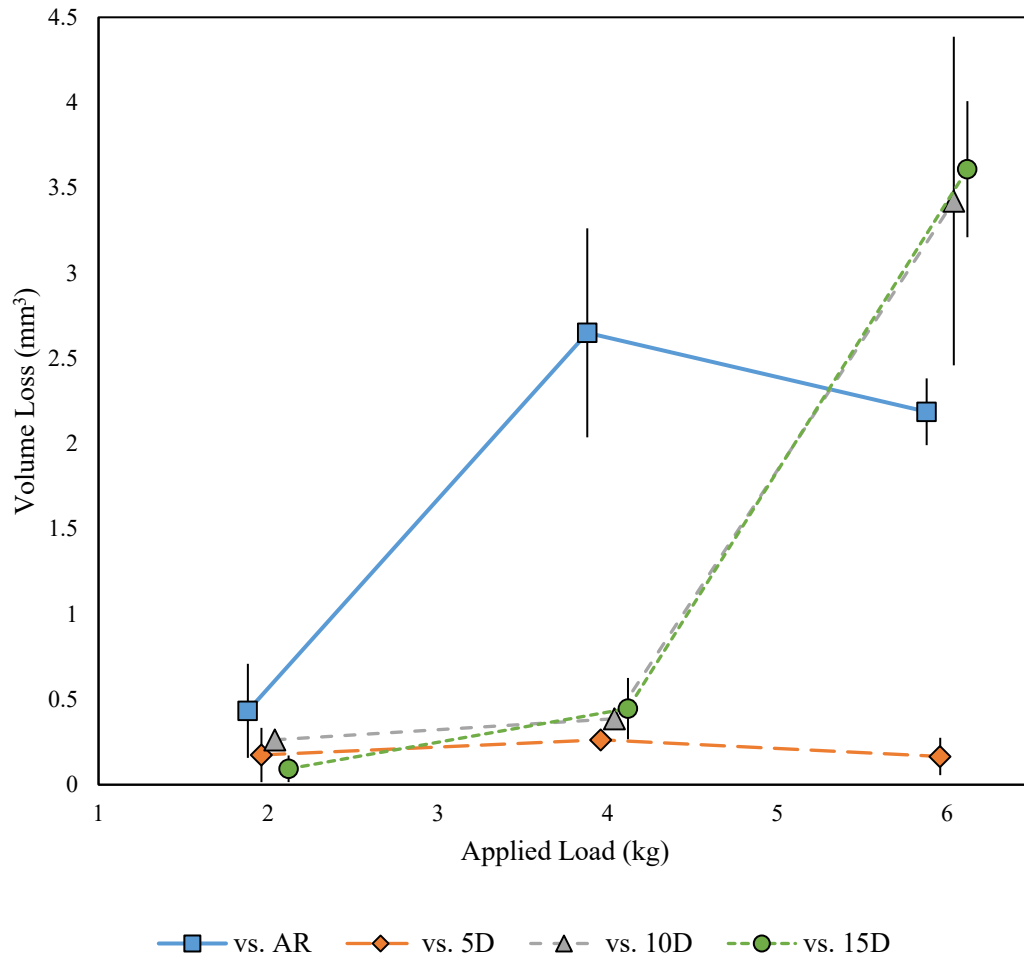
Figure 6.5 - Volume loss values of AISI 4330 discs from sliding against various degrees of cementite-spheroidised G350 cast iron pins. N = 3 for all tests.

Microstructural softening causes increased plastic matrix deformation and therefore inhibits the wear surface from effectively oxidising (Figures 6.6, 6.7, 6.8). The primary drivers of hardness reduction are carbide spheroidisation, increasing the mean true ferrite pathway [6.8], and matrix ferritisation [6.17], resulting in less carbides throughout the microstructure. In the other combinations of microstructure/load where mild wear occurs, a positive feed-back loop arose where little matrix damage allows for surface oxidation, producing further reduced matrix damage. Such mechanisms of beneficial oxidation have been documented in the tribological community by Lim and Ashby [6.19], [6.20], Quinn [6.21]–[6.24], and Stott [6.25], [6.26]. In the severe wear cases of 10D 6kg and 15D 6kg, the gross mechanical damage occurring prevents surface oxidation as there is no constant surface for oxide nucleation and growth (Figure 6.7, Figure 6.8(a) vs. 6.8(b)).

During the subcritical anneal, carbides grow with time and engulf smaller globules. Such increases in size are accompanied by a greater potential to cause abrasive wear through acting as hard particles. This further serves to increase volume losses and disrupt the worn surface which prevents oxide build-up. Bhattacharya [6.9] reported such instances of abrasive wear in spheroidal carbide microstructures which was presumed responsible for the transition from mild to severe wear. Presently, as the shift occurs for the two most spheroidised structures (10D and 15D) only at the highest load (Figure 6.4), the transition to severe is therefore a function of both microstructure and load. The potential for globules to act abrasively is therefore not the sole factor causing the transition. The applied load is postulated to govern whether the hard particles embed into the surface, abrasively slide, shatter and oxidise, or exit the tribosystem as debris. High magnification micrographs of possible damage from carbide particle abrasion are shown in Section 3.3.
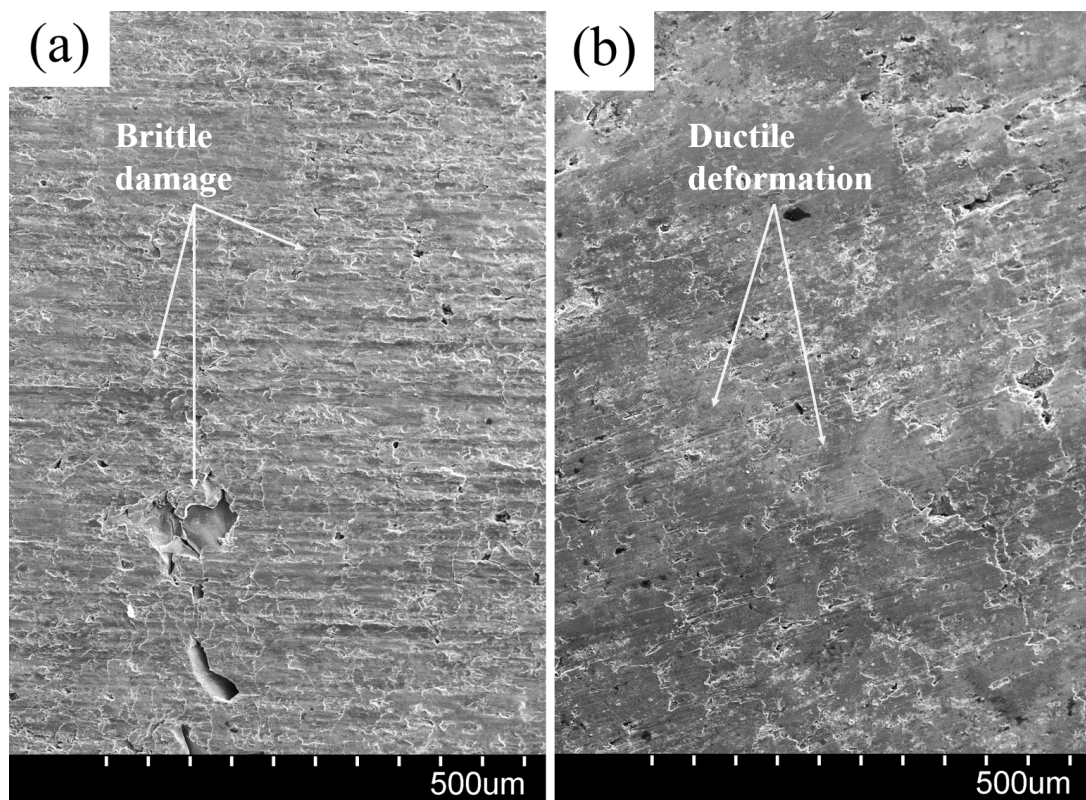

Figure 6.6 - SEM micrographs showing the differing damage mechanisms of an (a) AR pin and (b) 15D pin [x100].

Inspection of the cast iron pins (Figure 6.6) revealed different damage mechanisms between the AR pins and the heat treated pins. The AR pin worn surfaces showed

more brittle behaviour (smaller areas of spallation, cracking, and graphite pull-out) than the heat treated pins by virtue of their fully pearlitic microstructure. Conversely, the heat treated pins behaved in a ductile manner, through the typical smearing and ploughing mechanisms, as shown in Figure 6.6(b).

6.3.3.   *AISI 4330 Damage Mechanisms*

Cross-sectional profilometry of the AISI 4330 disc wear scars showed large differences between the mild and severe combinations (Figure 6.7). The mild wear cross-sections did not show significant depth or roughness changes from the unworn surface. In contrast, the severe wear cross-sections were distinct from the unworn surface and were largely jagged with varying depth. The surface profile of these scars oscillated in a wavy texture, indicating gross metallic damage had taken place.
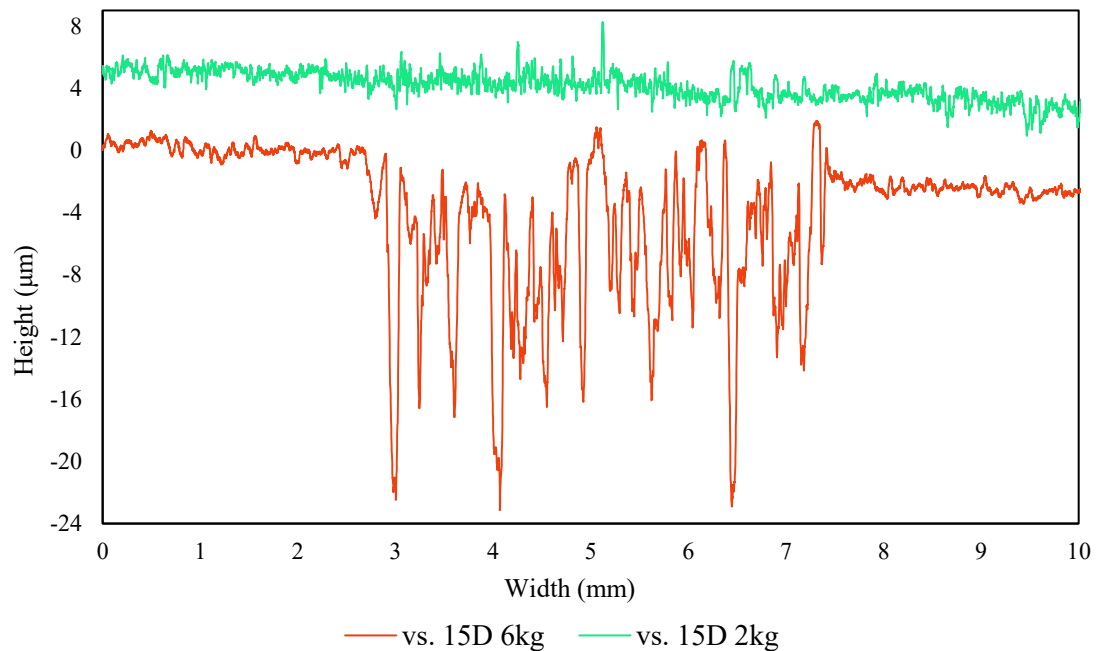
Figure 6.7 - Cross-sectional profile showing the difference between mild wear (top) and severe wear (bottom).

SEM inspection of the discs showed the distinct difference between mild and severe wear (Figure 6.8). The mild wear discs were covered in numerous oxide islands and displayed vestigial grinding lines from the unworn surface in some instances, evidencing the shallow depth/coverage. The severe wear discs experienced metallic damage in the form of ploughing and spalling, and areas of oxidation. The relative scale differences of damage seen in the cross-sectional profiles (Figure 6.7) was also

observable in Figure 6.8, where the severe wear discs showed larger macroscopic areas of damage, in the form of ploughing, cutting, fracture, and spallation.
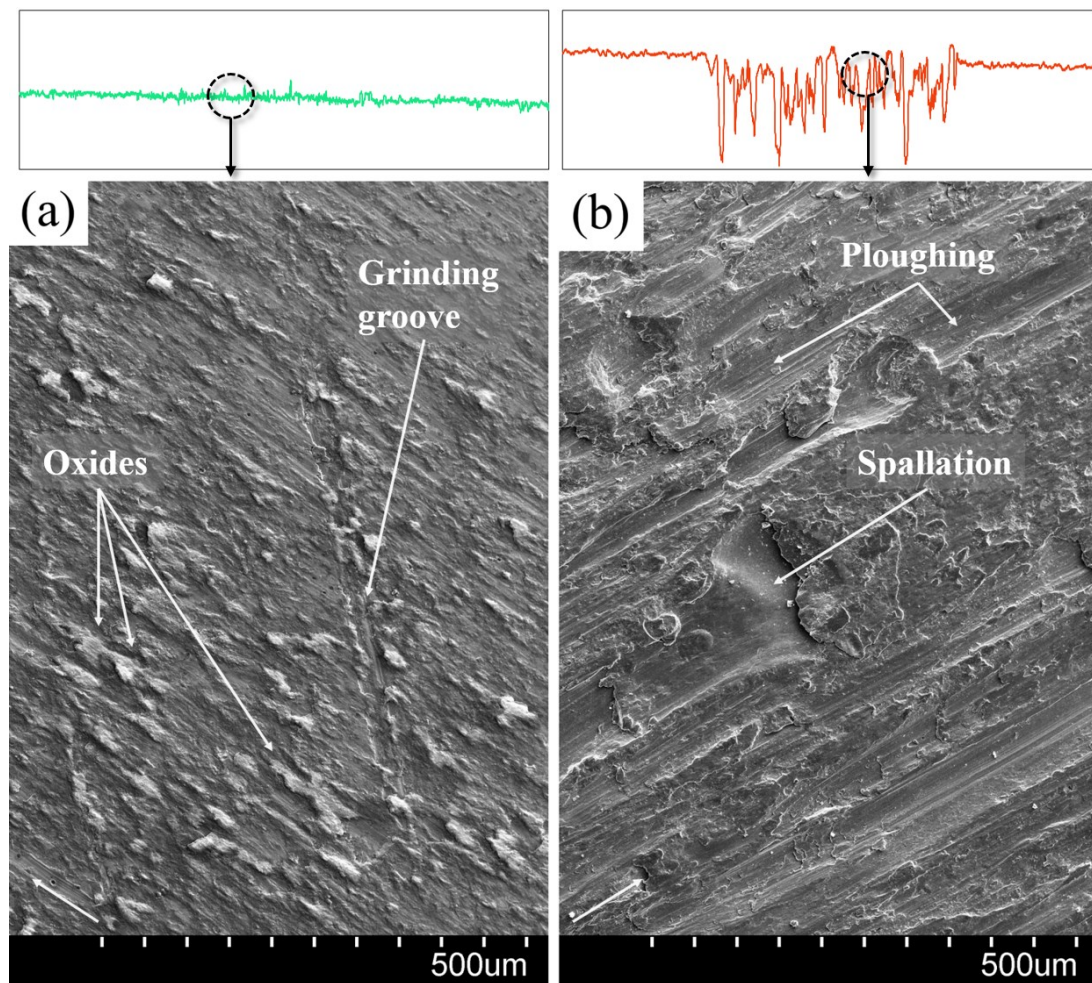

Figure 6.8 – Profiles and SEM micrographs highlighting the different AISI 4330 disc wear mechanisms between (a) 15D 2kg and (b) 15D 6kg wear tests [x100].

As discussed in Section 3.3, spheroidised carbide globules can act as hard particles and cause abrasive damage to the counter face in certain instances. This was observed during inspection of the AISI 4330 discs worn against 15D pins (Figure 6.9). In some areas, the bottom of ploughing troughs featured further micro ploughing on the same scale as enlarged carbide globules. Two sub-mechanisms were observed, such as Figure 6.9(a, b) which showed damage from deeply embedded carbides, and Figure 9(c, d) which showed traditional ploughing action but on a smaller scale in comparison to the macroscopic ploughing damage (Figure 6.8(b)). The difference between the two micro-ploughing mechanisms arises primarily from the depth of carbide globule embedment, with the former caused by carbides either significantly protruding from

the cast iron surface or detaching completely and fully embedding into the AISI 4330 surface before causing ploughing/cutting. The latter is caused by traditional ploughing mechanisms, but on a smaller scale in comparison to the macroscopic ploughing damage, where particularly harder areas of the cast iron pin – if a carbide is at or near to the surface – abrade the AISI 4330 counter face.
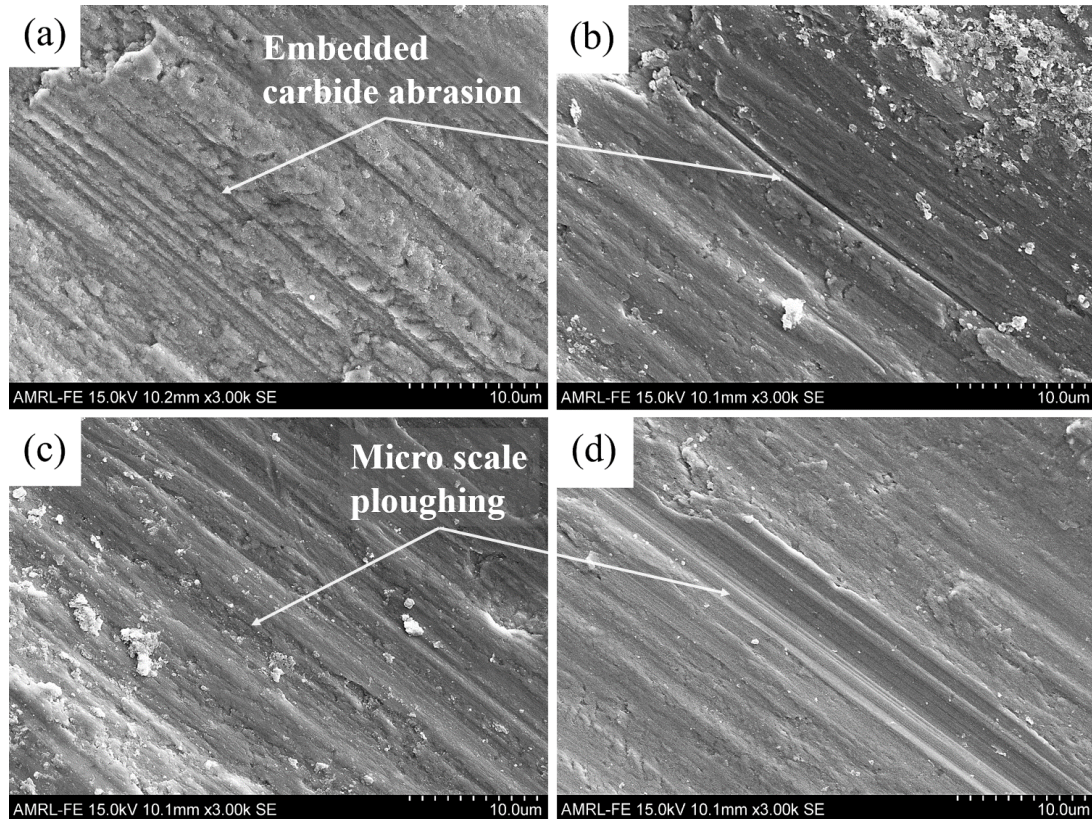
Figure 6.9 - Micro scale ploughing on a 15D 6kg disc caused by carbide abrasion [x3000].

The presence of oxides was inspected using comparative back scatted electron (BSE) images of the mild and severe wear scars. Lighter elements such as oxygen and carbon appear as darker areas in comparison to heavier elements such as iron. The BSE comparison (Figure 6.10) shows that mild wear scars are covered in a uniform distribution of oxide islands whereas the severe wear scar shows higher contrasts between oxidised areas and freshly exposed metallic areas.
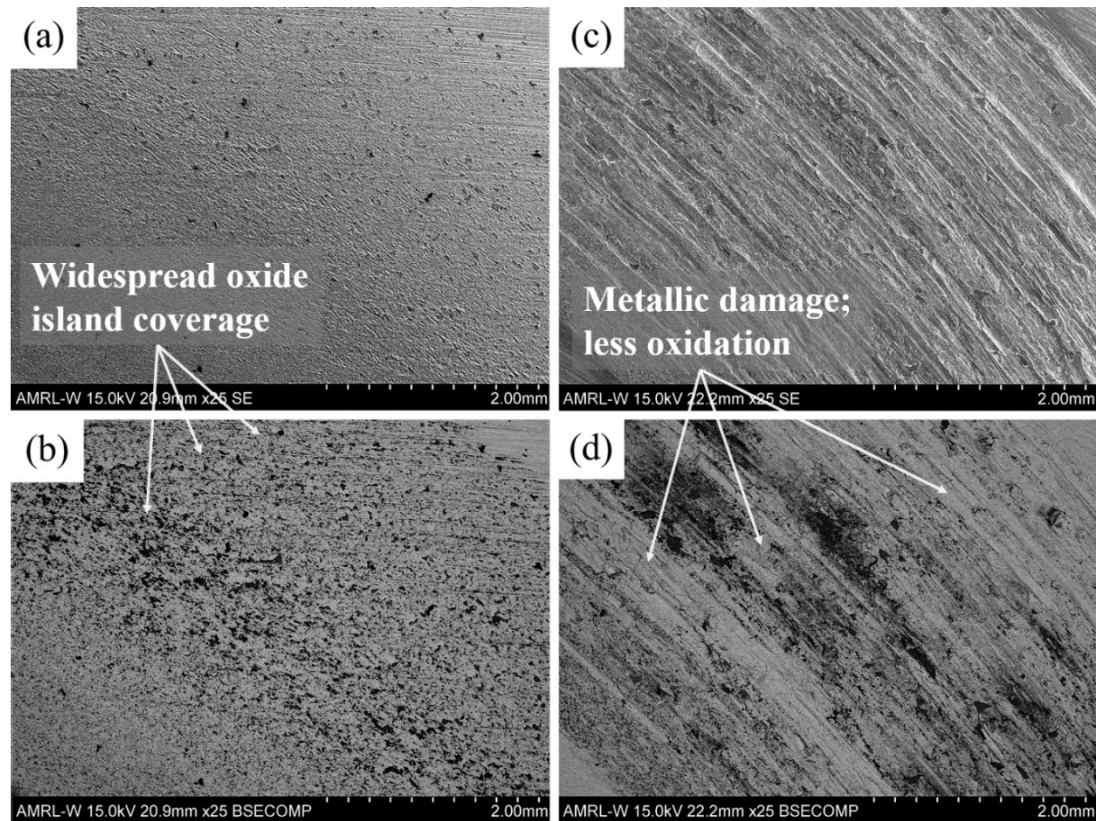
Figure 6.10 - SEM micrographs of mild and severe wear scars (a, c) and BSE micrographs showing oxide products (b, d) [x25].

EDS analysis highlighted the nature of the oxide coverage on the surface of the mild disc wear scars (Figures 6.10, 6.11, Tables 6.1, 6.2). Area analysis showed that the mild wear scar features oxides whereas the unworn surface does not (Figure 6.11, Table 6.1), and therefore this observed oxidation is an artefact of the wear process.
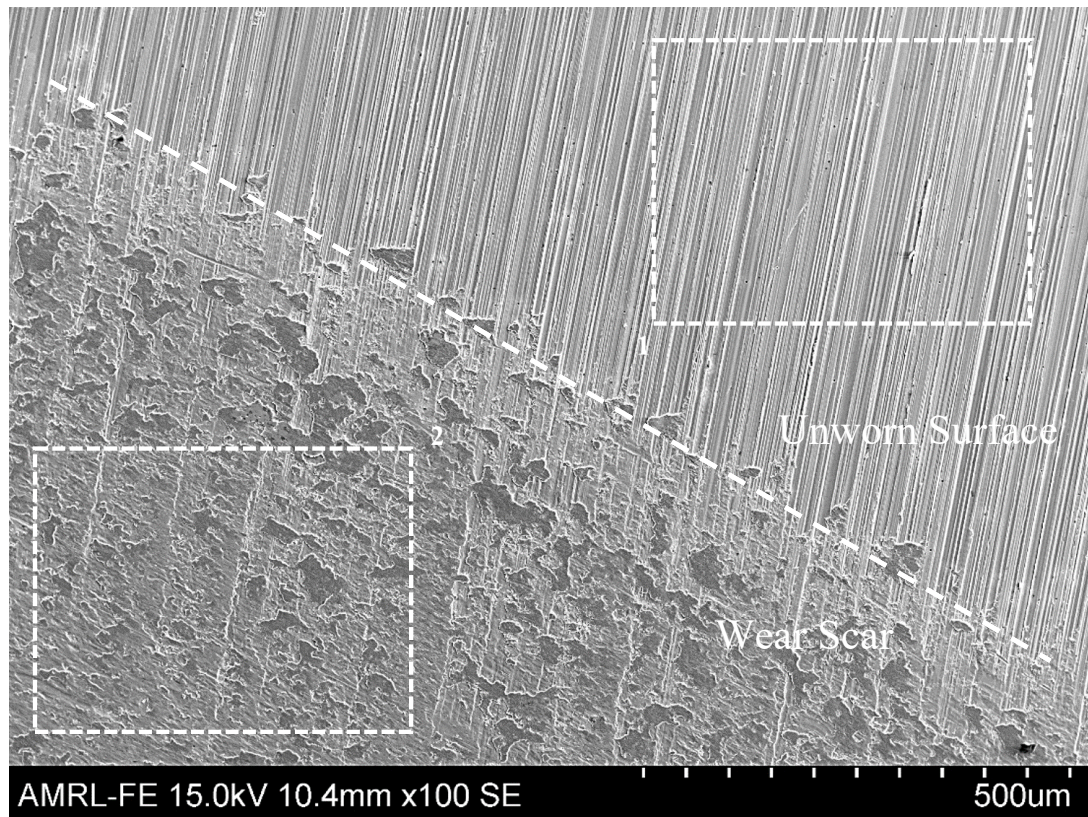
Figure 6.11 - EDS area analyses of the mild wear scar and unworn surface [x100].

Table 6.1 - EDS elemental results from the mild wear scar and the unworn surface (Figure 6.11).

Spectrum	O	Si	Cr	Mn	Fe	Ni
1	-	0.37	1.07	0.51	95.24	2.82
2	12.38	0.78	0.88	0.53	83.68	1.75

EDS spot analyses (Figure 6.12, Table 6.2) of the oxide islands showed a further increased oxygen concentration in addition to the blanket layer. Such oxide islands are notable for their upward protrusion due to parabolic growth, and are eventually sheared and smeared across the surface of the scar, further adding to the blanket coverage. The elemental analysis of the areas without oxide islands, such as Spectra 4, 5, 8, and 9, show that the smoother worn areas also have blanket oxide coverage. This coverage is attributed to the wearing of the oxide islands once they grow to a certain height and are sheared along the surface.

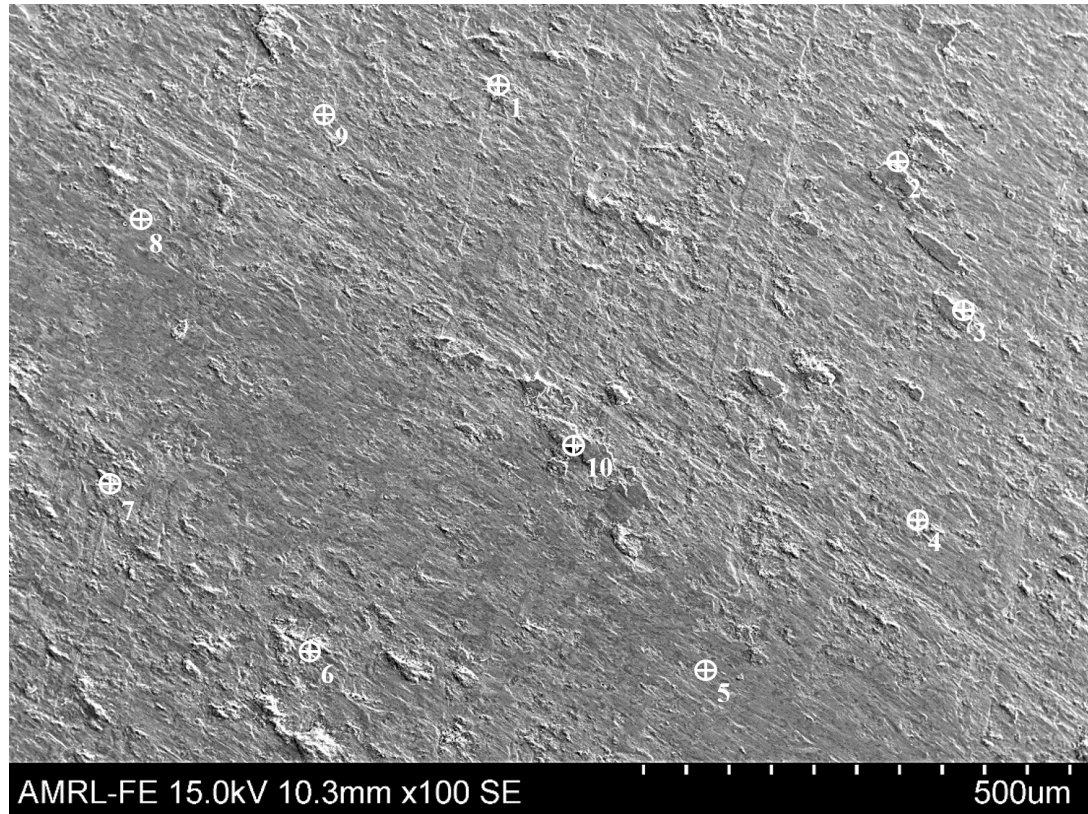Figure 6.12 - EDS spot analyses of various oxide islands and smeared oxide surface on a mild disc [x100].

Table 6.2 - EDS elemental results from oxide islands and smeared oxide surface (Figure 6.12).

Spectrum	O	Si	Cr	Mn	Fe	Ni
1	38.16	1.9	-	-	59.95	-
2	23.41	1.19	-	-	75.4	-
3	21.21	0.98	0.66	0.37	75.54	1.25
4	9.87	0.52	0.72	-	86.72	2.18
5	9.96	0.46	0.94	0.46	86.02	2.17
6	33.14	1.57	0.31	0.46	63.77	0.75
7	24.13	1.11	0.7	0.41	72.39	1.27
8	7.79	0.42	1.03	0.48	87.85	2.43
9	3.05	0.41	1.05	0.5	92.04	2.95
10	28.9	1.54	0.35	0.42	68.78	-

AISI 4330 disc wear scar residual stress results (Figure 6.13) illustrate the lasting effect of the sliding wear tests on the contact surface, where higher volume losses correlated with lower residual stress. The AR pins produced the lowest average normal stress in the discs wear scar across all three loads, while the 5D pins produced the highest. This correlates inversely with the disc volume loss results where discs worn

against AR pins lost significantly more on average than discs worn against 5D pins. The 10D and 15D pins experience a large decrease in stress at 6kg, showing clear evidence of the transition to severe.

The inverse relationship between volume loss and residual stress is due to the higher likelihood of spallation for combinations with higher volume losses. In combinations such as the discs worn against AR pins, the affected surface layer spalls and detaches from the sample, exposing fresh material underneath – resulting in lower residual stress values. Conversely, the discs worn against 5D pins had low volume losses and therefore the wear scar surface was repeatedly worn under load without spalling – producing higher residual stress values.

The residual stress values of the unworn disc surfaces were approximately uniform, due to them all being of the same material and manufactured and processed in the same way (turned then ground). This therefore allowed for relative comparisons of the wear scar residual stresses to be made.
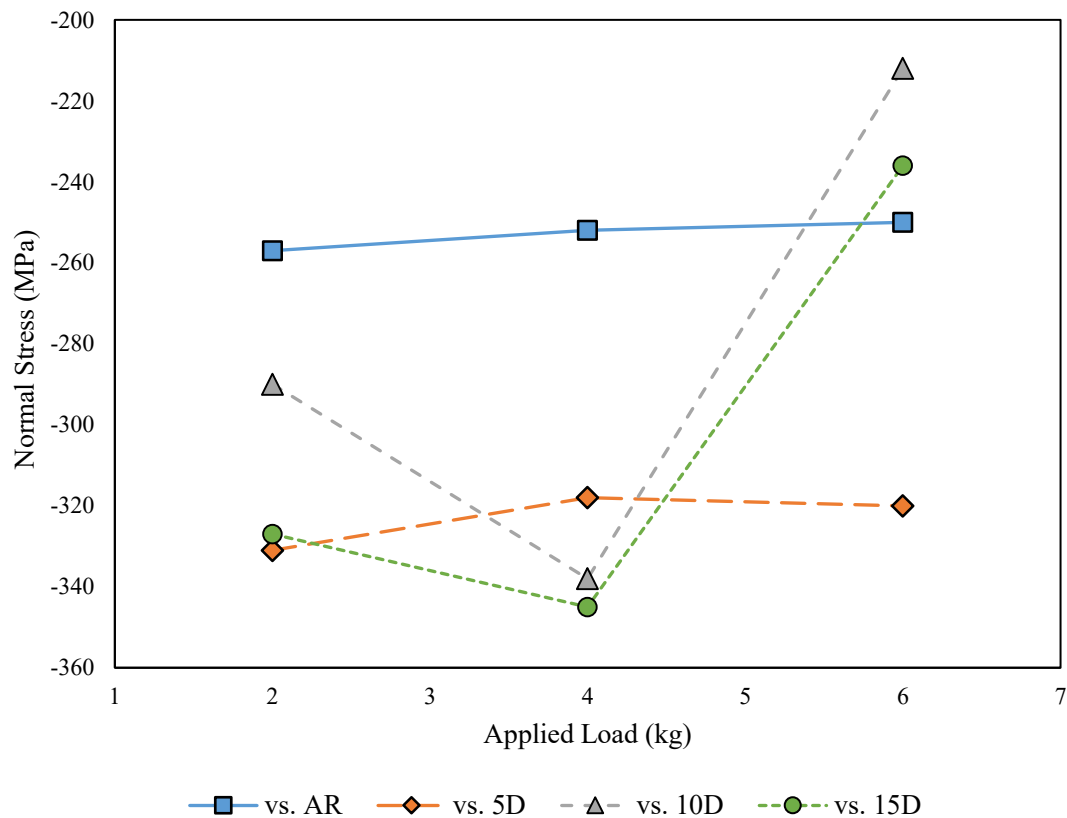

Figure 6.13 - Disc wear scar normal residual stresses after sliding wear. N = 1.

6.3.4. *Cast Iron Subsurface Deformation*

Subsurface deformation is visible in all cast iron pin conditions (Figure 6.14). Deformation is readily observable in the AR pins through the altered directionality of cementite lamellae. In the spheroidised conditions, it is observable in both the carbide globules and in the strained ferrite matrix. In some instances, carbide globules show directionality and fracture at a depth below that at which ferrite straining can be seen, indicating that subsurface damage is not always accompanied by visible ferrite strain (Figure 6.14(d)).
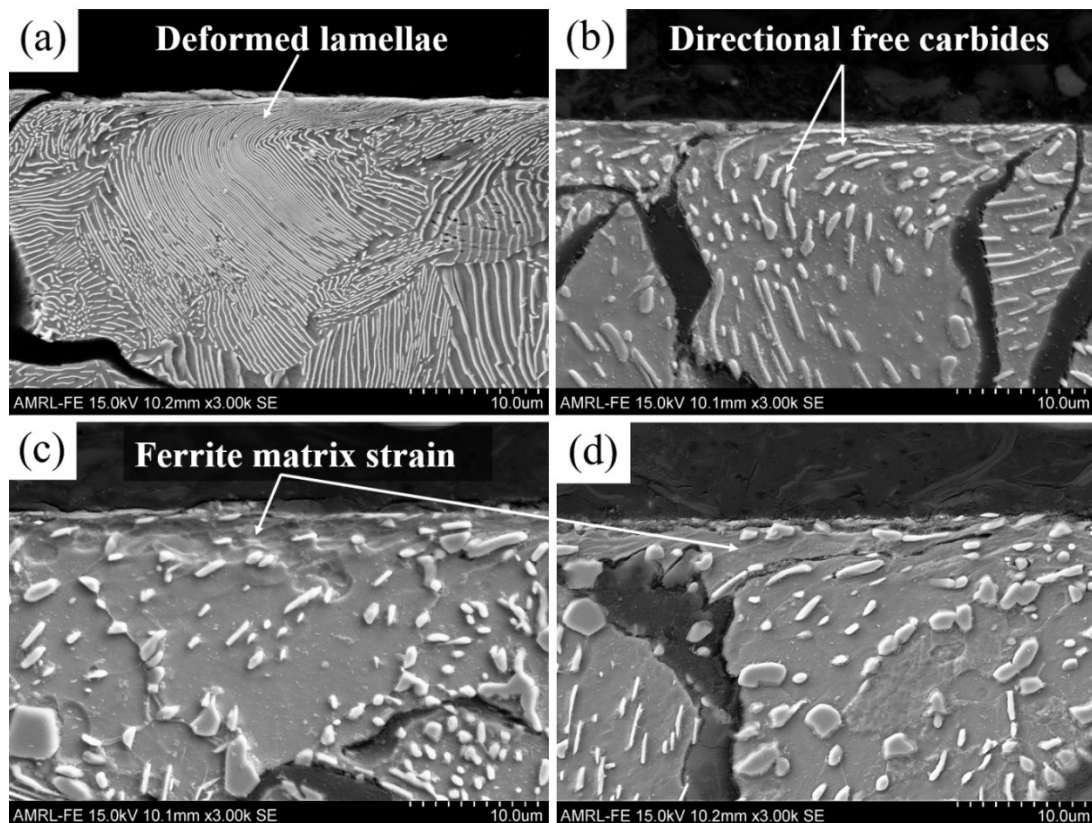
Figure 6.14 - SEM micrograph showing subsurface deformation for (a) AR 6kg (b) 5D 6kg (c) 10D 6kg (d) 15D 6kg [x3000 – nital].

The pearlitic AR pins show the shallowest subsurface deformation (Figure 6.15) by virtue of their coarse lamellar microstructure inhibiting dislocation movement. The heat treated pins show deeper damage with increasing annealing time. This is due to the spheroidisation and ferritisation of the heat treated samples, as also noted by Fegredo et al. [6.11], who concluded that softer, more spheroidised steel railway wheels wear more than harder materials. As the carbide globules coarsen and decrease in frequency, the overall microstructure softens. This allows more strain to take place,

emphasising the reinforcing role that carbide globules play in soft matrices, a reduction of which allows for more deformation. With increasing load, the depth of subsurface deformation increases at 4kg then decreases, with 2kg and 6kg producing approximately the same depth. This is ascribed to the 2kg being too light a load to deeply impact the ferrite, and the 6kg being too heavy, and therefore causing the affected surface layer to spall. Disc normal residual stress values (Figure 6.13) agree with the pin subsurface depth measurements and volume loss values.

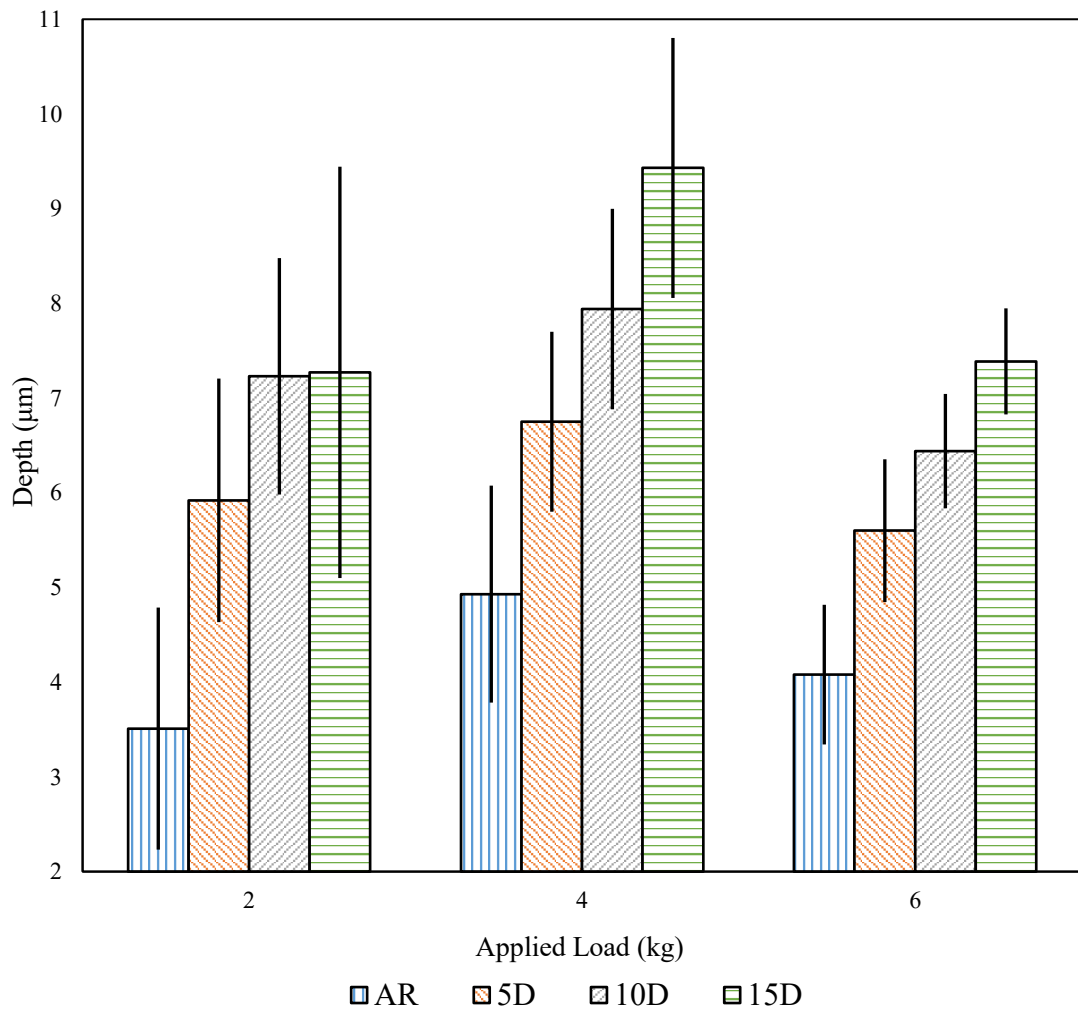Figure 6.15 - Subsurface deformation depth of G350 pins. N = 10.

The observed volumes losses and subsurface deformation results agree with those of Zambrano et al. [6.13] who found that pearlitic microstructures had greater wear resistance than globular cementite microstructures. The authors [6.13] noted that the greater degree of cementite lamellae deformation in comparison to the carbide

183

globules in the spheroidised structures indicates that more energy is consumed in deforming the pearlitic lamellae and results in lower volume losses. This trend is also seen in the results of this chapter, where increased annealing time produced less directionality, and therefore less energy expenditure. This is observed with the AR and 5D pins, showing deformed lamellae and directional carbides, in comparison to the 10D and 15D pins with less directionality (Figure 6.14).

The results presented in this chapter do not agree with the conclusion by Diao et al. [6.12] that cementite lamellae force crack propagation further into the substrate, resulting in higher volume losses. Instead the AR pins experienced the lowest volume losses of the four pin groups. This performance is due primarily to overall hardness and ductility – unlike the spheroidised pins, plastic deformation of ferrite in the AR pins is inhibited by the cementite lamellae. This prevents the ferrite matrix from deforming and yields lower volume losses. This feature of the AR pins is responsible for the highest volume loss of the AISI 4330 discs at loads of 2kg and 4kg. As AISI 4330 is a hard, tempered martensitic alloy, it is less able to deform plastically and, as such, wears through brittle fracture. Therefore, the discs wear less against the overly spheroidised pins (which deform easily) than the pearlitic pins (which do deform but to a lesser extent).

The primary difference to the results by Diao et al. [6.12] is due to their study of steel as opposed to cast iron in the current investigation. In grey cast irons, graphite flakes serve as crack initiation sites which eventually lead to failure [6.27], [6.28] due to fracture of matrix chips (Figures 6.6, 6.16). An additional reason for the observed disparities are the different testing conditions used, where the researchers [6.12] used higher loads and faster sliding speeds than in this chapter. Such testing variables change the tribosystem significantly and therefore may result in different damage mechanisms.
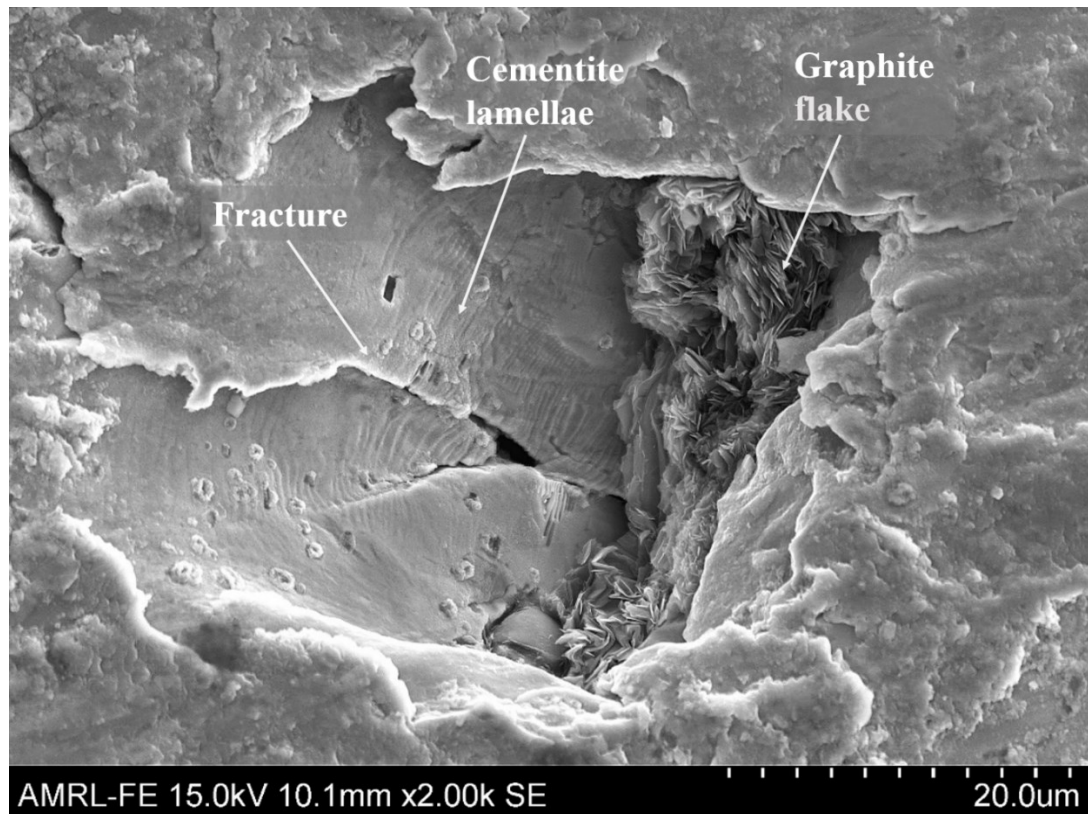
Figure 6.16 - SEM micrograph of a partially spalled graphite flake and residual empty cavity on an AR pin [x2000].

6.3.5.   Assessment of Sliding Wear Performance

Pin and disc wear summary maps were generated to compare the relative performance of each sliding combination. These were primarily based on the volume loss values (Figures 6.4, 6.5) but also take into account the modes of wear occurring during the test.

Assessing the relative pin performance (Figure 6.17), most combinations produced mild oxidative wear with low volume losses (green), apart from the highest load of the 10D and 15D combinations (red). As previously mentioned, the softening of the 10D and 15D pins sliding under the highest load produced gross plastic deformation of the metallic matrix. This in turn prevented them from supporting a beneficial oxide layer.
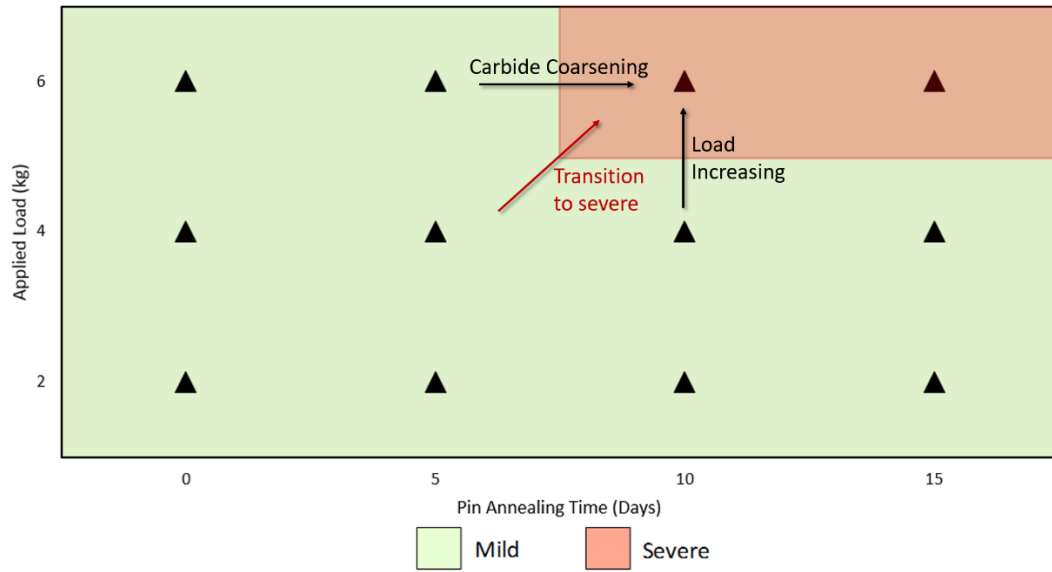
Figure 6.17 - Wear summary map of G350 pin volume losses.

A similar observation is seen on the disc wear map (Figure 6.18), where the gross plastic deformation of the 10D and 15D pins at the highest load also caused the AISI 4330 disc to wear severely (upper right area). An additional area of poor disc performance is seen in the upper left area, corresponding to the AR 4kg and AR 6kg combinations, from being worn against the as received pearlitic pins. As mentioned previously (Section 6.3.4), this is attributed to the higher hardness of the pearlitic pins in comparison to the spheroidised conditions.

Figure 6.18 - Wear summary map of AISI 4330 disc volume losses.

The wear maps (Figures 6.17, 6.18) show that the 5D pin combinations display green mild wear for all loads, for both disc and pin. This is unique among the other combinations as the 5D pins were the only group to not experience severe wear. Unlike the 10D and 15D pins, the 5D pins are not softened enough to experience gross mechanical damage of their metallic matrix, and thus do not destroy the beneficial oxide layer between the contact 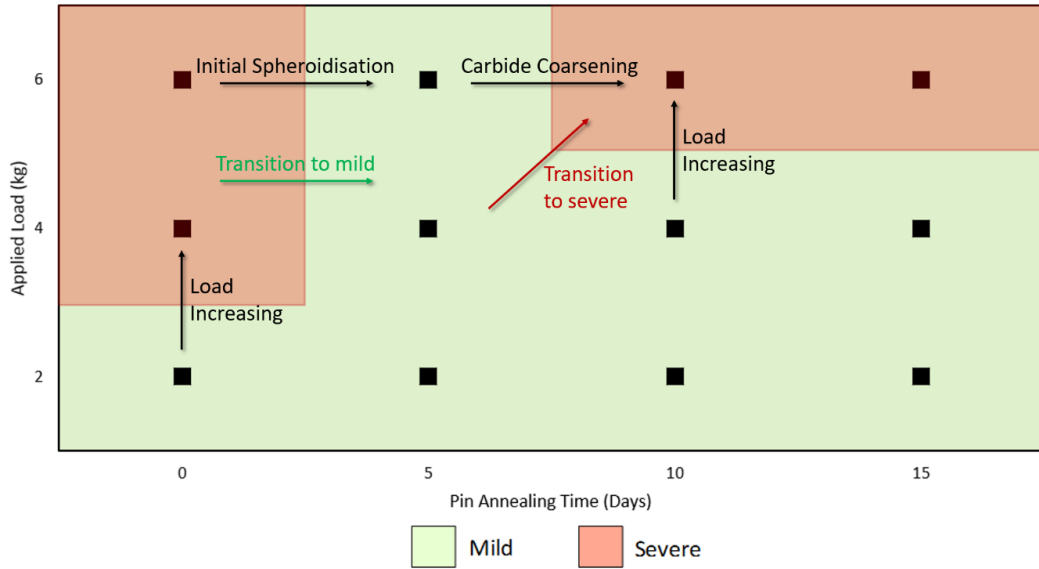faces. The 5D pins therefore possess an optimal balance of hardness in comparison to the AISI 4330 disc, which produces favourable wear results for all loads.

Microstructurally, the hardness values of the 5D pins are due to the partial spheroidisation of cementite lamellae into the fine globular morphology, while still possessing some elongated high aspect ratio carbides (Figure 6.19). Dislocation movement is impeded more by the high aspect ratio carbides in the 5D pins than in the 10D and 15D pins which show only spheroidal morphology. Moreover, the 5D spheroidal carbides have not coarsened to the same degree as the 10D and 15D pins. Most of the globular carbides in these pins are significantly finer than in the 10D and 15D pins, and these reinforce the 5D matrix to a greater degree, producing a harder microstructure.
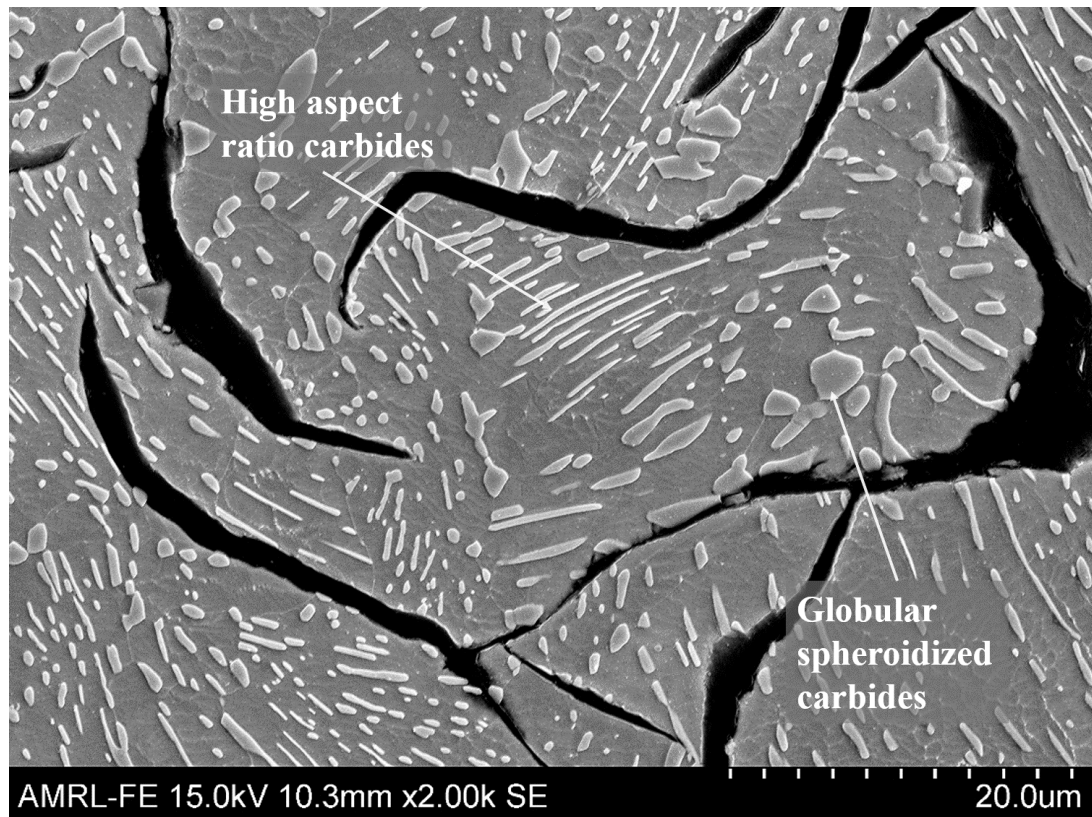
Figure 6.19 – Micrograph of 5D cast iron pin microstructure [x2000 – nital].

The optimum behaviour of the 5D pin combinations can also be confirmed through the other experimental findings, such as the higher disc residual stresses in the AISI 4330 wear scar (Figure 6.13) from repeated sliding contact without material removal. The 5D pins also show the shallowest subsurface deformation of the three spheroidised conditions, due to their greater resistance to plastic deformation and consistently having a protective oxide shield on their working surface.

6.4.   Conclusions

This study investigated the effects of long term spheroidising heat treatments on the sliding wear performance of G350 cast iron pins against AISI 4330 discs. Three durations of heat treatment were employed, 5, 10 and 15 days, the results of which were also compared to the as-received condition.

- The differences between disc and pin volume loss values are primarily governed by hardness. Due to the AISI 4330 being 100HV higher than that of the hardest pins, it wore significantly less in most cases. The most wear occurred with the most spheroidised pins, 10D and 15D, at the highest load of 6kg.

188

- All pins at 2kg and 4kg experienced mild wear. Beneficial oxidative wear prevailed in these groups where little matrix damage allowed a layer of oxide to further shield the underlying matrices, resulting in only very shallow damage and surface perturbations.

- Severe wear was experienced by 10D and 15D pins at 6kg. This transition from mild wear emerged because of global softening of the matrices from progressive spheroidisation and ferritisation, as well as the potential for large carbide globules to act abrasively.

- Only the 5D sliding combinations produced mild wear with low volume losses for both the disc and pin for all loads. This is attributed to the optimum combination of having a softened pin – therefore causing little damage to the disc – while still having enough structural integrity to resist gross plastic deformation of the cast iron pin matrix.

- Subsurface deformation was visible through carbide directionality and ferrite straining. Carbides were often fractured or deformed at a depth lower than that of visible ferrite strain, indicating not all subsurface damage results in visible ferrite strain.

- Subsurface deformation agreed with the volume loss results and highlighted the differences in wear modes such as the transitions from mild to severe. The depth of subsurface deformation increased with annealing time for all loads but did not increase with load for all loads. Instead subsurface deformation showed a maximum depth at 4kg. This is due to spallation of the affected surface layer at 6kg, thereby leaving a shallow subsurface zone.

- Disc wear scar residual stress analysis was indicative of the wear regime occurring and agreed with the sliding wear results. Stress values were inversely related to the volume loss values because higher volume loss discs have more frequent spallation at lesser deformations. Conversely discs with lower volume

losses showed higher residual stress values due to having repeated sliding wear on the same surface.

References

[6.1] R. E. Smallman and A. H. W. Ngan, "Cast Irons," in *Physical Metallurgy and Advanced Materials*, 7th ed., Elsevier, pp. 455–458.

[6.2] ASM International, "Permanent Mold Casting," in *Volume 15: Casting*, 1998, p. 609.

[6.3] ASM International, "Machining of Cast Irons," in *Volume 16: Machnining Processes*, pp. 648–666.

[6.4] M. Field, J. F. Kahles, and W. P. Koster, "Surface Finish and Surface Integrity," in *Volume 16: Machnining Processes*, ASM International, pp. 19–35.

[6.5] ASM International, "Spheroidizing," in *ASM Handbook Volume 4: Heat Treating*, ASM International, 1991, pp. 119–121.

[6.6] J. D. Verhoeven, "Spheroidized Microstructures," in *Steel Metallurgy for the Non-Metallurgist*, ASM International, 2007, pp. 35–37.

[6.7] H. T. Angus, "Heat Treatment of Grey Cast Irons," in *Cast Iron: Physical and Engineering Properties*, 1960, pp. 355–379.

[6.8] W. D. Callister and D. G. Rethwisch, "Spheroidite," in *Materials Science and Engineering: An Introduction*, 8th ed., John Wiley & Sons, Ltd., 2010, p. 373.

[6.9] S. Bhattacharyya, "Wear and friction in steel, aluminum and magnesium alloys I. Pearlitic and spheroidized steels," *Wear*, vol. 61, no. 1, pp. 133–141, 1980.

[6.10] W. You, P. Li, and (T C.Lei) Tingquan Lei, "Sliding wear behavior of pearlitic structures in eutectoid steel," *Wear*, vol. 143, no. 1, pp. 57–69, 1991.

[6.11] D. M. Fegredo, J. Kalousek, and M. T. Shehata, "The effect of progressive minor spheroidization on the dry-wear rates of a standard carbon and a Cr-Mo alloy rail steel," *Wear*, vol. 161, no. 1–2, pp. 29–40, 1993.

[6.12] G. Diao, Q. Yan, X. Shi, X. Zhang, Z. Wen, and X. Jin, "Improvement of wear resistance in ferrite-pearlite railway wheel steel via ferrite strengthening and

cementite spheroidization," *Mater. Res. Express*, vol. 6, no. 10, 2019.

[6.13] O. A. Zambrano, J. A. Gómez, J. J. Coronado, and S. A. Rodríguez, "The sliding wear behaviour of steels with the same hardness," *Wear*, vol. 418–419, no. April 2018, pp. 201–207, 2019.

[6.14] All Metals & Forge Group, "AISI / Alloy Steel 4330," *Alloy Steel*. [6.Online]. Available: https://steelforge.com/alloy-steel-4330/. [6.Accessed: 07-Aug-2022].

[6.15] BSI Standards Online, "BS EN ISO 945-1:2019 BSI Standards Publication: Microstructure of cast irons," 2019.

[6.16] ASTM Standards, "ASTM G99 - 17: Standard Test Method for Wear Testing with a Pin-on-Disk Apparatus."

[6.17] B. Kovacs, "Heat Treating of Gray Irons," in *ASM Handbook Volume 4: Heat Treating*, ASM International, p. 1456.

[6.18] B. L. Bramfitt and A. K. Hingwe, "Annealing of Steel," in *ASM Handbook Volume 4: Heat Treating*, ASM International, p. 106.

[6.19] S. C. Lim, M. F. Ashby, and J. H. Brunton, "Wear-rate transitions and their relationship to wear mechanisms," *Acta Metall.*, vol. 35, no. 6, pp. 1343–1348, 1987.

[6.20] S. C. Lim, "The relevance of wear-mechanism maps to mild-oxidational wear," *Tribol. Int.*, vol. 35, pp. 717–723, 2002.

[6.21] T. F. J. Quinn, "The oxidational wear of low alloy steels," *Tribol. Int.*, vol. 35, no. 11, pp. 691–715, 2002.

[6.22] T. F. J. Quinn and W. O. Winer, "The thermal aspects of oxidational wear," *Wear*, vol. 102, no. 1–2, pp. 67–80, 1985.

[6.23] T. F. J. Quinn, "Role of oxidation in the mild wear of steel," *Br. J. Appl. Phys.*, vol. 13, no. 1, pp. 33–37, 1962.

[6.24] T. F. J. Quinn, D. M. Rowson, and J. L. Sullivan, "Application of the oxidational theory of mild wear to the sliding wear of low alloy steel," *Wear*, vol. 65, no. 1, pp. 1–20, 1980.

[6.25] F. H. Stott, "The role of oxidation in the wear of alloys," *Tribol. Int.*, vol. 31, no. 1–3, pp. 61–71, 1998.

[6.26] F. H. Stott and G. C. Wood, "The influence of oxides on the friction and wear of alloys," *Tribol. Int.*, vol. 11, no. 4, pp. 211–218, 1978.

[6.27] A. Vadiraj, G. Balachandran, M. Kamaraj, and E. Kazuya, "Mechanical and wear behavior of quenched and tempered alloyed hypereutectic gray cast iron," *Mater. Des.*, vol. 32, no. 4, pp. 2438–2443, 2011.

[6.28] A. R. Riahi and A. T. Alpas, "Wear map for grey cast iron," *Wear*, vol. 255, no. 1–6, pp. 401–409, 2003.

Chapter 7.

Sliding Wear of Tempered Grey Cast Iron

Abstract

The tribological properties of G350 grey cast iron in various tempered conditions is discussed. Quench and temper heat treatments were conducted at four tempering temperatures, from 400°C to 700°C, to produce a range of tempered martensitic disc samples. Pins were slow furnace-cool annealed to produce a coarse pearlitic microstructure with some areas of ferrite. These samples were then used in pin-on-disc sliding wear tests.

The quench and temper heat treatments of the discs produced two distinct types of tempered martensite: acicular morphology, and finely spheroidised carbides in an equiaxed ferrite matrix. Hardness decreased with tempering temperature, from 400HV at 400°C to 200HV at 700°C. The two spheroidised carbide discs produced higher volume losses than the two acicular martensitic discs due to instability of the oxide layer on the softer substrate. Subsurface deformation was visible in the annealed pins and spheroidised discs which consisted of deformed cementite lamellae in the direction sliding and strained ferrite grains.

7.1.   Introduction

Grey cast iron is a versatile ferrous alloy used in a wide variety of industrial applications [7.1]. Ease of casting and affordability enable cast irons to be used for numerous components with intricate geometries [7.2] such as brake discs and flywheels. However, certain applications of cast iron require a combination of hardness, toughness, and wear resistance. This is particularly the case for automotive or pumping components such as selector forks, cam lobes, or slipper pads, where the material is sliding under load [7.3]. In these instances, the mechanical integrity of the material is imperative to prevent serious failure, therefore, tempered martensitic matrices are optimal due to their balance of mechanical properties. Industrial cast irons typically have a high alloying content, allowing for a multitude of possible microstructures and making them readily heat treatable [7.4]. Tempered martensitic matrices are therefore easily producible for grey cast irons [7.5].

Research on the sliding wear effects of tempering focusses primarily on steels. Ouyang et al. [7.6] investigated the sliding wear and mechanical properties of tempered 4Cr13 steel at various loads and sliding speeds. The researchers [7.5] found that mass loss increased with increasing tempering temperature and noted a transition to severe wear for all tested combinations at higher loads and sliding speeds. Wei et al. [7.7] studied the effects of tempering on the high temperature wear rate of H13 die steel. The authors [7.6] found that wear resistance was not proportional to the hardness of the tempered samples, and that in some instances, the softer sample had a lower wear rate due to its higher fracture toughness. This was postulated to be due to temper embrittlement in the harder samples caused by the precipitation of carbides on the grain boundaries. Trevisiol et al. [7.8] investigated the effect of varying tempering temperature on the sliding wear properties of 35NCD16 steel. The authors [7.7] noted that hardness decreased from 600HV to 350HV when tempering temperature increased from 200°C to 400°C. At approximately 430HV, from tempering at 400°C, the microstructure changed significantly from martensitic laths to equiaxed ferrite grains interspersed with carbides.

Research articles on the quench and tempering effects of cast iron in sliding wear are few and focus on comparisons between martensitic versus austempered microstructures, or compare the effect of alloying content on the tempering response.

Haseeb et al. [7.9] studied the performance of austempered versus quench and tempered ductile iron. Oxidation was found to be the dominant wear mechanism occurring for both conditions, and the austempered samples were found to be slightly more wear resistant than tempered martensite. However, the researchers [7.8] did not perform an examination of the subsurface deformation in detail and did not show how the worn surfaces change with increasing applied load. Such factors are important in evaluating the tribological response of the alloy.

Vadiraj et al. [7.10] studied the sliding wear properties of various cast irons at various tempers. The researchers [7.10] found that higher alloyed cast irons were less softened by the tempering treatment, and that tempering at 400°C provided an optimum balance of wear resistance, hardness, and toughness. However, the researchers [7.10] only showed and discussed the quantitative data produced from the heat treatments and sliding wear tests, instead of also including qualitative data such as characterisation of subsurface deformation and inspection of the worn surfaces. Moreover, only one set of sliding parameters was used, instead of altering key variables such as speed or load. This serves to compare the numerous alloys tested but does not show if the wear response changes over different conditions.

Little research exists on the effects of high temperature tempering for grey cast irons in sliding while altering the applied load, inspecting the worn surfaces, and characterising the subsurface deformation. The results presented herein rectify this through subjecting industrial grey cast iron to four degrees of high temperature tempering. The various heat treated samples are then subjected to pin-on-disc testing using three loads to characterise the sliding wear response of the material with load. Additional inspection of the worn surfaces and subsurface deformation then takes place, along with the scientific discussion of the results and significance of the findings.

7.2.   Materials & Methods

7.2.1.   Materials

Pins and discs were made of G350 cast iron (Table 3.1), in different microstructural conditions.

Cast iron was received in the martensitic condition with type I-A/C-5 graphite flakes in accordance with ISO 945 [7.11]. Pin samples were furnace-cool annealed from 900°C to room temperature over 12 hours. Discs were oil quenched from 900°C, followed by tempering at four temperatures, hereafter referred to as 700C (tempered at 700°C), 600C, 500C, and 400C. Tempering duration was 24 hours for all discs. Table 7.1 shows a summary of the five heat treatments.

Table 7.1 - Summary of cast iron heat treatments.

Sample	Heat Treatment	Type	Temperature (°C)	Duration (Hours)	Resultant Microstructure
Pins	Anneal	Furnace-cool	900 to room temperature	12	Coarse pearlite + ferrite
Discs	Quench & Temper	Oil	400, 500, 600, 700	24	Tempered martensite

Cast iron was examined in various microstructural combinations to (a) enhance the scientific tribological novelty, and (b) to provide industrial relevance by employing microstructural conditions seen for many cast irons in engineering applications. Pearlitic cast irons see everyday usage in the automotive industry as brake discs in numerous vehicles [7.12]. Martensitic cast irons feature in the aforementioned long lifespan components such as slipper pads in hydraulic rotary piston pumps [7.3].

The detrimental effects of using self-mated materials in sliding are avoided through the different heat treatments producing markedly different microstructural conditions of the cast iron pins and discs. These effects, such as the high likelihood of self-mated austenitic stainless steels to gall [7.13], [7.14], can result in seizure and high wear rates. However, as the pins exhibit a coarse pearlitic and ferritic matrix, and the discs exhibit tempered martensitic matrices, the similarity is reduced which avoids this problem. These different microstructural conditions effectively mean that the samples

are not self-mated, and can instead be treated as different materials despite having the same chemical composition.

7.2.2.   Methods

Wear behaviour was examined using dry pin-on-disc sliding wear tests as described in Section 3.2.1, and followed the procedure of ASTM G99 [7.15].

Other metallurgical analyses were used to accompany the sliding wear results as discussed in Chapter 3.

7.3.   Results

Furnace-cool annealing transformed the as-received martensitic matrix of the G350 pins into coarse pearlite and ferrite (Figure 7.1). Graphite morphology remained unchanged.
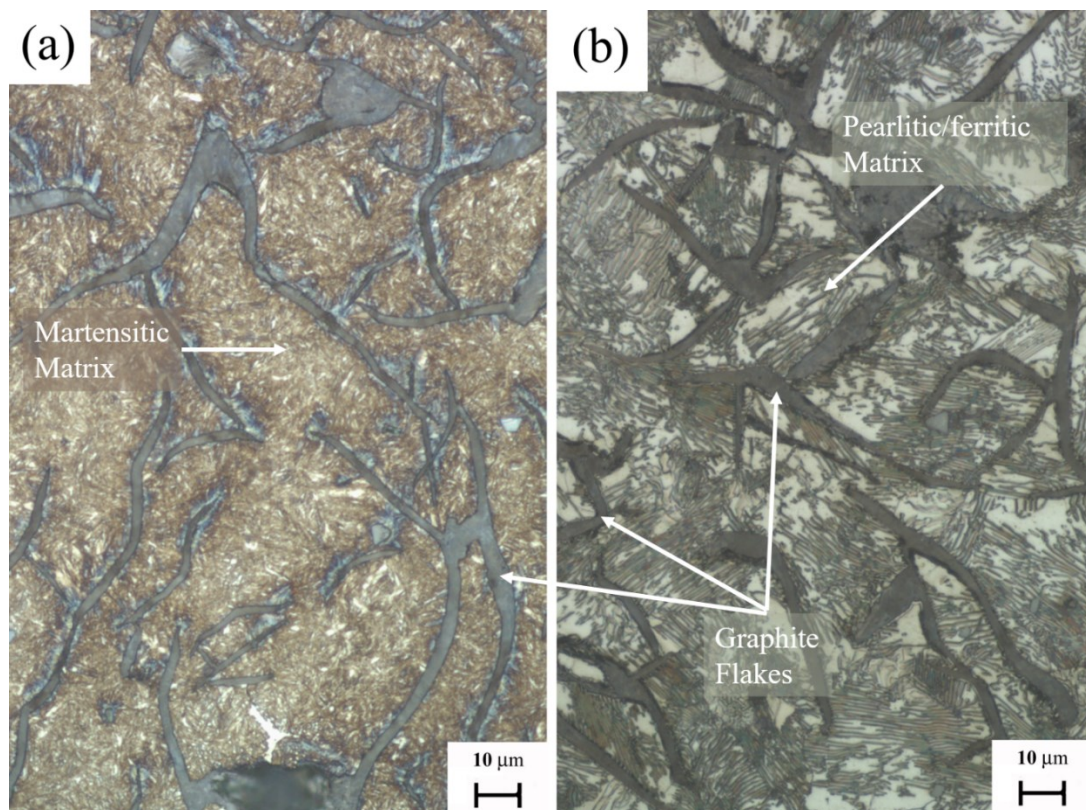

Figure 7.1 – Microstructures of (a) as-received cast iron and (b) furnace-cool annealed pins [x500 – nital].

The quench and tempering process of the discs produced two distinct types of tempered martensitic microstructures: acicular martensite (Figure 7.2(a, b)), and spheroidised carbides in a ferritic matrix. (Figure 7.2(c, d)).

The 400C and 500C discs displayed acicular martensitic microstructures interspersed by the unchanged graphite flakes. An evolution can be observed between 400C and 500C, where a rounding of the martensite needles occurred due to the increasing temperature (Figure 7.2(b)).
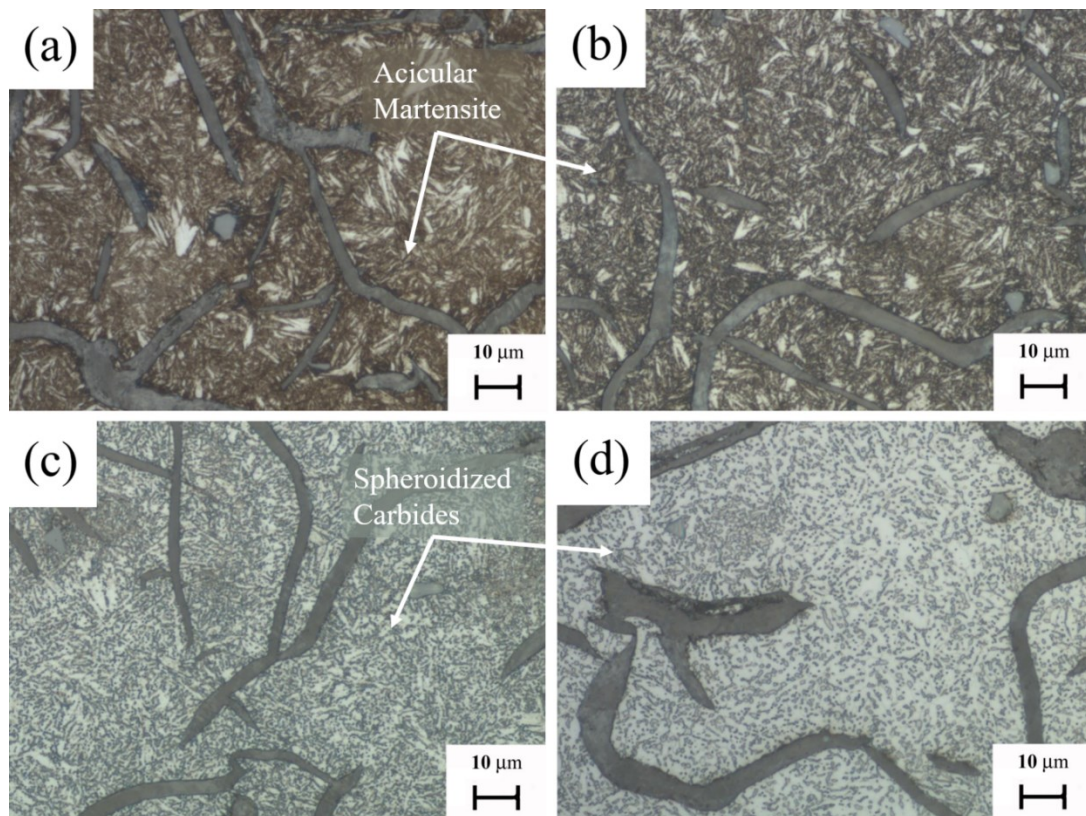

Figure 7.2 - Microstructure of the discs tempered at (a) 400°C (b) 500°C (c) 600°C (d) 700°C [x500 – nital].

The 600C and 700C discs appeared overly tempered and spheroidised (Figure 7.3) [7.16], with fine spheroidised carbide globules interspersed throughout the matrix. A coarsening of the carbide globules can be seen between 600C and 700C where the

increased temperature allowed the carbides to further spheroidise [7.17] (Figure 7.3(c, d)).
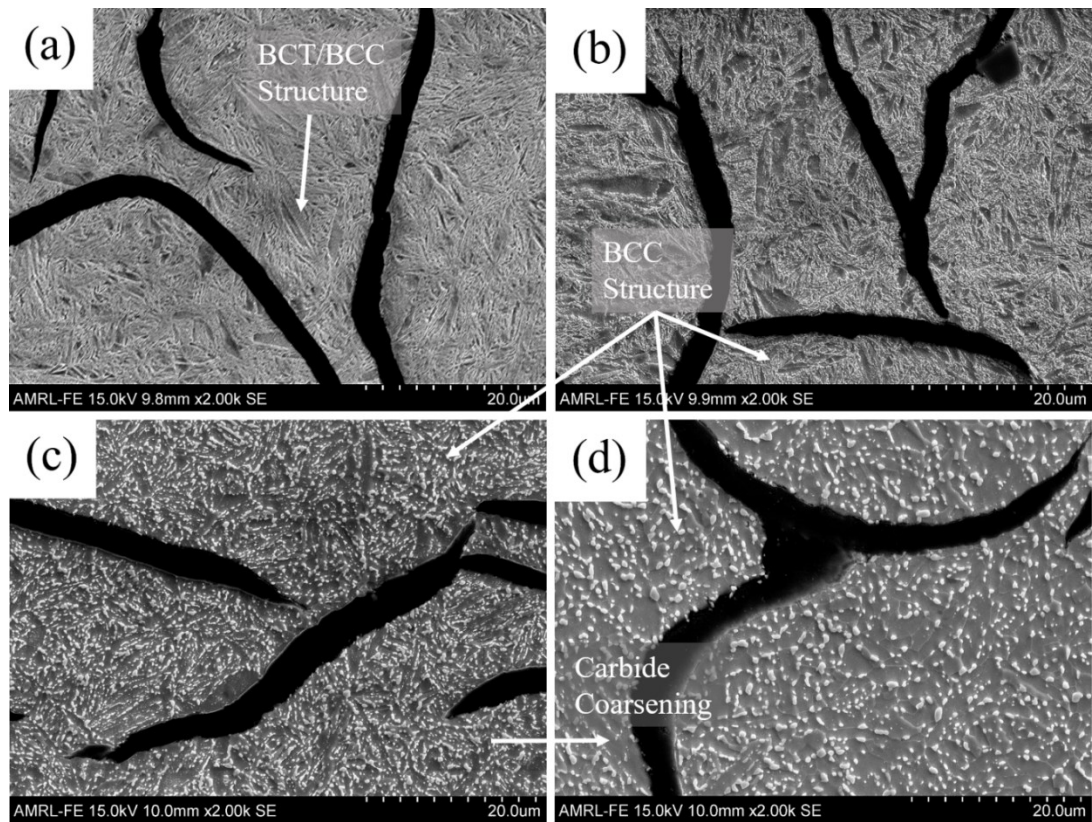

Figure 7.3 - Microstructure of the discs tempered at (a) 400°C (b) 500°C (c) 600°C (d) 700°C [x2000 – nital].

X-ray diffractometry (XRD) phase identification showed that the dominant phase of all four disc microstructures was alpha ferrite (Figure 7.4). The 400C discs showed the same ferrite peaks but with lower intensity, due to the additional presence of BCT martensite. This is evidenced by a peak identified as such for the 400C disc.
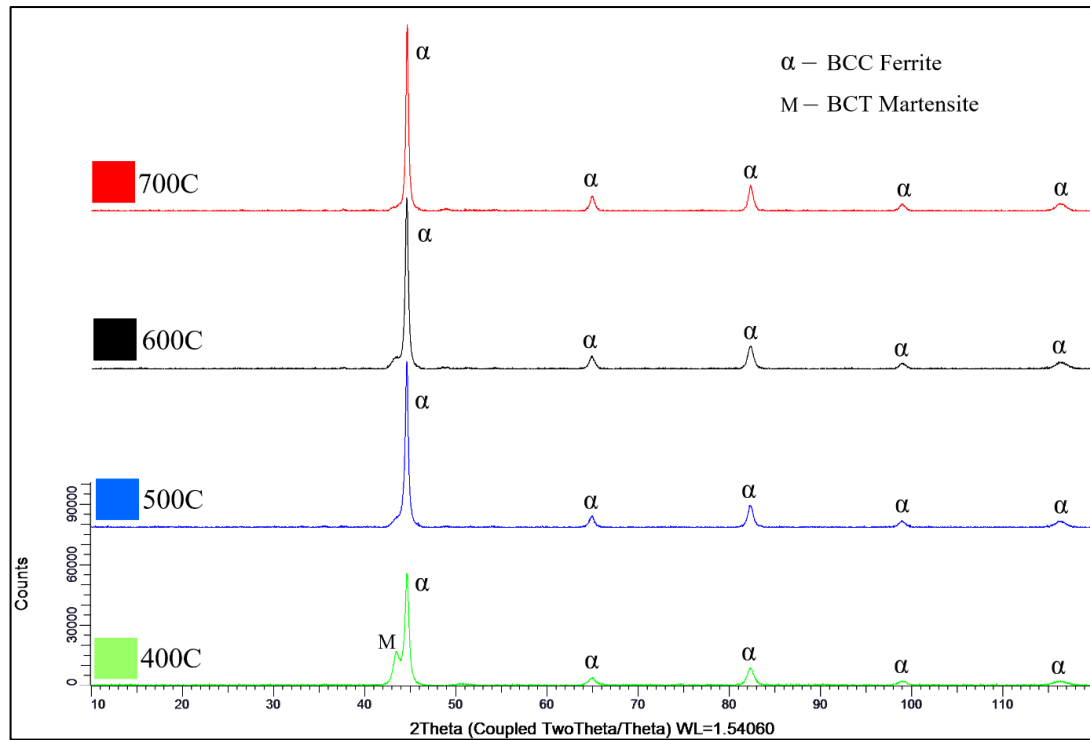
Figure 7.4 - XRD compositional peaks of the four disc conditions.

Micro and macro indentation hardness measurements (Figure 7.5) showed that hardness values decreased with increasing tempering temperature from 400HV at 400C to 200HV at 700C. The annealed pins were also approximately 200HV.
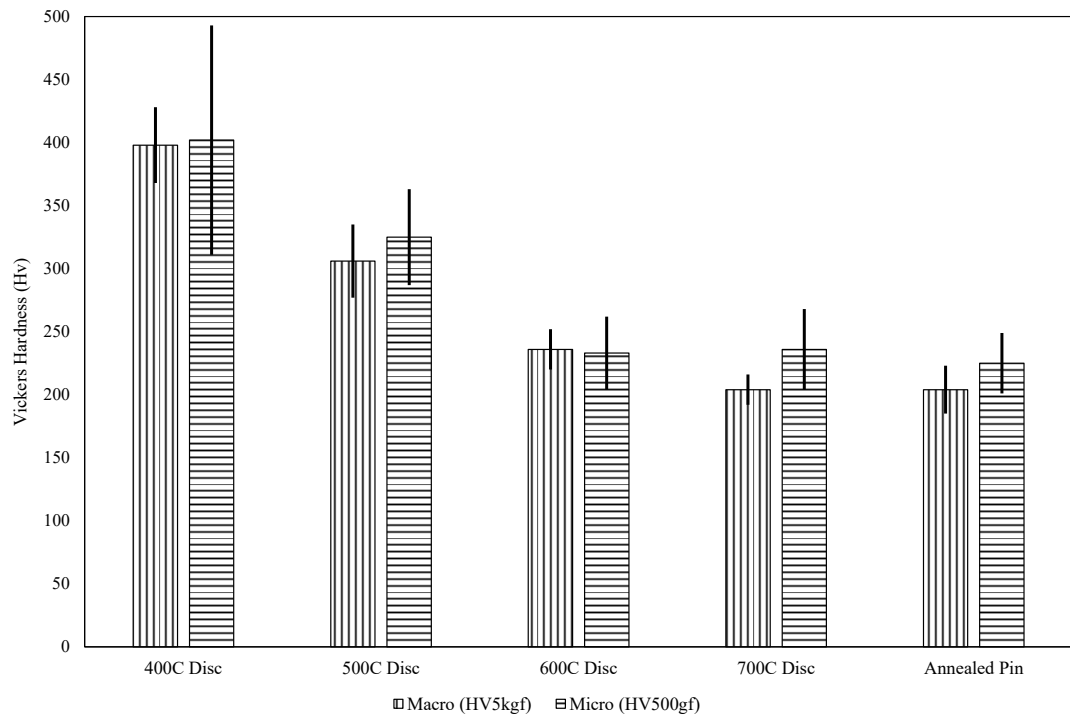
Figure 7.5 - Micro and macro indentation Vickers hardness values. N = 10 for micro indentation hardness values and N = 5 for macro indentation hardness values.

The pin on disc results show the volume loss values of the discs (Figure 7.6) and respective pins (Figure 7.7) from sliding wear.

For both discs and pins, the standard deviation of results generally increased with load. The disc volume loss values (Figure 7.6) show that the 700C discs experienced the highest volume losses for all loads, and that the 500C discs experienced the lowest volume losses for all loads, with the 400C and 600C discs falling in between these extremes.

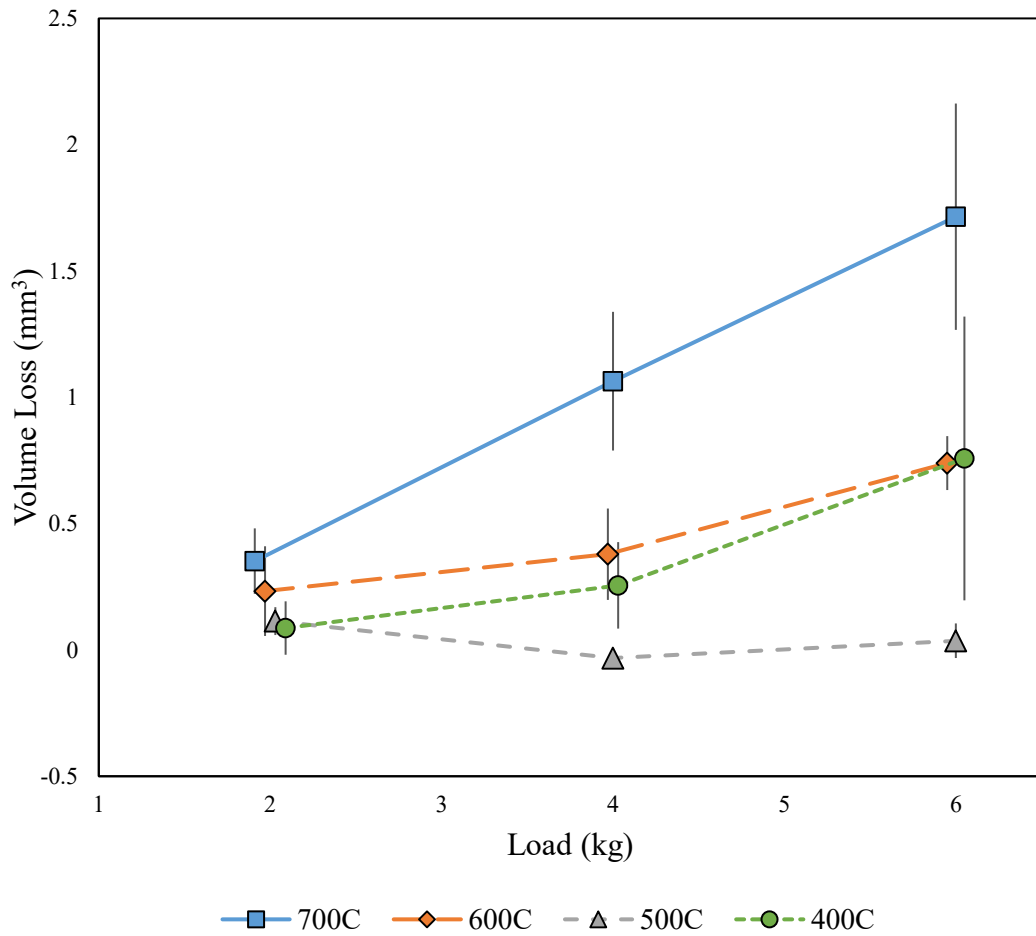Figure 7.6 - Volume loss results of the four degrees of tempered cast iron discs from being worn against the annealed pins. N = 3 for all tests.

The pin volume losses (Figure 7.7) generally increased and diverged with load.
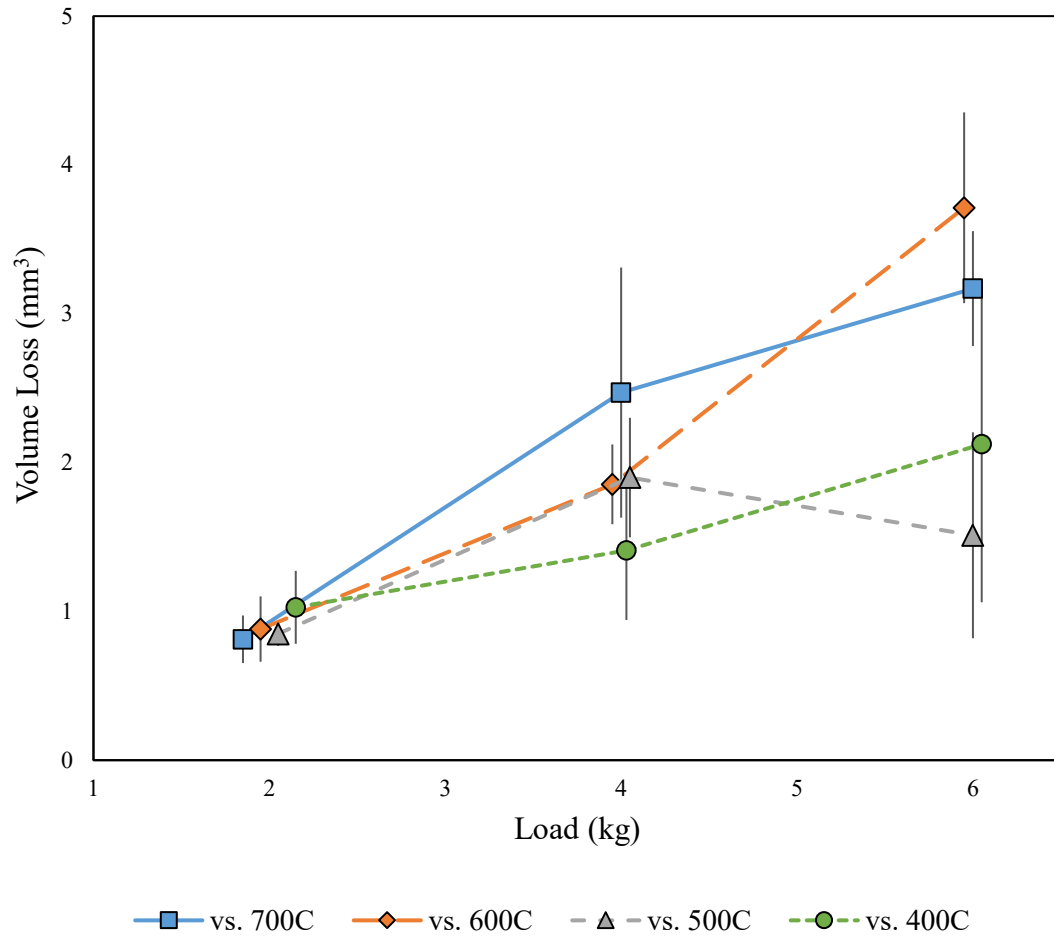
Figure 7.7 - Volume loss results of the annealed cast iron pins from being worn against four degrees of tempered cast iron discs. N = 3 for all tests.

Examining the worn surfaces using SEM showed damage mechanisms occurring near the end of the test (such examinations do not reveal wear mechanisms occurring at the start of the test as evidence would have been erased from further sliding cycles (following the initial running-in period, however, no transitions were observed to have occurred)). Oxidative wear was common for all discs and was the dominant mechanism at lighter loads (Figure 7.8(a)). Many worn surfaces were covered in oxide islands with little damage to the metallic surface. Residual grinding lines were often observed indicating that the pin did not wear itself into the disc surface significantly.
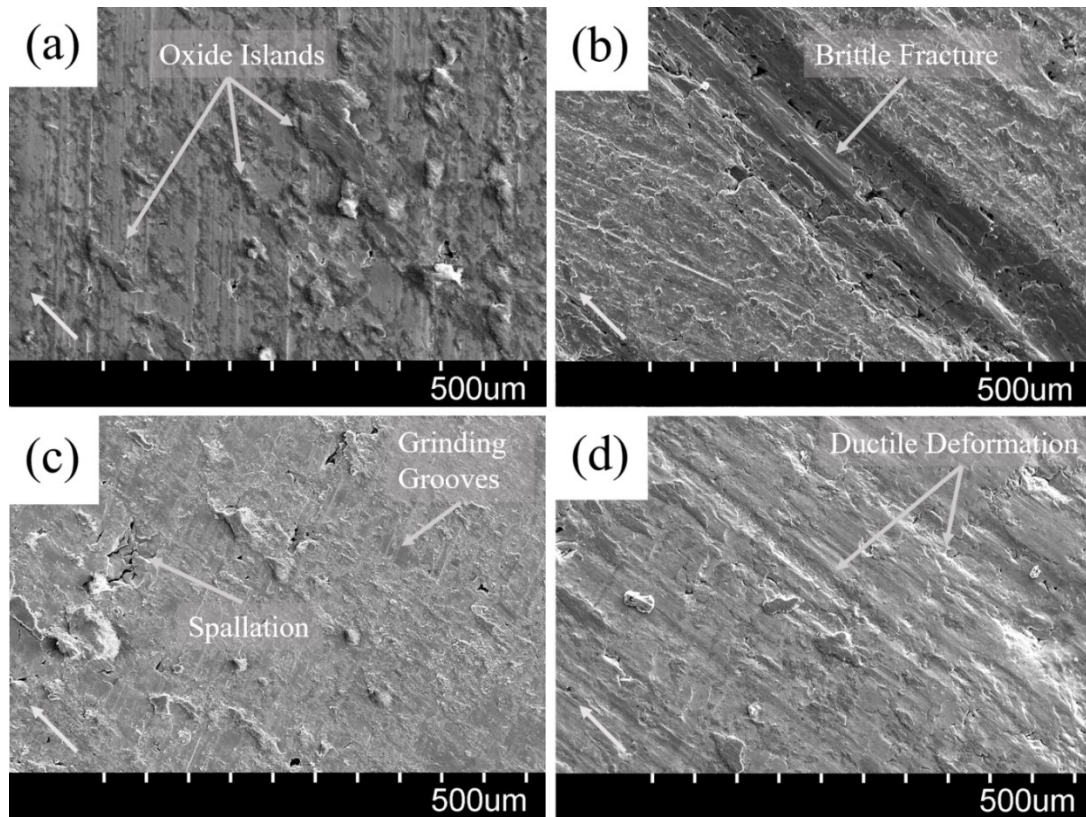
Figure 7.8 - Resultant disc damage on (a) 400C 2kg, (b) 400C 6kg, (c) 700C 2kg, (d) 700C 6kg [x100].

At higher loads, further damage of the metallic matrix took place which was seen through the presence of scuffing, scoring, and ploughing (Figure 7.8(b, d)). The softer discs deformed more plastically than the harder discs.

The difference between mild oxidative wear and severe mechanical wear was also observed in the cross-sectional profiles of the disc wear scars (Figure 7.9). The mild wear scars were indistinguishable from the unworn surface cross-section (seen from 0 – 2mm and from 8 – 10mm). Conversely, the more worn wear scars showed peaks and troughs of mechanical damage mechanisms.
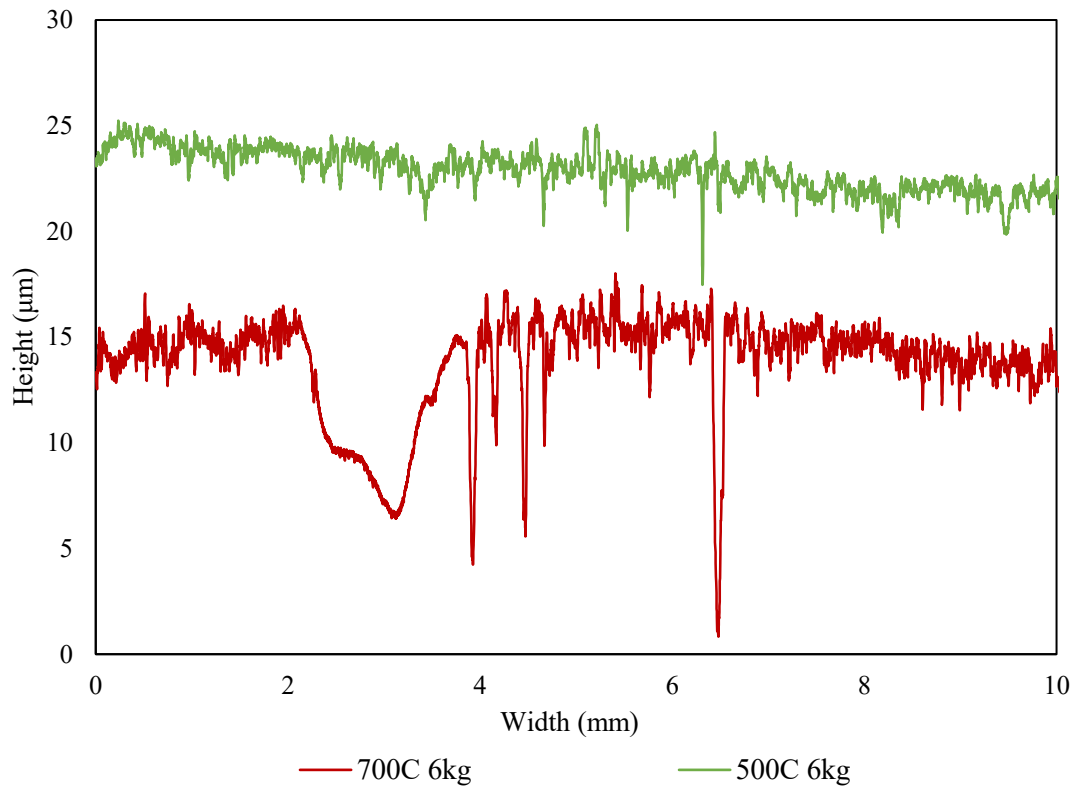
Figure 7.9 - Cross-sectional profiles of (green) oxidative wear scar and (red) oxidational + mechanical damage wear scar.

Disc wear scar surface roughness (Figure 7.10) showed that at 2kg and 4kg, roughness increased with tempering temperature. As load increased to 4kg, 700C and 600C increased in roughness while 500C and 400C decreased in roughness. Moreover, the order of roughness was maintained. At the highest load, three of the four combinations showed large standard deviations. The 700C, 600C, and 500C discs displayed a decrease in roughness, relative to 4kg applied load, and were in the same order. Conversely, the 400C scars increased in surface roughness and display a large standard deviation.
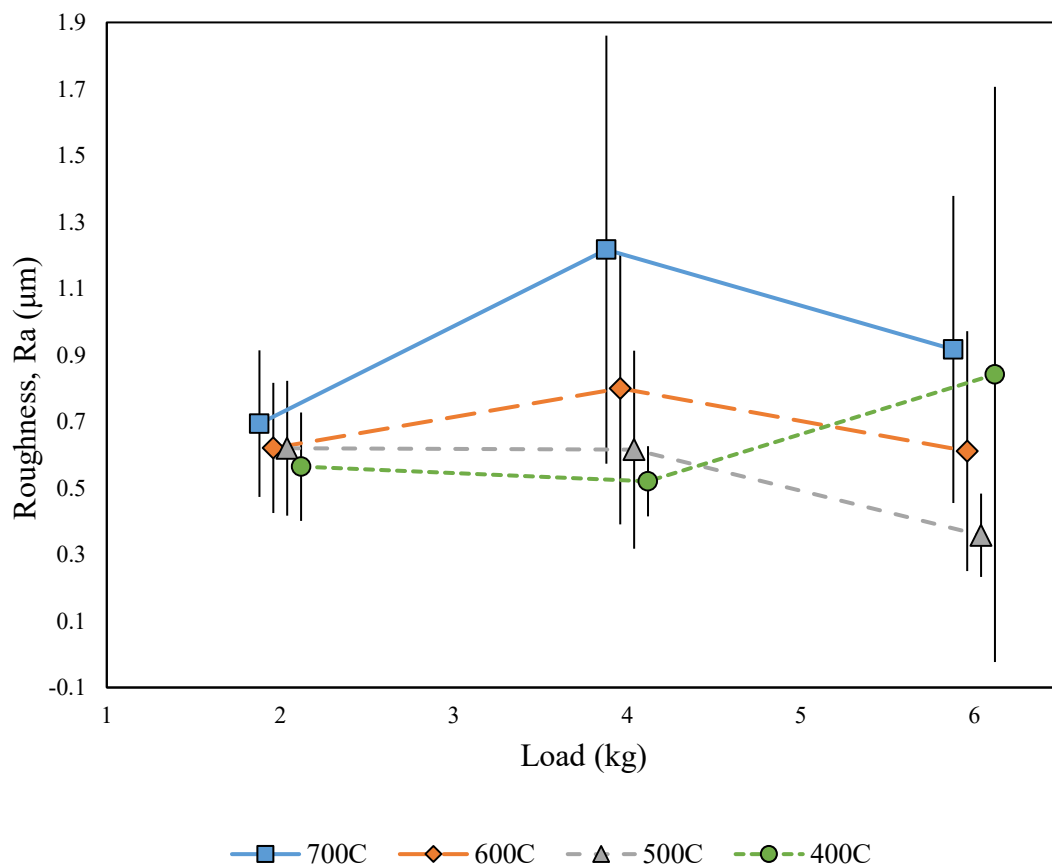
Figure 7.10 - Wear scar surface roughness, Ra. N = 3.

Oxide coverage varied with load. At 2kg, the oxide often appeared as smaller, crumbly islands on the surface, frequently worn off as powder. At higher loads, the oxide was an adhered layer which would instead spall, exposing fresh metal underneath to then oxidise (Figure 7.11).
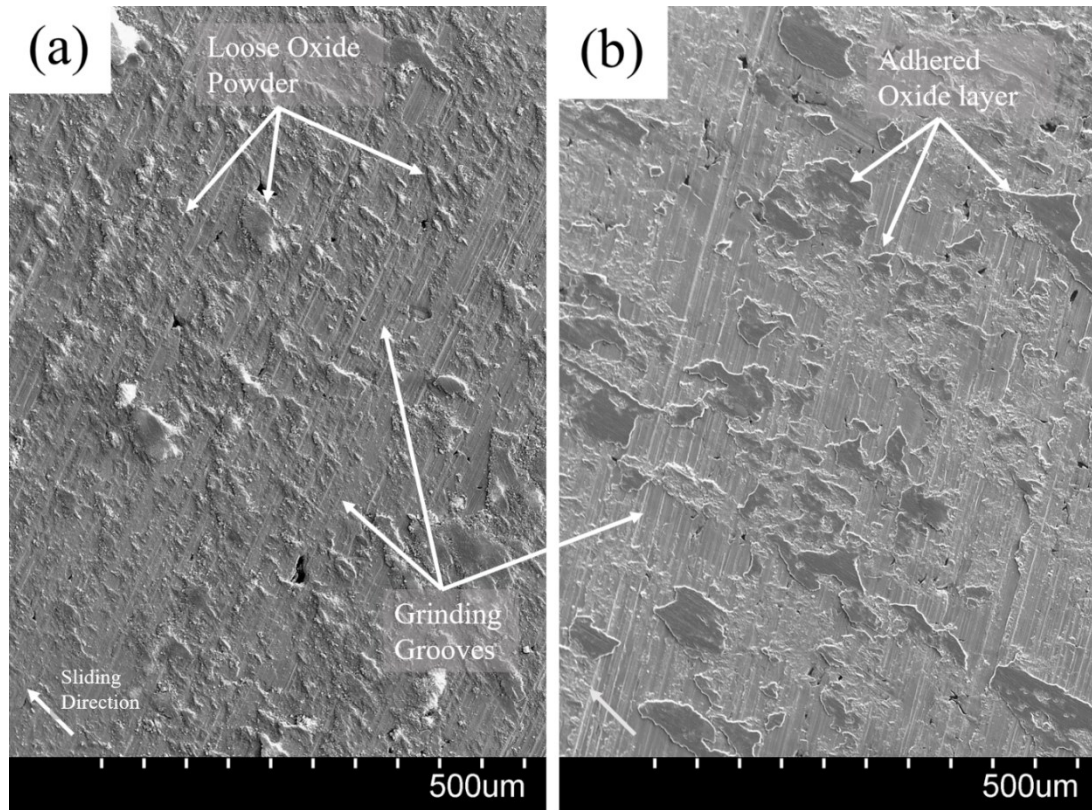
Figure 7.11 - Resultant disc damage on 500C discs from loads of (a) 2kg, (b) 6kg [x100].

Fewer oxide products were observed on the worn surfaces of the annealed pins, either due to a lack of oxidation occurring or because of transfer to the disc counter body. Many pins instead displayed highly polished areas with smooth, featureless surfaces at 2kg applied load (Figure 7.12). Such polishing effects have previously been observed for the same alloy [7.18]. In these particular areas, the only notable features were the exposed graphite cavities (Figure 7.13) from spallation.
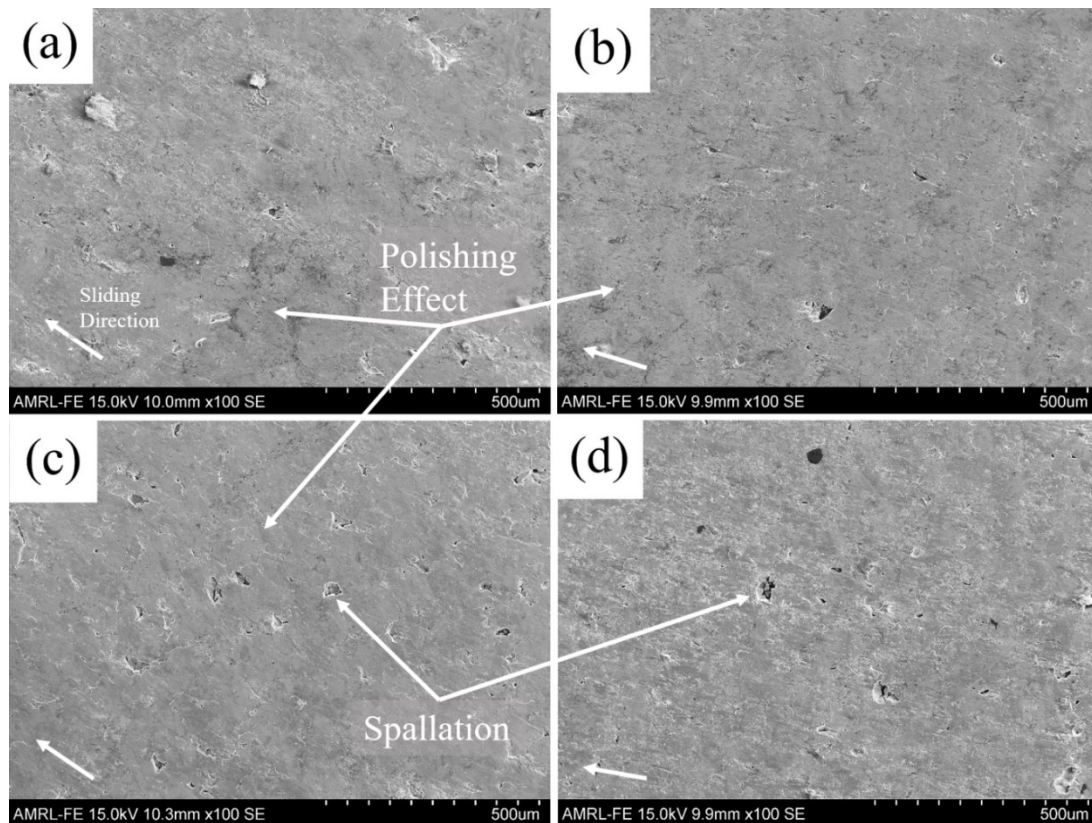
Figure 7.12 – Resultant 2kg pin damage on (a) 400C (b) 500C (c) 600C (d) 700C pins [x100].
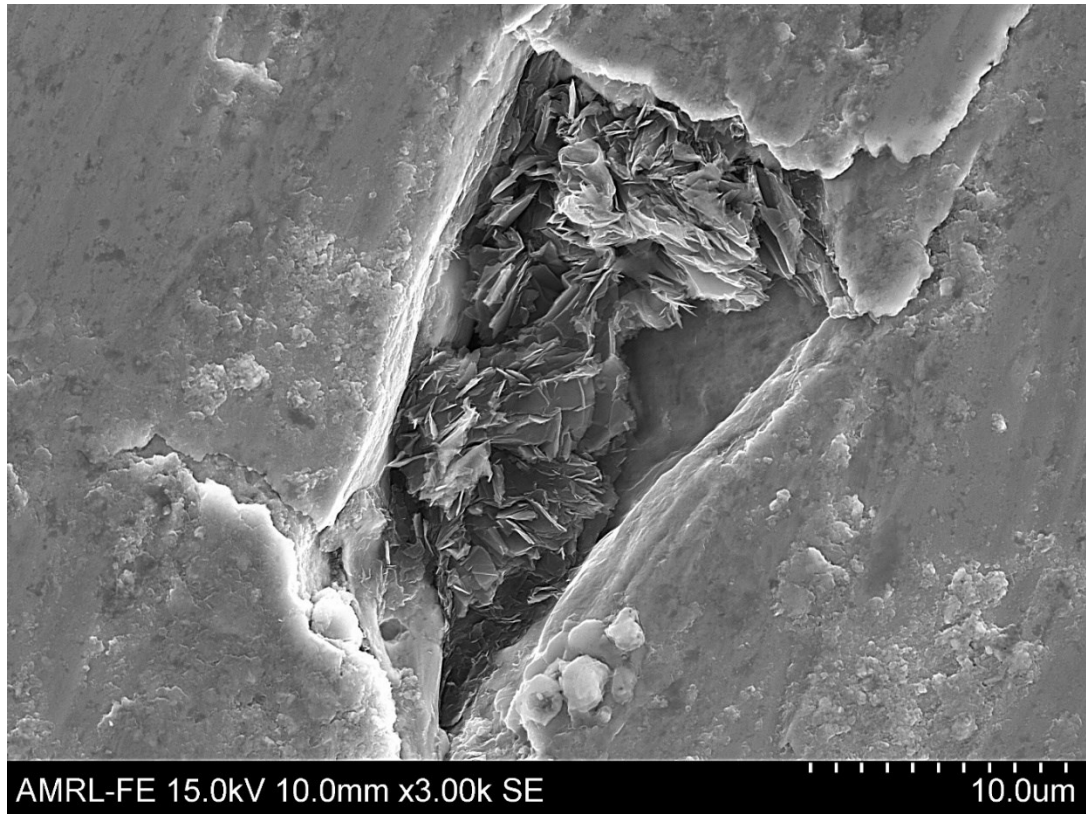
Figure 7.13 - Exposed graphite flake following spallation of the metallic cavity roof [x2000].

At 6kg applied load, more damage mechanisms occurred on the pin worn surfaces (Figure 7.14), such as increased oxidation and brittle ploughing. The pins worn against the acicular martensitic discs and the pins worn against the spheroidised carbide discs wore differently, whereby the former experienced more brittle ploughing with the latter experiencing more oxidation.
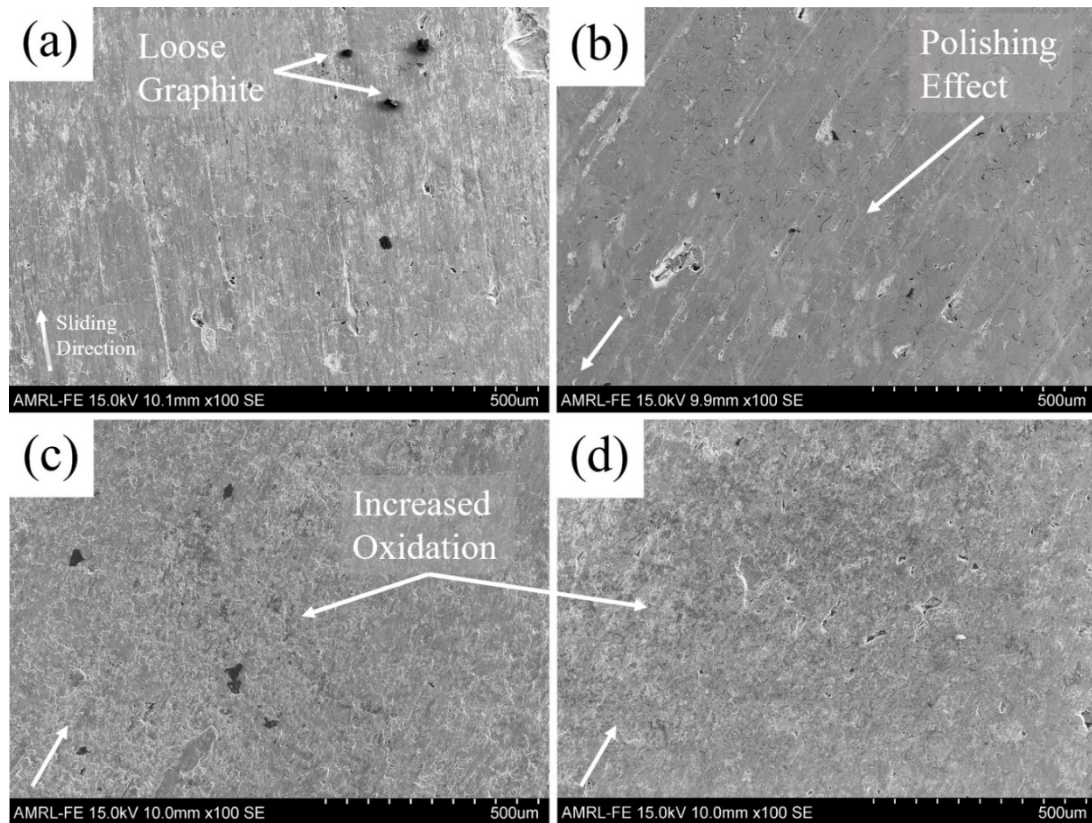
Figure 7.14 - Resultant 6kg pin damage on (a) 400C (b) 500C (c) 600C (d) 700C pins [x100].

Microstructural subsurface deformation was readily visible in the annealed pin cross-sections (Figure 7.15). Cementite lamellae deformed in the direction of sliding, parallel to the worn surface. Other features of subsurface deformation include ferrite grain strain (Figure 7.15(b)) and fracture of lamellae (Figure 7.16).
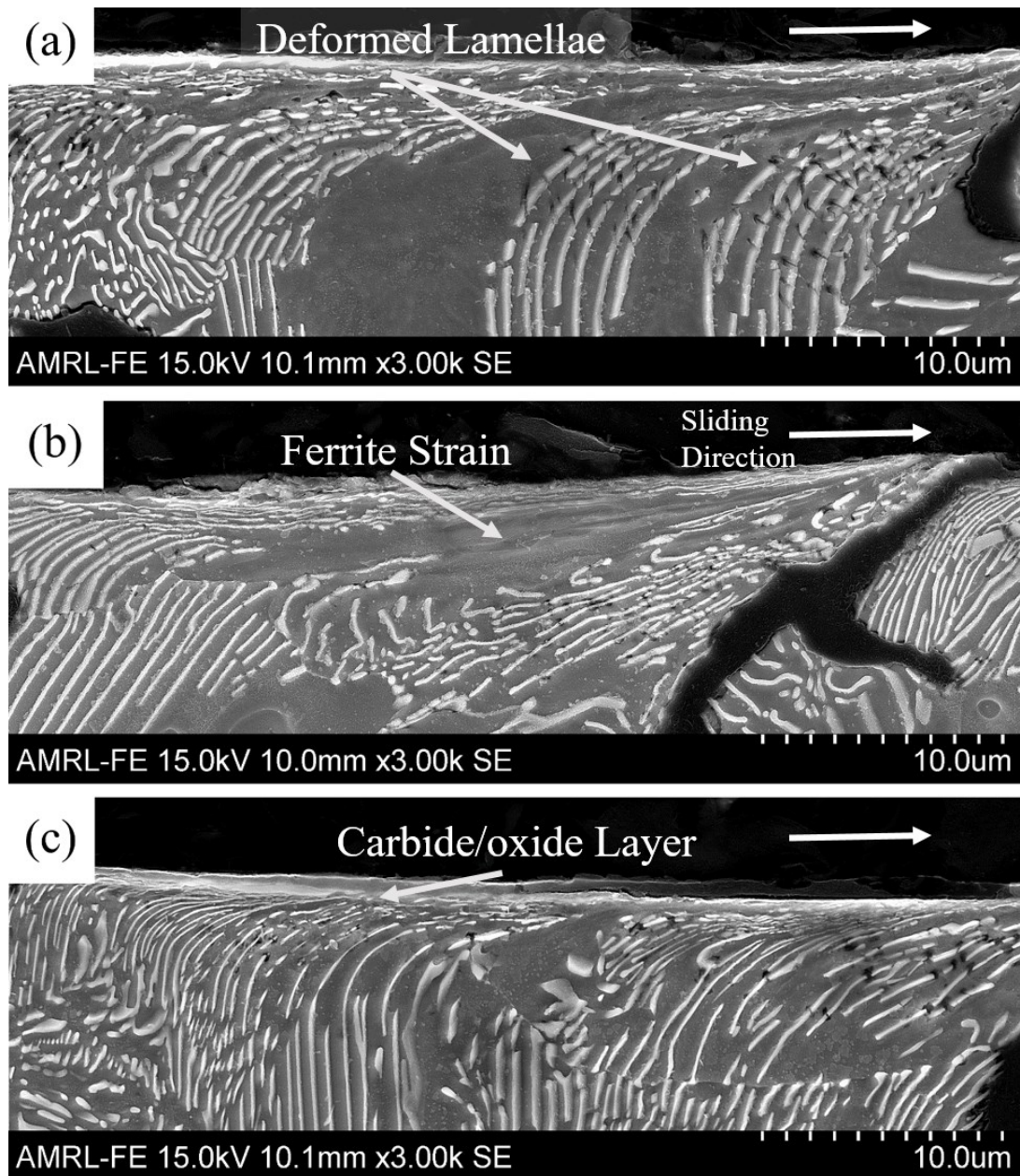
Figure 7.15 - Microstructural subsurface deformation of annealed pins. (a – c) From being worn against a 600C disc at 4kg applied load [x3000 – nital].

Dark areas surrounded the lamellae fracture sites (Figure 7.16), highlighting the voids left from delamination between the ferrite matrix and cementite plate.
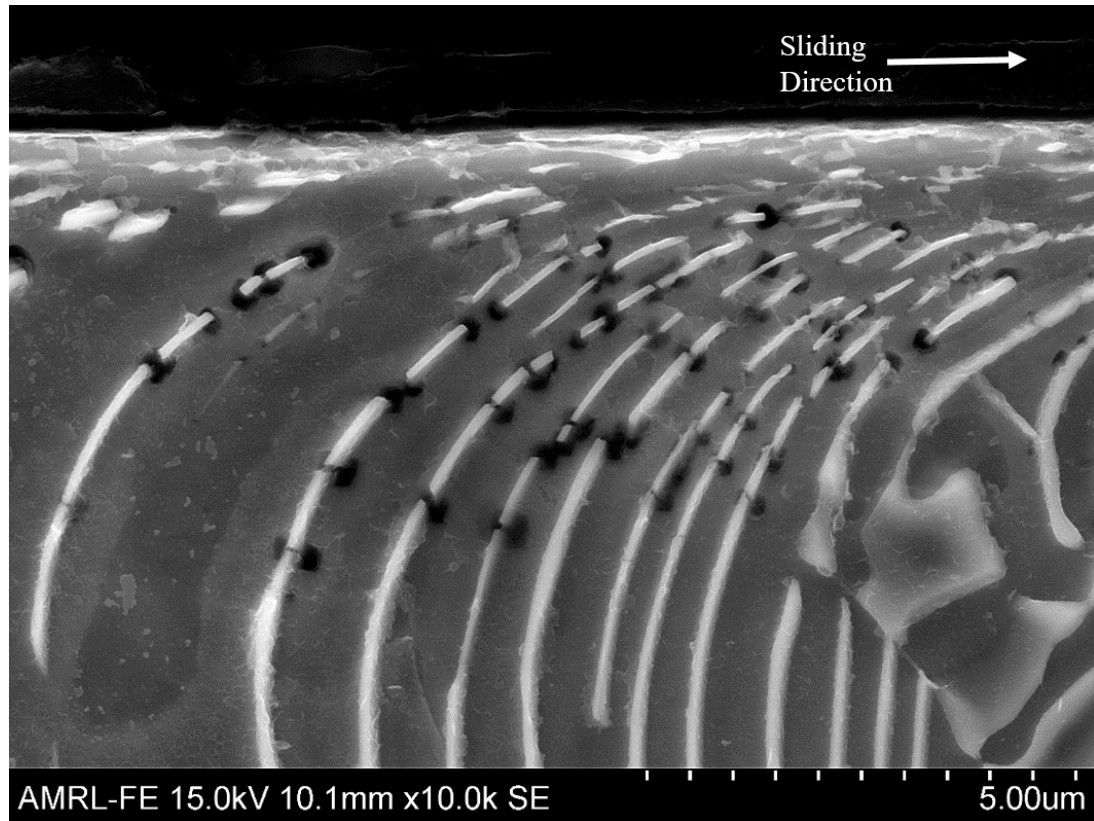
Figure 7.16 - Fractured cementite lamellae from sliding deformation [x10,000 – nital].

Near to the surface, lamellae sometimes refined and compacted into a mechanically mixed carbide-oxide layer (Figure 7.17, Table 7.2).
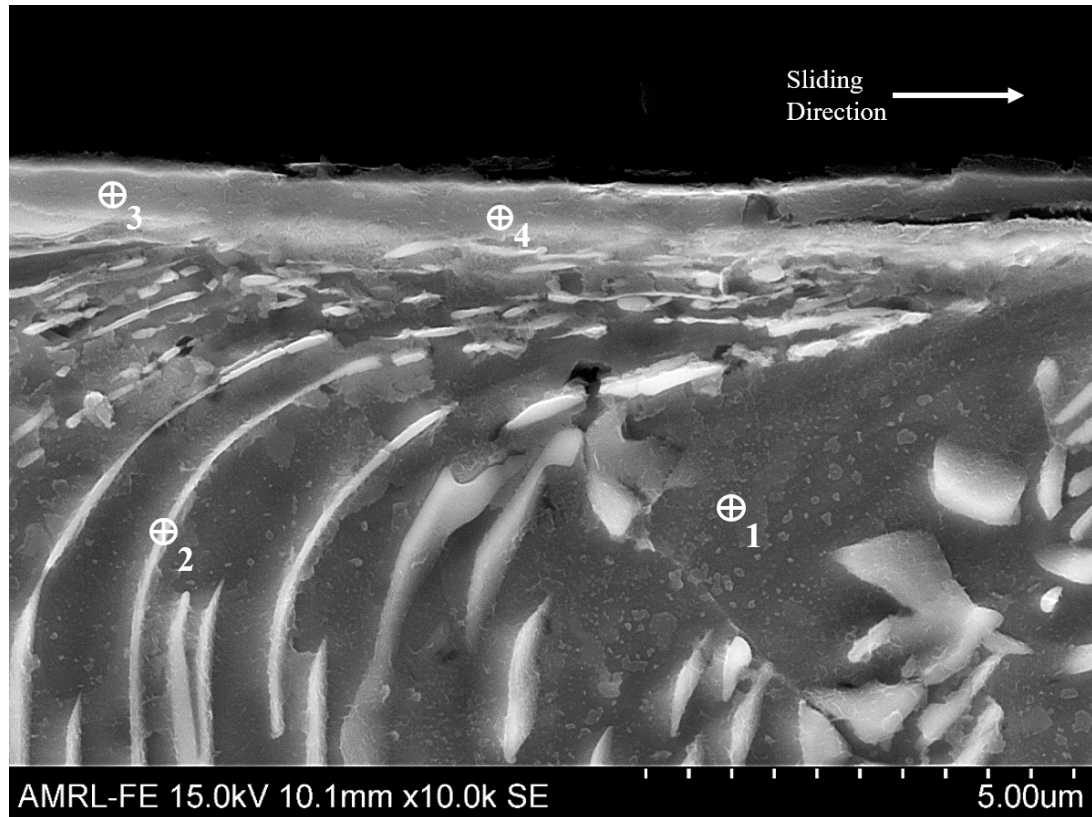
Figure 7.17 - Carbide/oxide surface layer and EDS points on 500C 6kg disc [x10,000 – nital].

Table 7.2 - EDS analysis of pin subsurface from Figure 7.17. Bold signifies changes from the bulk microstructure.

Spectrum	C	O	Mg	Si	Mn	Fe	Cu	Zn
1	4.23	-	-	2.82	0.4	90.8	1.76	-
2	6.09	1.63	-	2.63	0.39	87.64	1.61	-
3	**73.97**	**7.38**	-	0.72	-	**17.62**	-	0.31
4	**73.6**	**5.82**	0.12	0.77	-	**19.41**	-	0.28

Subsurface deformation was also visible in the spheroidised carbide globule discs (Figure 7.18). These discs only displayed such deformation through strained and directional ferrite grains. The strained directional ferrite is readily discernible in comparison to the bulk microstructure of the disc sample, showing non-directional equiaxed grains of ferrite.
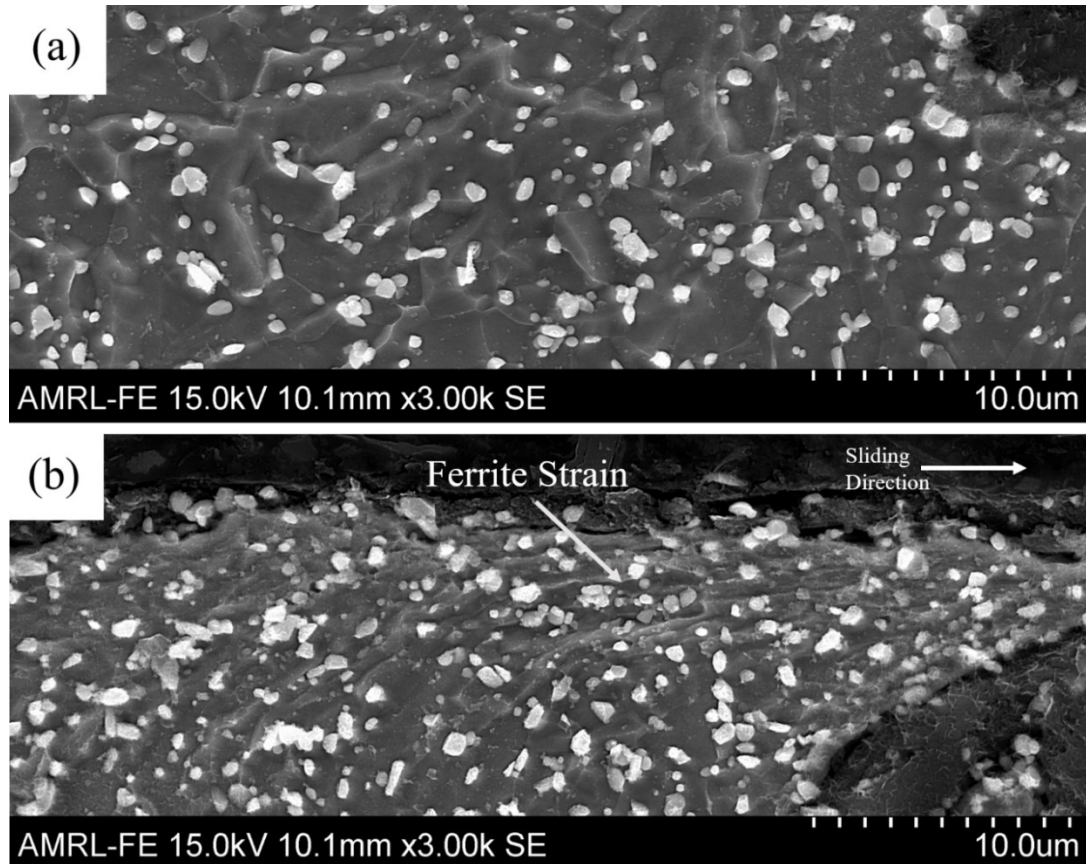
Figure 7.18 - (a) Bulk microstructure of 700C disc (b) subsurface deformation of 4kg 700C [x3000 – nital].

7.4.   Discussion

7.4.1.   Carbide Morphology

Hardness values are good indicators of wear resistance, however, microstructural morphology is also critical in governing the wear response. This has been documented by Diao et al. [7.19], Zambrano et al. [7.20], and Haseeb et al. [7.9] who tested steels and cast irons with the same hardness but different microstructures. The 600C discs, 700C discs, and annealed pins discussed herein have similar hardness values (Figure 7.5). However, different wear responses arise from the increased coarsening of the

carbide globules from 600C to 700C, and the pearlitic/ferritic microstructure of the annealed pins. Mechanistically, such differences between 600C and 700C may arise from the coarsening of carbide globules resulting in more abrasive action between the two worn surfaces [7.21], causing self-damage or wear to the counter body. Moreover, the coarsening of the globules reduces their reinforcement effect on the ferrite matrix, producing a greater vulnerability to damage mechanisms such as scoring and ploughing. Regarding the annealed pins, the mix of coarse pearlite and ferrite (Figure 7.1) bestows a harder bulk microstructure due to having cementite lamellae – plate morphology – instead of free carbide globules, resulting in greater resistance to deformation [7.17].

7.4.2.   *Crystallographic Transformations*

Disc hardness decreases with tempering temperature (Figure 7.5), which has also been observed by Vadiraj et al. [7.10]. The 400C discs show the maximum hardness (400HV), followed by the 500C discs (300HV). This decrease is due to two factors: the transformation from BCT martensite to BCC ferrite at approximately 400°C, and the loss of acicular morphology between 500°C and 600°C. The former transformation is observed through the XRD compositional analyses for the 400C discs (Figure 7.4), and indicates that the process of ferrite transformation is partially underway but not complete at 400°C. In contrast, the 500C disc scan only displays peaks for BCC ferrite indicating complete transformation. Despite this transformation, the 500C discs still display an acicular microstructure (Figures 7.2, 7.3), where the original acicular morphology of the BCT martensite remains while the underlying matrix has transformed to BCC ferrite. This change from acicular martensite to spheroidised carbide globules within equiaxed grains of ferrite was also observed by Trevisiol et al. [7.8], who noted this occurred around 500°C for their 35NCD16 steel. In this chapter, optical observation showed little difference between 400C and 500C discs, apart from a slight rounding of the needles (Figure 7.2). Through SEM, more contrast is seen (Figure 7.3) where coarsening and rounding of the needles indicate the eventual change to spheroidised carbides. The decrease in hardness from 500C to 600C (Figure 7.5) indicates that the change to ferrite with carbide globules also influences mechanical properties.

7.4.3.   Oxidative Wear

Despite the different hardness levels of the discs, their volume loss values (Figure 7.6) are similar. This is due to the dominance of oxidative wear [7.22]–[7.24] for most sliding pairs. Such typical wear behaviour is often seen for cast iron and alloy steels, and has been observed by Haseeb et al. [7.9] for cast irons in sliding. In the absence of wear transitions [7.25], oxidative wear produces little variation, even with changing parameters.

Mild wear occurs after establishment of an oxide glaze layer [7.26]–[7.29], and this persists, in most cases, for all loads discussed herein. Furthermore, inspection of the disc wear scars (Figures 7.8, 7.11) shows predominantly oxide islands, with other forms of damage only occurring at the highest applied load. The cross-sectional profiles (Figure 7.9) show that the oxidative mild cross-section worn area is barely distinguishable from the unworn surface, whereas the severe cross-section worn area has large peaks and troughs from ploughing action. Apart from these local areas of damage, the majority of the worn area is similar in roughness and waviness to the milder scar, showing that mild oxidative wear is still the dominant mechanism at higher loads. This is also apparent in the roughness values, Ra, of the disc wear scars, which are mostly similar and in the same order apart from the most brittle disc at the highest load. A key difference between the findings discussed presently and those of Ouyang et al. [7.6] is that no wear transition between mild and severe occurred for any samples or loads. The researchers [7.6] noted a transition to disproportionately higher volume losses when load increased beyond 90N at 1.06m/s, 80N at 1.47m/s, and 60N at 1.88m/s. However, as these variables are not consistent with those presently utilised, and through the use of different alloys, the exact points of wear transitions are likely to be different.

7.4.4.   The Influence of Hardness

The disc volume losses (Figure 7.6) show that the 700C discs experienced the most wear, followed by 600C, 400C, and 500C. The acicular martensite outperforming the spheroidised structure is in agreement with the volume loss results obtained by Ouyang et al. [7.6], who found that the 4Cr13 stainless steel tempered at 550°C lost more material than those tempered at 350°C and 200°C for all experimental conditions.

Of the two acicular martensitic discs discussed in this chapter, the harder 400C was outperformed by 500C. This is due to excessive brittleness causing the 400C discs to have more local areas of mechanical damage. SEM inspection shows that the 400C discs display some areas of severe brittle ploughing/scoring while the 500C discs only show partially spalled oxide coverage (Figures 7.8, 7.11). The combination of these areas of mechanical damage and areas of mild oxidation, on the same 400C discs, are responsible for the high values of standard deviations in their roughness, Ra, values. The brittleness of the 400C discs is due to their unique combination of BCT crystal structure and acicular morphology. In contrast, the complete transformation to BCC ferrite allows the 500C acicular martensitic discs to deform more plastically, avoiding the brittle fracture mechanisms, and therefore only experience oxidative wear. The higher losses of the 700C discs are due to the inability of the microstructure to effectively support a protective oxide layer at the highest loads. Should the substrate deform and distort in a significant way, the oxide glaze layer destructs and the beneficial oxidation – scrape – re-oxidation [7.30] feedback loop does not arise. Wei et al. [7.7] attributed the same reason for why their H13 steel pins tempered at 700°C experienced the highest volume losses.

Disc wear scar surface roughness trends, values, and standard deviations (Figure 7.10) are indicative of their corresponding wear mechanisms. At 2kg applied load, the roughness values are similar and display small standard deviations, as per the volume loss results (Figures 7.6, 7.7). At this load, little distinction exists because the majority of damage is only mild oxidative wear for all combinations. Oxidative wear is governed by surface conditions and testing parameters more so than microstructural condition, so at 2kg, the various microstructural conditions have minor effects on wear mechanisms and therefore also the roughness.

Despite this, at 2kg and 4kg it can be observed that roughness increases with tempering temperature in accordance with the hardness measurements (Figure 7.5) and volume loss results (Figures 7.6, 7.7). The higher tempering temperature produces spheroidised carbides in an equiaxed ferritic matrix (Figures 7.3(c, d)), which increases the propensity for mild scoring and mild ploughing to occur, resulting in a rougher wear scar. The harder, acicular, microstructure of the 400C and 500C discs can resist such damage at 2kg and 4kg and thus produce smoother wear scars.

Additionally, as load increases to 4kg, the 700C and 600C wear scars increase in roughness while 500C and 400C slightly decrease/remain at similar values. The increase for 600C and 700C is attributed to more plastic deformation causing perturbations on the wear scar surface. The minor decrease in roughness for 400C and 500C at 4kg applied load is postulated to be caused by the similarity in wear mechanisms for these discs at 2kg and 4kg. As 400C and 500C both have acicular microstructures, they are resistant to plastic deformation and instead exhibit oxidative wear at both 2kg and 4kg, resulting in similar roughness values.

At 6kg applied load, the 700C, 600C, and 500C wear scars experience a reduction in roughness compared to 4kg. Conversely, 400C increases in roughness and displays a large standard deviation. This increase is due to the inability of BCT martensite (which only the 400C discs consist of) to plastically deform and therefore experiences brittle fracture (Figure 7.8(b)) which increases the measured roughness. These instances of brittle damage also corrupt the measurement of roughness, resulting in the large standard deviation seen for 400C at 6kg. This is accomplished through the mixture of smooth intact surface morphology and brittle damage areas, the summation of which corrupts the measurement of Ra and gives a large scatter. The decrease is roughness for the other combinations is postulated to be due to increased plastic deformation resulting in more smearing than ploughing or scoring, which could smoothen out areas of graphite flake cavity spallation.

7.4.5.   Damage Mechanisms

The annealed pin volume losses (Figure 7.7) display similar values at 2kg but diverge at 4kg and 6kg due to amplification of their different wear responses from the increased load. Although both disc and pin experienced low volume losses, the values of the pin are approximately double that of the discs, due to microstructural considerations (coarse pearlite/ferrite versus tempered martensite) and the effect of the tribosystem (such as the worn area of the disc being allowed to cool between cycles whereas the pin is unable to due to experiencing constant contact).

SEM inspection showed exposed graphite flake cavities on the surfaces of all sliding samples (Figures 7.8, 7.12, 7.13, 7.14), indicating that flake cavity spallation is a damage mechanism that occurs for all loads and microstructural conditions. Exposed cavities frequently contain partial or full graphite flakes. Detached flakes can either

be ejected onto, or sheared out along the sample surface, entering into the tribosystem. Evidence of graphite ejection, in the form of 3D chips, can be seen in the SEM inspection of the worn surfaces (Figure 7.14(a)), while some evidence of beneficial shearing can be seen in the microstructural inspection of the subsurface (Figure 7.18(b)).

Beneficial graphite solid lubrication smearing was not observed during SEM inspection of the worn surfaces. This could be due to a number of reasons, such as it being removed during the post-test treatment, mixed in with or indistinguishable from the surface oxides, thin-film coverage rendering it invisible, or it simply being a rare occurrence. It is though that the latter is most likely, and that this rarity may be a result of the test conditions used, such as the relatively high sliding speed of 0.5 m/s for all tests. It is suspected that slower speeds would be more conducive to producing a beneficial graphite film due to the lower likelihood of graphite being expelled from the wear scar outward away from the samples, in addition to less destructive energy inputted to the contact faces which would allow for the flakes to beneficially smear. Intact 3D chips of graphite were observed in several instances (Figure 7.14(a)) on the worn surface of some samples, indicating that the expulsion of chips is more common than the smearing phenomena. Despite this, should graphite lubrication smearing occur, it is more likely to arise for the 600C and 700C discs than the 400C and 500C discs, as it is known to occur more readily for alloys with softer matrices [7.31]–[7.33].

7.4.6.   *Subsurface Deformation*

Subsurface microstructural deformation is important to analyse because it influences the subsequent wear occurring at the surface. Such subsurface microstructural deformation is visible in the annealed pins and spheroidised carbide discs (Figures 7.16 – 7.18) but not in the acicular martensitic discs. Such deformation occurs due to a combination of load and speed inputting energy to the contact faces. This energy is dissipated through a number of ways such as heat, volume loss, transformation, and chemical reactions (oxidation), as discussed by Kato [7.34]. An additional energy output is through the deformation of the material under the wear surface. The volume loss results and SEM inspection of the worn pin end faces show that the pin experienced more damage than the discs. This repeated wearing of the pin surface results in subsurface shear stresses which alters the directionality of lamellae. Subsurface deformation is highly localised due to grain orientation, where significant

deformation can be seen in certain grains directly adjacent to others that show no signs of directionality.

The refinement and convergence process of cementite lamellae is a continuation of directional deformation. As lamellae are deformed in the direction parallel to the surface, the inter-lamellar spacing, and lamellae width, decreases. Successive refinement and convergence with surface oxides results in the conglomeration of cementite into a continuous carbide/oxide surface layer (Figures 7.15(c), 7.17). When analysed using EDS, carbon, and to a lesser extent, oxygen, show an increased concentration in the layer (Table 7.2). However due to the small size of the layer, the surrounding Bakelite was also within the x-ray scanning spot which may have influenced the elemental analysis. Subsurface deformation of this kind is beneficial in nature due to the refinement of lamellae resisting plastic deformation and crack propagation. Finer microstructures inhibit dislocation movement and are thus harder than coarser ones.

Cementite lamellae often fracture from deforming in the direction of sliding (Figure 7.15(a), 7.15). This phenomenon is not uniformly constant, as many lamellae deform significantly without fracturing, whereas some fracture at relatively small angles of deformation. Plate thickness, 2D orientation, and curvature also do not correspond to lamella fracture. It is postulated that the primary influence is the 3D orientation of the cementite plate within the matrix, whereby excessive 3D curvature of the lamellae in a different direction to the sliding axis results in fracture. All sites of cementite plate fracture are accompanied by a dark area, postulated to be the void created from delamination of the cementite and ferrite matrix where the lamella originally resided. Such voids may be exacerbated by etching, where the nital may penetrate the delaminated area and result in localised crevice corrosion. Such fracture of lamellae and delamination of the lamellae-matrix interface is detrimental to further sliding wear resistance due to the stress concentrations surrounding such voids and their potential to serve as crack initiation sites.

Strained ferrite grains were the only visible subsurface feature seen in the carbide globule discs (600C and 700C) (Figure 7.18). The carbides in these discs do not show directionality like the pearlitic pins as an innate consequence of their morphology. However, the ferrite grain strain is readily visible and more pronounced than in the

annealed pins, due to the cementite lamellae in such pins being a barrier to matrix strain in most cases. Visible ferrite strain in this manner may also vary grain-to-grain due to local variations in the alloy chemistry. Vadiraj et al. [7.10] noted that wear resistance is a function of solid solution elements within the ferrite matrix. In G350 cast iron, local variations of such elements may be of significance, such as partially dissolved phosphide eutectic altering the ferrite wear resistance. Distorted ferrite grains are beneficial in sliding wear due to the increased hardness of the grain bestowing superior wear resistance and thus lowering material removal rates.

7.5.   Conclusions

The pin-on-disc sliding wear response of G350 tempered martensitic grey cast iron discs against pearlitic pins of the same alloy was discussed in this chapter. Four conditions of tempered martensite, and annealed pearlite/ferrite, were examined.

- A microstructural transition occurred when tempering between 500°C and 600°C. Tempering at 500°C and below resulted in acicular martensitic microstructures, whereas tempering at 600°C and above produced spheroidal carbide globules in equiaxed ferrite matrices.

- XRD showed that the 400C discs were partially BCT martensite while the other discs were BCC ferrite, indicating that the transformation to BCC ferrite is complete by 500°C. The loss of the acicular martensitic matrix in the 600C and 700C discs indicates that this evolution is complete by 600°C.

- Hardness values decreased from 400HV for the 400C discs, to 315HV for 500C, to 230HV for 600C, to 215HV for 700C discs. The small decrease between 600C and 700C show that further tempering has minimal influence on indentation hardness. The annealed coarse pearlitic pins displayed a hardness of 215HV.

- Pin-on-disc sliding wear volume losses were low for all combinations. The 700C and 600C discs produced the highest volume losses due their spheroidal carbide microstructural morphology. Of the acicular martensitic discs, 400C showed

higher volume losses than 500C due to excessive brittleness resulting in fracture of the matrix in some areas.

- Most combinations produced only mild oxidative wear. Residual grinding grooves were visible for most disc wear scars, indicating that the pin was unable to break-in to the disc surface. Many pins showed polished, reflective sections on the worn surface instead of metallic damage mechanisms. Due to the presence of graphite flakes, spallation was the most common mechanism to be seen for all samples.

- Microstructural subsurface deformation was visible in the annealed pins and spheroidised carbide discs. Cementite lamellae were deformed in the direction of sliding. Near the surface, lamellae were refined and converged into a mechanically mixed carbide/oxide layer. Lamellae would often fracture due to excessive deformation, however the occurrence of this is inconsistent and influenced by 3D factors. Ferrite strain was visible where grains significantly deformed due to energy input from sliding.

References

[7.1] R. E. Smallman and A. H. W. Ngan, "Cast Irons," in *Physical Metallurgy and Advanced Materials*, 7th ed., Elsevier, pp. 455–458.

[7.2] ASM International, "Permanent Mold Casting," in *Volume 15: Casting*, 1998, p. 609.

[7.3] L. Wei, Z. Zhang, S. Nie, and W. Xiangyang, "Direct and indirect corrosion wear erformance of AISI 630 steel for the slipper/swashplate pair in a water hydraulic pump," *Proc. Inst. Mech. Eng. Part J J. Eng. Tribol.*, vol. 233, no. 10, pp. 1605–1615, 2019.

[7.4] H. T. Angus, "Heat Treatment of Grey Cast Irons," in *Cast Iron: Physical and Engineering Properties*, 1960, pp. 355–379.

[7.5] ASM International, "Heat Treating Cast Iron," in *Heat Treater's Guide: Practices and Procedures for Irons and Steels*, 1995, pp. 824–834.

[7.6] J. H. Ouyang, Y. T. Pei, X. D. Li, and T. C. Lei, "Effect of tempering

temperature on microstructure and sliding wear property of laser quenched 4Cr13 steel," *Wear*, vol. 177, no. 2, pp. 203–208, 1994.

[7.7] M. X. Wei, S. Q. Wang, L. Wang, X. H. Cui, and K. M. Chen, "Effect of tempering conditions on wear resistance in various wear mechanisms of H13 steel," *Tribol. Int.*, vol. 44, no. 7–8, pp. 898–905, 2011.

[7.8] C. Trevisiol, A. Jourani, and S. Bouvier, "Effect of hardness, microstructure, normal load and abrasive size on friction and on wear behaviour of 35NCD16 steel," *Wear*, vol. 388–389, no. October 2016, pp. 101–111, 2017.

[7.9] A. S. M. A. Haseeb, M. A. Islam, and M. M. Ali Bepari, "Tribological behaviour of quenched and tempered, and austempered ductile iron at the same hardness level," *Wear*, vol. 244, no. 1–2, pp. 15–19, 2000.

[7.10] A. Vadiraj, G. Balachandran, M. Kamaraj, and E. Kazuya, "Mechanical and wear behavior of quenched and tempered alloyed hypereutectic gray cast iron," *Mater. Des.*, vol. 32, no. 4, pp. 2438–2443, 2011.

[7.11] BSI Standards Online, "BS EN ISO 945-1:2019 BSI Standards Publication: Microstructure of cast irons," 2019.

[7.12] P. J. Blau, J. J. Truhan, and E. A. Kenik, "Effects of the exposure to corrosive salts on the frictional behavior of gray cast iron and a titanium-based metal matrix composite," *Tribol. Int.*, vol. 40, no. 9, pp. 1335–1343, 2007.

[7.13] B. Bhusan, "Wear of Metals and Alloys," in *Introduction to Tribology*, 2nd ed., New York: Wiley, 2013, p. 372.

[7.14] I. Hutchings and P. Shipway, "Sliding Wear," in *Tribology: Friction and Wear of Engineering Materials*, 2nd ed., Butterworth - Heinemann, 2017, p. 293.

[7.15] ASTM Standards, "ASTM G99 - 17: Standard Test Method for Wear Testing with a Pin-on-Disk Apparatus."

[7.16] J. D. Verhoeven, "Spheroidized Microstructures," in *Steel Metallurgy for the Non-Metallurgist*, ASM International, 2007, pp. 35–37.

[7.17] R. G. Woodward, A. Toumpis, and A. Galloway, "The influence of cementite spheroidizing duration on the microstructure and sliding wear response of grey

cast iron against AISI 4330," *Wear*, vol. 488–489, p. 204155, 2022.

[7.18] R. G. Woodward *et al.*, "The Influence of Load on Dry and Tribocorrosive Sliding of AISI 4330 and 15-5PH against Cast Iron The Influence of Load on Dry and Tribocorrosive Sliding of AISI 4330 and," *Tribol. Trans.*, vol. 64, no. 5, pp. 956–967, 2021.

[7.19] G. Diao, Q. Yan, X. Shi, X. Zhang, Z. Wen, and X. Jin, "Improvement of wear resistance in ferrite-pearlite railway wheel steel via ferrite strengthening and cementite spheroidization," *Mater. Res. Express*, vol. 6, no. 10, 2019.

[7.20] O. A. Zambrano, J. A. Gómez, J. J. Coronado, and S. A. Rodríguez, "The sliding wear behaviour of steels with the same hardness," *Wear*, vol. 418–419, no. April 2018, pp. 201–207, 2019.

[7.21] S. Bhattacharyya, "Wear and friction in steel, aluminum and magnesium alloys I. Pearlitic and spheroidized steels," *Wear*, vol. 61, no. 1, pp. 133–141, 1980.

[7.22] F. H. Stott, "The role of oxidation in the wear of alloys," *Tribol. Int.*, vol. 31, no. 1–3, pp. 61–71, 1998.

[7.23] F. H. Stott and G. C. Wood, "The influence of oxides on the friction and wear of alloys," *Tribol. Int.*, vol. 11, no. 4, pp. 211–218, 1978.

[7.24] M. M. Stack, F. H. Stott, and G. C. Wood, "The effect of pre-oxidation of chromia and alumina forming alloys on erosion in laboratory simulated fluidized-bed conditions," *Corros. Sci.*, vol. 33, no. 6, pp. 965–983, 1992.

[7.25] W. Hirst and J. K. Lancaster, "Surface film formation and metallic wear," *J. Appl. Phys.*, vol. 27, no. 9, pp. 1057–1065, 1956.

[7.26] T. F. J. Quinn, "Role of oxidation in the mild wear of steel," *Br. J. Appl. Phys.*, vol. 13, no. 1, pp. 33–37, 1962.

[7.27] T. F. J. Quinn, "The oxidational wear of low alloy steels," *Tribol. Int.*, vol. 35, no. 11, pp. 691–715, 2002.

[7.28] T. F. J. Quinn and W. O. Winer, "The thermal aspects of oxidational wear," *Wear*, vol. 102, no. 1–2, pp. 67–80, 1985.

[7.29] T. F. J. Quinn, "The effect of 'hot-spot' temperatures on the unlubricated wear

of steel," *ASLE Trans.*, vol. 10, no. 2, pp. 158–168, 1967.

[7.30] I. Hutchings and P. Shipway, "Plasticity-dominated wear," in *Tribology*, 2nd ed., Elsevier Ltd., 2017, pp. 122–125.

[7.31] J. Sugishita and S. Fujiyoshi, "The effect of cast iron graphites on friction and wear performance I: Graphite film formation on grey cast iron surfaces," *Wear*, vol. 66, no. 2, pp. 209–221, 1981.

[7.32] J. Sugishita and S. Fujiyoshi, "The Effect of Cast Iron Graphites on Friction and Wear Performance II: ariables influencing graphite film formation," *Wear*, vol. 68, no. 1, pp. 7–20, 1981.

[7.33] J. Sugishita and S. Fujiyoshi, "The effect of cast iron graphite on friction and wear performance III: The lubricating effect of graphite under rolling-sliding contacts," *Wear*, vol. 77, no. 2, pp. 181–193, 1982.

[7.34] K. Kato, "Wear modes at asperity contacts in tribochemical wear," in *Tribocorrosion of Passive Metals and Coatings*, 2011, p. 79.

Chapter 8.

Conclusions & Further Research

8.1.   Concluding Remarks

This thesis has reported on a number of sliding wear studies on a range of engineering alloys. Four experimental studies have been reported on, in chronological order, which begin with seven engineering alloys and gradually narrow to one. The work covers a range of subtopics in the general tribology field, including comparative material selection, tribocorrosion, and microstructural transformation and its effects on wear. The findings and discussions are generally viewed through the lens of metallurgical engineering, and have an industrial emphasis, meaning that the most of the topics are discussed more from a material science, microstructural, or macro mechanical view point rather than a tribological or contact mechanics one, and that the author has primarily focussed on the practical effects and applications rather than more nanoscale effects or theoretical conclusions such as with modelling studies.

The significant conclusions from each experimental chapter are listed:

- Chapter 4 demonstrated that the sliding wear performance of nitrided steel, with a surface hardness approaching 1000HV, could almost be matched by the oxidative wear exhibited by an untreated alloy steel. This highlighted the proclivity of oxidative wear to produce very mild wear rates through protection of the underlying metallic material.

- Chapter 5 reinforced these observed benefits of oxidative wear through a direct comparison between dry sliding wear and sliding wear while submerged in NaCl solution. The submersion in fluid cooled the surfaces of the samples, preventing oxidative wear for occurring and resulted in higher volume loss for the alloy steel in comparison to dry sliding wear.

- Chapter 6 showed the importance of microstructural morphology to sliding wear performance, where the increasingly spheroidised microstructures exhibited a wear rate transition to the severe regime, resulting in gross metallic damage of the surface and high volume losses. In comparison, the slightly spheroidised microstructures and the pearlitic microstructures resisted these tendencies and produced only mild wear.

- Chapter 7 delved into four degrees of tempered martensite, and annealed ferrite/pearlite, for the same alloy, and evaluated their response to sliding wear. The annealed samples displayed various types of subsurface deformation such as deformed lamellae in the direction of sliding, strained ferrite grains, and a surface layer consisting of oxides, graphite, and carbides. The spheroidised carbides in a ferritic matrix experienced higher wear rates than the acicular martensitic samples due to their softer substrate being unable to support their oxide layer effectively.

These conclusions are novel within their sub-fields of tribology and improve the state-of-the-art of tribology relating to oxidative wear, the wear of cast irons, and the interplay of microstructural condition and wear volume losses. These findings achieve the aims set out at the beginning of the thesis, as they serve to improve the service life of industrial ferrous components and push the current understanding of tribology.

8.2.   Further Research

Further study is possible in numerous areas, to expand the conclusions of the thesis and give insight into tribological behaviour in alternative scenarios.

8.2.1.   Other Sliding Wear Geometries

This thesis discussed the unidirectional pin-on-disc sliding wear of engineering materials. There is great opportunity for future work to be conducted in a similar manner through application of alternative sliding geometries. In particular, it would be novel and experimentally valuable to produce similar data but in the reciprocating configuration, which would allow for good comparisons to be made into the effects of wear particle entrapment in the wear scar (as this usually happens less frequently in the reciprocating regime (see Section 1.6)).

Another sliding type worthwhile of further study is fretting wear. As the studied materials in this thesis are frequently employed in a variety of dynamic mechanical machinery, these would frequently be accompanied by vibration, such as when a car engine is running. There is therefore value in quantifying their resistance to fretting wear over long time periods.

8.2.2. *Effects of Nitriding Depth*

Future study is possible into the effect of varying the nitriding process on the wear resistance of 905 M39T steel. By varying the nitriding process, the resultant surface hardness would change and therefore influence the wear resistance. Microstructural characterisation of the nitrided surface layer could be accompanied by employing nano-indentation hardness measurements to allow for precise indentation placement on the surface of the individual nitride compound needles. Pin-on-disc tests could be left running for a longer duration to allow for appreciable wear to take place, followed by observation of the changing damage mechanisms with increasing scar depth (and therefore decreasing nitride content). In Chapter 4, the nitrided M39T samples were only used as a benchmark combination disc, and were therefore not subjected to intense wear or significant volume losses. By designing a study to exclusively focus on the nitrided samples, a greater understanding on the influence of nitriding wear resistance, and the effects of nitriding on tribo-oxidation could be obtained.

8.2.3. *Water-submerged Sliding Wear*

Chapter 5 examined the sliding wear of engineering alloys while submerged in NaCl solution, however, one of the key conclusions was that the tribocorrosive contribution to wear was minimal, and most of the effects of the regime were derived from being submerged in water. This could be evidenced more concretely by removing the NaCl effects and running the sliding wear tests while submerged in de-ionised, purified water.

By removing the NaCl and other ions, the majority of the chemical influence of the corrosive products is removed and therefore the influence of water alone could be identified. This would therefore allow further investigation such as whether or not the primary influence on wear is the cooling effect of the solution, or the reduced concentration of oxygen in the water compared to air.

8.2.4. *Graphite Flake Delamination*

Extensive experimental research is required to ascertain the delamination mechanics of graphite flakes from the surrounding matrix in grey cast irons. In the latter two experimental chapters of this thesis, graphite flakes were observed to deform in the direction of sliding, causing them to delaminate and leave a minute gap between the edge of the flake and the matrix (Figure 8.1). Numerous projects could investigate the

questions this raises regarding the sliding performance of cast irons, including the frequency of this occurrence for various sliding parameters and whether a certain severity of wear is required to cause this at a certain distance from the surface.

The incidence of delamination should be mapped according to distance from the surface, with the influence of orientation and shape taken into account. For example, the frequency of flake delamination should be compared to the rate of spheroidal graphite delamination for the same experimental parameters (and ideally, similar matrices). These could then be compared further by mapping the depth at which this can occur for each set of experimental parameters. These could be achieved with simple experimental procedures and basic SEM usage at reasonable magnifications.
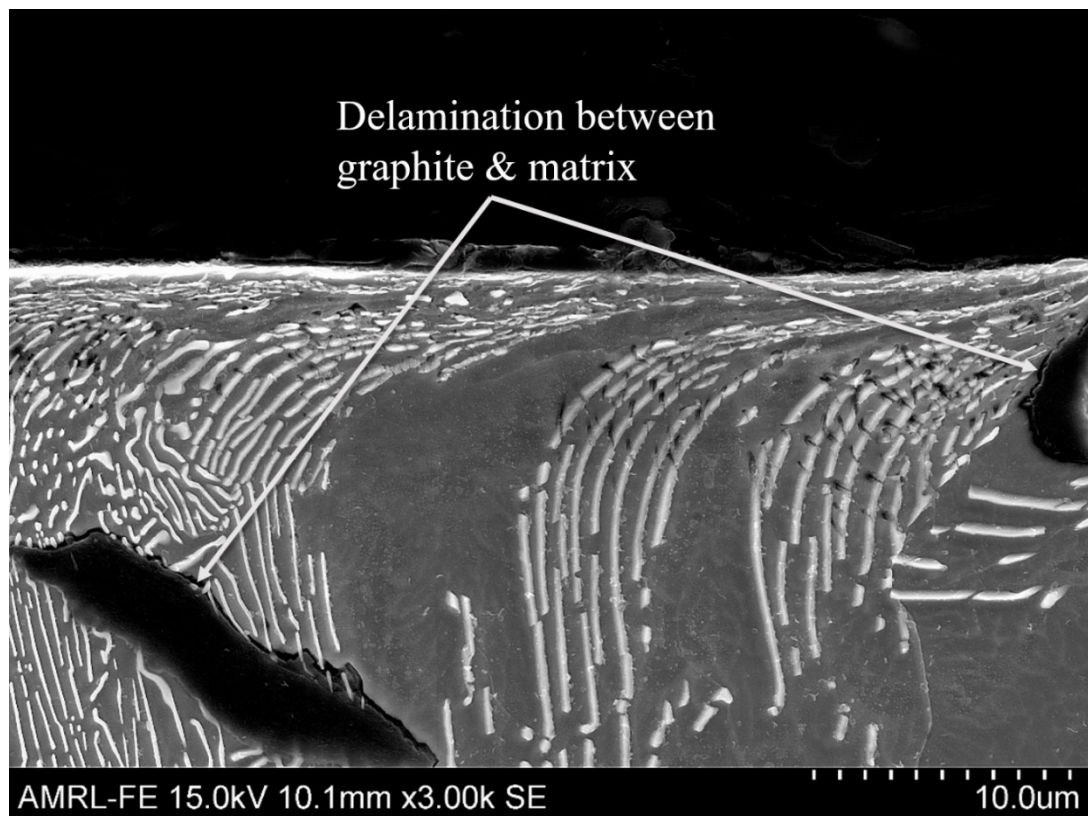

Figure 8.1 - Example of delamination between graphite flakes and matrix [x3000].

If taken further, more complex experimental procedures such as very high magnification SEM could be used to investigate the newly exposed surfaces of the matrix and graphite flake in question. This would give insight into the bonding that exists between the graphite flake and the cavity wall, and provide information on the solidification behaviour of the molten alloy. In cast iron melts, graphite precipitates

out of solution and solidifies first, due to its high melting point. It would be interesting to see the natural texture that graphite assumes upon solidification, and the effect this has on the surrounding matrix texture (a view of the imprinted matrix is shown in Figure 6.16).

Further experimental methods of value in this context are laser profilometry and x-ray computed tomography (XCT). XCT involves generating a 3D scan by passing x-rays through the sample. The behaviour of these x-rays, such as their refraction and reflection, allows for the mapping of internal features such as porosity. Applied to cast iron, the XCT would be able to build up a 3D model of the network of graphite flakes, and if using a fine enough resolution, may be able to differentiate between the graphite flakes and the cavity newly formed through delamination between the flakes and matrix.

The study of this has industrial relevance due to the primary damage mechanism of grey cast irons in sliding: spallation of graphite flake cavities. If the subsurface delamination of graphite flakes has any governance on the eventual spallation of the cavity roof then it is important to study this delamination effect to ascertain the influencing factors, which can then be minimised through: selection of alloy chemistry, control of microstructural condition, and variance of experimental parameters. If, for example, delamination of graphite flakes occurs more for ductile matrices such as ferrite than for brittle matrices such as martensite, then appropriate selection of martensite tempering temperature can be selected with this in mind. Of course, this would have to be balanced against other factors such as the resistance of the matrix to sliding wear at the surface.

Appendix 1 – Viva Notes

The viva for this PhD took place on Monday the 12th of September 2022 at the University of Strathclyde, Glasgow.

- **Date:** 12/09/2022
- **Time:** 0915 – 1300
- **Place:** Bell Room, Level 8, James Weir Building, University of Strathclyde
- **Internal Examiner:** Dr Reda Felfel, University of Strathclyde
- **External Examiner:** Prof. Tom Slatter, The University of Sheffield
- **Outcome:** Pass – minor corrections

The author is grateful to Dr Reda Felfel and Prof. Tom Slatter for the valuable discussions and constructive corrections that improved this thesis.